Die approbierte gedruckte Originalversion dieser Dissertation ist an der TU Wien Bibliothek verfügbar.
The approved original version of this doctoral thesis is available in print at TU Wien Bibliothek.
TU WIEN Bibliothek Your knowledge hub

TECHNISCHE UNIVERSITÄT WIEN
Vienna | Austria

Dissertation

Modelling and experiments of liquid phase healing in solder alloys.

carried out for the purpose of obtaining the degree of

Doctor technicae (Dr. techn.)

submitted at TU Wien, Faculty of Mechanical and Industrial Engineering, by

Mr. Georg Siroky, MSc.

Mat.Nr.: 00930349

2651 Reichenau an der Rax, Gartenweg 8, Austria

under the supervision of

Univ.Prof. Dipl.-Ing. Dr. Ernst Kozeschnik

Institute of Materials Science and Technology

Vienna, April 2021

Reviewed by

....

Prof. Aude Simar

Louvain School of Engineering

Place Sainte Barbe 2, 1348 Louvain-la-Neuve

Prof. Ralph Spolenak

ETH Zürich, Department of Materials

Vladimir-Prelog-Weg 1-5/10, 8093 Zürich

This work was supported by FFG within the framework of the project SOLARIS, project number: 864808.

I confirm that going to press of this thesis needs the confirmation of the examination committee.

Die approbierte gedruckte Originalversion dieser Dissertation ist an der TU Wien Bibliothek verfügbar.
The approved original version of this doctoral thesis is available in print at TU Wien Bibliothek.
TU WIEN Bibliothek Your knowledge hub

Affidavit

I declare in lieu of oath, that I wrote this thesis and performed the associated research myself, using only literature cited in this volume. If text passages from sources are used literally, they are marked as such.

I confirm that this work is original and has not been submitted elsewhere for any examination, nor is it currently under consideration for a thesis elsewhere.

City and Date | Signature

Acknowledgements

I would like to express my sincere gratitude to the members within the SOLARIS project who have offered me a unique opportunity to start my scientific career.

My sincere appreciations are dedicated to my thesis advisers, Dr. Werner Ecker and Prof. Ernst Kozeschnik for their guidance, help and constant support during my work. I would like to thank Dr. Elke Kraker, Dr. Julien Magnien, Mrs. Jördis Rosc and Dr. Roland Brunner for their technical and organizational support and the opportunity to work in their labs. I would like to thank Mr. Dietmar Kieslinger and Mr. Holger Rottmann for providing the framework of this exciting research project and their excellent teamwork.

I would like to especially thank Prof. Sybrand van der Zwaag for his exceptional mentorship and willingness to profoundly improve the quality and impact of our research.

I want to express my gratitude to Mr. Jakob Bayer for his active and motivated attitude that fundamentally helped to realize many aspects of the presented research. Furthermore, I am thankful to Mr. David Melinc for the fruitful collaboration and support he provided throughout our project.

I am thankful to my colleagues in the computational material design group at Materials Center Leoben. Thank you for many enjoyable discussions, coffee- and lunch breaks with Silvia Leitner, Oleg Peil, Maxim Popov, Lorenz Romaner, Vsevolod Razumovskiy, Andreas Drexler, Konstantin Prabitz and many others.

I am deeply grateful to my parents Waltraud and Erwin Siroky, who have equipped me with the required curiosity, interest, work-ethic and dedication to endure an academic path that has led me further than anyone expected. I also thank my siblings Catharina and Stefan for their advice and support during doubtful days.

My sincere gratitude is dedicated to my life-partner Marzieh Ovesy, who was a constant source of motivation, inspiration and reassurance during these busy and doubtful years of PhD life.

Thank you all!

Die approbierte gedruckte Originalversion dieser Dissertation ist an der TU Wien Bibliothek verfügbar.
The approved original version of this doctoral thesis is available in print at TU Wien Bibliothek.
TU WIEN Bibliothek Your knowledge hub

Die approbierte gedruckte Originalversion dieser Dissertation ist an der TU Wien Bibliothek verfügbar.
The approved original version of this doctoral thesis is available in print at TU Wien Bibliothek.
TU WIEN Bibliothek Your knowledge hub

Quoting the famous

is the trait of confined minds.

(unknown)

Table of Contents

Page

Abstract

Kurzfassung

Part I. Introduction **1**

1.1 Motivation 1

1.2 Economics of healing 2

1.3 Physics of healing 4

1.4 Mechanics of solder joints 12

1.5 Alloy composition and characterization 18

1.6 Summary & outlook 22

Part II. Scientific papers **24**

2.1 Lap Shear Test for solder materials: Local stress states and their effect on deformation and damage 25

2.2 A micromechanics-based model for liquid-assisted healing 45

2.3 Modelling of void collapse with Molecular Dynamics in pure Sn 67

2.4 Effect of solder joint size and composition on liquid-assisted healing 70

2.5 Analysis of Sn-Bi solders: X-ray micro computed tomography imaging and microstructure characterization in relation to properties and liquid phase healing potential 91

2.6 Simulation and experimental characterization of microporosity during solidification in Sn-Bi alloys 117

Literature

Die approbierte gedruckte Originalversion dieser Dissertation ist an der TU Wien Bibliothek verfügbar.
The approved original version of this doctoral thesis is available in print at TU Wien Bibliothek.
TU WIEN Bibliothek Your knowledge hub

Abstract

The degradation of solder joints is a limiting factor of microelectronics reliability. Thermo-mechanical loads initiate mechanical defects, such as cracks or voids, which leads to failure. An innovative approach to achieve higher damage resistance is to incorporate healing mechanisms in materials. The concept of liquid-phase healing in solders is investigated in the present work with contributions to solder characterization, micromechanical modelling of damage and healing, size and composition effects of healing in solder joints, 3D microstructural characterization of potential healing alloys and their solidification behavior.

The lap-shear experiment is a widely used method to characterize solder alloys under shear loads, which is the dominant deformation mode in solder joints. In order to quantify the beneficial effect of liquid-phase healing at early stages of damage formation, sensitive measurement methods are necessary. Experiments and computer simulations are used to assess shear properties under varying sample geometries.

The healing evolution of existing continuum mechanical models is based on phenomenological relations. A damage-healing model is proposed based on void collapse in liquid phase, which takes the defect-size into account. Furthermore, it gives the formal relationship of liquid-viscosity, surface tension, external loads and healing. Void collapse is modeled by means of the Rayleigh-Plesset equation and its applicability to the nanoscale is studied through molecular dynamics simulations. The healing evolution in solder joints arises from the solder joint size and its composition, which is formulated in a continuum-mechanical model. Capillary forces induce viscous material transport and increase the healing rate with smaller solder dimensions. The role of microstructural mobility depends on the presence of a liquid-phase network, which is accounted for by a model parameter, where high microstructural mobility enhances the healing rate.

Sn-Bi alloys are investigated through 3D X-ray micro computed tomography, which shows the variation of liquid phase morphology and its dimensions with regards to solder composition. The microstructure of potential healing alloys is categorized through morphology parameters and finite-element models are deduced from 3D data. Experiments and simulations highlight microstructural requirements of healing alloys under liquid-phase healing.

Part I of the present work introduces general concepts of solder joint mechanics, healing and imaging methods. Part II is comprised of six papers published in recognized scientific journals.

Die approbierte gedruckte Originalversion dieser Dissertation ist an der TU Wien Bibliothek verfügbar.
The approved original version of this doctoral thesis is available in print at TU Wien Bibliothek.
TU WIEN Bibliothek Your knowledge hub

Kurzfassung

Mikroelektronische Baugruppen bestehen aus Bauelementen die mittels Lotpunkten verbunden werden. Lote müssen mechanische Stabilität und elektrische Leitfähigkeit ermöglich und werden durch thermo-mechanische Lasten geschädigt. Ermüdung von Loten ist daher ein kritischer Faktor für Zuverlässigkeit von elektronischen Baugruppen und ist ein aktives Forschungsfeld. Lotwerkstoffe mit Heilungseigenschaften bieten einen neuartigen Zugang zur Verbesserung der Schädigungstoleranz von Lotverbindungen. Das Konzept der Flüssigphasenheilung wird in der vorliegenden Arbeit mittels theoretischen Modellen, Experimenten sowie 3D Bildgebungsverfahren untersucht.

Der Schubversuch ist ein häufig eingesetztes Experiment zur Bestimmung der Scherfestigkeit. Der Heilungseffekt bei geringer Schädigung erfordert Messmethoden mit hoher Genauigkeit, die durch geometrische Variationen der Probengeometrie oder systematischen Messfehlern beeinflusst werden. Die vorliegende Arbeit untersucht daher den Einfluss der Probengeometrie auf die Schereigenschaften sowie die Spannungszustände im Lot.

Bestehende Schädigungs-Heilungsmodelle basieren auf phänomenologischen Annahmen über die Heilungsevolution. Ein verbessertes Verständnis der physikalischen Zusammenhänge beim Flüssigphasenheilen wird durch Porenkollaps via Rayleigh-Plesset Gleichung beschrieben. Der Zusammenhang von Porengröße, Flüssigkeitsviskosität, Oberflächenspannung und äußeren Druck wird darin formal hergestellt. Die Anwendbarkeit des vorgeschlagenen Modells auf kleine Dimensionen wird mittels Molekulardynamik Simulationen gezeigt.

Die Heilungsevolution auf Lotpunktebene wird durch Größeneffekte und Mobilität der Mikrostruktur bestimmt. Geringe Lotspaltdicke führt zu höheren Kapillardrücken und zu beschleunigtem Materialtransport während der Heilungsphase. Die mikrostrukturelle Mobilität ergibt sich aus dem Anteil sowie der Morphologie der Flüssigphase. Diese Faktoren werden in einem kontinuums-mechanischen Modell zusammengefasst und Modellergebnisse mittels Experimenten interpretiert. Potentielle Heilungslegierungen aus dem binären Sn-Bi System werden untersucht. Mithilfe von röntgenbasierter Mikrotomographie werden Mikrostrukturparameter und Morphologie der Flüssigphase charakterisiert sowie Finite Elemente Modelle zur Simulation des Erstarrungsverhaltens abgeleitet.

Teil I der vorliegenden Arbeit beschreibt den aktuellen Stand der Technik und liefert allgemeine Grundlagen zur Mechanik von Lotpunkten, Heilung und Bildgebungsverfahren. Teil II besteht aus sechs wissenschaftlichen Arbeiten die in Fachzeitenschriften veröffentlicht wurden.

Die approbierte gedruckte Originalversion dieser Dissertation ist an der TU Wien Bibliothek verfügbar.
The approved original version of this doctoral thesis is available in print at TU Wien Bibliothek.
TU WIEN Bibliothek Your knowledge hub

Part I. Introduction

1.1 Motivation

The development of miniaturized and reliable microelectronic products motivates the exploration of new solder alloys, where solder joints provide mechanical connectivity and electric conductivity [1]. Mechanical degradation of solder joints arises from multi-physical loads during service and is a limiting factor for product lifetime [2–4]. A thorough understanding of damage-mechanisms and new strategies for improved reliability remains subject of current research and has led to a variety of solder compositions. The central objective for solder development is a high resistance against damage nucleation and propagation [5] under thermo-mechanical loads [6], electro- and thermo-migration [7] or corrosion [8]. The damage prevention paradigm [9] aims for new materials with improved damage resistance and has led to significant improvements among all material classes [10]. In this concept, material degradation or damage is not fully prevented and, depending on loads and service time, replacement of parts or materials will be necessary [9]. Without intervention, damage will either grow or remain in the material and reduces the safety margin to sustain rare events, such as, e.g. impact.

The damage management paradigm is a novel alternative to the damage prevention concept and employs self-repair or healing to improve the materials damage resistance [9] and provides a new path to improved reliability in electronics [11]. Nature has developed remarkable materials that implement both concepts of damage prevention and healing concurrently, such as, bone [12] or wood [13]. Yet, engineering materials with healing capabilities are still in their infancy [9]. Various healing concepts were studied in manmade materials, such as, polymers [14], concrete [15], ceramics [16] and metals [17] and highlight the damage management paradigm as a feasible and practical approach for future materials. The present work investigates several relevant aspects of healing in solders, such as, materials testing, continuum mechanical modelling and microstructural requirements of potential alloys, which incorporate liquid phase healing.

Part I of the present work presents aspects of general importance and provides necessary background information to motivate why healing solders should be explored beyond the current state of the art. Section 1.2 summarizes the economics of healing and defines functional units

Die approbierte gedruckte Originalversion dieser Dissertation ist an der TU Wien Bibliothek verfügbar.
The approved original version of this doctoral thesis is available in print at TU Wien Bibliothek.
TU Wien Bibliothek Your knowledge hub

of healing solder joints. Section 1.3 is dedicated to the physics behind healing and explains the mechanics, transport mechanisms and thermodynamic aspects. Section 1.4 provides the most essential damage modes in solder joints and discusses the possibility for liquid-phase healing. Section 1.5 concludes with additional information about example healing alloys and experimental methods in the present work.

Part II is comprised of scientific publications in recognized journals that deal with theoretical and experimental aspects of damage and healing in solders. The paper in 2.1 analyzes the lap-shear experiment by means of finite element (FE) simulations and provides a correction method to obtain objective material properties. In paper 2.2, a micro-mechanical model is developed to describe void healing on material scale, which highlights the effect of liquid viscosity, external loads and surface tension on void healing. In paper 2.3, the collapse of a void on nanoscale is simulated by means of molecular dynamics (MD) simulations and results are compared with the Rayleigh-Plesset equation. Paper 2.4 introduces a continuum damage-healing model and simulations on solder joint level are performed to analyze effects such as, solder joint size and solder composition during healing. Paper 2.5 investigates five solder composition of varying Bi content by means of X-ray micro-computed tomography (μ-XCT), where their microstructure is categorized based on morphology parameters and their potential for liquid phase healing is discussed. Paper 2.6 investigates the role of microporosity formation during solidification through FE simulations and experiments.

1.2 Economics of healing

Material development is motivated by technical and economic improvement of products. The economic benefit of solders in electronic products is diverse and manifests itself, e.g., in improved fatigue resistance [18], higher strength [19] or a substitution of hazardous alloying elements, such as, Pb [20]. This is typically achieved by developing new solder alloy compositions and involves elements such as Sn, Bi, Ag, Cu, Sb, Zn or Al, among others [20–22]. The solder composition largely determines its cost and is considered at early stages of alloy development. Several economic aspects are considered, such as, cost of raw materials, additional manufacturing efforts and recycling. Healing solders could provide an effective approach to extend the lifetime of products and contribute to a cost-efficient use of resources [23]. This section illustrates the expected additional effort for healing solder joints from an economics perspective, following the motto: “There is no free lunch”. A solder joint with

Die approbierte gedruckte Originalversion dieser Dissertation ist an der TU Wien Bibliothek verfügbar.
The approved original version of this doctoral thesis is available in print at TU Wien Bibliothek.
TU WIEN Bibliothek Your knowledge hub

healing ability of mechanical damage will likely come with additional costs compared conventional solder joints. The additional cost can stem from more expensive raw materials for the healing alloy, higher manufacturing efforts or additional systems, which are necessary to technically enable healing. It is worth to consider, in theory, a critical point that determines the economic benefit of incorporating a healing functionality in solder joints. This can be achieved through a break-even analysis [24], where the monetary benefit B_{h} of a healing system overcompensates its additional costs C_{h} and is written as

$$BE = \frac{B_{\mathrm{h}}}{C_{\mathrm{h}}}. \tag{1}$$

The healing functionality creates an actual advantage if $BE > 1$. The monetary benefit B_{h} could be, e.g., a higher market price due to enhanced reliability. The additional cost of the healing solder joint can be formulated as

$$C_{\mathrm{h}} = C_{\mathrm{a}} + C_{\mathrm{m}} + C_{\mathrm{s}}\,, \tag{2}$$

where C_{a}, C_{m} and C_{s} are the additional cost factors of the healing alloy (or generally, healing material), manufacturing process and support systems respectively. Although values for these variables depend on the specific technical product and manufacturing process, these considerations reveal two simple relations of a healable solder joint. First, a small monetary benefit as a result of the healing functionality could be sufficient, if it comes with low additional cost. Second, the three factors of additional cost C_{a}, C_{m} and C_{s} are equally important for the economic benefit of a healing system. The additional cost of a healing alloy can be quantified in comparison with current standard solders, such as, Sn-Ag-Cu (SAC) alloys and is primarily dictated by the market price of raw materials. Healing is enabled by a specific healing microstructure of solder joints and could cause additional manufacturing costs due to, e.g., surface finish, heat treatment or product manipulation. Finally, additional systems might be necessary to control or monitor the healing process [25]. Such components could deploy heat locally to accelerate healing [26], provide mechanical strength to keep the solder joint stress-free during healing [27] or provide condition monitoring to activate healing on demand [28]. Although these considerations seem rather theoretical, they provide a systematic decomposition of functionalities into healing alloy, manufacturing efforts and support systems. Healing of solder joints, therefore, should be viewed as a system property rather than a pure material property. Part II of the present work will address technical aspects of healing solder joints and alloys in more detail.

TU WIEN Bibliothek Your knowledge hub
Die approbierte gedruckte Originalversion dieser Dissertation ist an der TU Wien Bibliothek verfügbar.
The approved original version of this doctoral thesis is available in print at TU Wien Bibliothek.

1.3 Physics of healing

Mechanics of healing

The degradation of materials follows general physical principles and is governed by the 1st and 2nd principle of thermodynamics, which state conservation of energy and generation of entropy [29]. These fundamental principles also apply to healing, which can be understood as the reversing process of material degradation [30]. Before elaborating on theoretical aspects of healing, it serves the general understanding to motivate the mechanics of damage and healing in structural materials. Degradation in the present work is the formation of free surfaces, such as, cracks or voids on the micro-scale [31]. These form due to dissipative processes in the material and are, in case of ductile metals, proportional to inelastic material deformation. From a macroscopic perspective, these defects reduce the effective material cross-section and cause a gradual softening of the material. The stress-strain response of a hypothetical ductile material in Fig. 1 illustrates qualitatively the effect of damage and healing on the elastic stiffness. The elastic softening due to material degradation and healing is shown as "initial", "damaged" and "healed" in the stress-strain plot. The initial, damage-free material configuration exhibits the largest effective cross-section in absence of defects and, therefore, reveals the highest elastic stiffness, E_{I}. Although material imperfections, such as cracks or voids could be present in the initial configuration, the material is defined as damage-free [31]. Nucleation of new and growth of existing defects leads to material degradation and is shown in form of a lower elastic stiffness in the damaged configuration, E_{D}, in Fig. 1. A healing process has to reverse this evolution by local material transport and filling of mechanical defects. This increases the effective cross-section and subsequently leads to a regain of elastic stiffness in the healed configuration, E_{H}.

Die approbierte gedruckte Originalversion dieser Dissertation ist an der TU Wien Bibliothek verfügbar.
The approved original version of this doctoral thesis is available in print at TU Wien Bibliothek.
TU WIEN Bibliothek Your knowledge hub

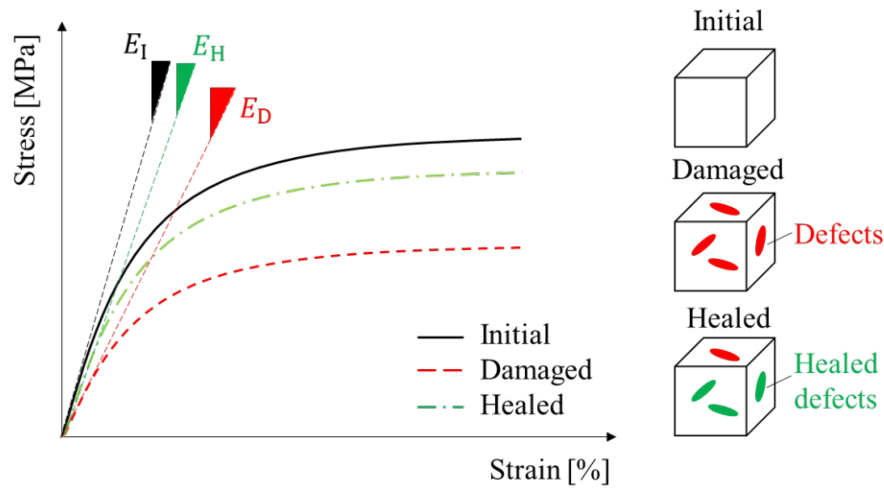

Fig. 1 Stress-strain response and elastic stiffness in initial, damaged and healed configuration

The concept of effective material cross-section is employed in the continuum-damage mechanics (CDM) theory developed by Chaboche and Lemaitre [32] and introduces a damage variable, D. It ranges from D=0 for the initial (undamaged) configuration to D=1 for the fully damaged configuration. The damage variable can be formulated in terms of material cross-section as

$$D = \frac{A_{\mathrm{D}}}{A_{\mathrm{I}}}, \tag{3}$$

where A_{D} and A_{I} are the damaged and initial cross-section area, respectively. A similar formulation using the elastic stiffness is achieved by inserting the elastic stress-strain relation under consideration of the strain equivalence principle [32]. The damage parameter is then written as

$$D = 1 - \frac{E_{\mathrm{D}}}{E_{\mathrm{I}}}, \tag{4}$$

with E_{D} the damaged elastic stiffness and E_{I} the initial elastic stiffness. One can propose a general relation among the three configurations, such as

$$E_{\mathrm{I}} \geq E_{\mathrm{H}} > E_{\mathrm{D}}. \tag{5}$$

These relations contain several assumptions about the healing process that are worth discussing. The first inequality states that the healed configuration, at its best, achieves the initial elastic stiffness. This requires complete defect filling with healing agent and ideal cohesion among healing agent and surrounding material. Additionally, it is assumed that the healing agent offers the same elastic properties as the original material. In the context of liquid phase healing, this assumption is reasonable because healing is achieved by partial melting, where the chemical composition of the material remains unchanged [33]. Yet, in a more general case, healing

Die approbierte gedruckte Originalversion dieser Dissertation ist an der TU Wien Bibliothek verfügbar.
The approved original version of this doctoral thesis is available in print at TU Wien Bibliothek.
TU Bibliothek WIEN Your knowledge hub

beyond the initial material properties is possible and is referred to as "super healing" [34]. It requires the formation of a healing agent of different chemical composition than the original material and might involve formation processes based on oxidation or diffusion [16]. Nevertheless, defect healing by partial melting is unlikely to lead to properties superior to its initial values.

The second inequality states the requirement for effective regain of material properties. Besides elastic stiffness, healing could possibly improve other degraded properties, such as, e.g. strength, toughness or strain at fracture. Therefore, similar relations as the one stated in eq. (5) could be re-formulated for other properties of interest. According to Barbero et al. [35], a continuum damage-healing formulation requires a healing variable, *H,* which is written as,

$$H = \epsilon_{\mathrm{H}} D, \tag{6}$$

where the proportionality factor, ϵ_{H}, describes the healing efficiency after consuming the full healing potential. The healing efficiency can be obtained, for example, from cyclic experiments and it is written in form of elastic stiffness as

$$\epsilon_{\mathrm{H}} = \frac{E_{\mathrm{D}} - E_{\mathrm{H}}}{E_{\mathrm{I}} - E_{\mathrm{H}}}. \tag{7}$$

The healing efficiency describes the maximum possible recovery of material properties, where no healing occurs if $\epsilon_{\mathrm{H}} = 0$ and full recovery is achieved if $\epsilon_{\mathrm{H}} = 1$. It depends on the healing process [36]. The time required to unfold the maximum healing efficiency also depends on the healing mechanism and might be longer than the available time for healing. In such cases, the healing rate is written as

$$\eta = \frac{D(t) - D(t + t_{\mathrm{H}})}{t_{\mathrm{H}}}, \tag{8}$$

with t_{H} the healing time and $D(t)$ the time-dependent damage parameter. It depends on several factors, such as, defect size or temperature and can range in metals from seconds to hours [37]. The healing rate is essential, since it determines the technological benefit of the healing concept. Eqs. (7) and (8) require experimental assessment of the shape and degree of mechanical damage, which was reviewed by Tasan et al. [31] for several methods. Voyiadjis et al. [38] provides a generalized derivation of continuum damage-healing mechanics under consideration of thermodynamic healing potential and healing hardening.

TU Bibliothek Your knowledge hub WIEN
Die approbierte gedruckte Originalversion dieser Dissertation ist an der TU Wien Bibliothek verfügbar.
The approved original version of this doctoral thesis is available in print at TU Wien Bibliothek.

Healing mechanisms in metals

Several healing mechanisms in metals were investigated in the past and have demonstrated the principles of damage-healing on various length scales. An overview of the healing mechanisms reported in literature by Grabowski and Tasan [39] is shown in Fig. 2.

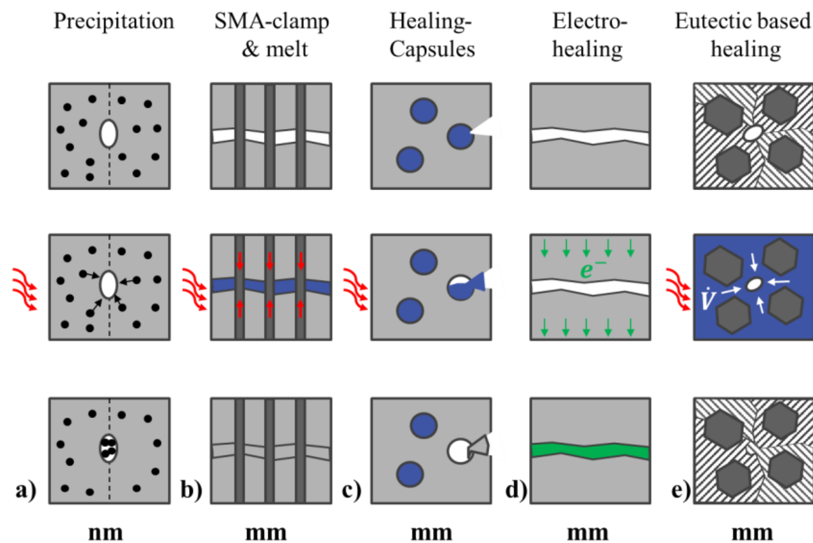

Fig. 2 Healing concepts and their transport mechanism of healing agent a) precipitation of healing agent from solid solution b) Shape memory wires embedded in low melting matrix b) healing capsules containing low melting healing agent d) electro-healing employing electric potentials for defect filling e) healing based on eutectic microstructure

Precipitation healing is illustrated in Fig. 2a and requires elevated temperatures and a supersaturated solid-solution microstructure. The solutes act as the healing agent and have a tendency to fill cavities, e.g., creep pores and extend the creep lifetime at elevated temperatures, which was demonstrated in Fe-based alloys [17,40]. Several solutes, such as, B [17], Au [40] or W [41] were investigated using X-ray computed tomography and revealed significant filling of creep pores. A specific requirement for this healing strategy is a high tendency of the solute to precipitate at free surfaces and a high nucleation barrier at internal precipitation sites, such as, grain boundaries or vacancies [37]. This concept works autonomously, where healing is initiated by the formation of defects. Yet, the healing process is limited by the amount of available healing agent and stops, once all solutes in the vicinity of the defect are consumed.

The shape-memory wire and clamp concept is illustrated in Fig. 2b and is based on the use of a fiber-reinforce metal matrix. Fibers made from shape memory alloys are embedded in a low-melting matrix material and bridge cracks in the matrix [42]. The martensite-austenite transition temperature of the shape memory wires is designed to coincide with the solidus temperature of the matrix material and induces a compressive force on the cracks [43]. The liquid phase in the matrix then fills cracks under compressive conditions and a regain of effective cross-section is

Die approbierte gedruckte Originalversion dieser Dissertation ist an der TU Wien Bibliothek verfügbar.
The approved original version of this doctoral thesis is available in print at TU Wien Bibliothek.
TU WIEN Bibliothek Your knowledge hub

achieved after solidification of the matrix. In principle, this concepts allows repetitive healing since the liquid matrix acts as the healing agent. A crucial limitation for structural applications is the loss of strength during the healing phase [37]. Yet, the experimental studies of Manuel et al. [33] and Fisher et al. [42] demonstrated the possibility of healing large cracks within several minutes.

The healing capsule concept is shown in Fig. 2c, making use of a low-melting healing agent embedded in a high-melting matrix. The healing agent is encapsulated in a fracture sensitive membrane, which is perforated by propagating cracks through the matrix. Healing is achieved by an external thermal trigger, which heats the material above the solidus temperature of the healing agent. Capillary forces infiltrate the crack with healing agent and exhibit a higher resistance against crack propagation after cooling [44]. The absence of external material transport prevents a complete filling of damaged cross-section and implies that the healing effect is limited to an increased resistance against crack propagation [39].

Electro-healing is illustrated in Fig. 2d and summarizes different healing concepts that are all governed by applying electric potentials. The pulsed current method was studied in structural steels and uses high electric currents to impose a compressive crack closing force [45,46]. Depending on the geometric dimensions of a crack and its orientation with respect to current flow, an electric field develops around the crack. If cracks are sufficiently small, they can collapse and lead to a regain of cohesive strength. A practical limitation of this method are the high electric currents to achieve crack-closing and the small dimensions of potentially healable damage. A different concept by Hsain et al. [47] utilized healing through galvanic deposition. The structural material consists of a metallic foam coated with a brittle polymer. Fracture of foam struts exposes the structural metal to an electrolyte. An external electric potential and the composition of the electrolyte allow material deposition at the fracture site. The energy consumption of this concept compared to thermally activated healing mechanism is several orders of magnitudes lower and allows healing of metallic foams at room temperature [37]. Despite the impressive healing results, it should be noted that providing the electrolyte in a practical material could require additional efforts.

The eutectic-based healing concept is illustrated in Fig. 2e, which is investigated in the present work. An external healing trigger heats the material above its solidus temperature, where liquid eutectic phase serves as the healing agent. Defects that form in the eutectic phase or at the interface of primary and eutectic phase can be filled through viscous material flow. After cooling below the solidus temperature, a regain of effective material cross-section could

Die approbierte gedruckte Originalversion dieser Dissertation ist an der TU Wien Bibliothek verfügbar.
The approved original version of this doctoral thesis is available in print at TU Wien Bibliothek.
TU WIEN Bibliothek Your knowledge hub

improve the load-carrying capacity. The effectiveness of this strategy is determined by the optimal microstructure that permits enough material flow. Similar to other healing strategies that utilize a solid-liquid phase transformation, the load-carrying capacity during healing is limited. Furthermore, it could be necessary to apply external loads on the material to enhance viscous material transport. The healing rate according to eq. (8) is determined by microstructural parameters, such as, liquid phase fraction, permeability, liquid channel thickness and liquid viscosity, among others.

The common principle among these healing concepts is local material transport that aims to fill voids or cracks. The illustrated examples in Fig. 2 utilize diffusion, viscous flow and electro-chemical transport mechanisms. More details on various healing mechanisms in metals can be found in [37,39].

Thermodynamics of healing

The previous sections illustrate that healing is a material transport process and, therefore, is governed by the laws of thermodynamics. Healing, like any other transport process, requires energy and a physical driving force [29]. Depending on the healing energy source and driving force, one can distinguish between "extrinsic-" and "autonomous healing". The latter provides the required energy for material transport within itself and the driving force for healing is generated by the degradation process [37]. The precipitation healing concept illustrated in Fig. 2a is an excellent example for this principle. The energy for material transport is stored in the solid solution microstructure during quenching. The use of solutes, such as, Au or B in Fe allows a site-specific precipitation, where the high tendency to form in creep pores provides the damage-dependent driving force. In contrast, liquid phase healing in Fig. 2e, is an example of extrinsic healing. The required energy enabling material transport has to be provided externally by a heat pulse [26]. A healing driving force can be induced by internal forces, such as, surface tension or capillary pressure in the liquid network or, alternatively, by external stimulus, such as, external hydrostatic pressure. A formal description of these relations and a discussion of involved parameters are given by employing the damage theory based on entropy production developed by Basaran and Yan [48]. The total entropy variation of a system can be written as

$$\mathrm{d}S = \mathrm{d}S_\mathrm{e} + \mathrm{d}S_\mathrm{i}, \tag{9}$$

where $\mathrm{d}S_\mathrm{e}$ is the external entropy transfer, e.g. through heat flow and $\mathrm{d}S_\mathrm{i}$ is the internal entropy production. For irreversible processes, the system internal entropy production has to satisfy

$$\mathrm{d}S_\mathrm{i} \geq 0, \tag{10}$$

Die approbierte gedruckte Originalversion dieser Dissertation ist an der TU Wien Bibliothek verfügbar.
The approved original version of this doctoral thesis is available in print at TU Wien Bibliothek.
TU Wien Bibliothek Your knowledge hub

while the external entropy production term can be positive, negative or zero, which is of great importance for healing. Basaran and Yan [48] introduced concepts from statistical mechanics to provide a new interpretation of the damage parameter D that leads further than the classical interpretation of reduced effective cross-section. Boltzmann formulated, in his famous equation, the connection between configurational states of a system and its absolute entropy as

$$S = k_0 \ln(W), \tag{11}$$

where k_0 is the Boltzmann constant and W is the disorder parameter describing the probability of finding the system in a given configuration. If the system has many possible configurations, its disorder and, subsequently, its entropy are high. Basaran and Yan [48] argue that the disorder W can be associated with mechanical degradation processes by rewriting Boltzmanns equation, with the disorder function as follows

$$W = e^{\frac{s\,\overline{m}}{R}}, \tag{12}$$

where $\overline{m}$ is the specific mass, R is the gas constant and s is the entropy per unit mass. A damage variable is now introduced by defining the change in disorder with respect to an arbitrary reference configuration W_0 and can be written as

$$D = \frac{\Delta W}{W} = \frac{W - W_0}{W}. \tag{13}$$

Combining eqs. (12) and (13), Basaran and Yan [48] write the damage parameter in the form

$$D = 1 - e^{-\frac{\overline{m}}{R}(s - s_0)}, \tag{14}$$

which states that damage increases with entropy production compared to the reference state. This relation reveals important implications for healing. The degradation process leads to entropy production and, therefore, cause continuous increase of the damage parameter. If healing aims to reduce mechanical damage, it is necessary that the healing process has to counteract entropy production. According to eqs. (9) and (10), this is only possible by a negative external entropy contribution and by providing healing energy. The entropy evolution in eq. (14) is expressed by Basaran and Yan [48] in more detail by reformulating the Helmholtz free energy and inserting the explicit relation for entropy change in a passive (non-healing) system with

$$\Delta s = \int_{t_0}^{t} \frac{\sigma : \dot{\varepsilon}^{\mathrm{p}}}{T\,\rho} dt + \int_{t_0}^{t} \frac{k}{T^2\,\rho} |\nabla T|^2 dt + \int_{t_0}^{t} \frac{r}{T} dt. \tag{15}$$

Entropy generation is composed of three terms which describe different dissipation mechanisms. The first term in eq. (15) is mechanical energy dissipation and is proportional to

Die approbierte gedruckte Originalversion dieser Dissertation ist an der TU Wien Bibliothek verfügbar.
The approved original version of this doctoral thesis is available in print at TU Wien Bibliothek.
TU Bibliothek WIEN Your knowledge hub

the inelastic deformation rate $\dot{\epsilon}^{\mathrm{p}}$ and stress σ. The second term in eq. (15) represents energy dissipation by thermal transport. This equation is based on the Maxwell equation for conductive heat transfer, with k being the thermal conductivity and ∇T the gradient of the temperature field. The third term in eq. (15) is entropy generation by internal heat production, where r is the internal heat generated per unit mass. The entropy production is obtained by integrating in the interval of reference time t_0 and current time t, where ρ is the mass density. The relations in eqs. (14) and (15) now provide a direct link between damage and energy dissipation [48]. Basaran and Yan [48] deduce that energy dissipation by thermal or mechanical processes leads to growing disorder, e.g., by inducing cracks or voids and, therefore, increases the damage parameter D. In classical damage mechanics theory, this relation states that D has to increase or remain the same in order to remain coherent with 2nd law of thermodynamics. In order to include healing in this relation, eq. (15) has to be extended with an additional energy term, W_{h}, as

$$\Delta s = \frac{W_{\mathrm{d}}}{T} + \frac{W_{\mathrm{h}}}{T}. \tag{16}$$

The internally dissipated energy W_{d} is equivalent to the expression in eq. (15). The contribution of W_{h} has to enter with a negative sign in order to reduce the entropy generation and does not violate the 2nd law of thermodynamics if provided by an external energy source. A direct conclusion of eq. (16) is that the energy required to heal damage has to balance the dissipated energy according to eq. (15). This only marks the ideal case, where the healing process itself is free of any dissipative effects and assumes that the applied energy directly leads to a reconstruction of the original material configuration. The healing process itself can come at certain dissipative “cost”, such as viscous flow, friction or heat generation and, therefore, requires additional energetic effort for healing of mechanical damage. A general statement of the healing energy is formulated as

$$\|W_h\| \geq W_{\mathrm{d}} + W_{\mathrm{hd}}, \tag{17}$$

where the value of W_{h} has to compensate the mechanical dissipation, W_{d}, and the inherent dissipation during the healing process, W_{hd}. Furthermore, it should be noted that the sign of W_{h} has to be negative in order to reduce entropy generation from the reference configuration of t_0.

Die approbierte gedruckte Originalversion dieser Dissertation ist an der TU Wien Bibliothek verfügbar.
The approved original version of this doctoral thesis is available in print at TU Wien Bibliothek.
TU WIEN Bibliothek Your knowledge hub

1.4 Mechanics of solder joints

Microelectronic assemblies are structured in functional units, where components, such as resistors, capacitors or light emitting diodes (LED), are connected through solder joints. They provide electric conductivity and mechanical strength of sub-assemblies and have to resist various loads that lead to degradation and failure. This chapter introduces the main failure and damage modes in solder joints and discusses the chance of liquid-phase healing under these damage mechanisms. The loading conditions can be categorized as:

- Thermal
- Thermo-mechanical
- Electric
- Corrosive

Thermal

Elevated temperatures lead to degradation of solder joints due to microstructural changes or aging. The standard for automotive electronic assemblies defines a temperature range between -20°C and +125°C for temperature shock tests, where the assembly is operated at ultimate temperatures up to 30 min. The Sn-Bi solders studied in the present work have a solidus temperature of 138°C and, therefore, operate at about 95% of their melting point. Commercial solders, such as, Sn-Ag-Cu (SAC) have a higher solidus temperature of 217°C, but still operate at 80% of their melting point during thermal cycling. High creep rates at elevated temperatures [49] and diffusion of elements from surrounding parts [50] (e.g. Cu) both contribute to mechanical degradation. The formation of intermetallic compounds (IMC) at the solder-substrate interface takes place due to diffusion of Cu atoms, where Sn-rich solder form Cu_3Sn and Cu_6Sn_5 [50]. The IMC layer provides effective mechanical strength between solder and substrate and is, therefore, necessary for solder joints. Yet, they also induce crack initiations sites due to the brittleness of IMCs and the formation of Kirkendall voids [51]. Furthermore, the crack path under shear loads is influenced by the IMC morphology, which was investigated in Sn-Bi solders by Goh et al. [52] and is illustrated in Fig. 3. Prism-like IMC layers in Fig. 3a form at reflow temperatures of 200°C, whereas the scallop-shaped IMC in Fig. 3b was found after reflow soldering between 230 to 260°C. Goh et al. [52] reported higher shear strength for samples with scallop-like IMCs, which they attributed to hardening due to Bi precipitation in

Die approbierte gedruckte Originalversion dieser Dissertation ist an der TU Wien Bibliothek verfügbar.
The approved original version of this doctoral thesis is available in print at TU Wien Bibliothek.
TU Wien Bibliothek Your knowledge hub

the Sn-Bi alloy at higher temperatures. They concluded that the interfacial strength of the prism-like IMCs must be higher than the scallop-shaped ones and, therefore, induces bulk failure rather than delamination at the IMC-solder interface.

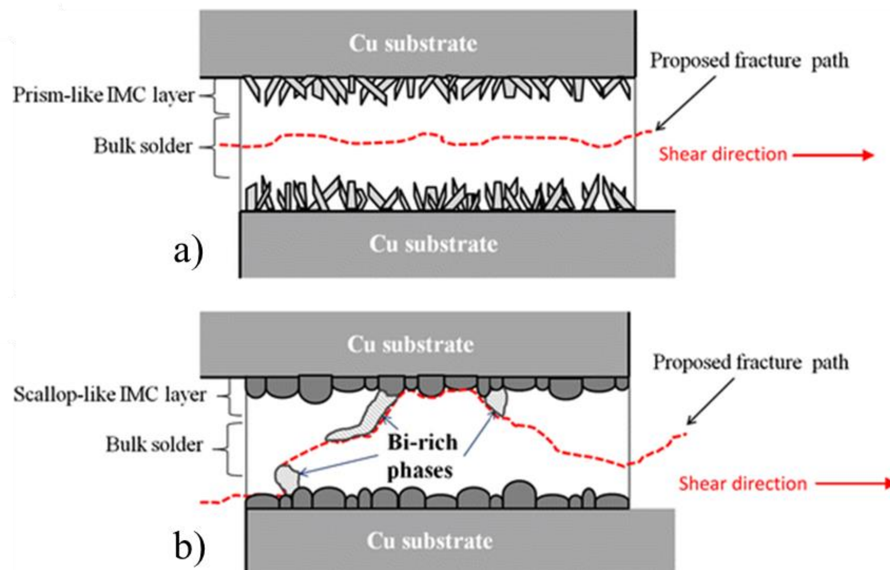

Fig. 3 Crack propagation under shear loads due to different IMC morphology a) Bulk failure of solder due to high strength of prism-like IMC layer b) Crack initiation at the interface induced by scallop-shaped IMC layer [52].

These findings pose a requirement for solders under liquid-phase healing. The solder composition and its melting point are shifted at the IMC interface, which limits the presence of a liquid healing agent at the interface. Therefore, bulk cracks, as the one illustrated in Fig. 3a, would be favorable for liquid-phase healing, since the liquid-phase network remains intact and promotes viscous flow of healing agent.

Thermo-mechanical

Thermo-mechanical fatigue is a common failure mode and depends on joint size and solder composition [53]. The ambient temperature change together with a mismatch of thermal expansion coefficients of solder, substrate and component induces mechanical stresses. A high number of temperature cycles leads to crack-initiation and propagation. The initiation sites differ depending on the grain morphology and crystallographic orientation. Martin et al. [54] investigated the role of grain-boundary orientation in SAC solders and found that large angle grain boundaries are favorable crack initiation sites. Erinc et al. [55] investigated this more closely through in-situ thermo-mechanical experiments and numerical simulation. They found that grain boundaries with an orientation mismatch > 15° were prone to void formation. Fig. 4. illustrates early stage defects arising from thermo-mechanical fatigue in flat samples with

Die approbierte gedruckte Originalversion dieser Dissertation ist an der TU Wien Bibliothek verfügbar.
The approved original version of this doctoral thesis is available in print at TU Wien Bibliothek.
TU Bibliothek WIEN Your knowledge hub

respect to the crystallographic orientation of the surrounding grains [55]. The grain-boundary mismatch is shown in Fig. 4a, where blue to black lines indicate a grain boundary mismatch of > 15° and are potential crack initiation sites [55]. The crystallographic orientation of grains is given in Fig. 4b. The SEM cross-section in Fig. 4c highlights the correlation of grain boundary mismatch and mechanical damage [55]. The voids (black) in the center of Fig. 4c are areas of de-cohesion among neighboring grains, with a grain boundary mismatch between 60° to 70° according to Fig. 4a. The early onset of void formation in Sn - 4wt.% Ag - 0.5 wt.% Cu solders was reported after 500 thermal cycles [55].

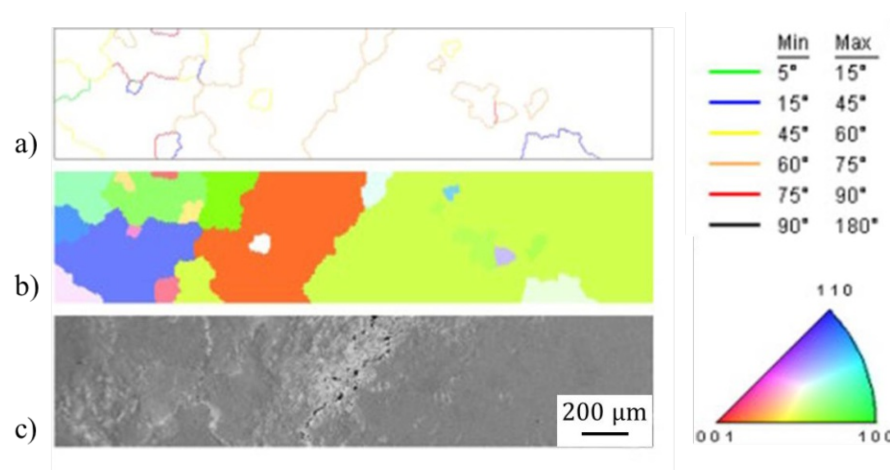

Fig. 4 Damage sites and their corresponding crystal orientation and grain-boundary mismatch after 500 temperature cycles a) Grain-boundary angle b) Crystallographic orientation of grains c) SEM cross-section of voids at grain-boundaries d) SEM image with thermo-mechanical fatigue damage (black) [55]

The morphology in Fig. 4c motivated the formulation of liquid-phase healing by means of micromechanics and void collapse in Part II of the present work. The early stage of thermo-mechanical damage shows spherical defects that are about one order of magnitude smaller than microstructural features ,such as, grain size or eutectic phase thickness. It is assumed that healing of early stage defects in the range of 1 to 20 µm requires minor material transport for defect filling and will be determined by the presence and morphology of the liquid phase. Defects such as cracks will require large volumes of healing agent and could potentially stretch through domains with no healing agents (primary phase). This shows that liquid phase healing at later stages of thermo-mechanical fatigue might be limited by available volume of healing agent.

Electric

The specific electric current in solder joints increases with further miniaturization. Electromigration is material transport due to electron current concentration and leads to erosion at the cathode side, as shown in Fig. 5. The threshold, where degradation due to

Die approbierte gedruckte Originalversion dieser Dissertation ist an der TU Wien Bibliothek verfügbar.
The approved original version of this doctoral thesis is available in print at TU Wien Bibliothek.
TU Bibliothek WIEN Your knowledge hub

electromigration becomes critical, is in the order of $10^3\ \mathrm{A/cm^2}$. Voids nucleate and grow parallel to the substrate as illustrated in Fig. 5a, where the SEM cross-section in Fig. 5b confirms the void formation at sites of local current concentration [56]. It was observed by Chang et al [57] through numerical simulation and 3D in-situ synchrotron laminography that multiple discrete voids form due to nucleation and growth in the early stage of electromigration. Consecutive agglomeration of these voids leads to large single voids close to areas of electric current concentrations. The initial voids are scattered around these concentration sites and were observed close to the solder-substrate interface at the cathode side of the solder joint.

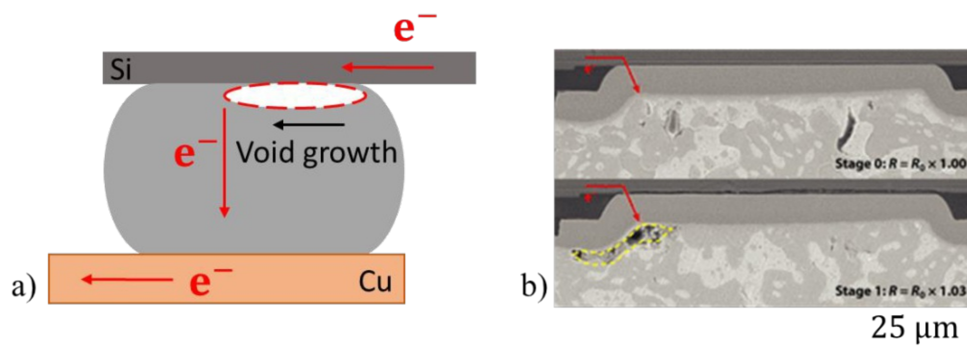

Fig. 5 Electromigration in solder joints a) Void formation at cathode side of solder joint with void growth direction parallel to substrate b) SEM cross-section of solder joint with voids under electromigration marked in yellow [56].

Electromigration has a significant influence on the microstructural evolution of Sn-Bi solders. Chen et al. [58] investigated the microstructural evolution of eutectic Sn-Bi solder under electromigration. They reported that Bi is the main diffusing species in eutectic Sn-Bi solders. The high mobility of Bi under current stressing leads to Bi depletion at the cathode and deposition at the anode, which is illustrated in Fig. 6. In this process, the alloy composition is considerably changed and a shift of the melting point towards higher temperatures at the cathode can be assumed. The SEM micrographs at the cathode in Fig. 6a shows a low content of Bi-rich phase, which reduces the presence of liquid phase. The contrary effect is observed at the anode side in Fig. 6b, where high fractions of Bi are deposited at the interface.

Die approbierte gedruckte Originalversion dieser Dissertation ist an der TU Wien Bibliothek verfügbar.
The approved original version of this doctoral thesis is available in print at TU Wien Bibliothek.
TU WIEN Bibliothek Your knowledge hub

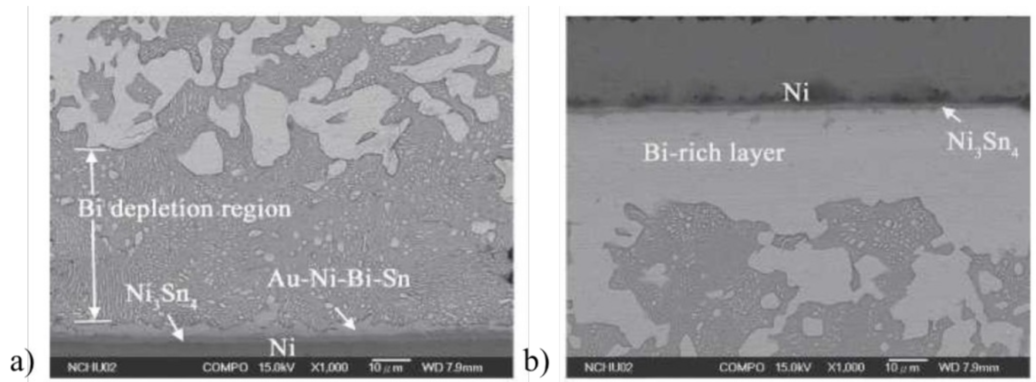

Fig. 6 Microstructural evolution of eutectic Sn-Bi solder joints under electromigration a) Bi depletion due to high diffusivity at the cathode b) Bi deposition at the anode side [58]

In principle voids, formed by electromigration could be repaired through liquid-phase healing. Yet, limitations arise due to damage locations close to the solder-substrate interface, where the solder composition is changed due to electromigration and limits the presence of liquid phase. Voids form primarily at the cathode side at locations of electric current concentrations. In case of eutectic Sn-Bi solder joints, a depletion of Bi-rich phase was observed at the cathode, which prevents the presence of healing phase in the vicinity of voids. This shows that healing of electromigration-induced damage will likely come with additional challenges due to microstructural changes.

Corrosion

Electronic assemblies are often exposed to harsh environments, such as, corrosive media. Therefore, it is important to discuss the possibility of employing liquid-phase healing to repair corrosive damage. The effect of corrosive media, such as, NaCl solutions was investigated on SAC and Sn-Bi solders and causes selective microstructural degradation. In SAC solders, the presence of Ag_3Sn leads to dissolution of Sn into the corrosive medium due to galvanic corrosion mechanisms [59]. Similarly, the corrosion of Sn-Bi solders largely affects the Sn-rich primary phase and leads to a significant degradation of mechanical properties. Fig. 7 shows the onset of corrosion damage in Sn-58 wt.% Bi solder joints after 96 h of exposure to the corrosive medium, which was reported by Mostofizadeh et al. [8]. The overview cross-section in Fig. 7a shows the progression of corrosive degradation from the surface. A magnified view in Fig. 7b of the solder joint microstructure reveals the remaining of Bi-rich eutectic phase (white), whereas the primary phase structure dissolved.

Die approbierte gedruckte Originalversion dieser Dissertation ist an der TU Wien Bibliothek verfügbar.
The approved original version of this doctoral thesis is available in print at TU Wien Bibliothek.
TU Bibliothek WIEN Your knowledge hub

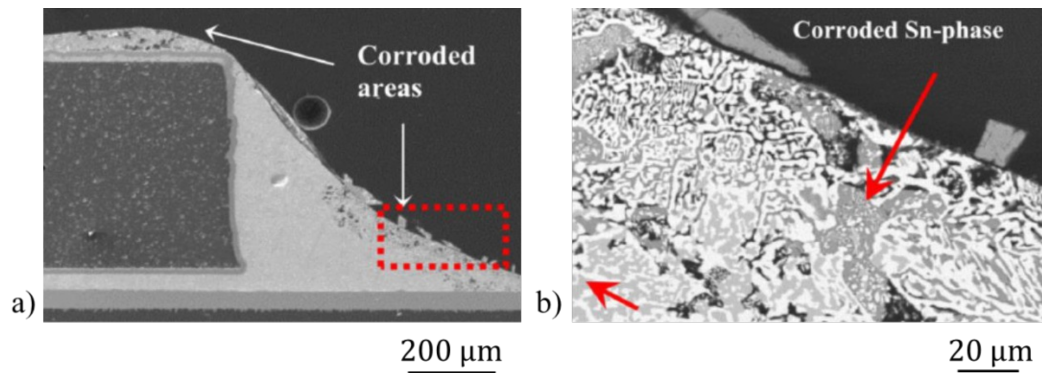

Fig. 7 SEM cross-sections of corrosion damage under salt spray test of Sn-58wt.%Bi solder joint a) Overview of solder filet with surface corrosion b) Corrosion damage of Sn-rich primary phase (dark grey) [8]

This example illustrates some challenges of repairing corrosion damage through liquid-phase healing. First, most corrosive damage develops from the surface area, where transport of healing agent might be limited by the free surface. Second, the liquid-phase healing concept builds upon a liquid network to provide healing agent. It is likely that viscous materials transport, which is driven by capillary forces, is obstructed by the dissolved primary phase in Fig. 7b and, at best, allows partial healing.

Summary

The major damage mechanisms in solder joints were introduced and the potential for liquid-phase healing was discussed. The literature review revealed that thermo-mechanical fatigue generates defects that appear as spheroids or voids at early stages of fatigue and have dimension at least one order of magnitude lower than microstructural features. Locations of such defects are found at grain or phase boundaries and appear in the bulk of the material. It is therefore theorized that such damage morphology and location is most favorable for defect healing by viscous transport during liquid-phase healing, since the defect is fully surrounded by healing agent. Bulk failure in solder joints can be facilitated by growth of prism-like IMC layers, which leads to damage at locations of highest healing efficiency. This shows that manufacturing of solder joints with healing functionality could require additional heat treatment steps to employ healing. However, damage due to corrosion, electromigration and failure at the solder-substrate interface poses additional challenges due to the microstructural evolution that might prevent delivery of healing agent. The proposed models and the presented experimental characterization in Part II were carried out with the aim of describing the healing process after thermo-mechanical fatigue damage as illustrated in Fig. 4.

Die approbierte gedruckte Originalversion dieser Dissertation ist an der TU Wien Bibliothek verfügbar.
The approved original version of this doctoral thesis is available in print at TU Wien Bibliothek.
TU WIEN Bibliothek Your knowledge hub

1.5 Alloy composition and characterization

Example healing alloy: Sn-Bi

Potential alloys utilizing liquid-phase healing have to provide a two-phase region, where solid and liquid phases co-exist. Sn-Bi alloys are promising candidates for Pb-free solder alloys, commercially available and, therefore, suitable to investigate liquid-phase healing [60]. Several mechanical properties of Sn-Bi alloys were studied before, such as, creep [61], fracture [22,62], tensile strength [63] and surface tension [64], among others, and provided a basic set of parameters for the present work. The most relevant domains in the Sn-Bi phase diagram are shown in Fig. 8. The alloy has a eutectic composition at 56 wt.%Bi and a hypo- and hyper-eutectic two-phase domain. The healing region, enclosed by the points A-B-E, will be investigated more closely in the present work. The Bi-rich compositions of > 58 wt.% Bi show brittle material behavior and are excluded.

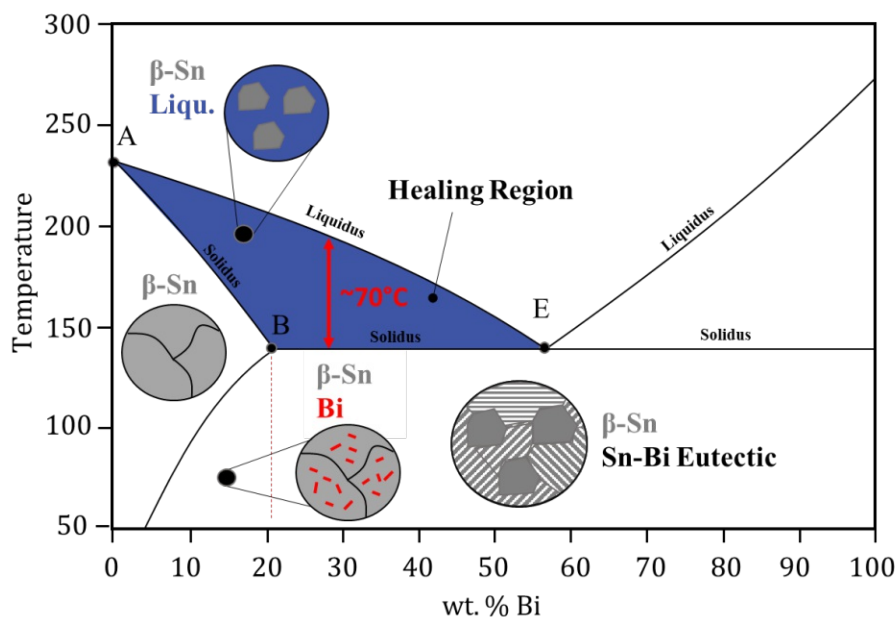

Fig. 8 Sn-Bi binary phase diagram, with semi-solid healing region A-B-E

Alloys with a Bi content between 0 and 20.5 wt.%Bi are composed of a Sn-rich primary phase with Bi in solid solution until 138°C and exhibit a temperature-dependent solubility of Bi. Fine Bi precipitates are found in the microstructure [62] at room temperature. Alloys with a Bi content between 20.5 and 56 wt.%Bi are composed of a eutectic phase, which melts instantly once the temperature is higher than the eutectic temperature of 138°C. The higher melting Sn-rich primary phase continuously melts until it exceeds the liquidus temperature. The melting

Die approbierte gedruckte Originalversion dieser Dissertation ist an der TU Wien Bibliothek verfügbar.
The approved original version of this doctoral thesis is available in print at TU Wien Bibliothek.
TU WIEN Bibliothek Your knowledge hub

range of the Sn- 30 wt.% Bi alloys is about 70°C, which decreases with increasing Bi content until the eutectic composition. The liquid phase fraction at the solidus temperature can be adjusted by varying the Bi content in the boundaries of point B and E in Fig. 8. The presence and morphology of a liquid-phase network is essential to achieve the desired healing effect, which is illustrated in Fig. 9. Ye et al. showed [22] that Sn-Bi alloys form defects preferably in the eutectic phase due to its brittle behavior. This provides a favorable case for liquid phase healing, since defects, such as the ones shown in Fig. 9a, are surrounded by healing phase. Defects at phase boundaries or fully within the eutectic phase are denoted as "healable". A temperature rise above T_S will melt the eutectic phase and viscous flow due to capillary forces fills defects as shown in Fig. 9b. The capillary forces depend on the morphology of liquid phase and determine the healing efficiency. The scientific papers in part II will formulate micromechanical models to describe viscous material transport and healing in a damage-mechanics framework. Furthermore, a 3D characterization of the liquid-phase network with respect to alloy composition in the Sn-Bi system is reported and the role of microstructural mobility for defect filling is investigated.

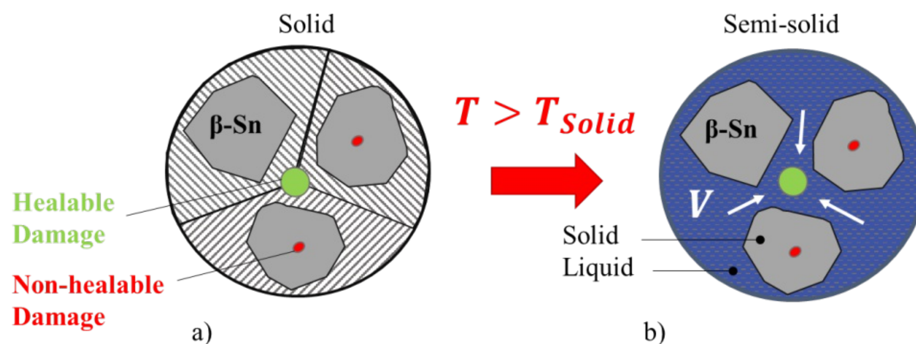

Fig. 9 Schematic of the liquid-phase healing concept a) Solid configuration with void-like defects in primary and eutectic phase b) Semi-solid (healing) configuration with viscous material flow from capillary forces

Light microscopy images of the healing process in a Sn-30 wt.%Bi alloy are given in Fig. 10. The initial crack in Fig. 10a was created in the cylindrical sample under tensile fatigue loading. A surface notch ensured crack initiation in the center of the sample. The sample was covered in silicon oil to avoid unwanted oxidation during healing. The sample length was kept constant during healing to induce compressive force during heating due to thermal expansion, which can be seen by crack closure in Fig. 10b. Once the crack surfaces are brought in close vicinity, a liquid film forms and fills the crack marked by black arrows in Fig. 10c. Fig. 10d shows the sample after cooling , where the crack is filled. These preliminary observations motivated the investigation of microstructural mobility and its effect on regain of mechanical strength in chapter 4 of part II.

Die approbierte gedruckte Originalversion dieser Dissertation ist an der TU Wien Bibliothek verfügbar.
The approved original version of this doctoral thesis is available in print at TU Wien Bibliothek.
TU WIEN Bibliothek Your knowledge hub

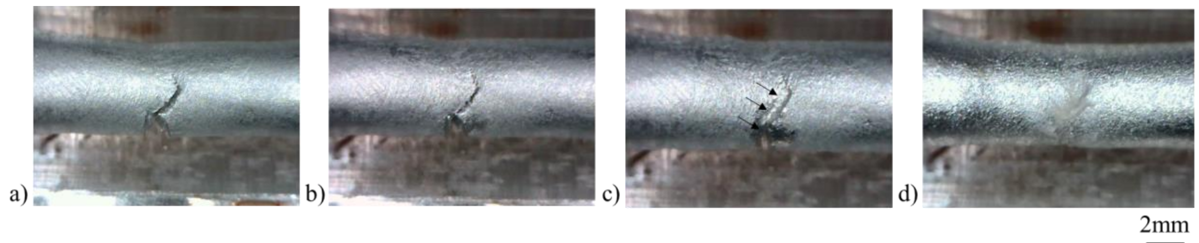

Fig. 10 Liquid-phase healing of a macroscopic crack in a cylindrical sample made from Sn-30 wt.%Bi alloy a) Initial crack after tensile loading b) Heating and compression due to thermal expansion c) Crack filling with liquid eutectic phase d) Healed crack after solidification

The liquid volume change at the solidus temperature is an important attribute of healing alloys. The usual case of liquid-solid phase transformation leads to volumetric shrinkage of the liquid phase. The Sn-Bi system exhibits a remarkable anomaly, which leads to volumetric expansion during solidification of the eutectic phase [65]. This could be potentially contribute to improved void healing upon solidification and will be investigated in the present work. Therefore, part II introduces a material model that implements the liquid-solid transition in a finite element framework, which is applied on 3D μ-XCT data of potential healing alloys of varying Bi content. The simulated solidification behavior is compared with experiments and poses additional requirement for liquid-phase healing alloys.

Materials testing

The development of new measurement techniques to determine material properties of solders is an active field of research [66,67]. Solder joints are loaded in shear dominated stress states with a stress-triaxiality close to pure shear. Yet, stress states can locally vary in solder joints due to shape variations and can range from multiaxial compression to multiaxial tension [68]. The lap-shear test is a widely used experiment to determine the elasto-plastic stress-strain response under monotonic [69] or cyclic deformation [70]. A common standard for the lap-shear test is missing, which has led to a variation of sample geometries in the literature. This allows at best a comparison of sample behavior within a study of same geometry and requires further analysis to distinguish between sample- and material properties. The advantageous effect of liquid-phase healing at early stage of fatigue damage might be small and requires accurate techniques and quantitative knowledge of uncertainty factors. The variance of measurements is caused by geometry variations, such as, solder gap, solder length and is also altered by voids, peel-off effects and local variation of stress-states. These considerations motivated the initial study reported in chapter 1 of Part II, which investigates the variation of stress-states arising from different sample geometries.

Die approbierte gedruckte Originalversion dieser Dissertation ist an der TU Wien Bibliothek verfügbar.
The approved original version of this doctoral thesis is available in print at TU Wien Bibliothek.
TU WIEN Bibliothek Your knowledge hub

Microstructural 3D imaging

X-ray computed micro tomography (μ-XCT) is a non-destructive 3D imaging method [71] and is used across disciplines such as materials science [72], biomechanics [73] or biology [12]. Absorption based μ-XCT imaging, which is commonly used in lab-scale setups, uses the difference in X-ray absorption coefficients of microstructural constituents for image reconstruction and is governed by the Beer-Lambert's law [74] as

$$I = I_0\, e^{-\int \mu(x)dx}, \tag{18}$$

where μ is the location-dependent absorption coefficient. I and I_0 are the transmitted and incident X-ray beam intensity, respectively. The absorption coefficient in the sample is determined by performing a number of projections through the sample, where received and incoming intensities I and I_0 are measured [74]. This provides the required information to solve the inverse problem governed by eq. (18) and allows to determine the location dependent value μ, represented in form of a 3D grey value image. Image contrast among microstructural phases arises from differences in the absorption coefficient and is a function of X-ray beam energy, which is shown in Fig. 11 for pure Sn and Bi [75]. The primary and eutectic phases of the example alloys in the present work are Sn-rich and Bi-rich, respectively, and their contrast is approximated by the absorption coefficient of pure Sn and Bi. The absorption coefficient of Bi for beam energies > 100 keV is about 5 times higher than Sn and offers sufficient contrast for grey-value based imaging of Sn-Bi alloys and supports the choice of the Sn-Bi system for the presented work.

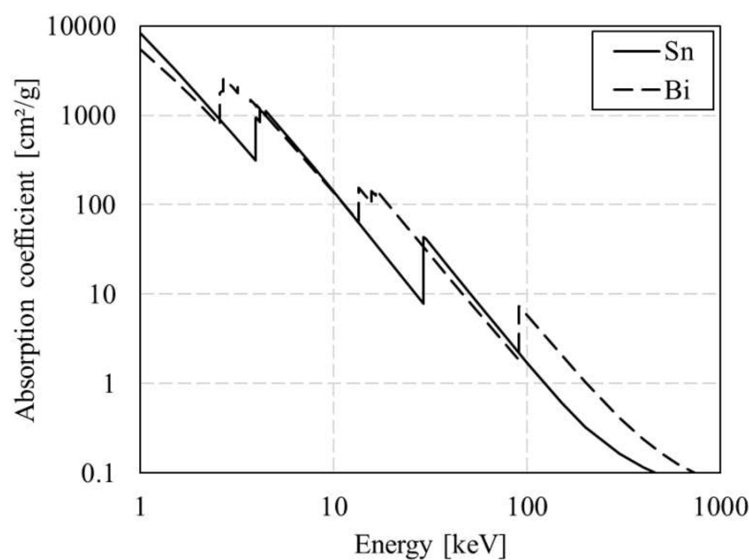

Fig. 11 Absorption coefficient over X-ray energy for pure Sn and Bi [75]

Die approbierte gedruckte Originalversion dieser Dissertation ist an der TU Wien Bibliothek verfügbar.
The approved original version of this doctoral thesis is available in print at TU Wien Bibliothek.
TU WIEN Bibliothek Your knowledge hub

1.6 Summary & outlook

The first chapter of the present work provides a thorough overview of theoretical and practical aspects of healing materials. The state of the art and current limitations of healing in metals are discussed. Aspects of reliability in solder joints are introduced and the mechanisms behind degradation and failure of solder joints are illustrated as well as fundamentals of Sn-Bi example alloys are explained. The second chapter provides scientific articles in recognized journals that extend the current state of knowledge. The following issues are addressed in the second chapter:

- Analysis of lap shear test for solder materials
- Micromechanics-based damage model for liquid-assisted healing
- Modelling of void collapse with molecular dynamics in pure Sn
- Effect of solder joint size and composition on liquid-assisted healing
- X-ray micro computed tomography analysis of Sn-Bi solders microstructure
- Microporosity formation during solidification in Sn-Bi alloys

These contributions establish new models and provide insights into the mechanics of liquid-phase healing in solders. The formal relationship of loading conditions and liquid phase properties is obtained by using the void collapse equation. It is shown that this concept remains applicable for very low length-scales. Therefore, the proposed micromechanical model can be applied even to early stage damage-healing, where damage appears as nano-voids. The size- and composition-dependency of healing in solder joints is addressed by numerical models, where the microstructural mobility is identified as a key factor of potential healing alloys. The X-ray computed tomography characterization provides insights in the morphology and microstructural features of potential healing solders of varying composition. Eventually, the solidification behavior of several solder compositions reveals that, below a liquid-phase threshold, porosity formation during the semi-solid configuration prevents healing. These findings reveal additional requirements for liquid phase healing microstructures.

Several more questions have to be addressed to develop liquid phase healing into a practical technology in solders. The following questions should be addressed in the future

- The effect of liquid state diffusion determines the growth of intermetallic phases and could potentially lead to rapid embrittlement of solder joints during healing. The effect

Die approbierte gedruckte Originalversion dieser Dissertation ist an der TU Wien Bibliothek verfügbar.
The approved original version of this doctoral thesis is available in print at TU Wien Bibliothek.
TU WIEN Bibliothek Your knowledge hub

of alloying elements to reduce unwanted growth of intermetallic phases would be of great relevance, not only in the context of liquid phase healing.

- The quest for low temperature healing requires solder alloys with sufficiently low melting range to avoid additional heating systems. Therefore, the search for alloys with similar microstructure as those in the present work, but lower melting range would be beneficial for a practical realization of liquid-phase healing.
- The aspect of health monitoring plays a vital role for efficiently employing liquid-phase healing and requires further research. A system to determine the actual state of damage in components or single solder joint would allow to trigger a healing phase selectively, e.g., by adjusting cooling parameters or by employing local heat sources.

Die approbierte gedruckte Originalversion dieser Dissertation ist an der TU Wien Bibliothek verfügbar.
The approved original version of this doctoral thesis is available in print at TU Wien Bibliothek.
TU WIEN Bibliothek Your knowledge hub

Part II. Scientific papers

Table of contents part II:

1st Paper:

2.1 Lap shear test for solder materials: Local stress states and their effect on deformation and damage; G. Siroky, J. Magnien, D. Melinc, E. Kozeschnik, D. Kieslinger, E. Kraker, W. Ecker; Microelectronics Reliability; Volume 109; June 2020; https://doi.org/10.1016/j.microrel.2020.113655 .... **25**

2nd Paper:

2.2. Micromechanics-based damage model for liquid-assisted healing; G. Siroky, E. Kraker, D. Kieslinger, E. Kozeschnik, W. Ecker; Volume 30; August 2020; International Journal of Damage Mechanics; https://doi.org/10.1177/1056789520948561 .... **45**

3rd Paper:

2.3. Modelling of Void Collapse with Molecular Dynamics in Pure Sn; G. Siroky, E. Kraker, D. Kieslinger, L. Romaner, E. Kozeschnik, W. Ecker; Proceedings (MDPI); Volume 56; December 2020; https://doi.org/10.3390/proceedings2020056029 .... **67**

4th Paper:

2.4. Effect of solder joint size and composition on liquid-assisted healing; G. Siroky, E. Kraker, J. Magnien, D. Melinc, D. Kieslinger, E. Kozeschnik, W. Ecker; Microelectronics Reliability; Volume 119; February 2021, https://doi.org/10.1016/j.microrel.2021.114066 .... **70**

5th Paper:

2.5. Analysis of Sn-Bi Solders: X-ray Micro Computed Tomography Imaging and Microstructure Characterization in Relation to Properties and Liquid Phase Healing Potential; G. Siroky, E. Kraker, J. Rosc, D. Kieslinger, R. Brunner, S. van der Zwaag, E. Kozeschnik, W. Ecker; Materials (MDPI); Volume 14; https://doi.org/10.3390/ma14010153 .... **91**

6th Paper:

2.6. Simulation and experimental characterization of microporosity during solidification in Sn-Bi alloys; G. Siroky, E. Kraker, D. Kieslinger, E. Kozeschnik, W. Ecker; Materials (MDPI); Submitted **117**

Die approbierte gedruckte Originalversion dieser Dissertation ist an der TU Wien Bibliothek verfügbar.
The approved original version of this doctoral thesis is available in print at TU Wien Bibliothek.
TU WIEN Bibliothek Your knowledge hub

2.1 Lap Shear Test for solder materials: Local stress states and their effect on deformation and damage

Georg Siroky (georg.siroky@mcl.at) [1], Julien Magnien[1], David Melinc[2], Ernst Kozeschnik[2], Dietmar Kieslinger[3], Elke Kraker[1], Werner Ecker[1]
[1] Materials Center Leoben Forschung GmbH (MCL), Roseggerstraße 12, 8700 Leoben, Austria
[2] TU Wien, Institute of Materials Science and Technology, Getreidemarkt 9, 1060 Wien, Austria
[3] ZKW Elektronik GmbH, Samuel Morse-Straße 18, 2700 Wiener Neustadt, Austria

Published in: Microelectronics Reliability Volume 109, June 2020, 113655,
https://doi.org/10.1016/j.microrel.2020.113655

Abstract

This work presents a detailed analysis of stress states and different strain measures of two lap-shear sample designs. The stress- and strain distribution are discussed for both sample designs through numerical simulation. Additionally, in-situ measurements of lap-shear experiments are performed to compare the large strain and damage behavior of the different sample designs. Despite the use of in-situ video-extensometer strain measurements, a deviation among elastic moduli from tensile- and lap-shear experiments is observed. Finite element analysis reveals that inhomogeneous strains due to boundary effects are the reason for the observed moduli deviation. A strain correction method is presented to correct video-extensometer measurements. The parameters of the correction function were obtained from numerical simulation and are provided for several sample dimensions. To illustrate the effectiveness of the proposed strain correction method, the correction function is applied to experimental lap-shear test data. The corrected shear moduli compare well with shear moduli calculated from tensile tests reported in literature.

1. Introduction

The analysis of shear, creep and thermal fatigue behavior of solder alloys is often done via lap-shear tests. This allows to determine material properties under shear dominated loads [76–79]. There are no specific standards for lap-shear samples with respect to materials testing. Therefore, several sample designs with variation in shape and dimension are common in material testing of solders. The lap-shear test characterizes the shear- and interfacial strength of solder joints [66,70,80–82]. A great number of studies exist that illustrate the strength and elastic deformation of bonded lap-shear joints through simulation and experiments [67,79,83–

Die approbierte gedruckte Originalversion dieser Dissertation ist an der TU Wien Bibliothek verfügbar.
The approved original version of this doctoral thesis is available in print at TU Wien Bibliothek.
TU WIEN Bibliothek Your knowledge hub

86], focusing on the structural behavior of the components but not on determining material properties of the joints. Experimental studies of Zimprich et al. [67] showed that measured properties depend on the sample design. The solder dimensions such as thickness t and length l play an important role for the loading condition [53,67,86].

Video-extensometer (VE) strain measurements are often used for in-situ studies of lap-shear experiments [82] [12] [21]. The VE measures displacements of patterns on the sample surface and displacements are subsequently used to calculated local strains of the sample. There are no reports how the sample dimensions affect the strains at the boundary and if such boundary effects are critical for the calculated shear moduli.

Lap-shear joints have been analyzed using linear and non-linear Finite Element Methods (FEM) [69,83,84,89–91] and also by deriving closed form solutions [77]. Studies focusing on lap-shear joints treat the solder elastic and consider the lap-shear sample under plane-strain condition. Cognard et al. [84] studied the stress distribution in solder joints under the assumption of a linear elastic adhesive, where significant peel-off effects at the boundary areas of the adhesive were demonstrated. The mechanics of bonding layers was studied and analytical solutions for the peel-off and shear stresses were derived by Abdelhadi et al. [92].

This work provides an analysis of the local stress state in the solder under the assumption of rate dependent material behavior. The stress state and stress distribution in both samples under variation of geometric dimensions are analyzed through numerical simulation for small deformations. Furthermore, the large strain deformation and damage behavior of both samples was investigated through in-situ experiments. Shear moduli determined from lap-shear experiments reveal significant deviation from its objective values. The root cause of this systematic error has, to the knowledge of the authors, not been investigated in literature. We propose a method to obtain corrected shear moduli for different sample designs. The well documented SAC305 solder was used to allow for quantitative comparison with literature data.

2. Numerical Model

The mechanics of the lap-shear test is studied using FEM modeling for small deformations. In Fig. 1 the sample geometries of the FEM models and their boundary conditions are illustrated. Design A represents the commonly used standard sample geometry, while Design B is an improved design. Previous studies have used similar sample designs [93,94], yet a quantitative comparison for different sample designs in terms of stress states and deformation behavior is missing in literature. Both sample-designs have the same thickness t_{Cu}. The solder domain is indicated by Ω_s, while ∂_{FF} denotes the cross section of all integration points used to quantify

Die approbierte gedruckte Originalversion dieser Dissertation ist an der TU Wien Bibliothek verfügbar.
The approved original version of this doctoral thesis is available in print at TU Wien Bibliothek.
TU WIEN Bibliothek Your knowledge hub

the acting forces. In Fig. 1 the Dirichlet boundary conditions (fixed displacements and rotations) are imposed on the surface nodes, while the surface nodes on the right are displaced in 1-direction. Design B consists of two additional features compared to the standard design. At the corner a circular drill hole is applied, while on the opposite edge shows a 0.5x45° chamfer. The circular hole offers the same functionality, while keeping manufacturing simple. These features are intended to maintain a soft load transfer from the substrate to the solder. The reference design with respect to the design variables is defined as: l=2mm, t=0.2mm, D=1mm and t_{Cu}=2mm. The solder length l and gap-width g denoted in Fig. 1 are kept equal in both sample designs for comparison.

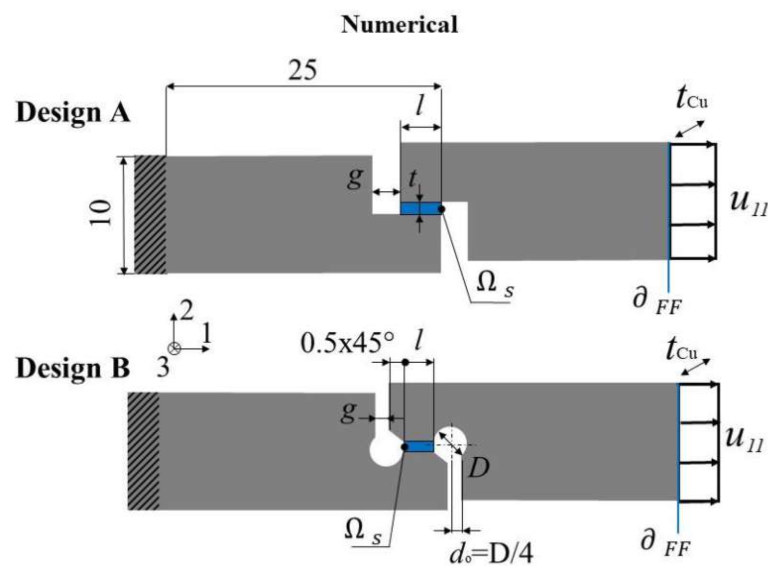

Fig. 1 Lap-shear sample design geometry with design parameters D, t, l, l_{fix}. Boundary conditions

The substrate and solder are modelled using 3D linear hexagonal brick elements with reduced integration (Abaqus element type C3D8R). A mesh size of 0.01mm is applied on the solder domain. Both substrates are considered to be linear elastic with elastic properties of pure Cu. The Sn-Ag3.0-Cu0.5 solder is modelled using a rate dependent elastic-creep constitutive model. Eq. 19 illustrates the hyperbolic-sine creep strain evolution, where A, B and n are material parameters, while Q is the activation energy, R is the gas constant and T is the temperature. The exponential expression is an Arrhenius type term that accounts for the temperature dependence of the creep strain evolution. The creep material properties summarized in Tab. 1 are taken from literature [95].

$$\dot{\varepsilon}_{cr} = A[\sinh(B\sigma)^n] \cdot e^{\frac{-Q}{RT}} \tag{19}$$

Die approbierte gedruckte Originalversion dieser Dissertation ist an der TU Wien Bibliothek verfügbar.
The approved original version of this doctoral thesis is available in print at TU Wien Bibliothek.
TU Bibliothek WIEN Your knowledge hub

Tab. 1 Material parameters of substrate and solder from [69], [95]

Material parameters: Substrates (Cu)	
Young's Modulus E:	110 GPa
Poisson Number ν:	0.34
Material parameters: Solder Sn-Ag3.0-Cu0.5	
Young's Modulus E:	55 GPa
Poisson Number ν:	0.36
Parameter A:	2631
Parameter B:	0.0453 1/MPa
Exponent n:	5
Activation Energy Q:	52.4 kJ/mol
Gas Constant R:	8.314 J/K

Two methods are applied to determine stresses and strains from the numerical models. First the representative stresses $\sigma_{ij,\mathrm{rep}}$ and strains $\varepsilon_{ij,\mathrm{rep}}$ are defined. The representative stresses and strains are evaluated at the central volume element of the solder according to Eq. 20 and Eq. 21 and as depicted in Fig. 2 by V_{Rep}. The representative strain measure can only be determined from numerical simulation and is not accessible through experiments.

$$\sigma_{ij,\mathrm{rep}} = \sigma_{ij}(\frac{l}{2},\frac{t}{2},\frac{t_{\mathrm{CU}}}{2}) \tag{20}$$

$$\varepsilon_{ij,\mathrm{rep}} = \varepsilon_{ij}(\frac{l}{2},\frac{t}{2},\frac{t_{\mathrm{CU}}}{2}) \tag{21}$$

Second, the nominal shear stresses σ_{Nom} are calculated according to Eq. 22, where l ant t_{Cu} are the solder dimensions and the summation term describes the total shear force in terms of nodal forces. The total number of nodes in the cross section is denoted as N_{FF}. The VE strain measure is computed in the model according to Eq. 23, where $u_{11,\mathrm{I}}$ and $u_{11,\mathrm{II}}$ are the displacement in 1-direction of point I and II as illustrated in Fig. 2. The small deformation engineering convention is applied. It is important to mention, that the VE strain measure can be determined in both numerical simulation and in the experiment. In cases of experimentally determined VE measures, the notation ϵ_{ij,VE_EXP} will be used. Whereas, $\epsilon_{ij,VE}$ refers to computational strain measures.

$$\sigma_{\mathrm{Nom}} = \frac{\sum_i^{N_{\mathrm{FF}}} F_{11,i}}{l \cdot t_{\mathrm{CU}}} \tag{22}$$

$$\varepsilon_{12,\mathrm{VE}} = \frac{(u_{11,I} - u_{11,II})}{t} \cdot 100\% \tag{23}$$

The stress distribution in the solder is analyzed on the path Γ_{s} in Fig. 2 which denotes all

Die approbierte gedruckte Originalversion dieser Dissertation ist an der TU Wien Bibliothek verfügbar.
The approved original version of this doctoral thesis is available in print at TU Wien Bibliothek.
TU Bibliothek Your knowledge hub WIEN

integration points N_{PS} along the central line of the solder. The central path Γ_s is equally evaluated for the designs A and B. Multiple quantities along the path Γ_s are illustrated, such as the stress in 1-direction σ_{11}, the stress in 2-direction σ_{22} (peel-off stress), the shear stress σ_{12} and the stress triaxiality σ_{TRIAX}. The stress triaxiality quantifies the stress state and is written as hydrostatic stress σ_{HYD} over von Mises stress σ_{M} as shown in Eq. 24. The hydrostatic stress is defined as the trace of the Cauchy stress tensor written in Eq. 25. The von Mises stress written in the form of principal stresses is denoted in Eq. 26. A stress triaxiality of σ_{TRIAX}=0 indicates pure shear, while σ_{TRIAX}=0.33 is pure uniaxial tension and σ_{TRIAX} =-0.33 represents uniaxial compression.

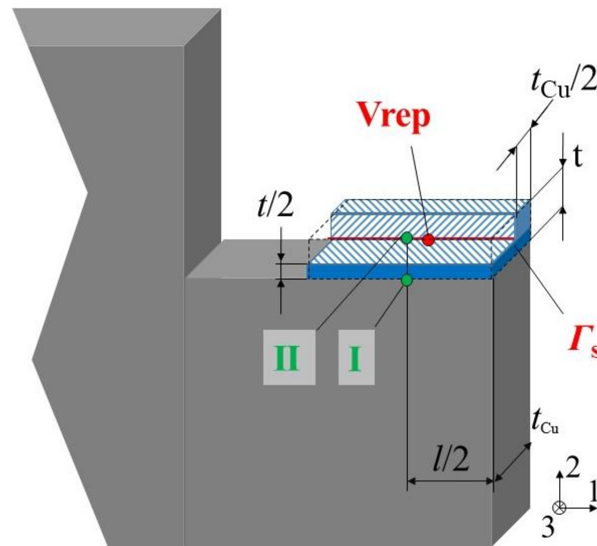

Fig. 2 Evaluation of integration points along path Γ_s within solder domain Ω_s, definition of the VE measurement positions I and II and indication of the representative position V_{rep} for strain evaluation.

$$\sigma_{\mathrm{TRIAX}} = -\sigma_{\mathrm{HYD}}/\sigma_{\mathrm{M}} \tag{24}$$

$$\sigma_{\mathrm{HYD}} = (\sigma_I + \sigma_{II} + \sigma_{III})/3 \tag{25}$$

$$\sigma_M = \sqrt{\frac{1}{2}[(\sigma_I - \sigma_{II})^2 + (\sigma_{II} - \sigma_{III})^2 + (\sigma_{III} - \sigma_I)^2]} \tag{26}$$

3. Sample preparation and experimental

Samples are produced to investigate large deformations and to apply the correction method of VE strain measurements. Both sample designs A and B are manufactured with the same procedure. Copper plates are cut, milled and polished according to the sample designs shown in Fig. 1. The solder surfaces were gradually ground with 1200 to 4000 grit size sand paper, rinsed with acetone and dried. Solid solder stripes of Sn-Ag3.0-Cu0.5 with thickness 0.2mm are produced and cut in 2x2mm patches. The samples are reflowed in an aluminum template to

Die approbierte gedruckte Originalversion dieser Dissertation ist an der TU Wien Bibliothek verfügbar.
The approved original version of this doctoral thesis is available in print at TU Wien Bibliothek.
TU Bibliothek WIEN Your knowledge hub

adjust the solder gap of t=0.2mm and to provide parallel orientation of the substrates. The samples are soldered on a heating plate and cooled by air flow cooling. The measured reflow temperature profile on the sample surface and heating plate profile are shown in Fig. 3. After the reflow process, samples were ground with sand paper of grit size 4000 on a grinding plate to reach the final thickness of t_{Cu}=2mm and to clean them from remaining solder spots. The samples are tested on an electro-mechanical uniaxial tensile test machine at a constant displacement rate of $\dot{d} = 0.012\frac{mm}{min}$ at room temperature. The shear force is measured using a 50kg load cell (AEP transducers®), while the solder deformation is measured with a VE and laser speckle at points indicated in Fig. 2. Furthermore, in-situ images of the solder joint under load are recorded using a digital microscope (Dino-Lite® Digital Microscope frame-rate=25fps) to determine the evolution of the local deformation behavior of the solder. After mechanical testing, the fracture surfaces are investigated through optical microscopy to compare the crack propagation with numerical results of the stress distribution of both sample designs. The experimental comparison of both samples allows to illustrate differences due to the sample design for large deformations.

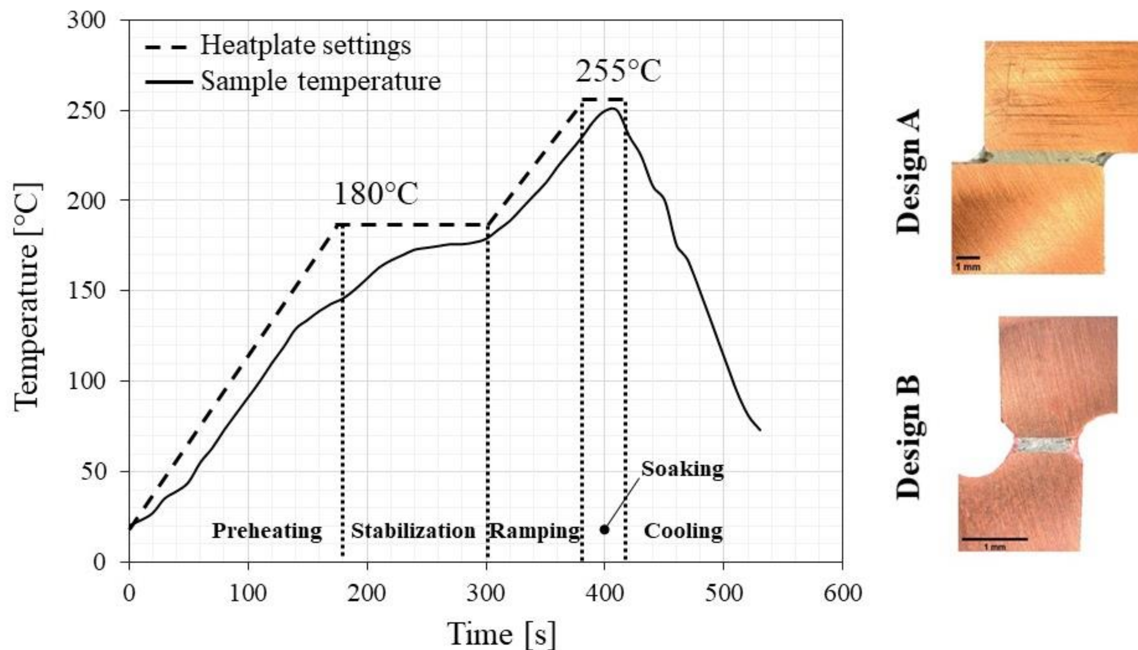

Fig. 3 Reflow temperature-profile for the lap-shear samples A & B (left) and cross sectional view of sample designs A & B (right)

4. Results and discussion

Stress distributions from numerical simulation of both designs are compared and the differences among design A and B are discussed. In-situ measurements are used to compare the damage

Die approbierte gedruckte Originalversion dieser Dissertation ist an der TU Wien Bibliothek verfügbar.
The approved original version of this doctoral thesis is available in print at TU Wien Bibliothek.
TU Bibliothek WIEN Your knowledge hub

behavior at large deformations of both sample designs. The deviation of representative- and VE strain measurements are analyzed numerically and a strain correction method is presented. The strain correction is applied on experimental data and comparisons with measurements from literature are discussed.

Numerical Analysis Sample Design A

Stresses along the path Γ_s of sample design A for two solder joint thicknesses *t=0.2mm, t=0.3mm and t=0.4mm* are calculated and compared. The plots in Fig. 4 show the stresses at an average shear strain of $\varepsilon_{12,ave}$=0.0102% for t=0.2mm, $\varepsilon_{12,ave}$=0.0937% for t=0.3mm and $\varepsilon_{12,ave}$=0.0887% for t=0.4mm. At this deformation level stress peaks are most prominent, because stress peaks have not been decreased by inelastic deformation. The graphs in Fig. 4 reveal the maximum stress peaks and the stress-triaxiality distribution. Variations of the solder thickness show the sample sensitivity with respect to t. The longitudinal stress σ_{11} is illustrated in Fig. 4a, where the local stress peaks are in the vicinity of the solder boundary. Fig. 4b shows a substantial amount of peel-off stress σ_{22}=18MPa for t=0.2mm at the boundary regions in the solder. The peel-off stress peak reduces to σ_{22}=12MPa for t=0.3mm , because the illustrated path Γ_s is 0.05mm farther away from the boundary. Fig. 4c illustrates the shear stress distribution. The shear stress peaks at position 0.1 and 0.9 indicate, in combination with longitudinal and peel-off stress peaks, that these regions are exposed to the highest mechanical loads. The peel-off stress considerably alters the stress state and incorporates loading states of $\sigma_{TRIAX}\neq 0$ at the boundaries. This effect can be seen through the stress triaxiality along the path Γ_s, shown in Fig. 4d. The boundaries undergo uniaxial tension, while the center region is loaded dominantly under shear ($\sigma_{TRIAX}\approx 0$). At the boundary region the stress triaxiality of σ_{TRIAX}=0.3 indicates a peel-off dominated loading which acts as a potential crack initiation site. For large solder thickness around t=0.4mm the stress triaxiality reduces to σ_{TRIAX}=0.17 indicating that the central region is shear dominated, whereas for thinner solders of t=0.2mm the peel off effect is manifested by a tensile dominated stress triaxiality of σ_{TRIAX}=0.35.

Die approbierte gedruckte Originalversion dieser Dissertation ist an der TU Wien Bibliothek verfügbar.
The approved original version of this doctoral thesis is available in print at TU Wien Bibliothek.
TU WIEN Bibliothek Your knowledge hub

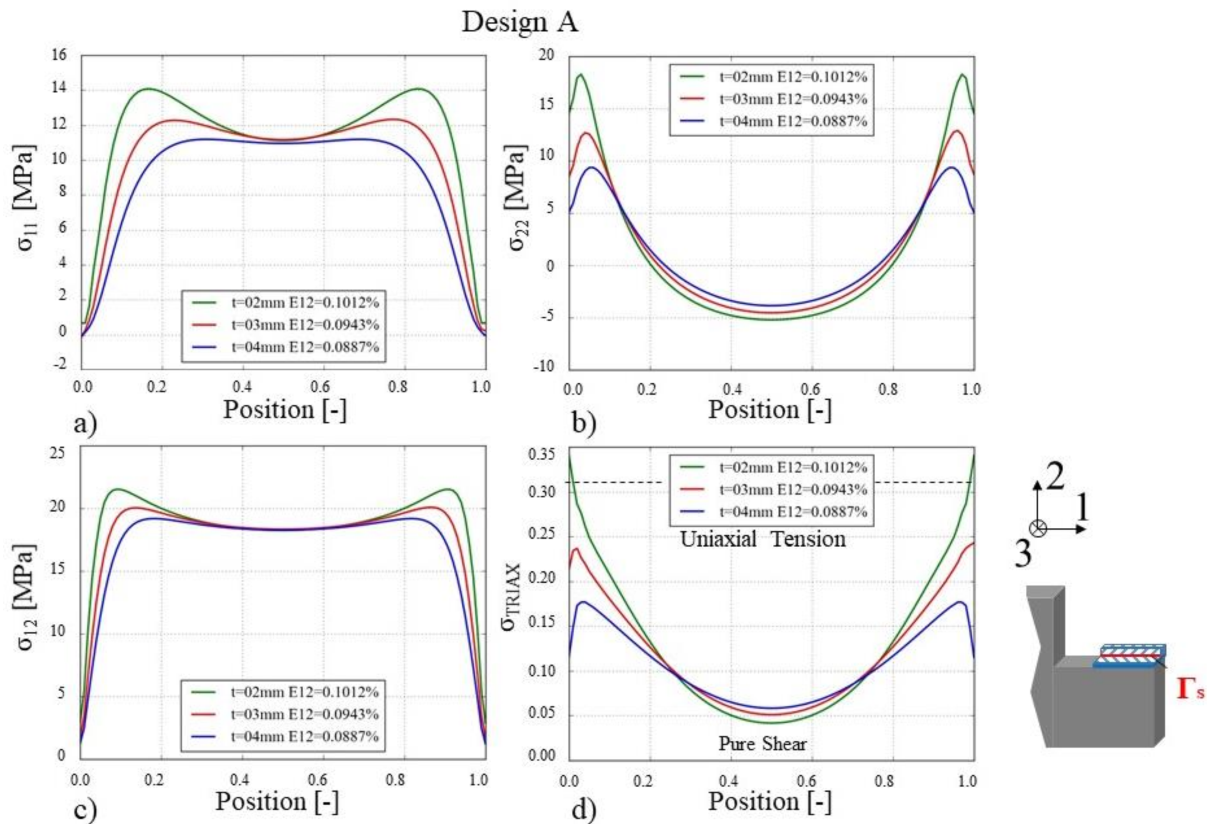

Fig. 4 Stress state along path Γ_s for sample design A, solder length l=2mm, variable solder thickness t, displacement u_{11}=0.005mm and displacement rate $\dot{u}_{11} = 0.002 \frac{mm}{s}$ a) Longitudinal stress b) Peel off stress c) Shear stress d) Stress triaxiality

In Fig. 5 the stress distribution under variation of the solder length *l* is illustrated. In Fig. 5a the relative position and magnitude of the longitudinal stress peaks are insensitive to the solder length *l* varying from *l*=2mm to *l*=4mm. The magnitude of longitudinal stress only varies between σ_{11}=14MPa and σ_{11}=11.5MPa. The peel-off stresses in Fig. 5b are also barely effected by increasing solder length. The stress peaks are positioned at 0.05*l* and 0.95*l* at a magnitude of σ_{22}=18.0MPa. In Fig. 5c the magnitude of shear stresses reveals are clear length dependency. For *l*=2mm the shear stress peaks are σ_{12}=21.6MPa and reduce to σ_{12}=15.5MPa for *l*=4mm. Most importantly, the stress triaxiality in Fig. 5d reveals an insensitive characteristic with respect to the solder length. The stress state within the solder exhibits tensile dominated areas at the boundaries (σ_{TRIAX}=0.35) and a shear dominated central region (σ_{TRIAX}=0.05). Overall, one can see from Fig. 4d and Fig. 5d that sample Design A shows boundary areas of tensile dominated loads. This determines the damage and fracture behaviour of solders tested with similar sample designs. The solder length has minor influence on the stress state in sample A.

Die approbierte gedruckte Originalversion dieser Dissertation ist an der TU Wien Bibliothek verfügbar.
The approved original version of this doctoral thesis is available in print at TU Wien Bibliothek.
TU Bibliothek WIEN Your knowledge hub

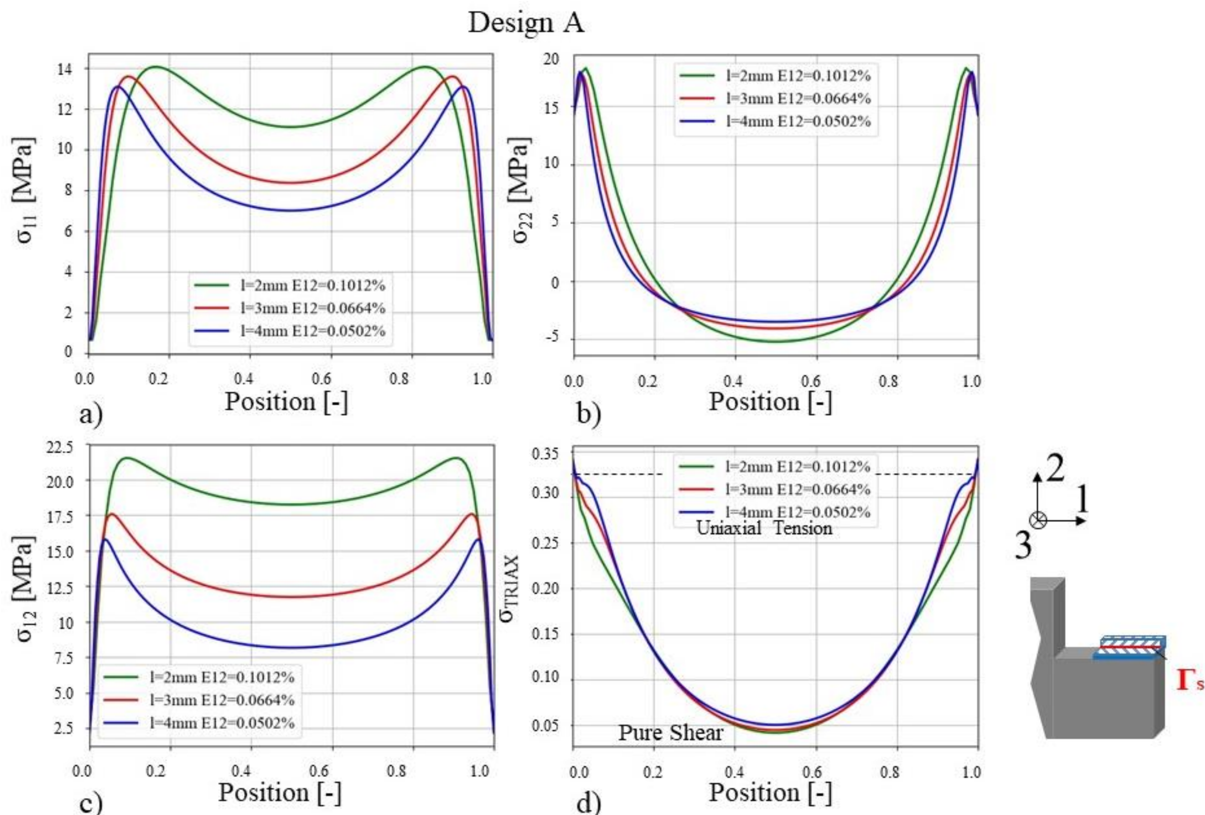

Fig. 5 Stress state along path Γs for sample design A, solder thickness t=0.2mm, variable solder length l, displacement u11=0.005mm and displacement rate u ̇_11=0.002 mm/s a) Longitudinal stress b) Peel off stress c) Shear stress d) Stress triaxiality.

Numerical Analysis Sample Design B

The stress state of lap-shear design B is analyzed under variation of the design parameter *D* and the solder length *l*. Fig. 6 illustrates the stress components and stress triaxiality along the solder path Γ_s under variation of the contour parameter *D*. The stresses are normalized with respect to lap shear design A for *t*=0.2mm and *l*=2mm (Fig. 4) for good comparison. The normalization values of each stress component are: $\sigma_{11,norm}$=14.0MPa, $\sigma_{22,norm}$=18.3MPa, $\sigma_{12,norm}$=21.6MPa and represent the stress peak values. In Fig. 6a, a bell shaped longitudinal stress distribution is observed, where stress peaks at the boundaries are smoothed compared with sample design A. Fig. 6b shows that the peel-off stress σ_{22} is reduced by 45% at *D*=1mm. With a contour diameter of *D*=3mm, a reduction of σ_{22} of nearly 90% is achieved. At the same time the shear stress σ_{12} (Fig. 6c) is reduced to 60% of the reference configuration for *D*=3mm and shear stress peaks at the boundaries are eliminated. The stress triaxiality of sample B are illustrated in Fig. 6d. Due to a reduction in peel-off stresses, the stress triaxiality is reduced to σ_{TRIAX}=-0.07 at the boundaries of the solder and deviates by $\Delta\sigma_{TRIAX}$=+/-0.075 from σ_{TRIAX}=0. This indicates shear dominated loads and slight compressive forces at the solder boundaries. Design B is able to maintain a shear dominated stress state along the path Γ_s. Fig. 6c reveals that the shear stress

Die approbierte gedruckte Originalversion dieser Dissertation ist an der TU Wien Bibliothek verfügbar.
The approved original version of this doctoral thesis is available in print at TU Wien Bibliothek.
TU Bibliothek WIEN Your knowledge hub

σ_{12} for larger D remains almost constant along the path Γ_s. The contour radius D=1mm leads to more significant shear-stress peaks at the boundary (90% of design A), while for D=3mm no shear stress peaks can be seen in Fig. 6c.

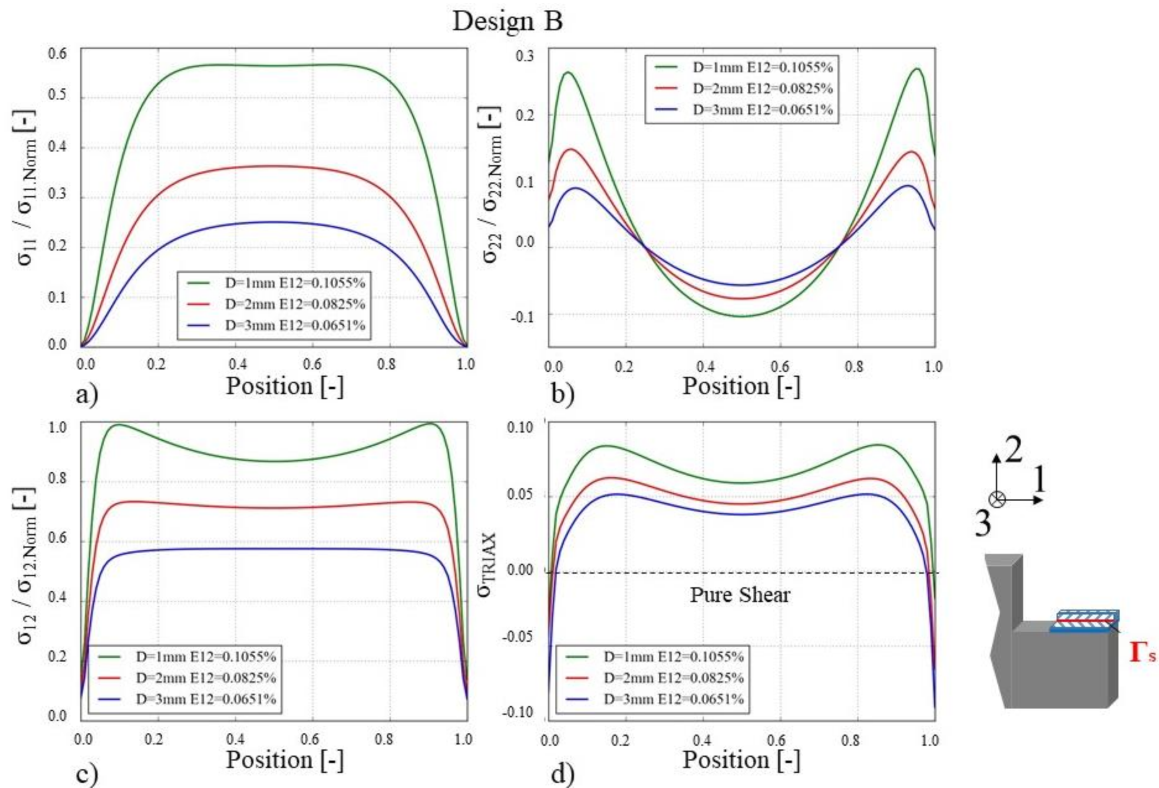

Fig. 6 Stress state along path Γ_s for sample design B, solder length l=2mm, t_{cu}=2mm, displacement u_{11}=0.005mm and displacement rate $\dot{u}_x = 0.002\frac{mm}{s}$ a) Longitudinal stress b) Peel off stress c) Shear stress d) Stress triaxiality

Fig. 7 illustrates the stress states along Γ_s under variation of the solder length l. The longitudinal stresses σ_{11} in Fig. 7a show a minor dependency with respect to l. The width of the bell-shaped stress distribution becomes wider for l=4mm, whereas the peak stress in σ_{11} remains unchanged for all solder lengths. Fig. 7b shows a reduction in peel-off stresses σ_{22} to a level of 8%, 12% and 18% for l=2mm, l=3mm and l=4mm respectively. This indicates that longer solder lengths l increase bending moments and therefore increase peel-off stress peaks. The geometry of sample design B allows to reduce the peel-off stress peaks by 90% to 75%. Fig. 7c shows that long solders (l=4mm) induce shear stress peaks at the boundaries. Shorter solders (l=2mm) show uniform shear stress distribution. It can also be seen that the total shear stress is reduced to 30% for l=4mm. The curve of l=2mm shows a uniform shear stress distribution, because for shorter solder lengths l, the boundary stress peaks interact and create a homogenous shear stress field. Fig. 7d shows the stress triaxiality for various lengths l. Shorter solders are advantageous for a homogeneous stress state. One obtains an σ_{TRIAX}≈0.05 for l=2mm at the outer boundaries,

Die approbierte gedruckte Originalversion dieser Dissertation ist an der TU Wien Bibliothek verfügbar.
The approved original version of this doctoral thesis is available in print at TU Wien Bibliothek.
TU Wien Bibliothek Your knowledge hub

while the stress triaxiality rises to σ_{TRIAX}≈0.13 for *l*=4mm. A length of *l*=2mm creates a more uniform stress triaxiality distribution, whereas longer solder lengths *l*=3mm and *l*=4mm show peel-off components σ_{22} of 15% and 18% of design A. Furthermore, the stress triaxiality shifts towards tension (positive stress triaxiality) at the boundaries, enhancing crack initiation.

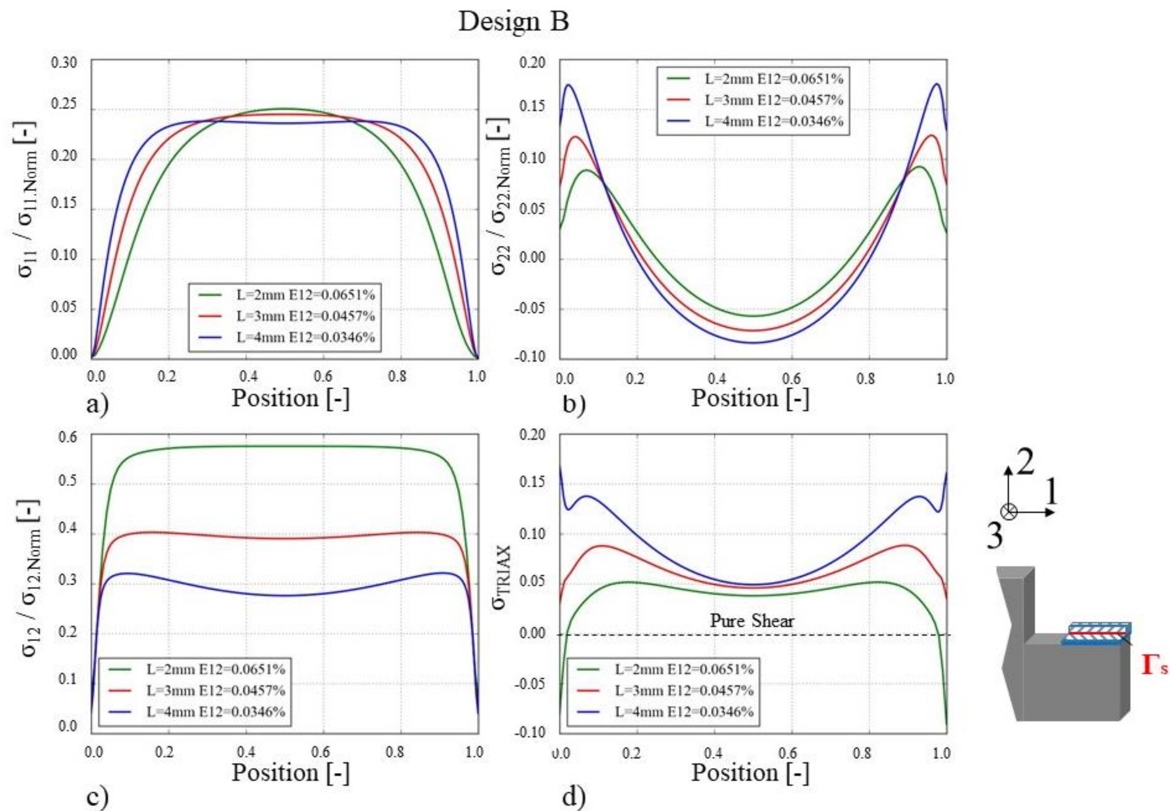

Fig. 7 Stress state along path Γ_s sample design B, D=3mm, displacement u_{11}=0.005mm and displacement rate $\dot{u}_x = 0.002\,\frac{mm}{s}$ a) Longitudinal stress b) Peel off stress c) Shear Stress d) Stress triaxiality

Experimental Deformation Analysis

The in-situ measurements of the experiment provide additional information to improve the understanding of the local deformation and damage evolution. It is intended to investigate extreme cases in terms of local stress and strain. The numerical analysis revealed that sample design B with shorter solder length *l* is beneficial for a homogenous shear stress state. Therefore, a solder length of l=5mm for sample A and l=2mm for sample B were defined. The two samples are referred to as sample design A and sample design B in the present section. A color lookup-table (ImageJ – ICA3) is applied on the in-situ images to enhance contrast and provide more details. Fig. 8a-f shows the gradual deformation of sample A, where Fig. 8a represents the un-deformed configuration. The corresponding location in the stress-strain plot of each in-situ image is illustrated in Fig. 8h. At a shear strain of *ε*=2.6% in Fig. 8c, crack initiation is indicated by blue arrows. Its position agrees well with the area of highest

Die approbierte gedruckte Originalversion dieser Dissertation ist an der TU Wien Bibliothek verfügbar.
The approved original version of this doctoral thesis is available in print at TU Wien Bibliothek.
TU Bibliothek WIEN Your knowledge hub

mechanical loads as determined from numerical simulation in Fig. 4a-d. The high stress triaxiality σ_{TRIAX}=0.3 (uniaxial stress) in this region enhances crack initiation due to reduced fracture strains. The fracture surfaces of sample design A are shown in Fig. 8g and the cross section is illustrated in Fig. 8i. In Fig. 8g the fracture surfaces at the interface are indicated with "Interface1" and "Interface2". The crack surface close to the substrate indicates peel-off dominated fracture. These experimental findings are in agreement with results of in-situ measurements of Zhang et al. [24] and Tao et al. [93,96]. Zhang et al. also showed that the solder-substrate interface is prone for crack initiation and rupture for this sample design.

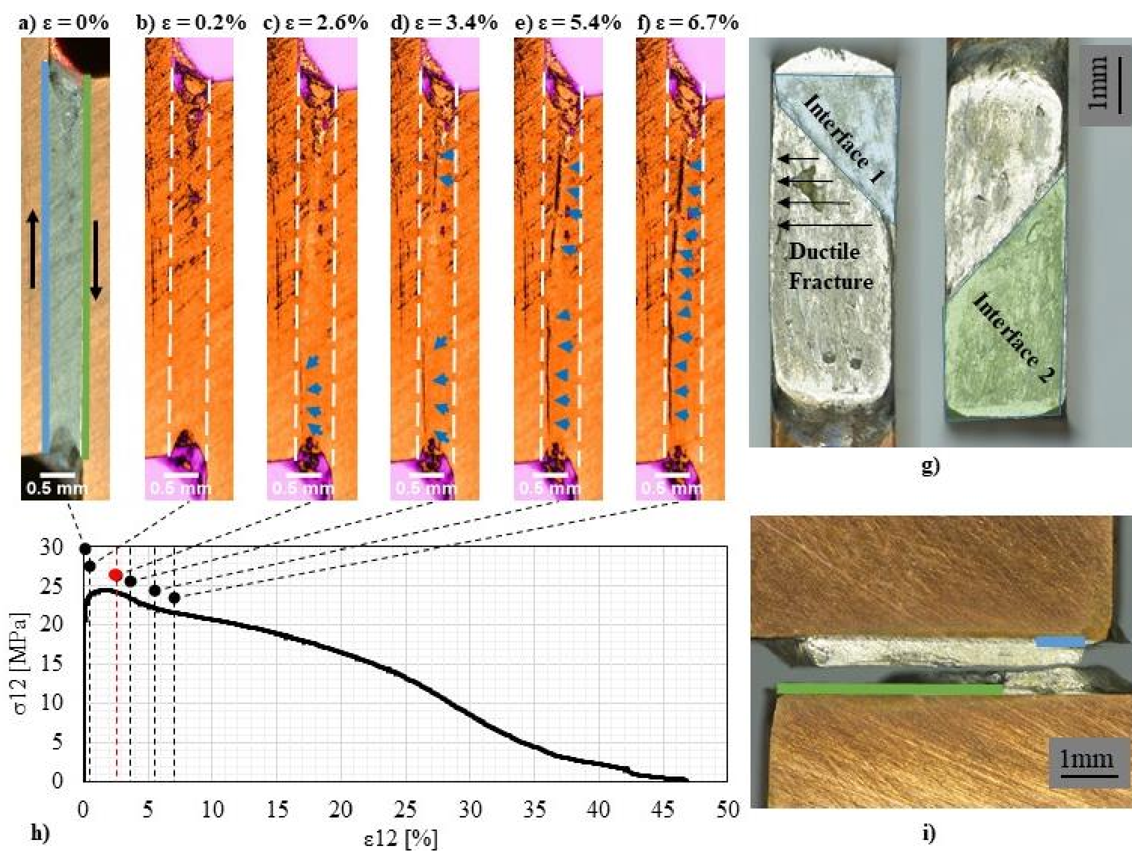

Fig. 8 In-situ shear test of sample A. a)-f) side view of the sample at different strains during testing showing the deformation and damage evolution. The blue arrows mark crack initiation and growth. Macro picture of the crack surfaces in g) top view and i) side view. h) Stress-strain curve of the test. The onset of damage is marked in red color

In-situ images of the lap-shear test and fracture analysis of sample design B are provided in Fig. 9. The un-deformed configuration is shown in Fig. 9a and the same color look-up table was applied as described for sample design A. The in-situ images at different strain levels are provided in Fig. 9a-f, where Fig. 9h indicates the corresponding position in the stress-strain plot for each in-situ image. The onset of shear deformation is visible in Fig. 9c indicated by green arrows. In contrast to sample design A, the deformation is well distributed across the solder

Die approbierte gedruckte Originalversion dieser Dissertation ist an der TU Wien Bibliothek verfügbar.
The approved original version of this doctoral thesis is available in print at TU Wien Bibliothek.
TU Bibliothek Your knowledge hub WIEN

thickness *t*. At large shear strains of ε_{12}=35% shown in Fig. 9e one can identify shear areas spanning across the full cross section marked with green arrows. Even for large local shear strains of ε_{12}>35%, no crack initiation is determined. Crack formation is visible in Fig. 9f. The in-situ data in Fig. 9 shows that sample B is able to maintain shear deformation until very large deformation and ductile final rupture. The fracture surface of sample B shown in Fig. 9g, does not reveal a pronounced crack propagation along the solder-substrate interface. The side-view in Fig. 9i shows that bulk solder is attached to both sides of the substrate. One can assume that uniform stress distribution in the solder leads to localized shear damage in the bulk region and slight compressive forces at the boundaries prevent crack initiation at an early stage. The fracture surface in Fig. 9g reveals a ductile failure mode, since necking in the lateral direction is identified. A similar fracture mode was observed by Tian et al. [97], where the deformation and fracture of solder bumps under shear loading was studied. Sample design B shows homogeneous deformation and ductile fracture characteristics up to large strains. The ability of sample B to deform until large shear strains is indicated in Fig. 8h and Fig. 9h. In both stress-strain plots the point onset of damage is indicated in red. In sample A cracking occurs before reaching a shear strain of ε_{12}=2%, whereas sample B shows non-localized deformation and no damage until ε_{12}=35% shear strain. This illustrates the advantage of sample B of maintaining homogenous shear deformation up to large shear strains.

Die approbierte gedruckte Originalversion dieser Dissertation ist an der TU Wien Bibliothek verfügbar.
The approved original version of this doctoral thesis is available in print at TU Wien Bibliothek.
TU WIEN Bibliothek Your knowledge hub

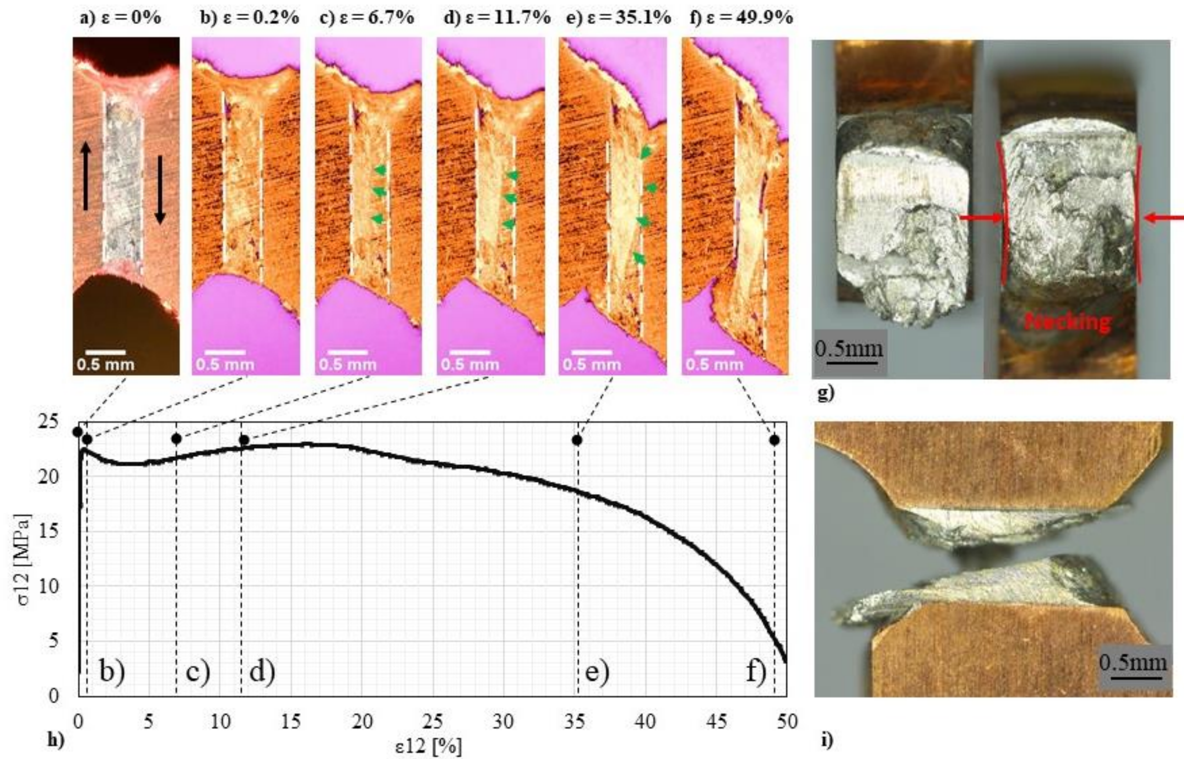

Fig. 9 In-situ shear test of sample B. a)-f) side view of the sample at different strains during testing showing the deformation and damage evolution. The green curve indicates traces from plastic deformation and the blue arrows mark crack initiation and growth. Macro picture of the crack surfaces in g) top view and i) side view. h) Stress-strain curve of the test. The onset of damage is marked in red color.

Strain measurement correction

VE strain measurements on the sample surface are the standard method for measuring the actual material deformation during tensile or shear testing. This approach allows to avoid strain corrections as proposed by Shen et al. [69] . Nevertheless, it is important to investigate the difference between strains measured on the surface, which are affected by boundary effects and compare them to a representative and objective material response in the bulk. The deviation between VE measurement and representative strains is illustrated in Fig. 10. A close-up for small strains is shown in Fig. 10a, whereas the complete strain evolution during monotonic shear testing is shown in Fig. 10b. The displacement rate $\dot{u}_{11}$ of the substrate is held constant throughout the test. The local strain-rate of the solder sample increases as the material starts yielding. The yielding is indicated in Fig. 10b and it leads to a distinct kink of the shear strain evolution at time 5s. The local strain rate increases due to reduced shear resistance of the material.

The deviation between VE and representative strain is indicated in Fig. 10a at 2.5s time. Both sample designs exhibit a similar error between VE strain measurements and representative

Die approbierte gedruckte Originalversion dieser Dissertation ist an der TU Wien Bibliothek verfügbar.
The approved original version of this doctoral thesis is available in print at TU Wien Bibliothek.
TU Bibliothek WIEN Your knowledge hub

strains. Whereas design A induces 25% higher shear strains than design B at 2.5s. Both designs exhibit a deviation of 47% and 52% of VE-strains and representative strains respectively. Since the applied constitutive model is strain-rate dependent and the lap-shear test induces varying shear-rates, one cannot easily compare the materials response of the test with a single material input stress-strain curve. Instead the material input hull-curves for the upper and lower shear strain rates are shown in Fig. 11a (blue). These material input curves were determined using a unit cell model under pure shear deformation. The upper curve is evaluated for $\dot{\varepsilon}_{12} = 10^{-2}\frac{1}{s}$, whereas the lower boundary is evaluated for $\dot{\varepsilon}_{12} = 2.5 \cdot 10^{-4}\frac{1}{s}$. The initial elastic deformation is not affected by the strain-rate dependence and the representative stress-strain curve reflects the elastic deformation at small shear strains adequately. The strain-rate alters the onset of yielding and shifts the yield point towards larger saturation stresses for increasing strain-rates (see Fig. 11a). Before inelastic deformation occurs, the representative strains follow the material curve at a strain rate of $\dot{\varepsilon}_{12} = 2.5 \cdot 10^{-4}\frac{1}{s}$. Once the stress plateau is reached, the representative stress-strain curve is converging towards the pure shear stress-strain curve at shear rate $\dot{\varepsilon}_{12} = 10^{-2}\frac{1}{s}$. VE measurements on the surface of samples A and B lead to a deviation of shear modulus G. This can be explained by a strain gradient in 3-direction as shown in Fig. 11b at the sample surfaces (O), where the VE measures deformation. This surface (O) shows larger shear strains than the bulk region (C). Both samples show a similar trend in Fig. 11b, yet sample B shows higher shear strains at the boundaries. A quantitative comparison of the relative errors of the apparent shear moduli is summarized in Tab. 2. This relative error reflects the systematic deviation of the apparent shear moduli. Sample design A exhibits a relative modulus error of 43% while sample B shows a modulus error of 53%. Due to the strain gradient in 3-direction shown in Fig. 11b, the solder reveals a lower apparent shear modulus through VE extensometer measurements than expected from tensile tests. The shear moduli from representative stress-strain curves are matching for both sample designs, indicating that the representative stress-strain curves are independent of the actual sample design and hence objective.

Die approbierte gedruckte Originalversion dieser Dissertation ist an der TU Wien Bibliothek verfügbar.
The approved original version of this doctoral thesis is available in print at TU Wien Bibliothek.
TU WIEN Bibliothek Your knowledge hub

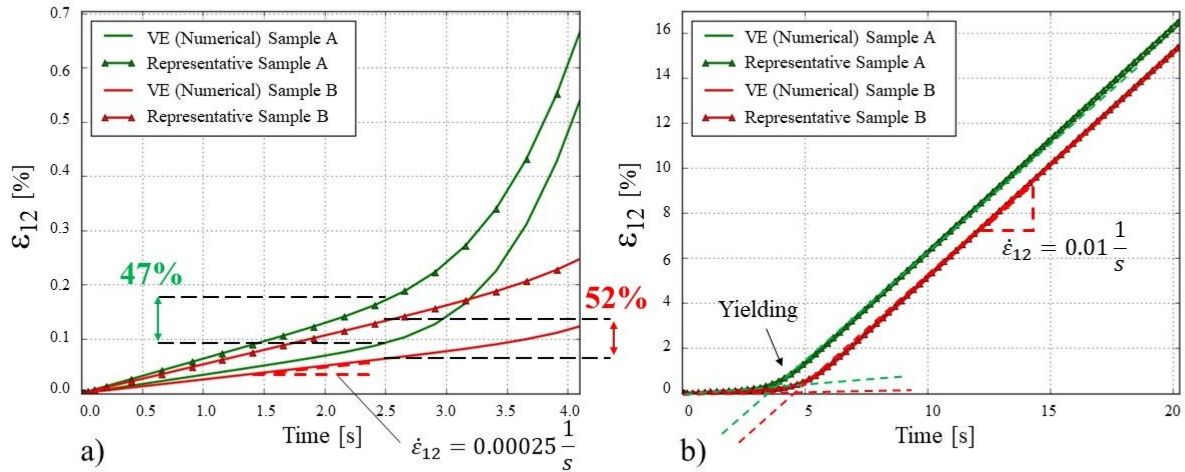

Fig. 10 VE and representative strain evolution for sample A and B. a) detail of small strain regime, b) complete strain evolution up to 20s testing time

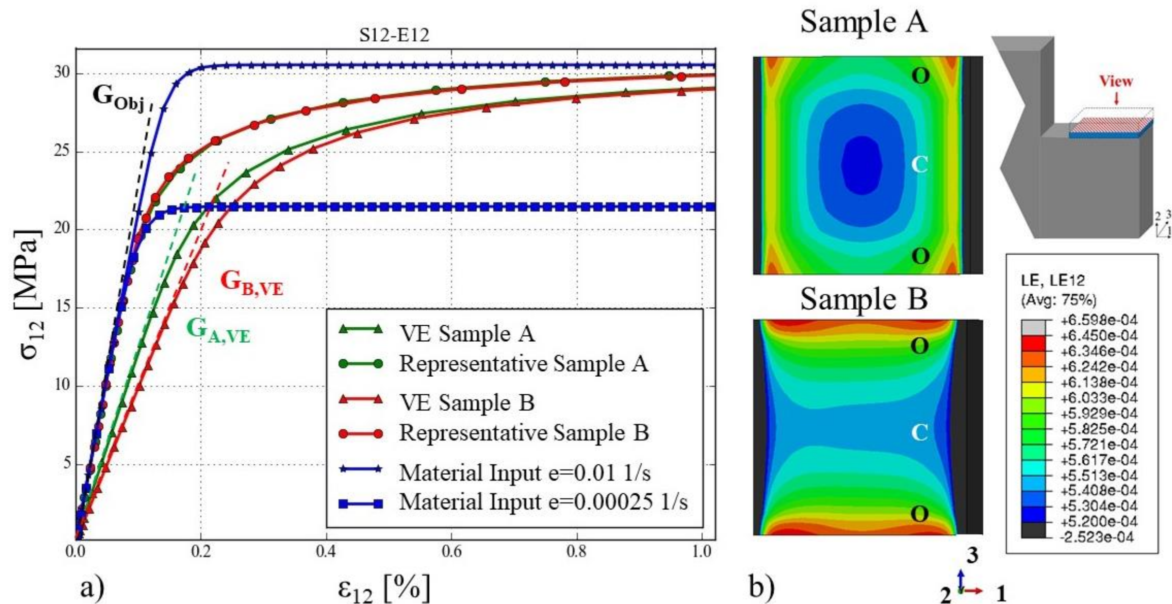

Fig. 11 Stress-strain plots for sample design A and B for different strain measures. a) comparison of input and resulting stress-strain curves. The objective shear modulus G_{Obj} is the input value in the simulation, b) shear strain distribution at t=2s across the cutting plane normal to 2-direction at half thickness of the solder for sample A and sample B. The central region is marked with C and the surface region with O

Tab. 2 Objective (G_{Obj}) and apparent (G_{VE}) shear moduli of sample design A and B for different strain measures and the error due to VE strain measurements

Sample	G_{Obj} / G_{VE} [GPa]	Error [%]
Sample A	21.1 / 12.1	43
Sample B	21.1 / 9.9	53

Die approbierte gedruckte Originalversion dieser Dissertation ist an der TU Wien Bibliothek verfügbar.
The approved original version of this doctoral thesis is available in print at TU Wien Bibliothek.
TU Bibliothek Your knowledge hub WIEN

In order to obtain representative stress-strain curves from VE measured lap-shear tests a correction function is proposed. The correction function applies a sample-dependent stiffness factor to account for the modulus error as

$$\varepsilon_{12,corr} = \varepsilon_{12,VE_EXP} - \frac{\sigma_{12}}{G_{VE} \cdot K} \tag{27}$$

The corrected strains are calculated using Eq. 27, where K is a shape factor of the sample geometry, ε_{12,VE_EXP} is the experimentally measured shear strain, σ_{12} is the measured shear stress and G_{VE} is the apparent shear modulus calculated from experimental VE measurements. Numerical simulations showed that the shape factor K depends on the sample geometry. The following stress-strain results with different shear strain measures were all obtained from numerical simulation. Therefore, the values of the shape factor K are extracted from numerical simulation. In Fig. 12 the variation of solder thickness t and solder length l are illustrated. Again the stress-strain curves at the representative volume are not affected by the sample geometry and therefore describe the objective material stiffness. In case of the VE measurement based evaluation, the solder thickness has minor influence on the stress-strain curves as seen in Fig. 12a, but the variation of solder lengths leads to a significant deviation of the apparent shear moduli as seen Fig. 12b.

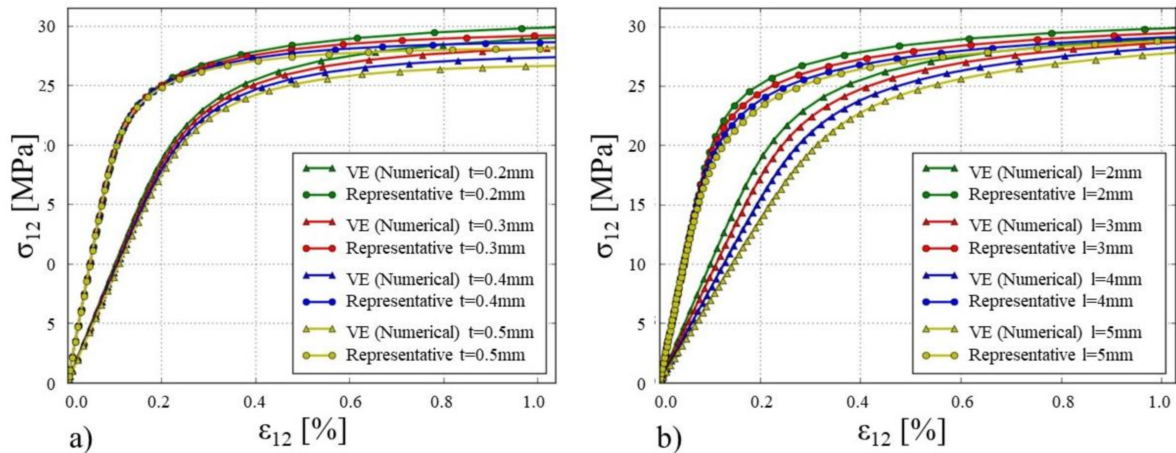

Fig. 12 Effect of parameter variation on the simulated stress strain results a) solder thickness t b) solder length l

Tab. 3 provides the shape factors K for various solder thicknesses and solder lengths. The shape factors were determined by fitting the shear modulus from VE measures of numerical simulations to the objective shear modulus which was input to the simulations, with an error of less than e<0.5%. The target for the fitting procedure was to match the initial slopes of the stress-strain curves in Fig. 12. Therefore, the correction function in Eq. 9 would transform the “VE (Numerical)” into the “Representative” stress-strain curve. It is important to emphasize

Die approbierte gedruckte Originalversion dieser Dissertation ist an der TU Wien Bibliothek verfügbar.
The approved original version of this doctoral thesis is available in print at TU Wien Bibliothek.
TU WIEN Bibliothek Your knowledge hub

that the shape factor K was obtained purely from numerical simulations and accounts for the compensation of geometric effects. This enables one to correct experimental VE-measurements for geometries deviating from the proposed nominal geometry (l=2mm, t=0.2mm). Only the corrected stress-strain curves allow to determine mechanically objective shear moduli.

Tab. 3 Shape factor K for various sample geometries

l=2mm	t=0.2mm	t=0.3mm	t=0.4mm	t=0.5mm
Sample A: K	2.45	2.28	2.16	2.08
Sample B: K	1.90	1.85	1.80	1.76
t=0.2mm	l=2mm	l=3mm	l=4mm	l=5mm
Sample A: K	2.45	2.34	2.13	1.93
Sample B: K	1.90	1.73	1.60	1.49

Correction of VE Measurements

VE strain measures on the solder surface introduce a systematic error in quantifying material strains. The proposed correction function (Eq. 9) considers the geometry and also the specific material properties through the shape factor K, which is listed for varying sample geometries in Tab. 3. In the presented work, the correction function is applied to experimental stress-strain curves. This should illustrate the applicability of the proposed correction function. Since the shape factor depends on sample geometry only, K is valid for all solders. The material properties of Sn-Ag3.0-Cu0.5 are well known from literature and provide a basis for comparison of the experimentally determined shear moduli of sample designs A and B. Since the shape factor K depends on the sample geometry only, it can be applied to any solder material. Tensile experiments conducted in [95,98] show that an elastic modulus lies in the range between E_{Min}=43GPa and E_{Max}=66GPa. An isotropic material behavior is assumed at this point with a Poisson number of ν=0.36. The shear modulus is therefore expected to be in the range of G_{Min}=16.2GPa and G_{Max}=24.3GPa. In Fig. 13a the measured (with VE) and corrected stress-strain curves from the shear experiment of sample A are shown. The VE measurement provides an apparent shear modulus of $G_{A,VE}$=13.4GPa and a corrected shear modulus of $G_{A,Corr}$=22.3GPa. Similarly, in Fig. 13b the corrected and measured stress-strain curves of sample B are illustrated. The measured shear modulus of $G_{B,VE}$=9.2GPa clearly lies outside the expected range. The strain measurement correction allows to obtain a reasonable shear modulus for sample B of $G_{B,Corr}$=18.4GPa within the bounds of $G_{Min}<G_{B,Corr}<G_{Max}$. The variation of

Die approbierte gedruckte Originalversion dieser Dissertation ist an der TU Wien Bibliothek verfügbar.
The approved original version of this doctoral thesis is available in print at TU Wien Bibliothek.
TU Bibliothek WIEN Your knowledge hub

values within G_{Min} and G_{Max} arise from deviations of material properties due to the actual soldering process, a deviation between idealized simulation and the actual sample geometry and due to local effects such as formation of voids or variation in grain size. Nevertheless, it is apparent and mechanically proven through numerical simulation, that VE measurements underestimate the shear modulus. The experimental results in Fig. 13 together with the expected range from literature support these findings [95,98]. The relative error of measured apparent shear modulus from reported values in literature can be reduced significantly for both sample designs by applying the proposed correction factor. Furthermore, it is important to discuss the variation of shear moduli due to intermetallic layers. Sn-Ag-Cu solders form the brittle intermetallic compounds (IMC) Cu_6Sn_5 and Cu_3Sn. The IMC´s reveal a considerably lower ductility than the bulk solder, which has been studied experimentally in detail by Choudhury et al. [99] and analytical solutions were derived in [92]. The results of the lap-shear test vary considerably dependent on the IMC layer thickness. The present study is limited to solder thicknesses where the IMC layer is mechanically negligible. Nevertheless, one can account for the IMC layer in Eq. 9 by choosing a shape factor in Tab.3, simply reducing the solder thickness by the IMC layer. Future studies need to consider the impact of IMC layers on both, the ductility and damage initiation in the lap-shear tests through numerical simulation.

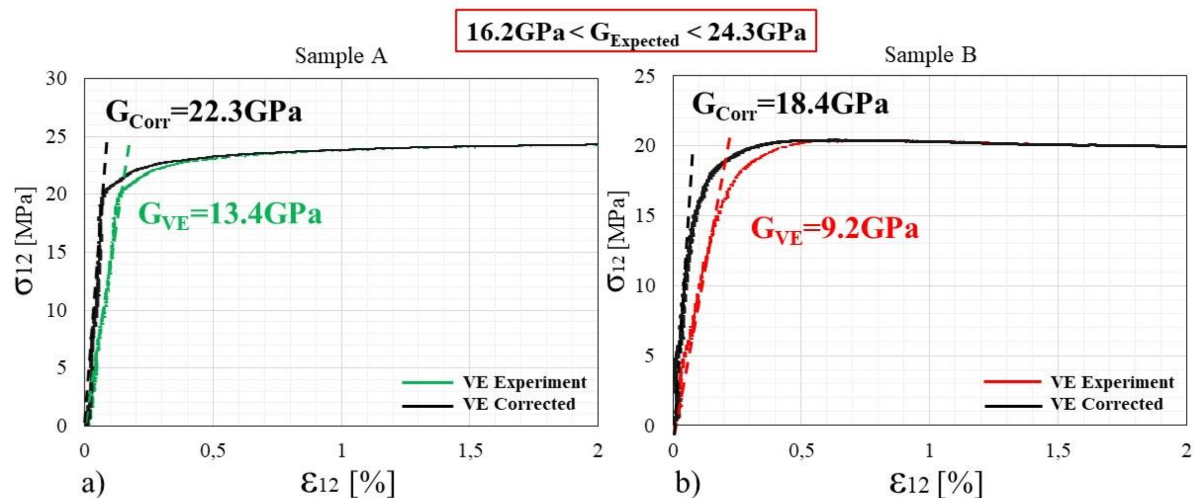

Fig. 13 Measured and corrected stress strain curve of sample design A (a) and sample design B (b)

5. Conclusion

This work provides insight into the mechanics of the lap-shear experiment. The lap-shear experiment is widely used, yet a detailed study of the local strain distribution and local stress state was missing. A correction method is presented to obtain more quantitative results from experimental results. The well-known Sn-3.0Ag-0.5Cu solder was studied numerically and

Die approbierte gedruckte Originalversion dieser Dissertation ist an der TU Wien Bibliothek verfügbar.
The approved original version of this doctoral thesis is available in print at TU Wien Bibliothek.
TU Bibliothek WIEN Your knowledge hub

through experiments to illustrate the underestimation of shear moduli. A common lap-shear designs (A) and an alternative one (B) are investigated. The following highlights are presented:

1. *Stress state in the solder:* The stress distribution inside the solder is shown through numerical simulation of the monotonic lap-shear tests. The influence of sample geometry and sample design are discussed based on numerical results. Special attention is brought to the importance of solder length for the stress distribution in the solder. The sample design B widely avoids peel-off stresses at low shear strains. Furthermore, the smallest solder pad length in sample design B show most homogeneous shear loads among the investigated samples, which motivates the use of small solder pad lengths for testing under homogeneous loading conditions.
2. *Large strain deformation behavior:* This work reported a quantitative experimental comparison of sample design A and sample design B with smaller solder length. In-situ measurements and stress-strain analysis are used to reveal the ability of both samples to measure large shear deformations. It was shown that sample A fails due to crack initiation at the boundaries close to the solder-substrate interface at shear strains of about ε_{12}=24%. Sample B maintains non-localized shear deformations up to shear strains of more than ε_{12}=35% until ductile failure occurs.
3. *Deviation of strain measures:* VE strain measurements capture lower shear strains on the solder surface. This leads to significant underestimation of shear moduli from lap-shear experiment. The presented experimental results underpin these findings from numerical simulation. The underestimation stems from a strain-gradient in 3-direction at the boundary of the lap-shear sample. Both sample designs reveal lower local strains because of this boundary effects. Therefore one obtains lower shear moduli than expected from other experimental methods, such as tensile tests.
4. *Strain correction method*: A strain correction method is presented, incorporating the measured shear modulus and a sample specific shape factor K. The shape factors for both sample designs and several sample dimensions are provided in this paper. The correction method is applied on lap-shear experiments of both sample designs. It was shown that only by use of the proposed correction method, the shear moduli are in the correct range expected from tensile tests. The proposed strain correction enables later studies to correct measurements and obtain quantitative shear moduli from lap-shear tests.

Die approbierte gedruckte Originalversion dieser Dissertation ist an der TU Wien Bibliothek verfügbar.
The approved original version of this doctoral thesis is available in print at TU Wien Bibliothek.
TU WIEN Bibliothek Your knowledge hub

2.2 A micromechanics-based model for liquid-assisted healing

Georg Siroky (georg.siroky@mcl.at) [1], Elke Kraker[1], Dietmar Kieslinger[2], Ernst Kozeschnik[3], Werner Ecker[1]
[1] Materials Center Leoben Forschung GmbH (MCL), Roseggerstraße 12, 8700 Leoben, Austria
[2] ZKW Elektronik GmbH, Samuel Morse-Straße 18, 2700 Wiener Neustadt, Austria
[3] TU Wien, Institute of Materials Science and Technology, Getreidemarkt 9, 1060 Wien, Austria

Published in: International Journal of Damage Mechanics, 30, 1, 123-144,
https://doi.org/10.1177/1056789520948561

Abstract

This work presents a damage evolution framework including liquid-assisted healing. The model incorporates contributions from void size, void pressure, surface tension and liquid pressure. Experimental motivation for the damage-healing model is provided with in-situ melting experiments, where the evolution of the void distribution under monotonic tension is illustrated. The damage evolution is based on nucleation and growth of voids, which are modeled in a unified creep and plasticity framework. The proposed damage formulation introduces a void collective, which computes the void distribution in the material and allows to describe void collapse using the Rayleigh-Plesset equation. The necessary conditions for healing are discussed with use of model results. Particularly, the role of external load during healing, the dependence on liquid viscosity and surface tension are investigated.

1. Introduction

Solder joints in microelectronic devices are exposed to multiple thermo-mechanical loads and need to fulfil increasing reliability requirements. The trend towards integrated packaging and miniaturization of solder joints increases local stresses and, subsequently, limits the service time of electronic devices. Mechanical damage in solder joints results from thermo-mechanical loads and manifests itself as voids, cracks and solder-substrate delamination [55,100,101] resulting from dissipative processes [102].

The development of new solders aims to tailor properties, such as, melting point, wettability, surface oxidation and mechanical properties (under, e.g., shock, tension, shear, electromigration [103], thermal [104]) among others, to improve the thermo-mechanical fatigue lifetime [105,106]. A possible approach to increase the damage resistance of microelectronic products (e.g. in solder joints or connectors) is the use of self-healing mechanisms to prevent or retard the damage progress. Healing in metals is still a comparably small domain of research,

Die approbierte gedruckte Originalversion dieser Dissertation ist an der TU Wien Bibliothek verfügbar.
The approved original version of this doctoral thesis is available in print at TU Wien Bibliothek.
TU WIEN Bibliothek Your knowledge hub

compared to other healable materials, such as, polymers [107,108] or concrete [109]. The challenging aspect about healing metals is the low atomic mobility, which only increases at elevated temperatures [110]. The healing mechanisms in metals studied are precipitation healing [111–113], healing under hot plastic deformation [114–116], healing under pulsed direct current [117–119] and liquid assisted healing [26,33,42,120]. To apply liquid assisted healing in the future (e.g. in microelectronics) the process of void collapse in the semi-solid configuration requires further analysis.

The present work focuses on a micromechanical-based description of liquid-assisted healing. The work of [33] investigated the healing behavior of a binary Sn-Bi matrix incorporating shape memory wires into a metal matrix composite. It was shown that macroscopic defects can be healed through heating, where the shape memory wires deform and introduce local compressive forces to improve bonding of cracks. In a follow up work by [121], the role of phase transformation of shape memory wires in metal matrix composites has been studied. On small length scales of a several micro-meters, the work of [26] has successfully demonstrated the concept of local healing through temporary melting of gold thin films.

Models describing damage and healing in engineering materials have been proposed for several material classes. Furthermore, general framework models have been derived from thermodynamic considerations. To the best knowledge of the authors, a mechanistic damage-healing model for liquid-assisted healing has not been published up to now, except a proceeding by the current authors, which presents a previous and simpler model [122]. An overview of several damage-healing models for specific and general purposes is provided in Tab. 4.

Tab. 4 Overview of proposed damage and healing models for different materials

Model (Authors)	**Material** (Healing Formulation)
Micromechanical [123]	**Cementitious** (material deposition in crack)
Micromechanical [124]	**Asphalt** (crack wetting and diffusion)
Micromechanical [125]	**Steel** (solute diffusion)
Continuum [126]	**Glass** (viscous and diffusional deposition)
Continuum [127]	**Polymer Composite** (phenomenological healing evolution)
Continuum [128]	**Polymers** (phenomenological healing evolution, time dependent)
Continuum [129]	**Glassy Polymers** (phenomenological healing evolution)
Continuum - Framework [130]	**General Framework** (thermodynamic healing variable)
Continuum Micro -Framework [131]	**General Framework** (phenomenological healing evolution)

Die approbierte gedruckte Originalversion dieser Dissertation ist an der TU Wien Bibliothek verfügbar.
The approved original version of this doctoral thesis is available in print at TU Wien Bibliothek.
TU Bibliothek WIEN Your knowledge hub

The literature overview shows that damage-healing models for metals and alloys are sparse. One of the few works on healing in metals is the work by [125,132], where a model for precipitation healing in alloys is introduced. A model proposed in [133] investigated healing of fatigue damage by laser repair. Other, more general works, present the thermodynamic relations of damage and healing [30,131,134–136] in a universal framework and independent of a particular material model. The healing evolution is derived in form of a healing potential, similar to an inverse dissipation potential. Yet, it is difficult to associate these healing potentials to observable micromechanical healing processes.

Many studies focus on the role of nucleation and growth of voids in ductile solids [137–146]. The contributions of [141] and [142] describe the growth of single voids in elastic-plastic media. Void growth at grain boundaries due to creep deformation has been studied by [147–151]. [152] have generalized the works of [141], [150] and [151] and obtained a combined creep and plasticity void growth expression. This formulation is of particular benefit as soon as multiple growth mechanisms are active simultaneously, such as, vacancy diffusion and plastic deformation.

In [153], an extensive review of inelastic deformation theories is provided. The work of [154] reviews several different damage frameworks for nucleation and growth and, furthermore, compares additive and multiplicative terms of nucleation and growth. In [139], a void nucleation model is introduced that allows for the decomposition of tensile, compression and torsion contributions to the overall number of nucleated voids. The model adapts established concepts for nucleation and growth for concurrent creep and plastic deformation [139,152] and combines these in a continuum mechanical damage mechanics framework [155,156]. The present study focuses on modelling healing of ductile voids, where voids nucleate under monotonic loading as suggested in [139]. In case of other loading conditions, the presented framework might require different nucleation and growth relations. A comprehensive overview on creep models of solders is provided in [157].

The present work introduces a micromechanical model to describe damage generation and liquid-assisted healing. A continuum damage mechanics (CDM) framework is used to obtain the evolution of voids in an elastic-viscoplastic solid. The classical CDM framework is extended through a void collective vector, which allows to obtain the void size distribution over time. The total damage is computed as the void volume over total volume. The effective damage variable in this framework can increase due to damage generation as well as decrease due to healing once heated into the semi-solid regime. Liquid assisted healing is modelled by means

Die approbierte gedruckte Originalversion dieser Dissertation ist an der TU Wien Bibliothek verfügbar.
The approved original version of this doctoral thesis is available in print at TU Wien Bibliothek.
TU WIEN Bibliothek Your knowledge hub

of single void collapse using the Rayleigh-Plesset equation. Therefore, the healing evolution can be physically interpreted and the contribution of material variables to healing can be shown. The effect of void size, surface tension, liquid viscosity and hydrostatic pressure on the healing evolution is discussed. To assist the damage and healing modelling, supplementary experimental results are carried out and CALPHAD calculations are performed to obtain the liquid fraction as a function of temperature using the software package MatCalc (http://matcalc.at) with the thermodynamic database from COST 531 [158].

2. Experimental Motivation

In Fig. 14, the damage-healing behavior under uniaxial tension is shown. Tensile samples made of Sn-30wt.%Bi are cast in a silicon mould. Defects, such as, cracks and voids, are induced by a cyclic tensile damage experiment, which is stopped shortly before rupture. The tested samples are exposed to a healing procedure as shown in Fig. 14a. During the healing process, the sample is kept above the solidus-temperature ($T_{\text{solidus}} = 138°\text{C}$) at $T = 145°\text{C}$ for $t = 5$ min.

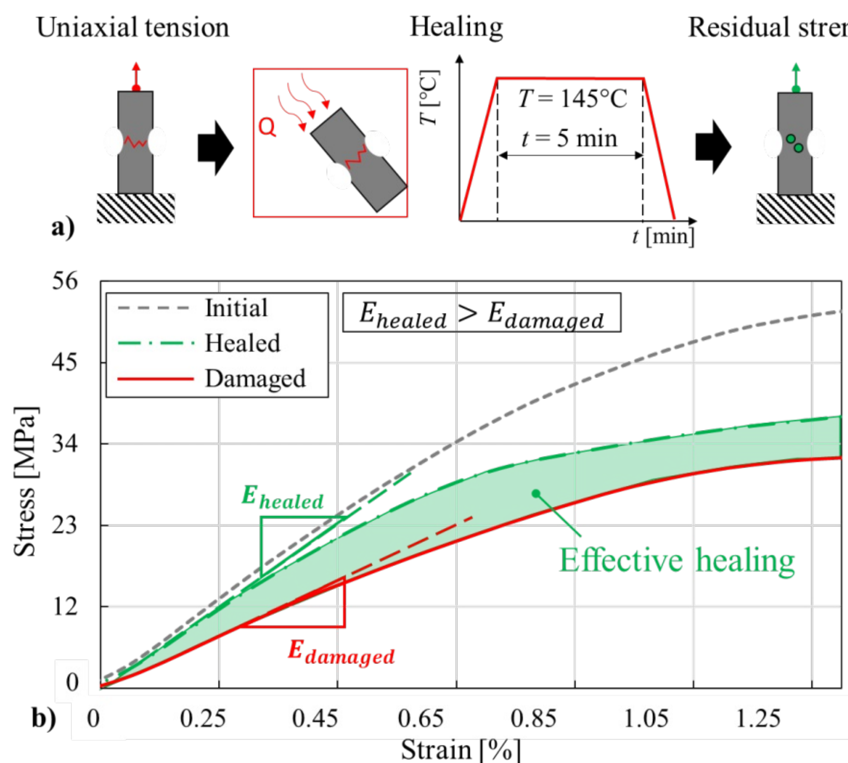

Fig. 14 Damage healing experiment under uniaxial tension a) Damage and healing procedure and healing temperature profile b) Typical stress-strain curves of damaged and healed tensile samples.

The residual strength of the samples is determined after healing. The initial loading cycle, a loading cycle before rupture and the loading cycle after healing are illustrated in Fig. 14b. The "damaged" configuration reveals the lowest strength and a substantial elastic softening,

Die approbierte gedruckte Originalversion dieser Dissertation ist an der TU Wien Bibliothek verfügbar.
The approved original version of this doctoral thesis is available in print at TU Wien Bibliothek.
TU WIEN Bibliothek Your knowledge hub

indicated by a lower initial stiffness, E_{damaged}. The "healed" configuration is located between the "initial" and the "damaged" configuration. This provides evidence that partial healing is achieved under the given experimental conditions.

It is important to outline the healing effect from the shape of the stress-strain curves (Fig. 14b). Accordingly, mechanical damage in these samples is associated with a reduction of effective material cross-section [155,156] due to pore nucleation and growth. This reduction is manifested in the reduced elastic stiffness in the damaged state. The advantageous effect of liquid healing is indicated by the green, dot dash line, where the "healed" stiffness recovers close to that of the "initial" sample due to void or crack closure.

A crucial aspect of the present model is the void distribution function, which is dependent on the degree of plastic deformation. To motivate the shape of the void distribution function, nucleation tests are performed as shown in Fig. 15a-e. Sn-30wt.%Bi samples are deformed under uniaxial, monotonic tension. The tensile tests are stopped at different strain levels as indicated in Fig. 15a.

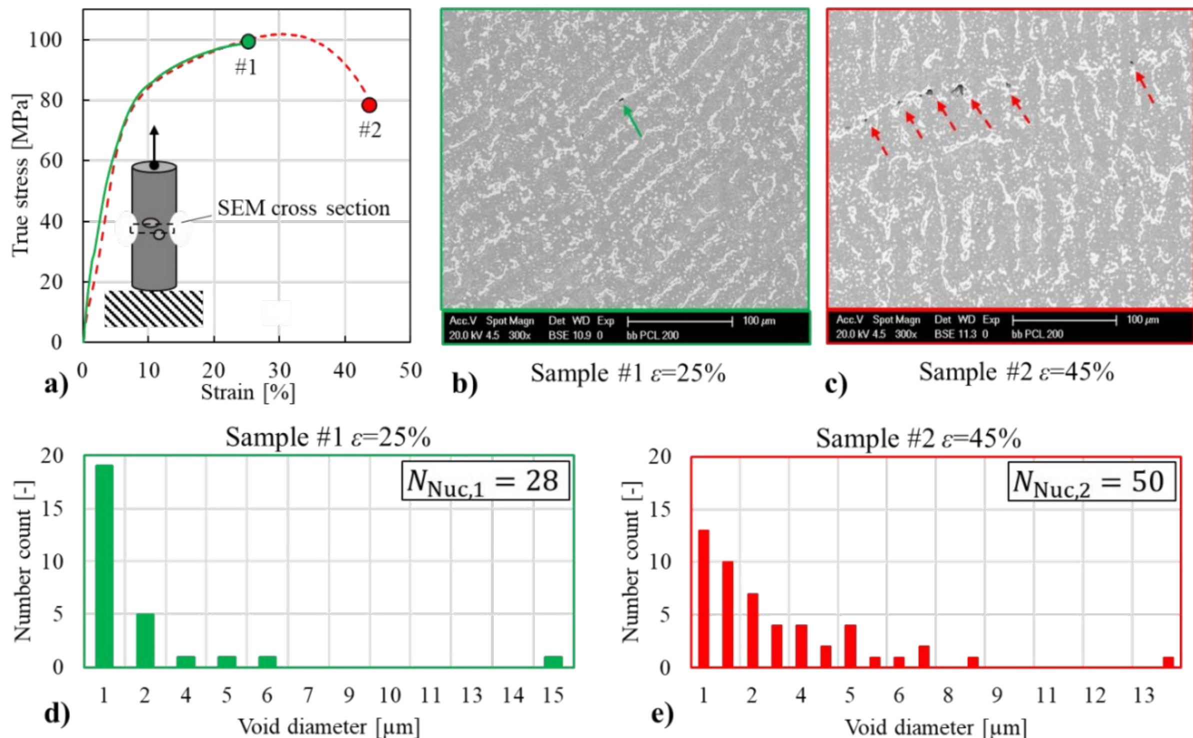

Fig. 15 Uniaxial tension void nucleation test. a) Stress-Strain curves of tensile test interrupted at 25 % (green solid) and 45 % (red dashed) b) SEM micrograph of 25 % strain sample c) SEM micrograph of 45 % strain sample d) Void size histogram of 25 % strain sample e) Void size histogram of 45 % strain sample

Die approbierte gedruckte Originalversion dieser Dissertation ist an der TU Wien Bibliothek verfügbar.
The approved original version of this doctoral thesis is available in print at TU Wien Bibliothek.
TU Bibliothek WIEN Your knowledge hub

The sample cross-sections after straining are investigated through Scanning Electron Microscopy (SEM) in Fig. 15b and Fig. 15c. In the sample with 25% strain, a single void is visible in the micrograph as indicated by the green arrow. The voids in the sample with 45% strain are mainly located at the phase boundary between eutectic phase (white) and β-Sn phase (gray) as indicated with red dashed arrows. The void distribution of the entire micrograph area is obtained by image processing using ImageJ [159]. Voids are segmented by gray-value thresholding. The void size and the average void diameter are shown in Fig. 15d and Fig. 15e.

The void distribution graphs, Fig. 15d and Fig. 15e, suggest a continuous void nucleation process throughout the deformation process. In case of a single nucleation event, a Gaussian-like void distribution would be expected around a single mean void diameter, however, the experiment shows an increasing number density of voids with increasing strain. Continuous void nucleation is also evident from the total number of voids nucleated in sample #1, $N_{\mathrm{Nuc},1} = 28$, and in sample #2, $N_{\mathrm{Nuc},2} = 50$. The number of nucleated voids increases linearly and proportional to the total strain ($\frac{\epsilon_2}{\epsilon_1} = 1.80$ comparing to $\frac{N_{\mathrm{Nuc},2}}{N_{\mathrm{Nuc},1}} = 1.78$).

To investigate void filling through liquid-assisted healing, a cuboid sample (9x9x20 mm, Sn-30wt.%Bi) is placed on a heating plate. A digital microscope (Keyence, VHX 6000, 500x-1000x magnification) is placed on the front surface to capture the melting process in-situ from a height of $h_{\mathrm{M}} = 2$ mm above the heating plate. A thermocouple is attached to the heating plate and the temperature is logged throughout the test.

A microstructural illustration of liquid filling of a single 10 µm void in the vicinity of the eutectic domain is shown in Fig. 16 (red dashed circle). The images display several snapshots during the filling process with the liquid phase of the semi-solid microstructure indicated in blue. Fig. 16a shows the initial microstructure at room temperature. The eutectic phase is visible in dark grey color and indicated by white arrows. The higher melting β-Sn phase (light grey) is marked by black arrows.

Die approbierte gedruckte Originalversion dieser Dissertation ist an der TU Wien Bibliothek verfügbar.
The approved original version of this doctoral thesis is available in print at TU Wien Bibliothek.
TU WIEN Bibliothek Your knowledge hub

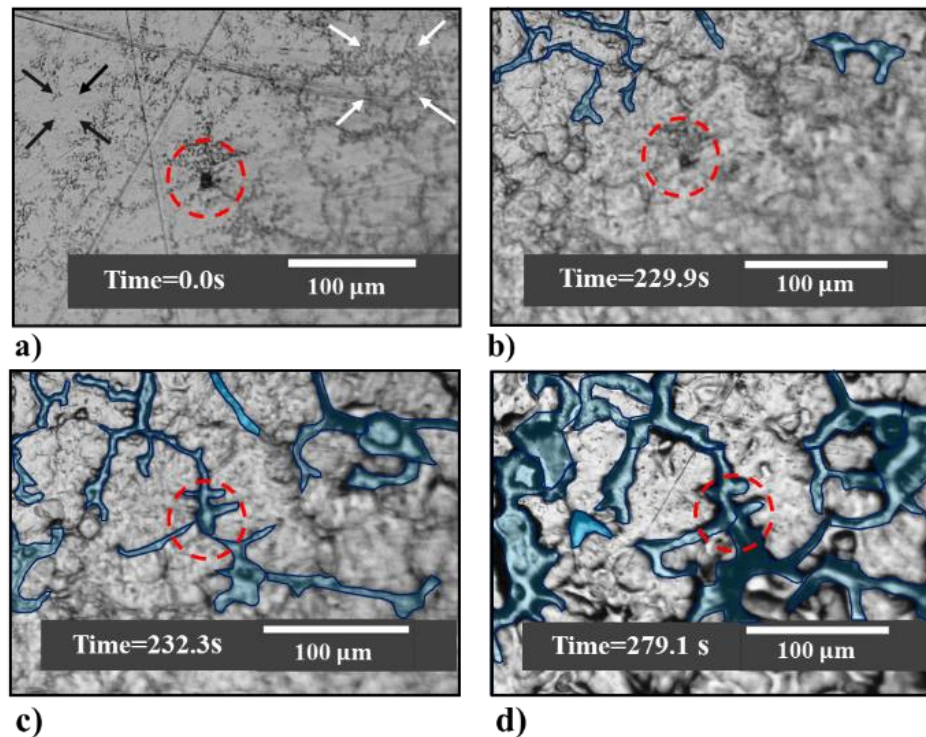

Fig. 16 In-situ heating experiment of Sn-30wt.%Bi. a) Initial microstructure, indicating a 10 µm void (dashed circle) close to eutectic domain (white arrow) and primary phase (black arrow). b) Onset of eutectic phase melting. c) Void filling with liquid eutectic phase. d) Semi-solid microstructure before re-solidification.

In Fig. 16b, the melting process commences from the top of the image, while the void is already filled with liquid in Fig. 16c. The timespan of void filling is estimated to be less than 2.4 s, as observable in the supplementary videos. From comparison of Figs. 3a and d, the correspondence of eutectic regions with liquified material is clearly visible.

Fig. 17 shows the liquid phase fraction from CALPHAD calculations as a function of temperature. The temperature history utilized in the experiments is displayed in Fig. 18. The healing process is initiated by heating the material above the liquidus temperature. For this, the plate is first brought to T=155 °C into a steady state. Within the time span of t=140 s to t=240 s, the temperature is gradually increased until liquid phase becomes visible in the field of view. It is important to emphasize that the temperature signal corresponds to the temperature of the heating plate and not the temperature of the sample. Due to heat loss, a higher plate temperature is required to exceed the eutectic (solidus) temperature of the alloy (approximately 138°C) at the top surface.

Die approbierte gedruckte Originalversion dieser Dissertation ist an der TU Wien Bibliothek verfügbar.
The approved original version of this doctoral thesis is available in print at TU Wien Bibliothek.
TU Bibliothek WIEN Your knowledge hub

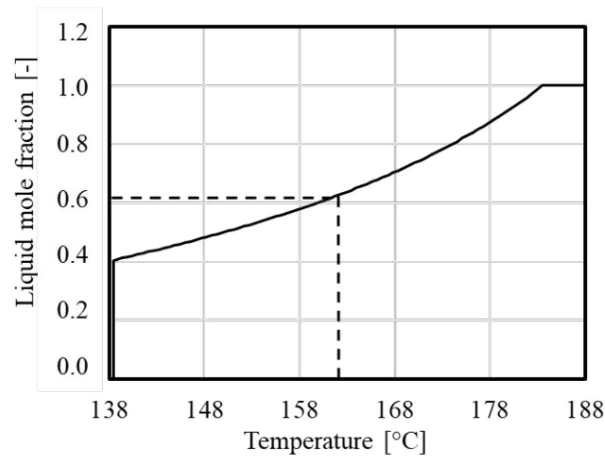

Fig. 17 Liquid phase fraction from CALPHAD calculations (eutectic point at approximately 138°C)

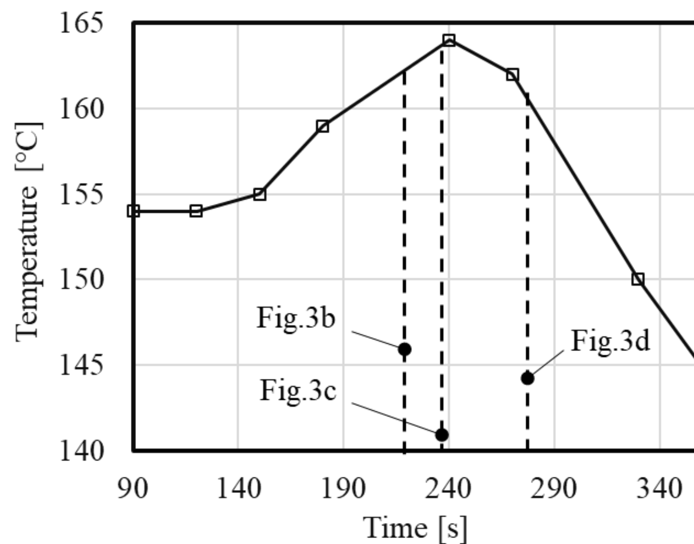

Fig. 18 Temperature profile measured at the heating plate.

3. Modelling

The kinematics of the present micromechanical model is based on the concept of unified creep-plasticity. The damage evolution in the solid domain is given by means of void nucleation and growth. The healing evolution in the semi-solid domain is formulated based on the Rayleigh-Plesset equation for voids in liquid and it is outlined in detail, subsequently.

Unified Creep-Plasticity

The deformation behavior of solders has been characterized, e.g., in [160] and reveals creep dominated deformation at low shear stresses and above $0.3 \cdot T_{\text{solidus}}$. For normalized shear stresses above $\frac{\tau}{G} = 2 \cdot 10^{-3}$, these authors observe that plasticity is the dominant deformation mechanism. Therefore, the kinematic and the damage evolution models are defined to cover both domains, creep and plasticity, in a unified manner.

Die approbierte gedruckte Originalversion dieser Dissertation ist an der TU Wien Bibliothek verfügbar.
The approved original version of this doctoral thesis is available in print at TU Wien Bibliothek.
TU WIEN Bibliothek Your knowledge hub

A corresponding creep-plasticity CDM framework for solders has been reported in [161] and in [162]. The equations for viscoplastic deformation and the coupling to the damage variable are adapted from [161]. In case of small deformations, the total strain rate tensor, $\dot{\boldsymbol{\epsilon}}$, can be decomposed into elastic, inelastic and thermal strain rate contributions, $\dot{\boldsymbol{\epsilon}}_{\mathbf{el}}$, $\dot{\boldsymbol{\epsilon}}_{\mathbf{in}}$ and $\dot{\boldsymbol{\epsilon}}_{\mathbf{therm}}$, as

$$\dot{\boldsymbol{\epsilon}} = \dot{\boldsymbol{\epsilon}}_{\mathrm{el}} + \dot{\boldsymbol{\epsilon}}_{\mathrm{in}} + \dot{\boldsymbol{\epsilon}}_{\mathrm{therm}}, \tag{28}$$

with

$$\dot{\boldsymbol{\epsilon}}_{\mathrm{in}} = \sqrt{\frac{3}{2}} A \left(\frac{S_{\mathrm{v}}}{d}\right)^{n} exp\left(B\left(\frac{S_{\mathrm{v}}}{d}\right)^{n+1}\right) \exp\left(\frac{-Q}{R_{\mathrm{g}}\, T}\right) \cdot \boldsymbol{N} \tag{29}$$

and

$$\boldsymbol{N} = \frac{\boldsymbol{S}-\boldsymbol{\alpha}}{\|\boldsymbol{S}-\boldsymbol{\alpha}\|}. \tag{30}$$

The coefficients A and B are material parameters, S_{v} is the viscous overstress, d is the drag strength and n is an exponential coefficient. The exponential term on the right side accounts for the temperature dependency of inelastic deformation and is formulated in an Arrhenius type expression. Q is the activation energy, R_{g} is the universal gas constant and T is the temperature. The vector $\boldsymbol{N}$ describes the inelastic flow direction. The driving force for inelastic deformation is the viscous overstress, S_{v}, given as

$$S_{\mathrm{v}} = \left\langle \sqrt{\frac{3}{2}} \frac{1}{1-D_{\mathrm{eff}}} \|\boldsymbol{S} - \boldsymbol{\alpha}\| - R \right\rangle. \tag{31}$$

The viscous overstress includes the effective damage variable, D_{eff}, which is defined by the damage-healing evolution law. The damage variable is denoted as “effective” to distinguish between the classic monotonically increasing damage variable, D, as defined in [155,156] and the effective damage variable that can be reduced due to healing. The term $\|\boldsymbol{S} - \boldsymbol{\alpha}\|$ introduces the deviatoric stress tensor, $\boldsymbol{S}$, and the deviatoric backstress tensor, $\boldsymbol{\alpha}$, to the viscous overstress. The yield-surface is defined by R and describes an isotropic hardening behavior. $\boldsymbol{\alpha}$ is the backstress tensor, which defines the center of the yield surface. The Macaulay brackets ($\langle X\rangle = X$ if $X \geq 0$, otherwise $\langle X\rangle = 0$) restrict the viscous overstress to non-zero values if $\|\boldsymbol{S} - \boldsymbol{\alpha}\| - R$ is greater or equal zero. The isotropic hardening evolution law is given in the form

$$R = R_0 + (R_\infty - R_0)\left(1 - e^{-b\epsilon_{\mathrm{in,eq}}}\right), \tag{32}$$

where R_0 is the initial yield stress and R_∞ is the hardening saturation value. Furthermore, b is a

TU WIEN Bibliothek Your knowledge hub
Die approbierte gedruckte Originalversion dieser Dissertation ist an der TU Wien Bibliothek verfügbar.
The approved original version of this doctoral thesis is available in print at TU Wien Bibliothek.

material constant and $\epsilon_{\mathrm{in,eq}}$ is the accumulated equivalent plastic strain. The hardening law of the yield surface in Eq. 32 has originally been formulated by [163,164] and was introduced in the viscoplastic framework by [161]. The deviatoric backstress tensor evolution is accordingly defined as

$$\dot{\boldsymbol{\alpha}} = (1 - D_{\mathrm{eff}})\, \mu\, \|\dot{\boldsymbol{\epsilon}}_{\mathrm{in}}\|\, \boldsymbol{N} - \beta \boldsymbol{\alpha}, \tag{33}$$

with μ and β being material parameters and $\|\dot{\boldsymbol{\epsilon}}_{\mathrm{in}}\|$ being the equivalent plastic strain norm.

Damage-Healing Evolution

The inelastic strain rate is coupled to the damage parameter, D_{eff}, as defined in Eqs. 31 and 33. Furthermore, the elastic material stiffness tensor is modified by the damage variable and the stress response is given according to

$$\boldsymbol{\sigma} = (1 - D_{\mathrm{eff}})\, \boldsymbol{C} : (\boldsymbol{\epsilon} - \boldsymbol{\epsilon}_{\mathrm{in}} - \boldsymbol{\epsilon}_{\mathrm{therm}}), \tag{34}$$

where $\boldsymbol{\sigma}$ is the Cauchy stress tensor and $\boldsymbol{C}$ is the elastic material stiffness tensor. The expression $(1 - D_{\mathrm{eff}})$ accounts for the mechanical damage due to a reduction in effective cross-section, where the elastic stiffness in the context of damage and healing is discussed by [165]. The effective damage variable can be defined by means of void volume fraction, as outlined by [137], with

$$D_{\mathrm{eff}} = \frac{V_{\mathrm{void}}[\boldsymbol{\psi}_{\mathrm{C}}, \boldsymbol{\psi}_{\mathrm{R}}]}{V_0}, \tag{35}$$

with

$$V_{\mathrm{void}}[\boldsymbol{\psi}_{\mathrm{C}}, \boldsymbol{\psi}_{\mathrm{R}}] = \sum_i^N \frac{4}{3} \cdot \pi \cdot \psi_{\mathrm{R},i}^3 \cdot \psi_{\mathrm{C},i}\,, \tag{36}$$

where V_{void} is the void volume functional of the void collective, which is written as the void number count vector, $\boldsymbol{\psi}_{\mathrm{C}}$, and the void radius vector, $\boldsymbol{\psi}_{\mathrm{R}}$. The entries of $\boldsymbol{\psi}_{\mathrm{C}}$ are scalar numbers of voids, $\psi_{\mathrm{C},i}$, nucleated at time i and are of dimension N. $\boldsymbol{\psi}_{\mathrm{R}}$ is also of dimension N, where the i-th entry provides the radius of voids, R_i, nucleated at time i. This increases the dimension N of the void collective $[\boldsymbol{\psi}_{\mathrm{C}}, \boldsymbol{\psi}_{\mathrm{R}}]$ with each time increment. The initial material volume is defined as V_0. The voids are assumed to be spherical in Eq. 35. Once a void reaches a subcritical radius due to, e.g., healing, the void is removed from the void collective and the dimension of $[\boldsymbol{\psi}_{\mathrm{C}}, \boldsymbol{\psi}_{\mathrm{R}}]$ decreases.

Void Nucleation

The nucleation model introduces new voids of critical size to the void collective $[\boldsymbol{\psi}_{\mathrm{C}}, \boldsymbol{\psi}_{\mathrm{R}}]$. The

Die approbierte gedruckte Originalversion dieser Dissertation ist an der TU Wien Bibliothek verfügbar.
The approved original version of this doctoral thesis is available in print at TU Wien Bibliothek.
TU Bibliothek Your knowledge hub WIEN

nucleation model presented in [139] is adapted here. These authors have proposed the void nucleation rate as

$$\dot{\eta} = \frac{\|\dot{\varepsilon}_{\mathrm{in}}\| \, d^{1/2}}{K_{\mathrm{IC}}} \cdot \eta \cdot \left\{ a \left[\frac{4}{27} - \frac{J_3^2}{J_2^3} \right] + b \, \frac{J_3}{J_2^{3/2}} + c \left\| \frac{I_1}{\sqrt{J_2}} \right\| \right\}. \tag{37}$$

The parameters a, b and c are weighting factors of different stress states. These are determined from nucleation experiments under specific stress states. The expressions I_1, J_2, J_3 are the first stress invariant, the second deviatoric invariant and the third deviatoric invariant, respectively. The pre-factor to the left of the round brackets contains the norm of the inelastic strain rate, a length scale parameter, d, and the fracture toughness, K_{IC}. The fracture toughness accounts for a material specific nucleation rate and reduces the nucleation rate for tough materials.

For the sake of simplicity, the original model is restricted in the current work to void nucleation under positive stress triaxialities in the uniaxial case. Therefore, the terms including the parameters a and b are neglected. Furthermore, it has been shown in the previous experimental section that the number of nucleated voids follows a linear relation with respect to strain. The pre-factor is reformulated and combines the expression $(d^{\frac{1}{2}} \cdot \eta \cdot c)/K_{\mathrm{IC}})$ to the variable η_{init}, which can be interpreted as the initial number of potential nucleation sites. The simplified and reformulated version of the nucleation rate then reads

$$\dot{\eta} = \|\dot{\varepsilon}_{\mathrm{in}}\| \, \eta_{\mathrm{init}} \left\langle \frac{\sigma_{\mathrm{hydro}}}{\sigma_{\mathrm{eff}}} \right\rangle. \tag{38}$$

The nucleation rate, Eq. 29, is in agreement with the form postulated by [166,167]. The parameter η_{init} can be estimated from nucleation experiments by counting the number of nucleating voids at a given strain level (compare Fig. 15).

The number of critical sized voids nucleated at time *i* is finally given with

$$\boldsymbol{\psi}_{\mathrm{C}} = \begin{bmatrix} \psi_{\mathrm{C},1} \\ \vdots \\ \psi_{\mathrm{C},i} \\ \vdots \\ \psi_{\mathrm{C},N} \end{bmatrix}, \tag{39}$$

with $\psi_{\mathrm{C},i} = V_0 \cdot \dot{\eta} \cdot dt$. The critical voids nucleated at time *I* are subsequently added to the void radius vector according to

Die approbierte gedruckte Originalversion dieser Dissertation ist an der TU Wien Bibliothek verfügbar.
The approved original version of this doctoral thesis is available in print at TU Wien Bibliothek.
TU WIEN Bibliothek Your knowledge hub

$$\boldsymbol{\psi}_{\mathrm{R}} = \begin{bmatrix} \psi_{\mathrm{R},1} \\ \vdots \\ \psi_{\mathrm{R},i} \\ \vdots \\ \psi_{\mathrm{R},N} \end{bmatrix}, \tag{40}$$

with $\psi_{\mathrm{R},i} = \psi_{\mathrm{R,Crit}}$.

Void Growth

The void radius vector, $\boldsymbol{\psi}_{\mathrm{R}}$, is updated at each time increment according to the void growth model of [152], which is used to obtain a consistent model formulation with both, creep and plasticity contributions. The radius growth increment of the *i*-th void entry is calculated according to

$$d\psi_{\mathrm{R},i} = \psi_{\mathrm{R},i}\left[\frac{1}{2}\left(\frac{\Lambda_{\mathrm{q}}}{\psi_{\mathrm{R},i}}\right)^3 f\left(\frac{\Lambda_{\mathrm{q}}}{\psi_{\mathrm{R},i}}\right) - \frac{3}{8} + \alpha_{\mathrm{RT}} \sinh\left(\frac{3}{2}\,\frac{\sigma_{\mathrm{hydro}}}{\sigma_{\mathrm{eff}}}\right)\right] d\|\epsilon_{\mathrm{in}}\| \tag{41}$$

The first term in brackets describes the creep contribution due to vacancy diffusion [152], whereas the sinh-term accounts for plastic void growth as originally proposed by [141]. The diffusion path parameter, Λ_{q}, is given in a generalized form of triaxial stress states with

$$\Lambda_{\mathrm{q}} = \left(\frac{\sigma_{\mathrm{hydro}}}{\sigma_{\mathrm{eff}}}\right)^{\frac{1}{3}}\left(\frac{D_{\Lambda}\sigma_{\mathrm{eq}}}{\dot{\epsilon}_{\mathrm{in,eq}}}\right)^{\frac{1}{3}}, \tag{42}$$

$$D_{\Lambda} = \frac{\Omega\, D_{\mathrm{b}}\delta_{\mathrm{b}}}{kT}, \tag{43}$$

and

$$f(\Lambda_{\mathrm{q}}/\psi_{\mathrm{R},i}) = \left[ln\left(\frac{\psi_{\mathrm{R},i}+\Lambda_{\mathrm{q}}}{\psi_{\mathrm{R},i}}\right) + \left(\frac{\psi_{\mathrm{R},i}+\Lambda_{\mathrm{q}}}{\psi_{\mathrm{R},i}}\right)^2\left(1 - \frac{1}{4}\left(\frac{\psi_{\mathrm{R},i}+\Lambda_{\mathrm{q}}}{\psi_{\mathrm{R},i}}\right)^2\right) - \frac{3}{4}\right]^{-1}. \tag{44}$$

D_{Λ} is the vacancy diffusion coefficient, σ_{eq} the equivalent stress, $\dot{\epsilon}_{\mathrm{in,eq}}$ the equivalent inelastic strain rate, Ω the atomic volume, D_{b} the grain boundary diffusivity and $\delta_{\mathrm{b}}$the grain boundary thickness.

Void Healing

Due to the availability of the void collective $[\boldsymbol{\psi}_{\mathrm{C}}, \boldsymbol{\psi}_{\mathrm{R}}]$, the Rayleigh-Plesset equation can be utilized to describe the void healing evolution. Once the healing condition is fulfilled, a single void surrounded by liquid collapses, as observed experimentally (Fig. 16). The healing condition is formulated in the form $T > T_{\mathrm{solidus}}$. The Rayleigh-Plesset equation is given as

Die approbierte gedruckte Originalversion dieser Dissertation ist an der TU Wien Bibliothek verfügbar.
The approved original version of this doctoral thesis is available in print at TU Wien Bibliothek.
TU WIEN Bibliothek Your knowledge hub

$$\frac{(p_{\mathrm{v}}-p_{\mathrm{hyd}})}{\rho_{\mathrm{L}}} = \frac{3}{2}\dot{\psi}_{\mathrm{R},i}{}^{2} + \psi_{\mathrm{R},i}\ddot{\psi}_{\mathrm{R},i} + 4\frac{\eta_{\mathrm{visc}}\,\dot{\psi}_{\mathrm{R},i}}{\psi_{\mathrm{R},i}} + 2\frac{\sigma_{\mathrm{surf}}}{\rho_{\mathrm{L}}\psi_{\mathrm{R},i}}. \quad (45)$$

$\dot{\psi}_{\mathrm{R},i}$ and $\ddot{\psi}_{\mathrm{R},i}$ are the void radius velocity and void radius acceleration, respectively. The void pressure, p_{v}, and hydrostatic liquid pressure, p_{hyd}, describe the pressure gradient. p_{v} is assumed to be zero in the following evaluation. The pressure gradient is balanced by the fluid flow term, drag term, surface tension term (σ_{surf}) and liquid viscosity term (η_{visc}). Since there exists no general analytical solution of Eq. 45, a numerical solution is required by, e.g., the Finite Difference (FD) method. The work of [168] provides a thorough analysis of numerical solutions. In [169], analytical solutions for the special case of the inviscid Rayleigh-Plesset equation is given. In the current work, a solution of Eq. 45 is obtained by an Euler-FD scheme, using the void radius acceleration given as

$$\ddot{\psi}_{\mathrm{R},i} = -\frac{3\dot{\psi}_{\mathrm{R},i}}{2\,\psi_{\mathrm{R},i}} + \frac{p_{\mathrm{v}}-p_{\mathrm{hyd}}-2\frac{\sigma_{\mathrm{surf}}}{\psi_{\mathrm{R},i}}}{\rho_{\mathrm{L}}\,\psi_{\mathrm{R},i}} - \frac{4\,\eta_{\mathrm{visc}}\dot{\psi}_{\mathrm{R},i}}{\rho_{\mathrm{L}}\,\psi_{\mathrm{R},i}^{2}}. \quad (46)$$

with the initial conditions $\psi_{\mathrm{R},i}(t=0) = \psi_{\mathrm{R0},i}$ and $\dot{\psi}_{\mathrm{R},i}(t=0) = 0$.

The numerical procedure of the damage-healing framework is summarized in Fig. 19. A temperature criterion, $T > T_{\mathrm{solidus}}$, at the start of each increment selects either the update algorithm of the solid or the semi-solid regime. In the solid regime, the growth of existing voids is computed according to Eq.41, where the cycle symbol indicates to apply it on all N entries of the void radius vector $\boldsymbol{\psi}_{\mathrm{R}}$. Next, the nucleation rate according to Eq. 38 is computed and a new void group is introduced to the void collective (Eqs.39 and 40). The damage variable is calculated using the total void volume fraction based on Eqs.35 and 36.

In case that the healing condition is active, the update algorithm follows the procedure of the semi-solid regime. The void radius vector is updated by numerically solving Eq. 45 and subcritical voids are removed from the void collective. The last operation of the algorithm is to compute the damage variable accordingly.

Die approbierte gedruckte Originalversion dieser Dissertation ist an der TU Wien Bibliothek verfügbar.
The approved original version of this doctoral thesis is available in print at TU Wien Bibliothek.
TU Wien Bibliothek Your knowledge hub

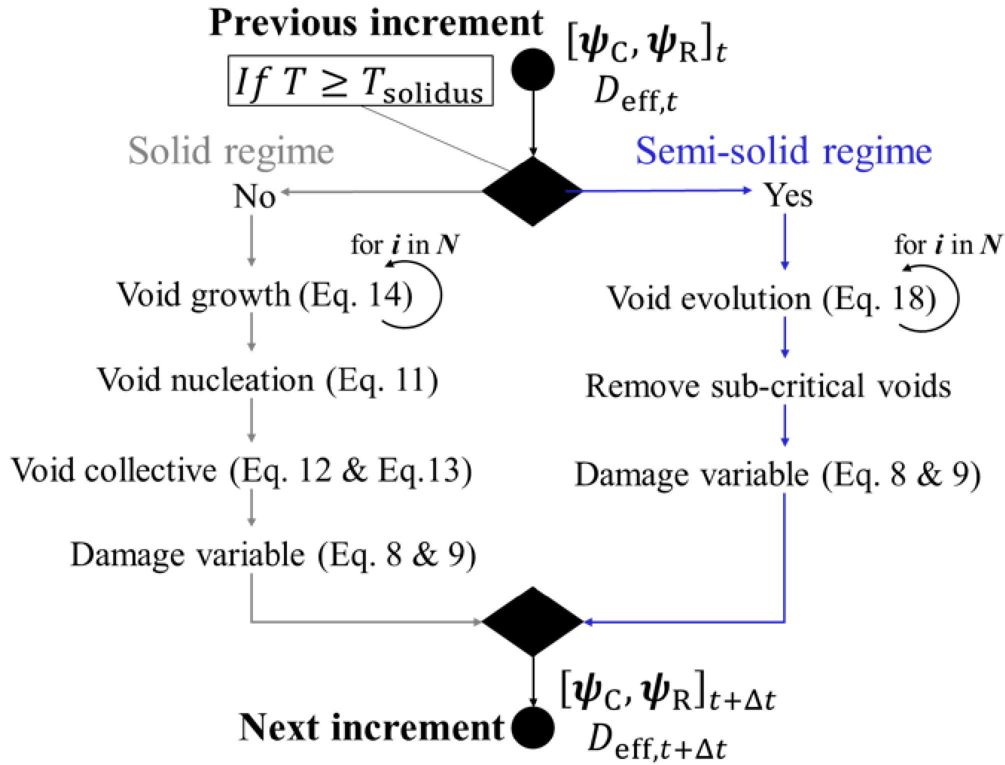

Fig. 19 Update algorithm of the damage-healing model

4. Results and Discussion

The results provide a discussion of the damage and healing characteristic. The damage response is computed in comparison with tensile experiments. Healing under variation of liquid surface tension, σ_{surf}, viscosity, η_{visc}, and hydrostatic pressure, p_{hyd}, is illustrated.

Damage Results

Model results under uniaxial tension are summarized in Fig. 20 and Fig. 21. The elastic-creep-plasticity model parameters are given in Tab. A1. The stress strain response in Fig. 20a is computed until $\epsilon_{11} = 25\ \%$ (green solid) and $\epsilon_{11} = 45\ \%$ (red dot dash). Furthermore, experimental data (black dashed) is given for comparison.

The computed stress-strain response agrees well with the experimental data in the initial linear regime until $\epsilon_{11} = 10\ \%$, as well as the hardening regime for strains $10\% < \epsilon_{11} < 30\ \%$. The model in this work is evaluated on a single material point and, therefore, neglects structural effects, such as, sample necking. This deviation of model and experimental results is observed at strains > 30 %.

The graph in Fig. 20b shows the damage parameter evolution over total strain. At $\epsilon_{11} = 25\ \%$, the damage level is negligible and increases exponentially from $\epsilon_{11} > 40\ \%$. The void

Die approbierte gedruckte Originalversion dieser Dissertation ist an der TU Wien Bibliothek verfügbar.
The approved original version of this doctoral thesis is available in print at TU Wien Bibliothek.
TU Bibliothek WIEN Your knowledge hub

distribution in Fig. 20c ($\epsilon_{11} = 25$ %) and Fig. 20d ($\epsilon_{11} = 45$ %) gives further insight into the damage evolution. At $\epsilon_{11} = 25$ %, the void distribution shows a maximum void size of 0.3 µm, where for a strain level of $\epsilon_{11} = 45$ % the largest void has grown to 80 µm.

The computed void distribution in Fig. 20c and 20d are qualitatively supported by the experimental void distribution in Fig. 15d and 15e. It is emphasized at this point that, in order to compare the total number of voids of experiments with the model, the assessment of voids has to be improved. The experimental void count has been determined from sectional SEM micrographs, which potentially underestimates the total void number.

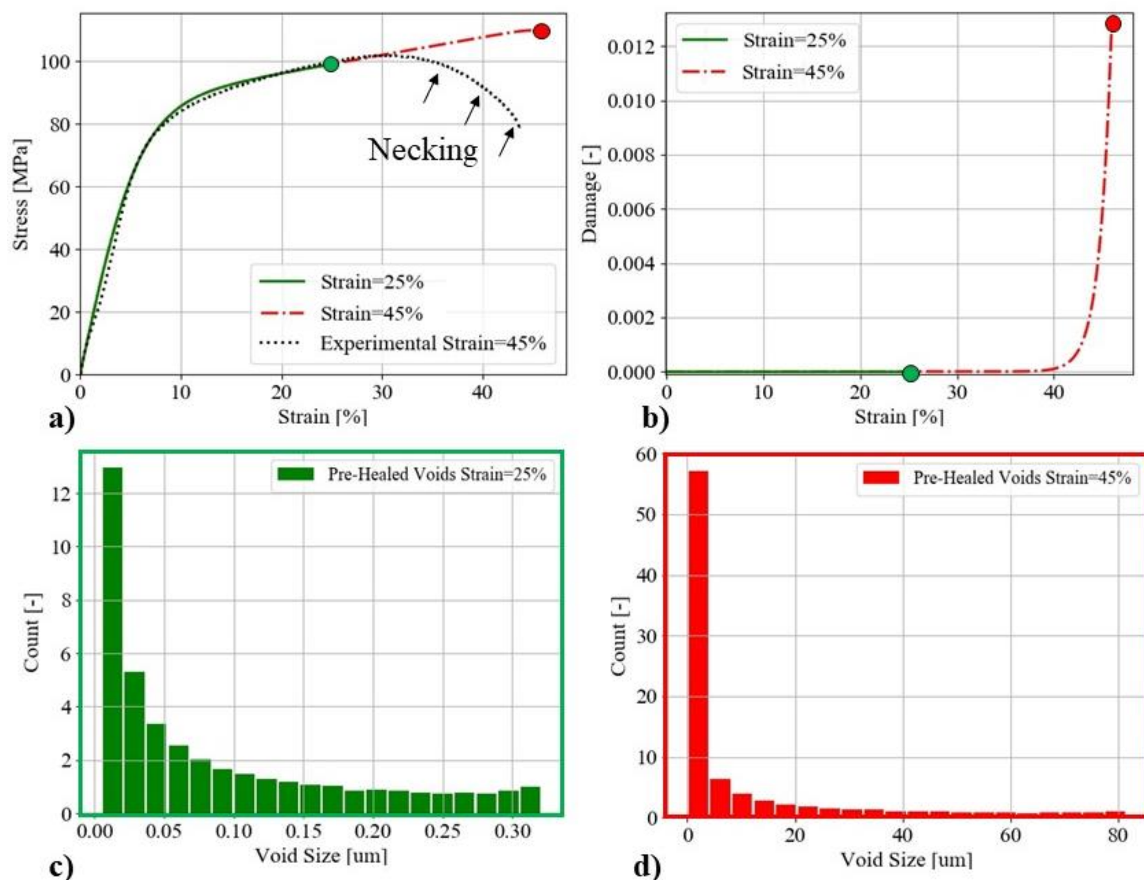

Fig. 20 Damage response and void distribution of the proposed material model. a) Stress-strain curve interrupted at $\epsilon_{11} =$ 25 % and $\epsilon_{11} = 45$ % and experimental stress-strain curve.. b) Damage evolution over strain. c) Void distribution at $\epsilon_{11} = 25$ % d). Void distribution at $\epsilon_{11} = 45$ %.

The nucleation characteristic of the model is illustrated in Fig. 21 using the nucleation and growth model parameters provided in Tab. A2. The relation in Eq.38 introduces the correspondence between the number of nucleated voids and the strain evolution. This relation is shown in Fig. 21a, where two nucleation domains are identified. For low strains (< 10 %),

Die approbierte gedruckte Originalversion dieser Dissertation ist an der TU Wien Bibliothek verfügbar.
The approved original version of this doctoral thesis is available in print at TU Wien Bibliothek.
TU Bibliothek WIEN Your knowledge hub

the void evolution is non-linear (transient nucleation rate) and fades into a linear domain (constant nucleation rate) for strains > 10 %. The conversion from transient to constant nucleation rate is given in Fig. 21b, where about 90% of the final nucleation rate is reached at a strain of $\epsilon_{11} = 10$ %. The linear generation of voids with respect to strain is discussed through experimental findings in section 2.

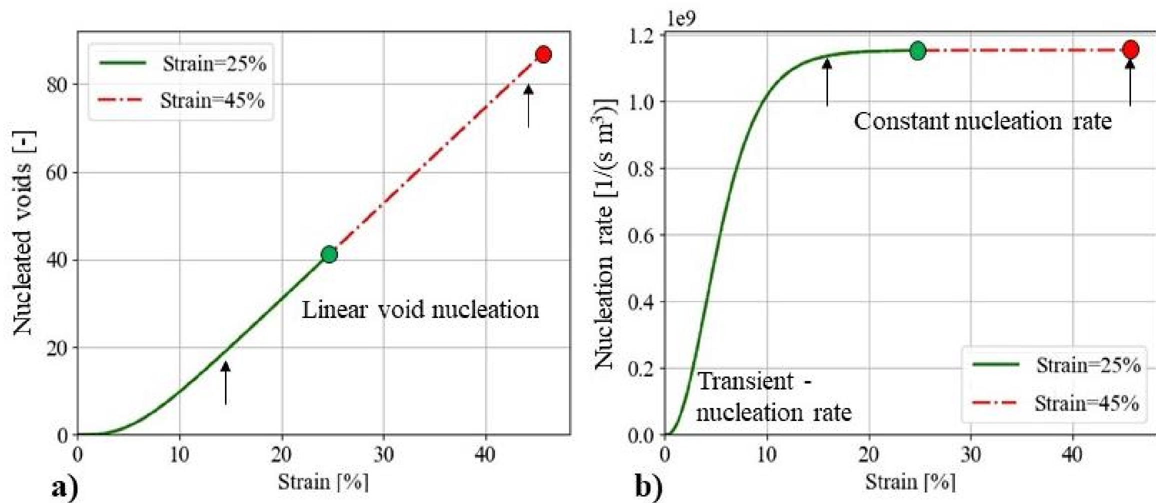

Fig. 21 Nucleation behavior for a) number of nucleated voids over total strain and b) nucleation rate over total strain.

Healing Results

Fig. 22 demonstrates the healing process under variation of liquid viscosity ($T > T_{\text{solidus}}$ at $t = 0$ s) where the damage variable is computed using the semi-solid algorithm (Fig. 19) in absence of external loads, i.e., $p_{\text{hyd}} = 0$ Pa. The healing parameters are provided in Tab. A3 and have been taken from the literature of an Sn-Bi alloy of eutectic composition [170].

In Fig. 22a, the void radius evolution of the largest void group is illustrated. The collapse starts from an initial radius $\psi_{\text{R}} = 80$ µm, where the void is filled depending on the liquid viscosity after $t = 0.5$ ms to $t = 6.5$ ms. The radius evolution is slowed down for increasing fluid viscosity and relates linearly in the range of $\eta_{\text{visc}} = 0.4$ mPas (red dot dash) to $\eta_{\text{visc}} = 0.2$ mPas (green dot). With further decreasing values to about $\eta_{\text{visc}} = 0.02$ mPas, the radius evolution becomes increasingly non-linear due to lower significance of the viscous term in Eq. 45. The linear dependence of void radius over healing time is similar to the response reported by [126] using a phenomenological approach. The evolution of the damage parameter is given in Fig. 22b, where healing times range from $t = 0.5$ to $t = 6.5$ ms. Comparing with Fig. 22b, it follows that the void collapse time of the largest void group is the upper limit for the healing time. This serves as rule of thumb to estimate the complete healing time. The healing time linearly reduces with

Die approbierte gedruckte Originalversion dieser Dissertation ist an der TU Wien Bibliothek verfügbar.
The approved original version of this doctoral thesis is available in print at TU Wien Bibliothek.
TU WIEN Bibliothek Your knowledge hub

increasing fluid viscosity. The void distributions in Fig. 22c to 29e shows the initial void collective at t = 0 ms as well as after t = 1ms and t= 3 ms of healing. The initial void distribution in Fig. 22c has a maximum void count at $\psi_{\mathrm{R}} = 1$ µm and a maximum void size of $\psi_{\mathrm{R,max}} =$ 80 µm. After 1ms of healing, the maximum void size in Fig. 22d decreases to $\psi_{\mathrm{R,max}} = 70$ µm and about 13 subcritical voids have been removed from the collective. After t = 3 ms (Fig. 22e), the void collective has further collapsed to about $\psi_{\mathrm{R,max}} = 45$ µm.

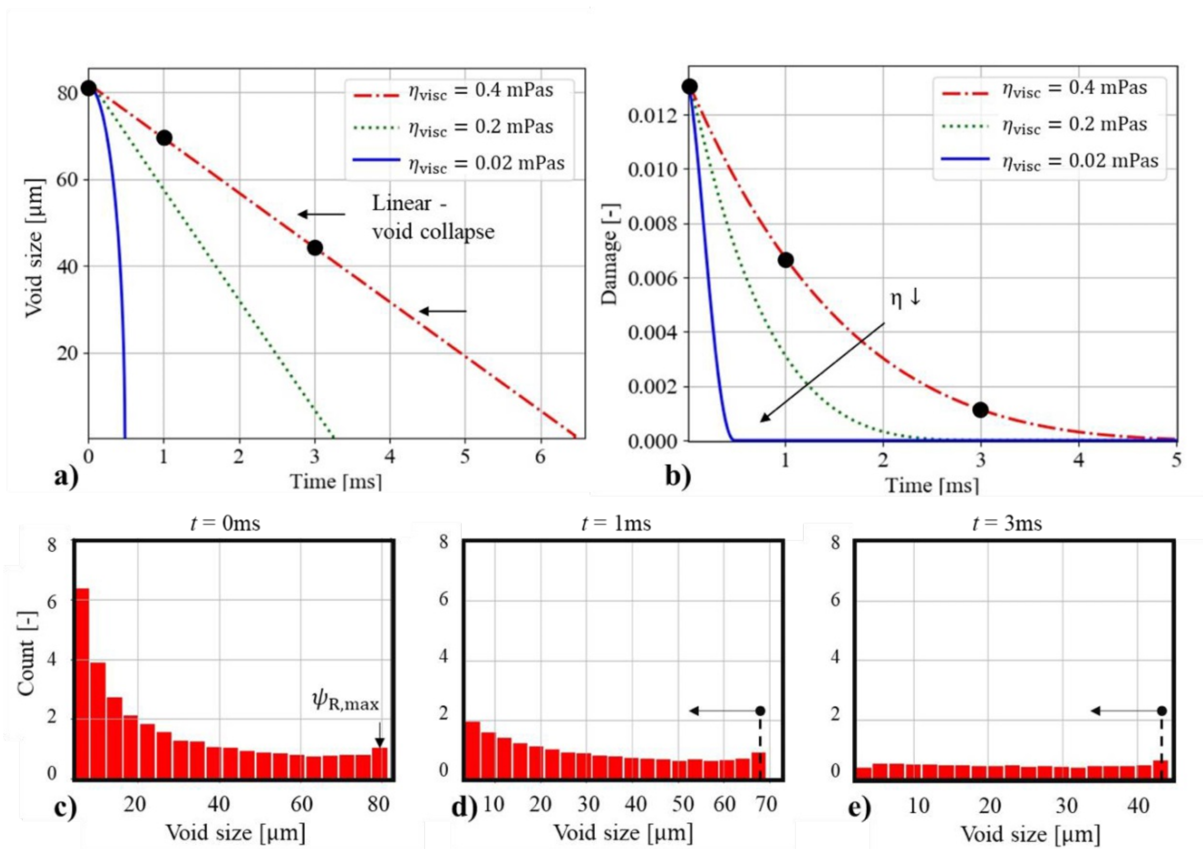

Fig. 22 Healing response under variation of liquid viscosity. a) Void size evolution of largest void group in collective. b) Damage parameter evolution indicates total damage. c) Void size distribution at t = 0 ms. d) Void size distribution at t = 1 ms. e) Void size distribution at t = 3 ms.

The surface tension can change significantly among materials and influences the healing evolution. The model accounts for its contribution and computed results under variation of σ_{surf} are illustrated in Fig. 23 ($T > T_{\mathrm{solidus}}$ at t = 0 s and $p_{\mathrm{hyd}} = 0$ Pa). Collapsing of the largest void group is shown in Fig. 23a where the surface tension, σ_{surf}, ranges from 0.01 N/m to 0.1 N/m. The collapse time scales linearly due to a liquid viscosity of $\eta_{\mathrm{visc}} = 0.4$ mPas in Fig. 23a and the void collapse time is reduced from $t = 6.2$ ms for $\sigma_{\mathrm{surf}} = 0.01$ N/m down to $t = 0.62$ ms for $\sigma_{\mathrm{surf}} = 0.1$ N/m. This reveals a linear relation of surface tension and void collapse time. The damage evolution in Fig. 23b shows healing times ranging from t = 6.2ms to t = 0.62ms, which corresponds to the collapse time of the largest void.

Die approbierte gedruckte Originalversion dieser Dissertation ist an der TU Wien Bibliothek verfügbar.
The approved original version of this doctoral thesis is available in print at TU Wien Bibliothek.
TU Bibliothek WIEN Your knowledge hub

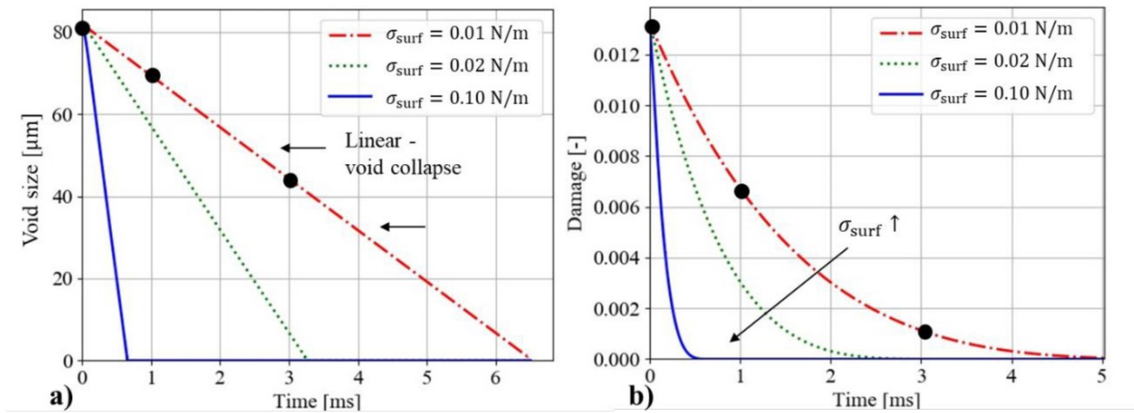

Fig. 23 Healing response under variation of liquid surface tension. a) Void size evolution of largest void group in collective. b) Damage parameter evolution indicates total damage.

The effect of the externally imposed hydrostatic pressure, p_{hyd}, in the semi-solid regime is incorporated in the proposed model. A variation is shown in Fig. 24 for $\eta_{\mathrm{visc}} = 0.4$ mPas and $\sigma_{\mathrm{surf}} = 0.01\ \mathrm{N/m}$, where values range from $p_{\mathrm{hyd}} = -2.7$ kPa (tension) to $p_{\mathrm{hyd}} = 2.7$ kPa (compression). The evolution of the largest void group ($\psi_{\mathrm{R,max}} = 80\ \mu\mathrm{m}$) in Fig. 24a shows two trends. In the load-free (green dot) and compressive case (blue solid), void collapse is possible as indicated. Yet, under tensile loads (red dot dash), voids further expand.

In Fig. 24b and 31c, complete damage under hydrostatic tension (red dot dash) is shown. Complete damage occurs after about t = 3 ms, as illustrated in Fig. 24c. In case of hydrostatic compression (blue solid), the healing period is reduced to t = 0.5 ms compared to t = 3.2 ms in the load-free case. This shows that the hydrostatic pressure, in addition to the surface tension, can contribute as a driving force to void collapse.

The initial void collective and its evolution after t = 1ms and t = 3 ms under hydrostatic tension ($p_{\mathrm{hyd}} = -2.7$ kPa) is shown in Fig. 24d to 31f. The initial void distribution in Fig. 24d shows a peak for voids of $\psi_{\mathrm{R}} = 1\ \mu\mathrm{m}$ and a maximum size of $\psi_{\mathrm{R,max}} = 80\ \mu\mathrm{m}$. After a healing period of t = 1 ms in Fig. 24e, the void groups of $\psi_{\mathrm{R}} < 8\ \mu\mathrm{m}$ have collapsed due to an overcompensation of surface tension over hydrostatic tension, whereas voids $> 8\ \mu\mathrm{m}$ can grow under tensile load. This shows that the model is able to account for a void size dependence of healing. Although, the total void volume evolves towards complete damage, small voids show the contrary evolution. This shows the benefit for modelling liquid-assisted healing using the proposed void collective.

In Fig. 24f, the void collective close to full damage is shown, where the peak of the distribution is shifted to the largest void group. This arises from the reduced significance of surface tension acting on larger voids.

Die approbierte gedruckte Originalversion dieser Dissertation ist an der TU Wien Bibliothek verfügbar.
The approved original version of this doctoral thesis is available in print at TU Wien Bibliothek.
TU WIEN Bibliothek Your knowledge hub

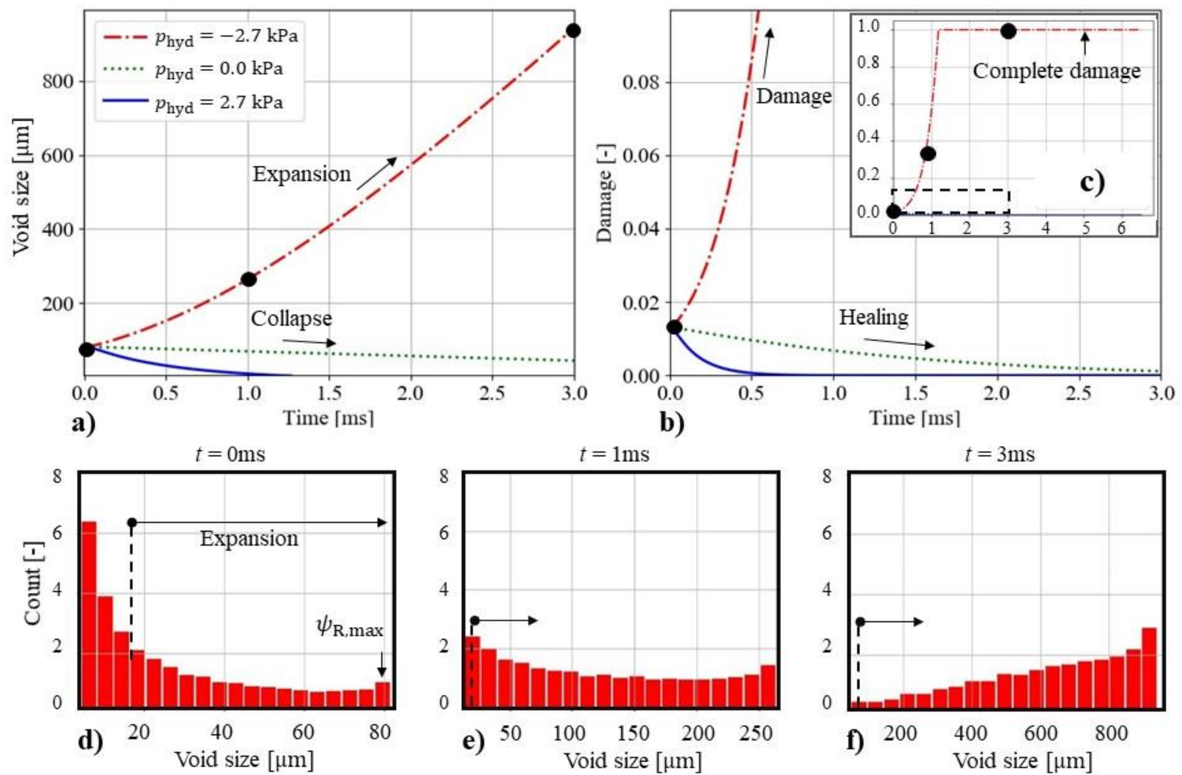

Fig. 24 Healing response under variation of hydrostatic pressure. a) Void size evolution of largest void group in collective. b) Damage parameter evolution indicates total damage at the onset of healing. c) Damage parameter evolution of complete healing period. d) Void size distribution at t = 0 ms. e) Void size distribution at t = 1 ms. f) Void size distribution at t = 3 ms.

These results allow further conclusion for an improved understanding of liquid-assisted healing. A void of given size has a critical hydrostatic pressure, p_{crit}, at which the external tensile pressure and the surface tension are in balance. The critical hydrostatic pressure can be derived from Eq. 45 in the static limit with $\psi_{\text{R},i}(t = 0) = \psi_{\text{R0},i}$, $\dot{\psi}_{\text{R},i}(t = 0) = 0$ and $\ddot{\psi}_{\text{R},i}(\text{t} = 0) = 0$. Inserting these in Eq.45 leads to the critical hydrostatic pressure, which is shown in Fig. 25. The green area shows the domain where voids can collapse despite external tensile loads. The model has incorporated this dependency due to the novel void collective formulation.

Two healing criteria have to be fulfilled in order to achieve liquid-assisted healing. First, the thermal criterion of $T > T_{\text{solidus}}$ has to be true to allow sufficient material mobility. Second, the hydrostatic pressure around a single void has to be higher than its critical pressure $p_{\text{hyd}} > p_{\text{crit}}$. The second criterion was shown experimentally in the work of [33], where compressive forces were locally applied during healing.

TU Bibliothek Your knowledge hub WIEN
Die approbierte gedruckte Originalversion dieser Dissertation ist an der TU Wien Bibliothek verfügbar.
The approved original version of this doctoral thesis is available in print at TU Wien Bibliothek.

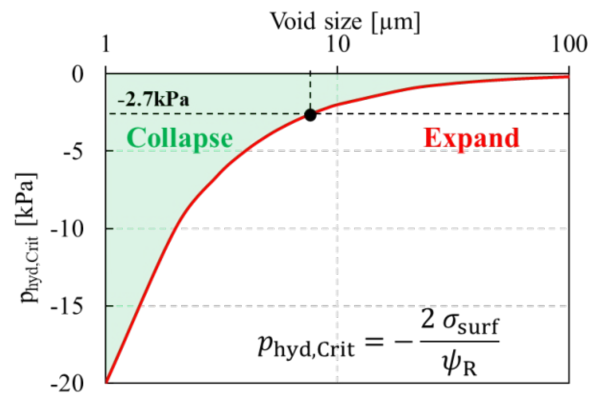

Fig. 25 Critical hydrostatic tension over void size.

It is important to mention the role of local microstructural mobility on the void evolution. The presented model assumes immediate void collapse under external loads or due to void surface tension. Yet, the potential influence of a solid skeleton in the semi-solid state has to be addressed in future works.

5. Conclusion

This work proposes a comprehensive micromechanical damage-healing framework for liquid-assisted healing in solder alloys. It introduces physical healing parameters, such as, hydrostatic pressure, liquid viscosity and surface tension. The model is based on a continuum damage mechanics (CDM) approach, with a damage variable based on a void collective vector. To account for the common deformation mechanisms of solder alloys, e.g., Sn-Bi alloys, the kinematic equations and void growth law are formulated in a unified creep-plasticity framework. To justify the proposed model, experimental motivation for macroscopic damage and healing, void nucleation and void collapse is shown. The local void collapse of voids in the eutectic phase is illustrated in a model alloy through in-situ observation. The local melting of eutectic phase and the subsequent collapse of single voids motivates the introduction of the Rayleigh-Plesset equation to model void healing. The following model results are presented:

1. The number of nucleated voids relates linearly with increasing tensile strain as shown from experiment. The continuous character of void nucleation is incorporated in the model. The void distribution, computed by the model, provides a similar distribution as observed in experiment.
2. The in-situ melting experiment shows the immediate collapse of a void within the eutectic phase.

Die approbierte gedruckte Originalversion dieser Dissertation ist an der TU Wien Bibliothek verfügbar.
The approved original version of this doctoral thesis is available in print at TU Wien Bibliothek.
TU Bibliothek Your knowledge hub WIEN

3. The void collapse time increases for higher liquid viscosities. Low viscosities of $\eta_{\mathrm{visc}} < 0.1$ mPas show a non-linear void radius evolution. The non-linear radius evolution stems from the greater impact of surface tension.
4. The surface tension is a strong driving force for void collapse in small dimensions. It allows voids to collapse even for $p_{\mathrm{hyd}} < 0$ Pa dependent on the void size. Void collapse and healing is faster for higher surface tension.
5. The role of hydrostatic tension and compression for healing is shown. Void collapse and healing is enhanced for compressive hydrostatic loads. The model is able to describe damage increase in the semi-solid regime. A critical hydrostatic pressure is identified up to which void collapse is possible despite hydrostatic tensile loads.
6. Two healing criteria are concluded from the discussed results. First, sufficient mobility of the healing agent (liquid eutectic phase, $T > T_{\mathrm{solidus}}$) is required. Second, the hydrostatic pressure needs to exceed the critical hydrostatic pressure, from which follows $p_{\mathrm{hyd}} > p_{\mathrm{crit}}$.

Appendix

A. Model Parameters

Tab. A1 Elastic and unified creep-plasticity model parameters

Elastic – Creep – Plasticity Parameters	
Parameter	Value [Unit]
E	65 [GPa]
ν	0.3 [−]
A	18200 [1/s]
B	0.001 [−]
d	50.0 [MPa]
n	2.0 [−]
Q	38.0 [kJ/mol]
R_∞	500.0 [MPa]
R_0	2.0 [MPa]
b	18.0 [−]
μ	0.0 [MPa]
β	0.0 [MPa]

Die approbierte gedruckte Originalversion dieser Dissertation ist an der TU Wien Bibliothek verfügbar.
The approved original version of this doctoral thesis is available in print at TU Wien Bibliothek.
TU Bibliothek WIEN Your knowledge hub

Tab. A2 Nucleation and Growth Parameters

Nucleation and Growth Parameters	
Parameter	Value [Unit]
η_{init}	$9.0 \cdot 10^{12}$ [1 / m^3]
$\psi_{\mathrm{R,Crit}}$	$5.0 \cdot 10^{-9}$ [m]
α_{RT}	0.56 [−]
$D_{\mathrm{b}}\delta_{\mathrm{b}}$	$7.35\ 10^{-15}\ \exp(-\frac{9452}{1.987\,T})$
Ω	$2.71 \cdot 10^{-29}$ [m^3 / mol]

Tab. A3 Initial healing parameters to compute healing evolution [171]

Healing Parameters	
Parameter	Value [Unit]
η_{visc}	0.4 [m · Pa · s]
p_{v}	0.0 [Pa]
σ_{surf}	0.01[N/m]
ρ_{L}	8 [g/cm^3]

Die approbierte gedruckte Originalversion dieser Dissertation ist an der TU Wien Bibliothek verfügbar.
The approved original version of this doctoral thesis is available in print at TU Wien Bibliothek.
TU Bibliothek WIEN Your knowledge hub

2.3 Modelling of void collapse with Molecular Dynamics in pure Sn

Georg Siroky (georg.siroky@mcl.at) [1)], Elke Kraker[1)], Dietmar Kieslinger[2)], Lorenz Romaner[1)], Ernst Kozeschnik[2)], Werner Ecker[1)]
[1)] Materials Center Leoben Forschung GmbH (MCL), Roseggerstraße 12, 8700 Leoben, Austria
[2)] ZKW Elektronik GmbH, Samuel Morse-Straße 18, 2700 Wiener Neustadt, Austria
[3)] TU Wien, Institute of Materials Science and Technology, Getreidemarkt 9, 1060 Wien, Austria

Published in: Proceedings 2020, 56, 1, 29,
https://doi.org/10.3390/proceedings2020056029

Presented at: 4th International Conference nanoFIS 2020

Abstract

This work simulates the collapse of a spherical void in pure Sn during melting using molecular dynamics (MD). Simulations were performed for two temperatures with a modified embedded atom method (MEAM) potential, which was reported to be in good agreement with respect to melting point and elastic constants. Solutions of the Rayleigh–Plesset (RP) equation are used for comparison under the assumption of macroscopic surface tension and liquid viscosity. Despite a qualitative correlation, longer collapse times were observed in MD simulations, which arose from partial solid structures and the incubation time for melting.

1. Introduction

Healing in metals has recently gained attention as an innovative concept to reduce mechanical damage [1]. A micromechanical model was reported to formulate the liquid-assisted healing of a void collective, which is based on the Rayleigh–Plesset (RP) equation [2]. Molecular dynamics (MD) simulations can potentially provide a better understanding of processes on the nano-scale. Therefore, a modified embedded atom method (MEAM) potential for pure Sn was investigated for agreement with the RP solution [3]. In particular the collapse time due to viscosity and surface tension were evaluated with the MD simulations.

2. Materials and Methods

MD Simulations of a void in pure Sn were performed using an isothermal-isobaric (NPT) ensemble with unit cell size of 30 Å. The ensemble was equilibrated at room temperature for 120 ps and then heated up to 500 K and 600 K for each simulation, respectively. After holding the peak temperature for 100 ps, the system was cooled to room temperature. The Rayleigh–Plesset equation describes the dynamics of a bubble in a viscid fluid. The void pressure p_v and

Die approbierte gedruckte Originalversion dieser Dissertation ist an der TU Wien Bibliothek verfügbar.
The approved original version of this doctoral thesis is available in print at TU Wien Bibliothek.
TU WIEN Bibliothek Your knowledge hub

liquid pressue p_l on the left balances with the spherical flow-, inertia-, viscous- and surface tension term on the right in Equation (1).

$$\frac{(p_V - p_l)}{\rho_L} = \frac{3}{2}\dot{R}^2 + R\ddot{R} + 4\frac{\eta_{visc}\,\dot{R}}{R} + 2\frac{\sigma_{surf}}{\rho_L R}. \quad (47)$$

3. Results and Discussion

The void evolution during the heating cycle is illustrated in Fig. 26. The initially spherical void in Fig. 26a is surrounded by a liquid domain in Fig. 26b, which is almost fully collapsed. In Fig. 26c the recrystallized area is separated from the final liquid domain in green. Fig. 26d shows the final structure after 600 ps, the void collapsed and several dislocations were generated.

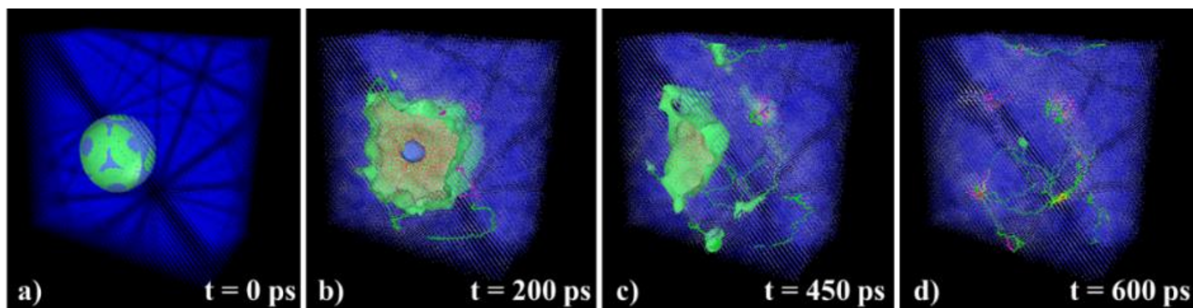

Fig. 26 Void evolution during molecular dynamics (MD) simulation (a) initial configuration t = 0 ps, (b) void collapse in progress t = 200 ps, (c) completed void collapse t = 450 ps, (d) final stage of solidification t = 600 ps.

Fig. 27 shows the void evolution for both temperatures of the MD simulation (red solid), the inviscid RP solution (dashed) and the viscid RP solution (dot dash). The results reveal a qualitative agreement of the MD simulations with the inviscid solution. Nevertheless, the collapse time for the MD simulations is about four times longer for $T = 500$ K and 1.5 times longer for $T = 600$ K, compared to the viscid solution. The simulation at $T = 500$ K in Fig. 26 reveals only partial melting around the void. Therefore, a longer void collapse time was expected due to the stability of the surrounding crystal.

Die approbierte gedruckte Originalversion dieser Dissertation ist an der TU Wien Bibliothek verfügbar.
The approved original version of this doctoral thesis is available in print at TU Wien Bibliothek.
TU WIEN Bibliothek Your knowledge hub

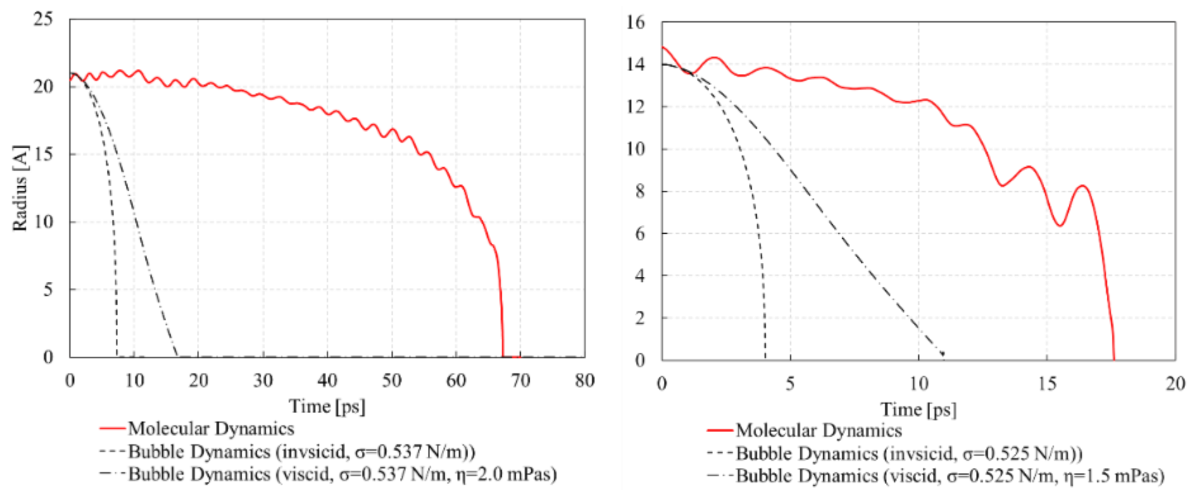

Fig. 27 Void collapse computed with Rayleigh–Plesset (RP) equation and MD simulations (left) $T = 500$ K (right) $T = 600$ K.

4. Conclusion

The application of a MEAM potential reported by Ravelo [3] for pure Sn revealed a qualitative agreement with the inviscid solution. A good agreement with the experimental surface tension was reported in the literature for the potential [4]. A four times longer void collapse time was observed in the MD simulations at $T = 500$ K, which can be associated with partial melting and a higher mechanical stability than that assumed in the RP model. At elevated temperatures the MD simulation showed a 1.5 times longer collapse time, which can be explained by the incubation time required for melting.

Die approbierte gedruckte Originalversion dieser Dissertation ist an der TU Wien Bibliothek verfügbar.
The approved original version of this doctoral thesis is available in print at TU Wien Bibliothek.
TU WIEN Bibliothek Your knowledge hub

2.4 Effect of solder joint size and composition on liquid-assisted healing

Georg Siroky (georg.siroky@mcl.at) [1)], David Melinc[2)], Julien Magnien[1)], Elke Kraker[1)], Dietmar Kieslinger[3)], Ernst Kozeschnik[2)], Werner Ecker[1)]
[1)] Materials Center Leoben Forschung GmbH (MCL), Roseggerstraße 12, 8700 Leoben, Austria
[2)] TU Wien, Institute of Materials Science and Technology, Getreidemarkt 9, 1060 Wien, Austria
[3)] ZKW Elektronik GmbH, Samuel Morse-Straße 18, 2700 Wiener Neustadt, Austria

Submitted to: Microelectronic Reliability (accepted)

Abstract

This work presents an experimental and numerical investigation of liquid-assisted healing with respect to solder joint composition and size. A damage-healing model is formulated based on entropy generation of damage and viscous material transport during healing. The model accounts for a composition-dependency of healing by introducing the liquid film thickness, the liquid viscosity and a microstructural mobility parameter. The size dependencies enter the healing model in form of the local capillary pressure of the solder joint. A viscous flow experiment illustrates the compositional dependency of local material transport and a cyclic tensile experiment shows the regain of mechanical properties, such as, stiffness and strength after healing. The flow experiment shows that material transport is retarded for solders of low liquid fraction and crack healing is limited due to partial filling of the crack. Simulation results of a solder array suggest the capillary pressure as the driving force for healing, which leads to a size-dependency of the healing evolution. The required time for complete healing increases with reduced solder dimensions due to higher capillary pressures. High microstructural mobility due to high liquid fractions also facilitates faster healing.

1. Introduction

Solder joints under service have to withstand thermal load conditions occurring in cyclic viscoplastic deformation, which causes thermo-mechanical fatigue (TMF). The mismatch of thermal expansion coefficients in microelectronic assemblies leads to high local stresses and causes the formation of fatigue cracks over time in the solder joint or at the solder-substrate interface [55]. The thermo-mechanical fatigue lifetime is improved through development of solder alloys [105], where the role of alloying elements and intermetallic compounds on the mechanical properties is subject of ongoing research [172–175]. Alternatively, healing mechanisms in solder materials can improve the service lifetime of microelectronic components, e.g. when the interconnection is restored after fatigue. This concept has not been

Die approbierte gedruckte Originalversion dieser Dissertation ist an der TU Wien Bibliothek verfügbar.
The approved original version of this doctoral thesis is available in print at TU Wien Bibliothek.
TU WIEN Bibliothek Your knowledge hub

studied in solder joints and requires a fundamental understanding of material and component behaviour with respect to healing. For the sake of simplicity binary Sn-Bi alloys were chosen as experimental healing alloys. The liquid-fraction and liquid-network thickness is adjusted by varying the Bi content between 20 and 58 wt.% Bi [176] and the microstructure contains the assumed features for liquid-phase healing. Furthermore, the alloy systems serves as a practical example for low-melting solder applications [177].

Healing in metals is an innovative approach to repair damage in-situ and increase their damage resistance. Defects, such as, voids or cracks are filled through local material transport, which can be achieved through different transport mechanisms [37]. Several proof of concept studies investigated precipitation [41], electro pulsing [46], electro-chemical [47] and liquid-assisted healing [26,42] in bulk metals. Danzi et al. [26] investigated healing for application in microelectronics through reactive nano-foils to trigger local melting and healing in thin films. Liquid-assisted healing in solders was not reported in literature, although healing effects from electromigration were discussed in principle [117].

A thermodynamically consistent damage-healing model of visco-plastic materials was proposed by Voyiadjis et al. [30,129]. The thermodynamic damage-healing framework requires a monotonically increasing healing variable to describe effective damage after healing. Micro-mechanics based models with focus on specific healing kinetics are reported for liquid healing of ductile voids [178], precipitation healing of creep cavities [125], healing of cement [123], viscous crack healing in glass [126] and healing in asphalt mixtures [124]. Viscous material transport was also formulated for liquid-phase sintering, where pores can shrink during the manufacturing process [179]. Previous studies formulated healing solely as a material property, where the combined effect of material and assembly were neglected.

Several damage models for solders were formulated [180–183]. Wen et al. [180] proposed a constitutive model for micro-cracking under isothermal fatigue. Kuna and Wippler [183] proposed a damage model for thermo-mechanical fatigue of ball grid arrays and chip resistors, where solder joints were modelled as homogeneous solids. Ubachs et al. [181] proposed a non-local damage model and investigated the role of local grain anisotropy during thermal fatigue. Basaran and Nie [182] proposed a general thermodynamic framework of fatigue damage in solder joints, where the damage metric is based on entropy generation.

The present work presents an experimental and numerical analysis of liquid-assisted healing for solder joints. A damage-healing model is proposed to formulate healing under consideration

Die approbierte gedruckte Originalversion dieser Dissertation ist an der TU Wien Bibliothek verfügbar.
The approved original version of this doctoral thesis is available in print at TU Wien Bibliothek.
TU WIEN Bibliothek Your knowledge hub

of solder alloy composition and solder size in a continuum damage mechanics framework. The damage evolution is based on works of Basaran and Nie [182] and uses the concept of entropy generation to quantify fatigue damage. The healing response is obtained by modelling viscous material transport and is adapted from Liu et al. [179]. The healing model includes the local capillary pressure, liquid film thickness, liquid viscosity and microstructural mobility. Microstructural mobility of four Sn-Bi alloys with 20, 30, 47 and 58 wt.% Bi is studied with a viscous flow experiment. The filling ratio as a function of alloy composition is evaluated and shows the effect of microstructural mobility on defect filling. A tensile experiment shows the principal strength and stiffness recovery after crack healing under cyclic deformation. Thermo-mechanical simulations of a linear solder array are performed with the damage-healing model. The linear solder array is a 2D representation of a ball grid array (BGA). Local deformation, shear stresses and stress states are analyzed and the most critical solder joint for healing is determined. The healing evolution as a function of solder joint composition and solder size is discussed by means of simulation results

.

2. Materials and Methods

Modelling

The Garofalo deformation law describes visco-plastic deformation [95], where the total strain tensor is decomposed in an elastic and creep strain with

$$\epsilon = \epsilon^{\mathrm{el}} + \epsilon^{\mathrm{cr}}. \tag{48}$$

The creep rate is written as

$$\dot{\epsilon}^{\mathrm{cr}} = A \cdot sinh(B \cdot \bar{\sigma})^{n} \cdot e^{-\frac{Q}{RT}}, \tag{49}$$

where A, B and n are material parameters, $\bar{\sigma}$ is the uniaxial equivalent deviatoric stress, Q is the activation energy, R is the gas constant and T is the temperature. The Arrhenius term on the right side introduces the temperature dependency. The elastic stiffness tensor is reduced due to damage according to Lemaitre [184] and is written as

$$\bar{C}_{ijkl} = (1 - D_{\mathrm{eff}}) \cdot C_{ijkl}, \tag{50}$$

where C_{ijkl}, $\bar{C}_{ijkl}$ are the undamaged and damaged stiffness tensors, respectively, and D_{eff} is the effective damage variable, which includes healing. The damage variable D_{eff} doesn't affect the creep rate directly, yet, the elastic softening due to damage reduces the uniaxial equivalent deviatoric stress and therefore the creep rate.

Die approbierte gedruckte Originalversion dieser Dissertation ist an der TU Wien Bibliothek verfügbar.
The approved original version of this doctoral thesis is available in print at TU Wien Bibliothek.
TU WIEN Bibliothek Your knowledge hub

Damage Model

The damage model in the present work is built on the entropy formulation proposed by Basaran and Nie [182]. Damage is an increase of disorder in the material due to irreversible processes and is quantified by its entropy with

$$s = \frac{N_0 k_\mathrm{B}}{\overline{m}_\mathrm{s}} \cdot \ln(W), \tag{51}$$

where k_B is the Boltzmann constant, $\overline{m}_\mathrm{s}$ is the unit atomic mass and N_0 is Avogadro's number and W is the number of thermodynamic states. The Helmholtz free energy ϕ provides a relation of the internal energy and is defined as

$$\phi = e - Ts, \tag{52}$$

where e and s are the specific internal energy and the specific entropy, respectively. The function W is obtained by substituting Eq.51 into Eq.52 and is written as

$$W = e^{\frac{(e-\phi)\overline{m}_s}{N_0 k_\mathrm{B} T}}. \tag{53}$$

Basaran and Nie [182] proposed a damage parameter, which is written as the relative change of the materials disorder

$$D = \frac{W_0 - W}{W_0} = \frac{\Delta W}{W_0}, \tag{54}$$

where W_0 is a reference configuration. The damage parameter can be reformulated in terms of relative change in internal energy and Helmholtz free energy as

$$D = 1 - e^{\frac{(\Delta e - \Delta\phi)\overline{m}_s}{N_0 k \theta}}. \tag{55}$$

The change in internal and free energy is formulated according to the equilibrium equation in solid mechanics and the first law of thermodynamics. The relative energy change is given as

$$\Delta e - \Delta\phi = \frac{1}{\rho}\int_{\varepsilon_0}^{\varepsilon} \sigma_{ij} d\varepsilon_{ij}^{\mathrm{in}} - \int_{t_0}^{t} \frac{1}{\rho}\frac{\partial q_i}{\partial x_i} dt + \int_{t_0}^{t} \dot{\gamma} dt \tag{56}$$

with the internal energy change due to inelastic deformation $d\varepsilon_{ij}^{\mathrm{in}}$ and the relative change in thermal energy due to heat flux $\frac{\partial q_i}{\partial x_i}$ and internal heat production $\dot{\gamma}$. The heat generation within the system as well as the heat flow across the system boundaries contribute to the disorder. This model furthermore assumes that a uniform temperature change does not increase damage. The presented study neglects damage due to internal heating $\dot{\gamma}$.

Die approbierte gedruckte Originalversion dieser Dissertation ist an der TU Wien Bibliothek verfügbar.
The approved original version of this doctoral thesis is available in print at TU Wien Bibliothek.
TU WIEN Bibliothek Your knowledge hub

Healing model

Healing is the reduction of mechanical damage due to local material transport and defect filling. In the present case, healing is modelled as viscous flow of the liquid eutectic phase above the solidus temperature T_s, which is T_s= 138 °C for the Sn-Bi example alloys studied in this work. The material deforms like a semi-solid due to the liquid phase and exhibits a reduced shear strength of about 2 MPa according to similar experimental studies [170]. Once the β-Sn phase is fully surrounded by liquid eutectic, a mean liquid film λ forms among the solid primary region. The viscous flow relation proposed by Liu et al. [179] defines material transport in this condition and is written as

$$V = \frac{\tau \lambda}{\eta}. \tag{57}$$

with V the flow velocity, τ the shear stresses, λ the mean liquid film thickness and η the liquid viscosity. In case of a solder joints, local shear stresses are induced in the microstructure by capillary forces F_{CB}. Therefore, the flow velocity is taken as proportional to the capillary pressure P_{CB} in the solder joint according to

$$V \propto \frac{P_{CB} \lambda}{\eta}. \tag{58}$$

The solder joint with a typical geometry used in ball grid arrays (BGA) is illustrated in Fig. 28 and the capillary pressure is calculated with

$$P_{CB} = \frac{F_{CB}}{r_s^2 \pi}, \tag{59}$$

where r_s is the radius of the solder joint and F_{CB} is the capillary force, which, in case of two parallel plates, can be calculated according to

$$F_{CB} = 2\pi \gamma_{12} r_s \sin(\psi) - 2\pi \gamma_{12} r_s^2 t_s, \tag{60}$$

where ψ is the contact angle between the substrate and the solder, t_s is the capillary thickness and γ_{12} is the surface energy [185]. The capillary forces FCB could potentially contain additional terms, arising from external forces on the solder joints induced by e.g. underfill material. Such additional driving force is neglected in the current study for the sake of simplicity and can be accounted for by adding an external force term in eq. 60.

Die approbierte gedruckte Originalversion dieser Dissertation ist an der TU Wien Bibliothek verfügbar.
The approved original version of this doctoral thesis is available in print at TU Wien Bibliothek.
TU WIEN Bibliothek Your knowledge hub

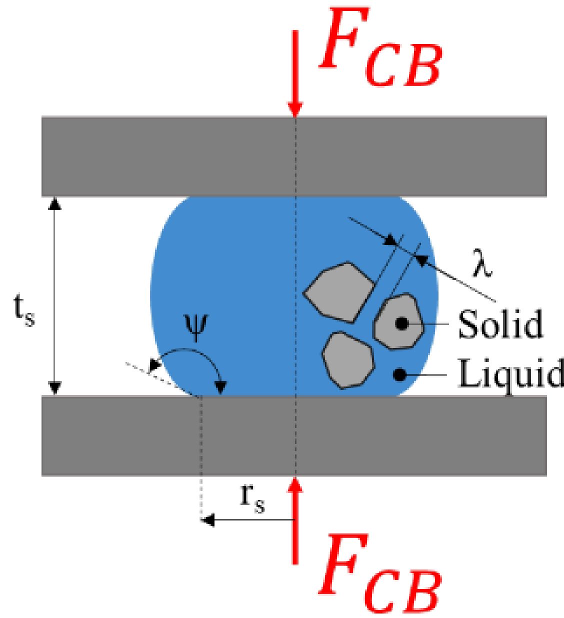

Fig. 28 Solder joint between two substrates and capillary forces.

The capillarity determines the liquid pressure in the semi-solid solder joint, which is the driving force for liquid healing. The solder has a certain resistance against viscous flow according to its liquid film thickness and liquid viscosity. The liquid film can be determined experimentally from micrographs or by using analytical relations. An analytical form of the liquid film thickness was proposed by Liu et al. [179] and is written as

$$\lambda = \frac{2(2-C)}{(1-C)} \cdot \frac{C_1^{2/3}}{C_2} \cdot \frac{1}{N_V^{1/3}} \cdot \frac{\Phi_L}{(1-\Phi_L)^{2/3}}, \tag{61}$$

where the contiguity parameter C quantifies the surface fraction of grains in contact with liquid, Φ_L is the liquid fraction, C_1 and C_2 are geometric constants and N_V is the number of grains per unit volume, which is given with

$$N_V = \frac{(1-\Phi_L)}{\frac{4}{3} r_G^3 \pi}, \tag{62}$$

where r_G is the estimated β-Sn grain radius. The viscosity of an Sn-Bi alloy of eutectic composition according to [170], is written as

$$\eta = \eta_0 e^{\left(\frac{\delta}{T} - \kappa\right)}, \tag{63}$$

where the parameters are δ= 797.5, κ= 0.847, η_0= 1 Pa s and T is the temperature. According to Liu et al. [179], the linear shrinkage of a porous semi-solid is written as

$$d\left(\frac{\Delta L}{L_0}\right) \mathrm{d}t = k\, P_{CB}\, \frac{\lambda}{\eta}\, \mathrm{d}t, \tag{64}$$

Die approbierte gedruckte Originalversion dieser Dissertation ist an der TU Wien Bibliothek verfügbar.
The approved original version of this doctoral thesis is available in print at TU Wien Bibliothek.
TU WIEN Bibliothek Your knowledge hub

where k is the microstructural mobility parameter, which accounts for material specific resistance to viscous flow. A value of k= 1 represents the ideal case of fluid mobility. The linear shrinkage in solder joints is assumed to be proportional to void filling and the healing variable H is given in terms of volumetric shrinkage as

$$H = \frac{\Delta V}{V_0} = 1 + (\frac{\Delta L}{L_0} - 1)^3. \quad (65)$$

Damage and healing

The damage parameter D is based on works of Chaboche and Lemaitre [156,184] and was extended for damage-healing models by Darabi et al. [186] by introducing the effective damage D_{eff}. For thermodynamic consistency, the damage parameter D and the healing parameter H are required to be monotonically increasing functions [30]. Following the formulation of Chaboche and Lemaitre [156,184], damage is the reduction of effective cross-section and is written as

$$D = \frac{A_{\mathrm{D}}}{A_0}, \quad (66)$$

with A_{D} and A_0 being the damaged and reference cross section respectively. A value of D= 1 represents the fully damaged condition. Healing is modelled for the sake of simplicity as shrinkage of voids, which is estimated with the mean void radius calculated with

$$r_{\mathrm{P}} = (\frac{A_{\mathrm{D}}}{N_{\mathrm{PA}}\,\pi})^{\frac{1}{2}} = (\frac{D\,A_0}{N_{\mathrm{PA}}\,\pi})^{\frac{1}{2}}, \quad (67)$$

where N_{PA} the number of voids. The total void volume V_{P} follows by the number of voids per unit volume N_{PV} with mean radius r_{P} as

$$V_{\mathrm{P}} = N_{\mathrm{PV}}\,\frac{4}{3}\,(\frac{D\,A_0}{N_{\mathrm{PA}}\,\pi})^{\frac{3}{2}}\,\pi. \quad (68)$$

The effective void volume $V_{\mathrm{P,eff}}$ after healing is given as

$$V_{\mathrm{P,eff}} = V_{\mathrm{P}} - H \cdot V_{\mathrm{P}}, \quad (69)$$

where inserting Eq. 68 leads to

$$N_{\mathrm{PV,eff}}\,\frac{4}{3}\,(\frac{D_{\mathrm{eff}}\,A_0}{N_{\mathrm{PA,eff}}\,\pi})^{\frac{3}{2}}\,\pi = (1 - H)N_{\mathrm{PV}}\,\frac{4}{3}\,(\frac{D\,A_0}{N_{\mathrm{PA}}\,\pi})^{\frac{3}{2}}\,\pi. \quad (70)$$

It is assumed that voids of similar size shrink simultaneously, which requires that the number of pores per area and volume remain the same in the effective (healed) and damaged configuration with $N_{\mathrm{PV,eff}} = N_{\mathrm{PV}}$ and $N_{\mathrm{PA,eff}} = N_{\mathrm{PA}}$. This assumption is necessary to avoid a more complex consideration of void collectives as proposed by Siroky et al. [178]. Therefore, the damage-healing relation due to void shrinkage is written as

$$D_{\mathrm{eff}} = (1 - H)^{2/3} D. \quad (71)$$

Die approbierte gedruckte Originalversion dieser Dissertation ist an der TU Wien Bibliothek verfügbar.
The approved original version of this doctoral thesis is available in print at TU Wien Bibliothek.
TU Bibliothek WIEN Your knowledge hub

This model leads to a full recovery of material properties after sufficiently long healing time. A potential healing limit is considered in form of an efficiency factor H_e. The current study assumes a healing efficiency of $H_e = 0.9$, although a physically sound value requires further experimental investigation. The final formulation of effective damage is written as

$$D_{\mathrm{eff}} = (1 - H_{\mathrm{e}} \cdot H)^{2/3} D. \tag{72}$$

Simulation of solder joints

The damage-healing material model is applied in a two-dimensional finite element (FE) model of a linear solder array as illustrated in Fig. 29a. Solder balls are placed between a copper and aluminum substrate with a dielectric layer. The larger solder joint on the left in Fig. 29a acts as an anchor point, which induces gradual damage among the solder joints numbered 1 to 5. Solder 5 is expected to show the highest mechanical load and, therefore, the maximal local damage. Heat transfer among the array and environment is modelled through a film condition with a heat transfer coefficient of $h = 23\ \mathrm{W/m^2K}$. The ambient temperature profile is given in Fig. 29b and acts as the driving force for thermo-mechanical fatigue. Four temperature shock cycles are performed with a transition time of 10 s and a dwell time of 30 min. Healing is activated by heating the array to $T_{heal} = 158$°C. The damage-healing material model is implemented in the commercial FE package Abaqus (www.3ds.com) by means of a user-defined field variable subroutine (USDFLD). The solder array is modelled under generalized plane strain condition only allowing for a collective expansion of the system in the y-direction with hexahedral elements with linear shape functions and reduced integration (C3D8R). The model parameters are taken from literature [179,187,188], where the values used for simulation are provided in Tab.A1.

The role of capillary dimensions is investigated by varying the solder gap t_s, which causes a change in capillary pressure. The solder joints are scaled to preserve geometric self-similarity, where the solder gap to solder radius ratio, t_s/r_s, remains constant. Furthermore, material effects on the healing efficiency of solder joints are highlighted by varying the microstructural mobility parameter k.

TU Bibliothek, WIEN Your knowledge hub. Die approbierte gedruckte Originalversion dieser Dissertation ist an der TU Wien Bibliothek verfügbar. The approved original version of this doctoral thesis is available in print at TU Wien Bibliothek.

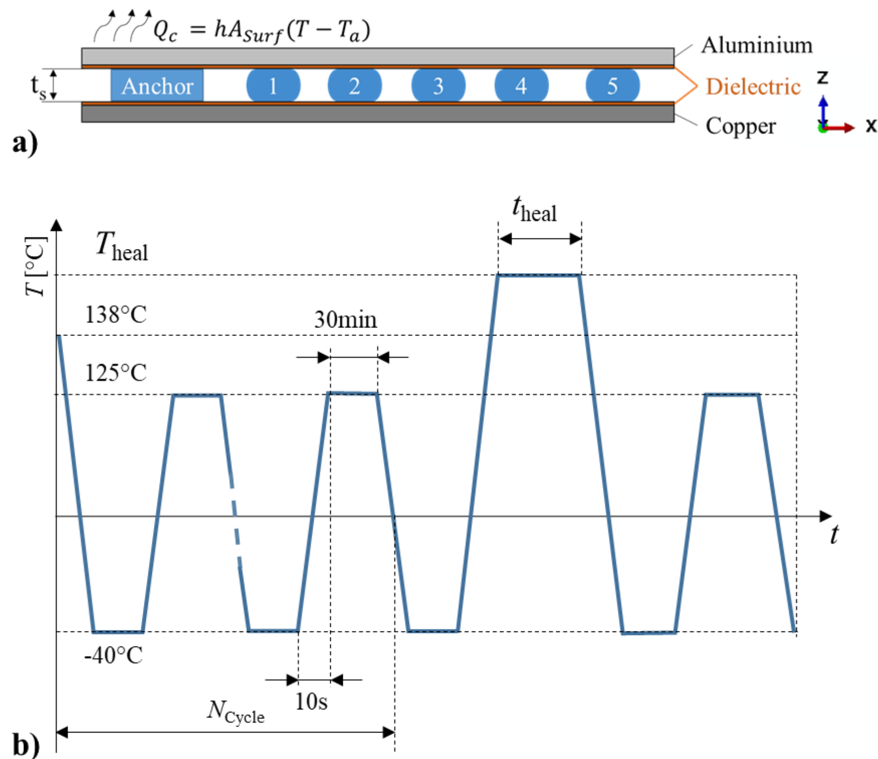

Fig. 29 Solder array for numerical modelling of solder healing a) Geometry and thermal boundary conditions b) Temperature shock cycles with healing period above Ts= 138°C.

Viscous flow experiment

The analytical relation for material transport in Eq.64 introduces the microstructural mobility parameter *k*, which scales the viscous flow and, subsequently, the healing kinetics. The microstructural dependency of viscous material transport is investigated on solders in a geometric confinement, similar to solder joints. A copper template of dimension 40 x 40 x 3 mm is cut and groves of ø5 x 2 mm are milled according to Fig. 30a. Templates are cleaned in acetone bath through sonication and oxide layers are removed by immersing the plates in citrate acid. Sn-Bi solder alloys with varying Bi content of 20, 30, 47 and 58 wt.% are pre-alloyed under argon atmosphere in a silicate glass using a magnetic stirrer. Alloys are homogenized at *T*= 400°C for 60 min before pipetting alloys in glass tubes. Pre-alloyed solder rods are cut in pellets of 1 g and a total solder mass of 3 g is placed per groove. The template undergoes reflow soldering under Argon atmosphere, with a holding time of 1 min at 250°C. The reflow temperature profile is given in Fig. 30b and the position of the thermocouple is indicated by a red dot in Fig. 30a. Excess solder is ground and polished manually to obtain an even filling of the grooves. Defects of ø1 x 2 mm are drilled in the solder according to Fig. 30a and their depth profile is measured using an optical microscope (Keyence, VHX 6000). The template is then heated to 150°C for 5 min under argon atmosphere to allow viscous material transport and

Die approbierte gedruckte Originalversion dieser Dissertation ist an der TU Wien Bibliothek verfügbar.
The approved original version of this doctoral thesis is available in print at TU Wien Bibliothek.
TU Bibliothek WIEN Your knowledge hub

filling of defects. The post-healing defect cross-section is measured and the filling ratio *FR* is calculated according to

$$FR = \frac{\Delta V}{V_0}, \tag{73}$$

where V_0 is the reference volume of the defect prior to healing and ΔV is the filled volume.

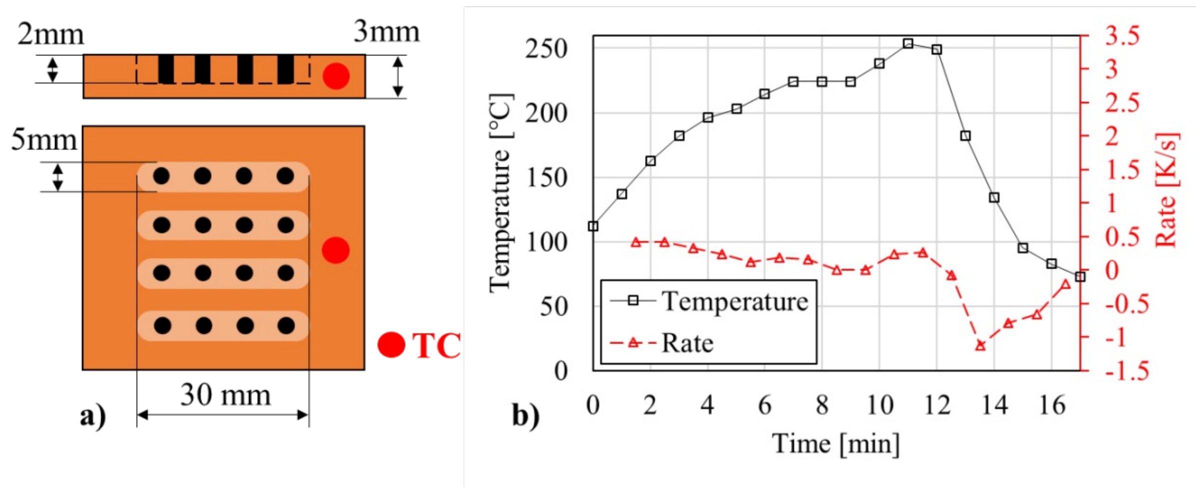

Fig. 30 Confined viscous flow experiment a) copper template with solder grooves and drill holes b) temperature and cooling rate during reflow of copper templates.

Tensile damage-healing experiment

The damage-healing experiment quantifies the effective regain of material properties, such as, stiffness and strength. Cylindrical samples of Sn-40 wt.% Bi composition are cast in a silicone mold with an average cooling rate of 1 K/s. The microstructure of as-cast samples is analyzed using scanning electron microscopy (FEI Philips XL30) and the eutectic thickness is measured with the software ImageJ (ImageJ 1.53c, National Institutes of Health) [189]. The protocol of the damage-healing experiment is illustrated in Fig. 31. First, samples are deformed under cyclic tension until partial fracture on a uniaxial tensile test machine (Zwick Z050) and, subsequently, healed at 145°C for 5 min on an aluminum template. The healing effect is quantified in a post-healing loading cycle until complete fracture. The deformation history of the sample is measured with a video extensometer.

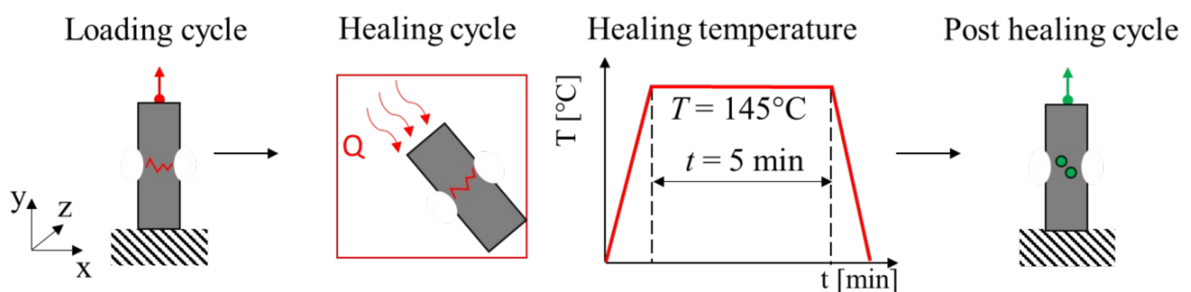

Fig. 31 Damage-healing procedure: Loading sequence induces a local crack, the sample is healed at 145°C for 5 min and the post healing cycle measures the mechanical healing.

Die approbierte gedruckte Originalversion dieser Dissertation ist an der TU Wien Bibliothek verfügbar.
The approved original version of this doctoral thesis is available in print at TU Wien Bibliothek.
TU Bibliothek Your knowledge hub WIEN

3. Results & Discussion

Defect filling

The healing efficiency of the material is determined by its microstructural mobility, where a network of solid primary phase inhibits material flow. A comparison of defect filling over alloy composition is shown in Fig. 32, where alloy compositions of 20, 30, 47 and 58 wt.% Bi are given in Fig. 32a-d, respectively. The initial configuration before healing is shown on the left and the post-healing cross-section is given on the right. The Sn-20 wt.% Bi alloy in Fig. 32a exhibits low mobility, likely due to high solid fraction and the presence of a solid network of primary phase. The initially cylindrical defect in Fig. 32a remains cylindrical and shows radial shrinkage, but no substantial filling is observed. The Sn-30 wt.% Bi alloy in Fig. 32b shows an increase of filling in radial direction and viscous material transport is indicated by cascades at the z=2561 µm. The Sn-47 wt.% Bi alloy in Fig. 32c reveals high filling, where the initially cylindrical defect becomes funnel shaped, with highest filling volume between z=0 and z=800 µm. The Sn-58 wt.%Bi alloy of highest liquid fraction exhibits the highest filling ratio among the investigated alloys. The cylindrical defect evolves into a narrow funnel shaped domain, with high filling degree at the bottom close to z= 0 µm as shown in Fig. 32d.

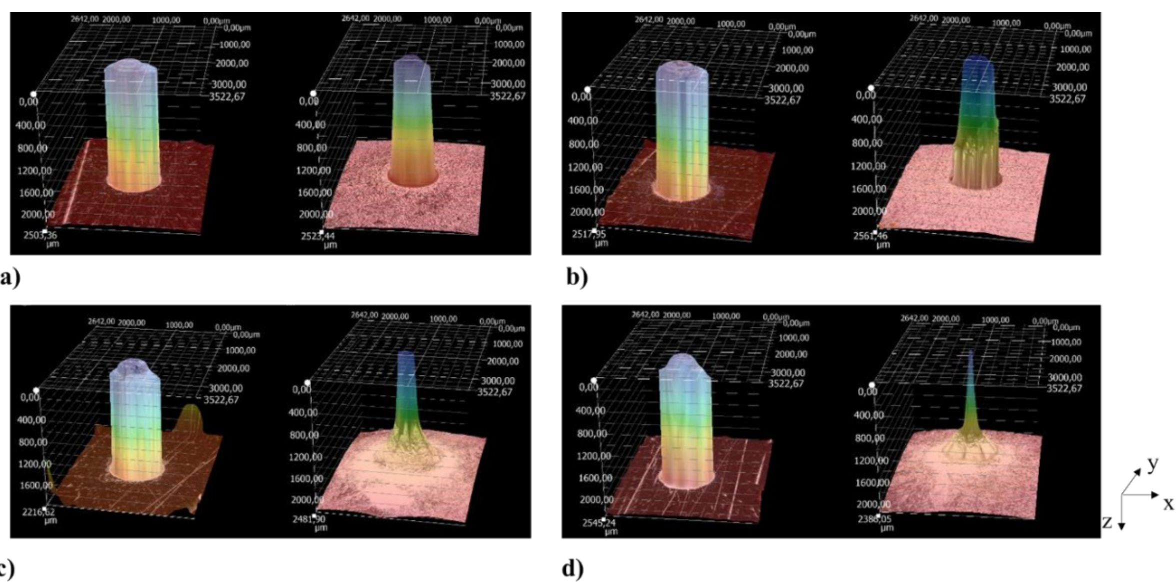

Fig. 32 3D measurements of defects in pre- and post-healing configuration a) Sn-20 wt.% Bi alloy, b) Sn-30 wt.% Bi alloy, c) Sn-47 wt.% Bi alloy, d) Sn-58 wt.% Bi alloy. Original configuration (left) and healed configuration (right).

The measured filling ratio over alloy composition for a healing time of 5 min is given in Fig.33. Four defects per alloy are evaluated with variations indicated by error bars. The liquid fraction increases with rising Bi content among the investigated alloys, where the Sn-20 wt.% Bi alloy has the lowest liquid fraction of $\Phi_{\mathrm{L}} = 18.5\%$ and the Sn-58 wt.% Bi alloy shows the highest

Die approbierte gedruckte Originalversion dieser Dissertation ist an der TU Wien Bibliothek verfügbar.
The approved original version of this doctoral thesis is available in print at TU Wien Bibliothek.
TU Bibliothek WIEN Your knowledge hub

with $\Phi_L = 91.2\%$ at $T = T_s$. A transition between alloys with 30 and 47 wt.% Bi can be seen, which raises the filling ratio from *FR*=30.3% to *FR*=73.9%. The filling ratio remains low at about *FR*=20% for alloys with <30 wt.% Bi. This indicates that the microstructural mobility of alloys with $\Phi_L > 40\ \%$ is significantly increased, possibly due to the presence of a continuous liquid network and thicker liquid channels.

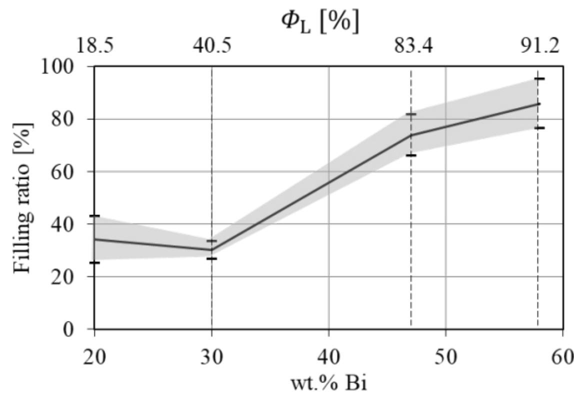

Fig. 33 Filling ratio at 150°C after healing for 5 min over alloy composition and liquid fraction at $T= T_s$

Liquid film model

Results of the liquid film model according to Eq.61 are compared with measurement from SEM micrographs in Fig. 34 and model parameters are provided in Tab. 5. The liquid film thickness at $T= T_s$ is assumed to be equal to the eutectic domain thickness. Therefore, the model results are limited to temperatures close to the melting point. The model proposed by Liu et al. [179] shows a correlation with eutectic thickness for alloys close to Sn-47 wt.% Bi content. In the range of $35\ \% < \Phi_L < 65\ \%$, the relative error among measurement and model results is <30%. The concept of a liquid film in alloys with $\Phi_L < 35\ \%$ appears invalid, due to their low liquid fraction. Alloys, such as, the Sn-20 wt.% Bi, show regions of eutectic, which are embedded in a solid network of primary phase. In such cases, a liquid film forms with increasing temperatures since more primary phase melts. Furthermore, for alloys of liquid fraction $\Phi_L > 75\ \%$, such as, Sn-58 wt.% Bi, the liquid film concept does not apply either due to the dendritic microstructure and wide thickness of the liquid domain.

Die approbierte gedruckte Originalversion dieser Dissertation ist an der TU Wien Bibliothek verfügbar.
The approved original version of this doctoral thesis is available in print at TU Wien Bibliothek.
TU Bibliothek WIEN Your knowledge hub

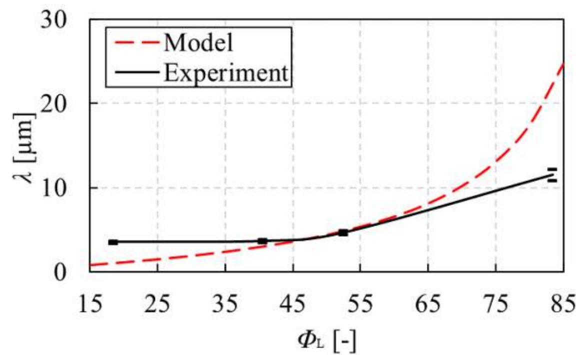

Fig. 34 Eutectic thickness of liquid film model and measurements from micrographs

Tab. 5 Liquid film model parameters for approximating liquid film in Sn-Bi alloys

	Value	Unit
C	0	[-]
C_1	2	[-]
C_2	40	[-]
r_g	17	[µm]

Crack healing

The damage-healing experiment shows an effective regain in elastic properties as summarized in Fig. 35. The overall stress-strain response of the loading sequence (red dot-dash) and post-healing sequence (green solid) are shown in Fig. 35a. In addition, an undamaged control sample (black dash) is exposed to the healing sequence without mechanical damage. The loading sequence in Fig. 35a shows a sample deformation of $\epsilon = 38\%$ and reveals an initial hardening regime before fracture. The control sample reaches the same ultimate strength of 85 MPa, yet, a lower strain at fracture of $\epsilon = 28\%$ is observed. The post-healing sequence shown in green solid illustrates the strength regain after fracture. The initial stiffness recovers to the level of the loading sequence and the strain at fracture is reduced significantly to $\epsilon = 10\%$. Furthermore, the ultimate strength in the post-healing sequence reaches 40 MPa, which is about 50% of the pre-healing strength. The second cycle for each sequence is illustrated concurrently in Fig. 35b and the stiffness recovery is indicated with E_L and E_H. The ultimate strength of the post-healing sequence (green solid) in Fig. 35b appears to be about 5 MPa higher than the loading sequence (red dot dash) and about 10 MPa higher than the control sample (black dash). The SEM micrographs of the fracture surface in Fig. 35c and Fig. 35d illustrate the effect of the healing sequence on the effective cross-section. The fracture surface of the control sample in Fig. 35c shows a smooth surface without cavities or voids, whereas, in Fig. 35d, the post-healing

TU WIEN Bibliothek Your knowledge hub
Die approbierte gedruckte Originalversion dieser Dissertation ist an der TU Wien Bibliothek verfügbar.
The approved original version of this doctoral thesis is available in print at TU Wien Bibliothek.

sample reveals local voids and rounded canal-like structures marked by white arrows. This indicates partial filling of the fracture surface during healing due to incomplete wetting of the crack surface. This specifies the self-wetting properties as an essential feature of future alloy development with healing capacity. The proposed model suggests, that healing is promoted by hydrostatic pressure, which can be induced from either external loads or volumetric swelling of the liquid during the liquid solid transformation. The role of hydrostatic pressure on healing of micro-meter sized voids was shown in theory by Siroky et al. [178,190] and potential microstructural effects on the healing evolution were discussed in Siroky et al. [176]. Crack healing in the tensile sample in Fig. 35d is incomplete, possibly due to the absence of external compressive forces. This is in qualitative agreement with findings of Fisher et al. [42] and it is conceived by the authors that compressive forces in solder joints during healing could be achieved by adequate assembly design.

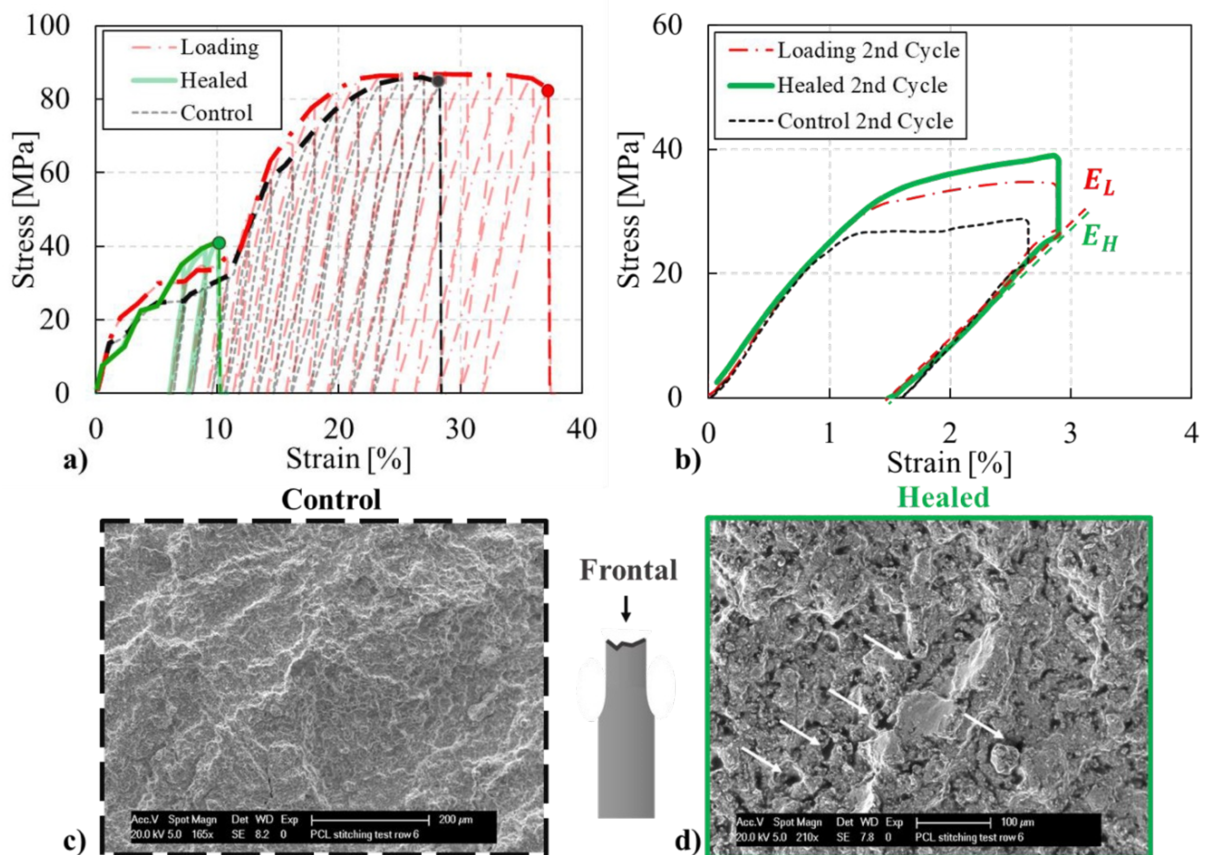

Fig. 35 Results of damage-healing experiment. a) Stress-strain of initial loading sequence (red dot dash), post-healing sequence (green solid) and of a control sample (black dashed). b) 2nd stress-strain cycle of sample at initial loading sequence (red dot dash), post-healing sequence (green solid) and of control sample (black dashed). c) Fracture surface of control sample. d) Fracture surface of sample after post-healing loading sequence.

Die approbierte gedruckte Originalversion dieser Dissertation ist an der TU Wien Bibliothek verfügbar.
The approved original version of this doctoral thesis is available in print at TU Wien Bibliothek.
TU WIEN Bibliothek Your knowledge hub

Solder joint analysis

Results of the thermo-mechanical fatigue simulations are given in Fig. 36. The plots in Fig. 36a-c illustrate the shear strain, shear stress and stress triaxiality at the end of the fourth loading cycle, respectively, and illustrate the condition before healing. A gradual increase in shear strains among solder joints 1 to 5 is observed in Fig. 36a with solder joint 5 exhibiting the highest shear strains of $\epsilon_{\mathrm{xz,max}} = 0.8$ % at T=125 °C. The shear stresses in Fig. 36b show a similar trend among solder joints with a maximum shear stress in solder 5 of $\sigma_{\mathrm{xz,max}} = 7$ MPa at T=125 °C. The maximal shear stresses in solder joints 1 to 4 are around of $\sigma_{\mathrm{xz,max}} = 2.3$ MPa at the temperature peak. The intended highest mechanical load of solder joint 5 arises from boundary effects of the solder array. The high mechanical stress and deformation leads to an early onset of mechanical damage in solder joint 5, which is, therefore, a potential healing candidate. Tensile stresses should be avoided in the healing configuration due to the low mechanical strength of the liquid film. The stress state is illustrated in Fig. 36c through plotting the stress triaxiality close to the healing temperature. The stress triaxiality indicates tension-dominated stresses with values > 0, compression-dominated stresses with values < 0 and pure shear stresses with values around 0. The stress state in Fig. 36c at T=125°C in solder joint 5 shows a negative stress triaxiality with a mean value of -0.35 and few areas of positive stress triaxiality at the solder-substrate interface. The requirement for compressive load during the healing configuration is also fulfilled for solders joints 1 to 4. At low temperatures, the material combination of the substrates indicates tensile stresses in all solder joints with peak values for the stress triaxiality of 0.7, which indicate biaxial tensile loads. The simulation results in Fig. 36c highlight the system character of healing in solder joints, which requires a combination of microstructural mobility and thermo-elastic deformation. Stress states, which promote healing, can be obtained by modifying the structural response of the component, through e.g. choosing favorable combination of substrates.

Die approbierte gedruckte Originalversion dieser Dissertation ist an der TU Wien Bibliothek verfügbar.
The approved original version of this doctoral thesis is available in print at TU Wien Bibliothek.
TU WIEN Bibliothek Your knowledge hub

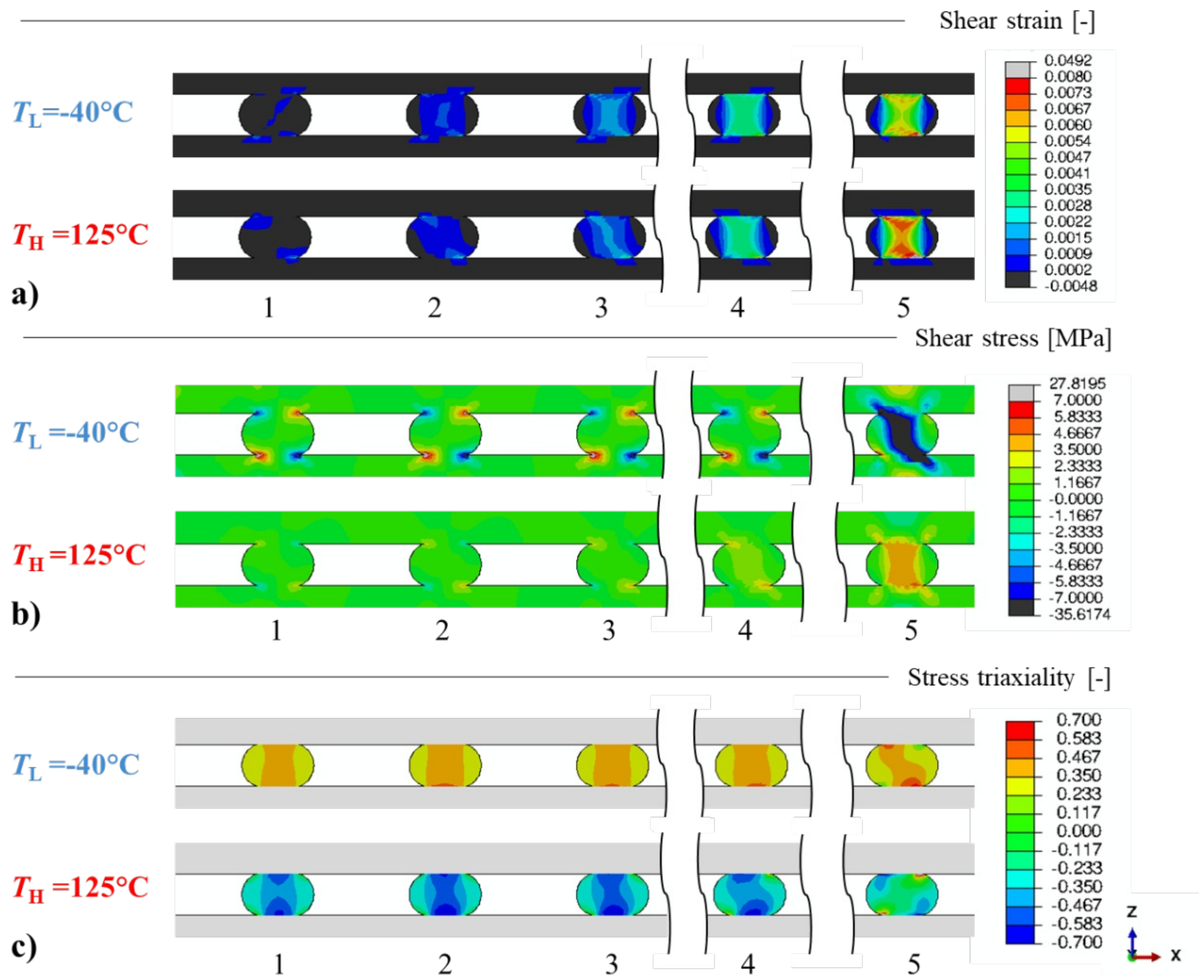

Fig. 36 Simulation results of linear solder array at high and low temperature configuration a) shear strain b) shear stress c) stress triaxiality

The damage location and evolution is illustrated in Fig. 37, where Fig. 37a shows the damage location in solder joint 5 and Fig. 37c illustrates the damage evolution of solder joint 1 to 5 during thermo-mechanical fatigue simulations. In Fig. 37a, damage initiates at the solder substrate interface due to the misfit of expansion coefficients among copper substrate and solder. The comparison of maximum damage among solder joints in Fig. 37b shows the highest damage values for solder joint 5. It was discussed in Fig. 37 that the highest degree of damage in solder joint 5 is induced by high stresses and deformation due to boundary effects, which is reflected in Fig. 37. The healing evolution is analyzed for the location marked by a red circle in Fig. 37a.

Die approbierte gedruckte Originalversion dieser Dissertation ist an der TU Wien Bibliothek verfügbar.
The approved original version of this doctoral thesis is available in print at TU Wien Bibliothek.
TU WIEN Bibliothek Your knowledge hub

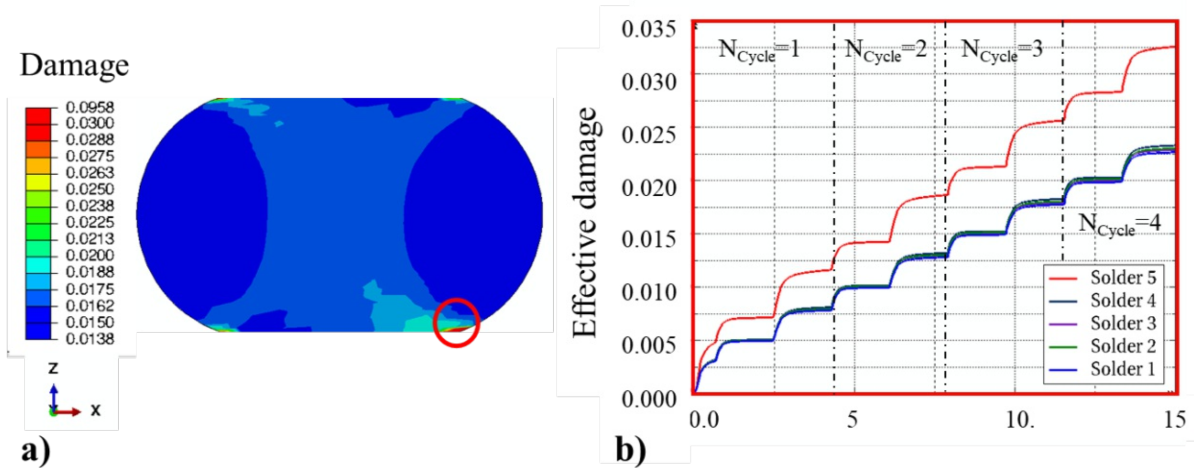

Fig. 37 Damage location and evolution a) damage location in solder 5 b) maximal damage evolution in solder 1 to 5

Healing evolution in solder joint

Healing in solder joints, according to the proposed model, is driven by the capillary pressure and delayed due to restricted microstructural mobility. According to Eqs. 59 and 60, the capillary pressure in the solder joint is size-dependent, which is shown in Fig. 38 with a thickness to radius ratio of the solder ball of $t_s/r_s = 1.17$. Results in Fig. 38 are computed with a contact angle $\psi = 136°$ and a surface energy of $\gamma_{12} = 0.438$ N/m. It shows that the capillary pressure in a solder joint of $r_s = 0.2$ mm is about two times higher than for a solder joint with $r_s = 0.4$ mm. Therefore, a rapid healing of small solder joints should be observed in the damage-healing simulations following a higher driving force for healing.

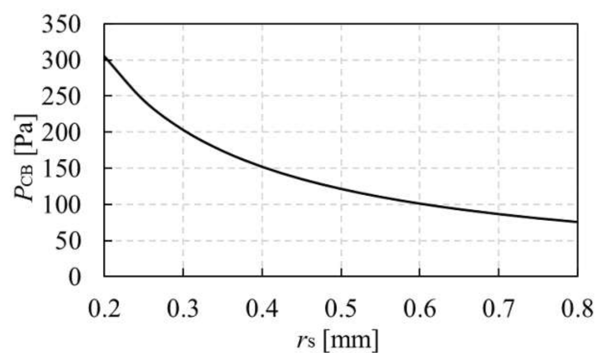

Fig. 38 Capillary pressure as a function of solder joint radius with a thickness to radius ratio of $\frac{t_s}{r_s} = 1.17$

The healing progress with respect to solder joint composition and size is shown in Fig. 39, with the temperature profile given in Fig. 39a. The healing configuration is marked with dashed lines and ranges from 255 to 285 min. The effect of alloy composition is shown in Fig. 39b, with a hypothetical healing efficiency parameter H_e= 0.9 and an idealized microstructure parameter

Die approbierte gedruckte Originalversion dieser Dissertation ist an der TU Wien Bibliothek verfügbar.
The approved original version of this doctoral thesis is available in print at TU Wien Bibliothek.
TU WIEN Bibliothek Your knowledge hub

k=1 for the Sn-47 wt.% Bi alloy. The viscous flow experiment in Fig. 32 shows a filling ration of *FR*= 74 % for the Sn-47 wt.% Bi and *FR*= 30% for the Sn-30 wt.% Bi alloy. The relative reduction of microstructural mobility is estimated from these values, where the Sn-30 wt.% Bi alloy has only 41% of the Sn-47 wt.% Bi alloys mobility according to *FR*. Therefore, a value of *k*= 0.41 is assumed in the simulations for Sn-30 wt.% Bi, where absolute values of *k* require further experimental analysis of healing in solder joints. A comparison of healing histories for Sn-30 wt.% Bi and Sn-47 wt.% Bi is shown in Fig. 39b, where the Sn-47 wt.% Bi alloy saturates at a theoretical healing limit of $D_{\mathrm{eff}} = 0.8 \cdot 10^{-2}$ within the given healing period. In case of the Sn-30 wt.% Bi alloy, the required period for complete healing is longer. In this case, a value of $D_{\mathrm{eff}} = 1.6 \cdot 10^{-2}$ is achieved due to the reduced microstructural mobility parameter and the 3 µm lower liquid film thickness. The healing efficiency can be computed from these number as

$$HE = \frac{(D_{\mathrm{eff,i}} - D_{\mathrm{eff,e}}) \cdot 100}{D_{\mathrm{eff,i}}}, \tag{74}$$

with $D_{\mathrm{eff,i}}$ and $D_{\mathrm{eff,e}}$ the effective damage parameter before and after healing, respectively. This shows a healing efficiency of HE= 77 % for the Sn-47 wt.% Bi alloy and $HE = 57$ % for the Sn-30 wt.% Bi. The healing evolution with respect to solder size is given in Fig. 39c. According to Fig. 38the capillary pressure of a solder ball with $r_{\mathrm{s}} = 0.43$ mm reduces from about 150 Pa to 75 Pa with $r_{\mathrm{s}} = 0.8$ mm. The reduced healing driving force is reflected in the simulation results shown in Fig. 39c. The damage value in case of the larger solder joint with $r_{\mathrm{s}} = 0.8$ mm is $D_{\mathrm{eff}} = 1.1 \cdot 10^{-3}$ compared to $D_{\mathrm{eff}} = 0.8 \cdot 10^{-2}$ for the smaller one, which indicates a 38% lower healing efficiency for large solder joints.

Die approbierte gedruckte Originalversion dieser Dissertation ist an der TU Wien Bibliothek verfügbar.
The approved original version of this doctoral thesis is available in print at TU Wien Bibliothek.
TU WIEN Bibliothek Your knowledge hub

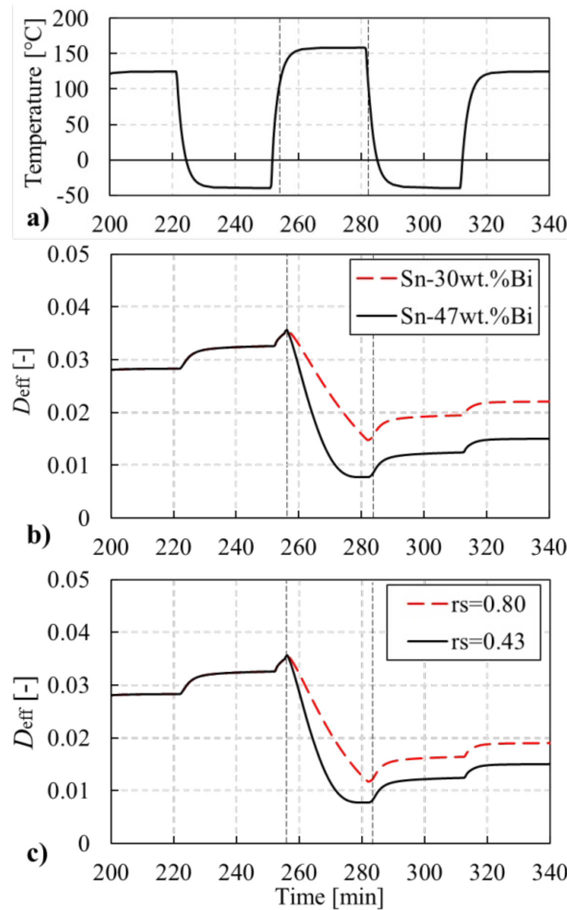

Fig. 39 Healing evolution dependent on alloy composition and solder joints size a) temperature profile b) damage parameter during healing under varying alloy composition c) damage parameter during healing under varying solder joint size.

4. Conclusion

This work presents a composition- and size-dependency of liquid-assisted healing in solder joints. A damage-healing model formulates healing as a function of liquid viscosity, liquid film, microstructural mobility and capillary pressure, where the latter is determined by the solder joint size in the healing configuration. The model suggests a microstructural dependency of material transport, represented by the parameter k. A comparison of microstructural mobility is given by comparing the filling ratio of cylindrical defects in Sn-Bi alloys with 20, 30, 47 and 58 wt.% Bi from a viscous flow experiment. A crack healing effect is observed from a tensile damage-healing experiment with partial recovery of material strength in the absence of external compressive loads. Simulation results of a linear solder array suggest a combined effect of solder joint size and composition on the healing efficiency. The following conclusions are extracted from results:

1. The theoretical derivation introduces a microstructural parameter k, which influences the viscous material transport and the healing evolution. A parameter of k= 1 represents a

Die approbierte gedruckte Originalversion dieser Dissertation ist an der TU Wien Bibliothek verfügbar.
The approved original version of this doctoral thesis is available in print at TU Wien Bibliothek.
TU WIEN Bibliothek Your knowledge hub

microstructure governed by pure viscous transport, where semi-solid microstructures are expected to be in the range $0 < k < 1$.

2. The viscous flow experiment shows that Sn-Bi alloys with liquid fractions of $\Phi_s <$ 40 % are comparably immobile, with filling ratios of < 20%. A higher liquid fraction in Sn-47 wt.% Bi and Sn-58 wt.% Bi alloy of $\Phi_L >$ 40 % allows filling ratios of > 80%. It is assumed that the presence of a liquid network highly promotes microstructural mobility.
3. The tensile damage-healing experiment indicates a strength and stiffness recovery after crack healing. Partial crack filling is observed through electron microscopy, which leads to a brittle response in the post-healing loading cycle.
4. The influence of solder joint dimension on the healing evolution is found through simulation of the linear solder array. An increase of solder joint size from $r_s = 0.43$ mm to $r_s = 0.8$ mm leads to a 38% reduced healing efficiency due to the lowered capillary pressure.
5. The composition dependence of liquid-assisted healing in solder joints is shown through simulation. The healing efficiency computed with the presented model of Sn-30 wt.% Bi alloy is about 20 % lower compared to the Sn-47 wt.% Bi alloy. The higher microstructural mobility and wider liquid film of Sn-47 wt.% Bi alloy promotes fast healing.

Die approbierte gedruckte Originalversion dieser Dissertation ist an der TU Wien Bibliothek verfügbar.
The approved original version of this doctoral thesis is available in print at TU Wien Bibliothek.
TU WIEN Bibliothek Your knowledge hub

Appendix

A. Model parameter

Tab.A1 Material parameters used in linear solder array model

Parameter	Value	Unit
γ_{12}	0.438	[N/m]
r_G	17.0	[µm]
Elastic Modulus Sn-30wt.%Bi	42.1	[GPa]
Elastic Modulus Sn-47wt.%Bi	41.0	[GPa]
Elastic Modulus Dielectric	16.0	[GPa]
A / B / n	2631 / 0.0155 / 5	[1/s] / [1/MPa] / [-]
Q	45	[kJ/mol]
$\bar{m}_s$	328.65	[g/mol]
C_1	2	[-]
C_2	40	[-]
Thermal exp. coeff. Sn	$22.0 \cdot 10^{-6}$	[1/K]
Thermal exp. coeff. Al	$23.1 \cdot 10^{-6}$	[1/K]
Thermal exp. coeff. Cu	$17.0 \cdot 10^{-6}$	[1/K]
Thermal exp. Coeff DiEl	$26.0 \cdot 10^{-6}$	[1/K]
Heat cap. SnBi	$232.0 \cdot 10^{6}$	[J/kg K]
Heat cap. Al	$897.0 \cdot 10^{6}$	[J/kg K]
Heat cap. Cu	$400.0 \cdot 10^{6}$	[J/kg K]
Heat cap. DiEl	$232.0 \cdot 10^{6}$	[J/kg K]
Heat cond. SnBi	58.0	[W/m K]
Heat cond. Al	235.0	[W/mK]
Heat cond. Cu	400.0	[W/mK]
Heat cond. DiEl	220.0	[W/mK]

Die approbierte gedruckte Originalversion dieser Dissertation ist an der TU Wien Bibliothek verfügbar.
The approved original version of this doctoral thesis is available in print at TU Wien Bibliothek.
TU Bibliothek WIEN Your knowledge hub

2.5 Analysis of Sn-Bi solders: X-ray micro computed tomography imaging and microstructure characterization in relation to properties and liquid phase healing potential

Georg Siroky (georg.siroky@mcl.at) [1], Elke Kraker[1], Jördis Rosc[1], Dietmar Kieslinger[3], Roland Brunner[1], Sybrand van der Zwaag[4], Ernst Kozeschnik[2], Werner Ecker[1]

[1] Materials Center Leoben Forschung GmbH (MCL), Roseggerstraße 12, 8700 Leoben, Austria
[2] TU Wien, Institute of Materials Science and Technology, Getreidemarkt 9, 1060 Wien, Austria
[3] ZKW Elektronik GmbH, Samuel Morse-Straße 18, 2700 Wiener Neustadt, Austria
[4] TU Delft, Faculty of Aerospace Engineering, Kluyverweg 1, 2629 HS, Delft, The Netherlands

Published in: Materials, 14, 1, 153, https://doi.org/10.3390/ma14010153

Abstract

This work provides an analysis of X-ray micro computed tomography data of Sn-xBi solders with x = 20, 30, 35, 47, 58 wt.% Bi. The eutectic thickness, fraction of eutectic and primary phase are analyzed. Furthermore, the 3D data is evaluated by means of morphology parameters, such as, shape complexity, flatness, elongation and mean intercept length tensor. The investigated alloys are categorized in three groups based on their morphology, which are described as "complex dominant", "complex- equiaxed" and "mixed". The mechanical behavior of Sn-Bi alloys in the semi-solid configuration and the correlation with microstructural parameters are discussed. A varying degree of geometric anisotropy of the investigated alloys is found through the mean intercept length tensor. Representative volume element models for finite element simulations (RVE-FEM) are created from tomography data of each alloy to analyze a correlation of geometric and elastic anisotropy. The simulations reveal an elastic isotropic behavior due to the small difference of elastic constants of primary and eutectic phase. A discussion of properties in the semi-solid state and liquid phase healing is provided.

1. Introduction

Efforts to reduce the environmental impact of microelectronic products led to the development of lead-free solder alloys with varying content of Ag, Bi, In, Cu, Ga and Zn among other alloying elements [1–6]. The effort to reduce the environmental impact of Pb containing solders led to several alloys of varying Sn, Ag and Cu content [7]. Recently, low melting point solders gained interest in the research community, where the Sn-Bi system is a promising candidate for soldering of temperature-sensitive components [2]. Studies investigated Sn-Bi alloys with

Die approbierte gedruckte Originalversion dieser Dissertation ist an der TU Wien Bibliothek verfügbar.
The approved original version of this doctoral thesis is available in print at TU Wien Bibliothek.
TU WIEN Bibliothek Your knowledge hub

respect to alloying elements [8–10], thermal parameters [11], magnetic stirring [12] and directional solidification [13,14]. The effect of In addition in Sn-Bi alloys on melting point and mechanical properties was shown by Wu et al. [8] and microstructural effects due to Cu and Ag additions were investigated by Silva et al. [9]. A strengthening effect of Ag addition to Sn-Bi alloys was reported by Ren et al. [10]. Elastic properties and their temperature-dependence were investigated by means of pulse echo overlap method [12], ultrasonic transmission [15,16] and nano-indentation [3,17]. Despite the thorough mechanical characterization, a 3D microstructural analysis of Sn-Bi alloys based on tomographic data is missing in literature.

Micro X-ray computed tomography (μ-XCT) imaging offers a non-destructive spatial analysis of materials and parts [18]. It was applied on solder materials to investigate several microstructural features such reflow porosities [19–21] or phase morphology [22–26]. The size distribution of spherical reflow porosities in solder joints was re-ported by Jiang et al. [19] and Rauer et al. [20]. Shi et al. [21] investigated the deformation of reflow porosities in fatigue experiments with μ-XCT imaging and finite element simulations. A combined approach of μ-XCT imaging and focused ion beam (FIB) tomography was reported by Yazzie et al. [22] and highlighted the local microstructure and morphology of Sn-rich solders. The size distribution and morphology of intermetallic phases in Sn-rich solders was reported by Kaira et al. [24] and the primary phase dendrites in Sn-Pb solder were assessed with μ-XCT imaging by Mertens et al. [25]. A three-dimensional morphometric characterization of Sn-Ag-Cu solder microstructures was reported by Maleki at al. [26]. The microstructural evolution of flip-chip solder joints under electromigration were investigated by [27] using in-situ 3D laminography and finite element simulations. X-ray tomography data of solders was used for numerical modelling of thermal and mechanical properties, where Michael et al. [28] used tomography data to numerically investigate the thermal resistance of solder joints with respect to reflow porosities. The elasto-plastic response of Sn-Ag-Cu solders after aging was studied by Maleki et al. [26,29] and highlighted the possibility to compute the stress-strain response from tomography data. Besides these reported studies on thermal and mechanical behavior, other properties also depend on the microstructural morphology, such as semi-solid deformation [30–32], hot tearing [33,34] or liquid phase healing [35,36]. These properties have not been reported in literature for Sn-Bi alloys and it is the aim of the present work to provide the essential parameters to enable such studies.

The volumetric phase fraction and local grain or phase thickness are commonly evaluated parameters and can be determined from 2D- [37] and 3D measurements [25]. In addition, the

Die approbierte gedruckte Originalversion dieser Dissertation ist an der TU Wien Bibliothek verfügbar.
The approved original version of this doctoral thesis is available in print at TU Wien Bibliothek.
TU Bibliothek WIEN Your knowledge hub

mean intercept length (MIL) parameter is used to describe the geometric anisotropy [38]. It quantifies the number of phase boundaries along randomly oriented trajectories through the volume of interest (VOI). The degree of anisotropy (DA) can be derived from the eigenvalues of the MIL tensor and provides a scalar measure with DA = 0 representing an isotropic and DA = 1 a perfectly aligned anisotropic microstructure [38]. A new morphology categorization was reported by Fang et al. [39], which is based on the shape complexity parameter [40,41], elongation and flatness [42,43]. They determined shape classes based on these three morphology parameters and distinguished among spherical, equiaxed, rod, sheet and complex shaped domains [39]. This enables the quantification of morphologic similarities among alloys and provides the basis for generic microstructure creation.

This study provides an analysis of several microstructural descriptors from µ-XCT images. Five samples of varying Bi content (20 wt.%, 30 wt.%, 35 wt.%, 47 wt.% and 58 wt.% Bi) and a microstructure representative of that obtained during industrial reflow processing are prepared. The reconstructed tomography data is segmented into Sn-rich primary- and Bi-rich eutectic phase and microstructural parameters are evaluated from the segmented tomography data, such as, eutectic phase fractions, mean intercept length of phase boundaries, volume to surface ratio, complexity parameter, flatness and elongation. The mechanical behavior of Sn-Bi alloys in the semi-solid state is discussed using the extracted morphology parameters and literature data. Representative volume element models for finite element simulations (RVE-FE) are derived from the µ-XCT data for finite element simulations and the correlation between geometric and elastic anisotropy is investigated. The work ends with a morphology-based prediction of which alloy composition is most likely to yield the best liquid phase-assisted self-healing behavior.

2. Materials and methods

Sample preparation

Alloys of composition Sn- 20, 30, 35, 47 and 58 wt.% Bi were prepared on an induction heat plate and held at 250 °C for 60 min for homogenization. Cylindrical samples of dimension ø 3 mm × 10 mm were cast in a silicon mold and solidified under air cooling. The temperature in the silicon mold was measured using a contact thermometer. The temperature and cooling rates in the mold are illustrated in Fig. 40. The average cooling rate in the initial phase of solidification was 1.5 K/s. The solidus temperature of T_s = 138 °C was reached after 55 s. Cylindrical pins of ø 0.5 mm × 1 mm were machined from the as-cast samples on a lathe under oil cooling. The pins were glued to cylindrical glass rods for positioning in the µ-XCT setup.

Die approbierte gedruckte Originalversion dieser Dissertation ist an der TU Wien Bibliothek verfügbar.
The approved original version of this doctoral thesis is available in print at TU Wien Bibliothek.
TU Bibliothek WIEN Your knowledge hub

Samples were prepared for SEM (scanning electron microscopy) imaging by mechanical grinding and polishing for comparison with measurements from µ-XCT data. The homogeneity of the sample microstructure was assessed by measuring the eutectic phase fraction from SEM crosssections, where sample dependencies were insignificant.

Images of sample crosssections were obtained on a SEM (FEI Philips XL30, Philips, Amsterdam, The Netherlands) in electron back scatter mode (BSE) and with 20kV acceleration voltage.

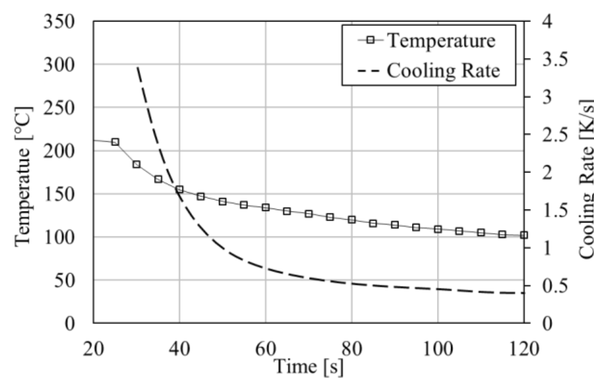

Fig. 40 Temperature (solid squares) and cooling rate (dashed) during sample casting of Sn-20 wt.% Bi sample.

Imaging and segmentation

The samples were scanned on a lab-scale µ-XCT device (GE nanotom m, General Electric, Boston, Massachusetts, USA) with an isotropic voxel size of about 1.8 µm. The acceleration voltage was set to 116 kV and the X-ray tube current was 100 µA. These settings were chosen to allow transmission in the samples and to minimize image artefacts. No pre-filters were applied on the X-ray tube and the VOI of scanned samples had the dimensions of approximately 400 × 400 × 1050 µm3.

The Sn-rich primary phase and Bi-rich eutectic phase were segmented with the commercial image analysis software Avizo 2019.1 (www.thermofischer.com). Prior to segmentation, the signal-to-noise ratio was enhanced by applying a median filter with a kernel of 3 × 3 × 3 voxels, which improves the detectability of phase boundaries. The segmentation of dendrites was achieved using the top-hat transform algorithm. This includes two steps, first, a closing operation on the grey value image and second, the selection of a threshold value to detect the dark primary phase regions in the data. This approach reduces noise, improves the detectability of structures on the length scale of several voxels and reduces non-uniformities caused by beam-hardening artefacts.

Die approbierte gedruckte Originalversion dieser Dissertation ist an der TU Wien Bibliothek verfügbar.
The approved original version of this doctoral thesis is available in print at TU Wien Bibliothek.
TU WIEN Bibliothek Your knowledge hub

The segmentation delivered a binary data set which consists of the primary phase and the surrounding eutectic phase. A representative grey value image after image acquisition and the segmented primary phase are illustrated in Fig. 41a,b, respectively. The comparison of grey value and segmented image in Fig. 41a,b shows that morphological features, such as, dendrites or phase boundaries are well represented. The segmented data is compared with scanning electron microscopy (SEM) images to verify the eutectic thickness. Furthermore, phase fractions from µ-XCT measurements are compared with CALPHAD (Calculations of Phase Diagrams) calculations using the software package MatCalc 6.03 (http://matcalc.at) with the thermodynamic database COST 531 [44], to quantify the agreement of theoretical and measured phase fractions. A phase diagram of the binary Sn-Bi system is provided in Fig. A1.

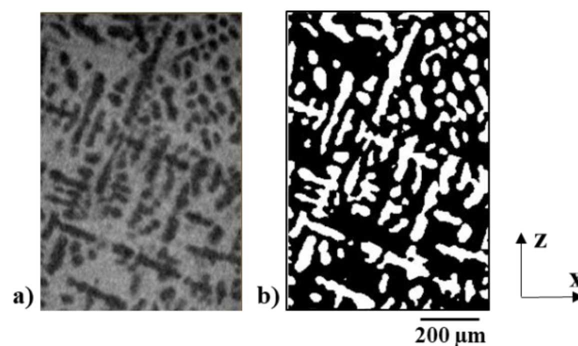

Fig. 41 Representative image obtained in the x-z plane from the 3D data for the Sn 58 wt.% Bi alloy. a) Grey value image displays the primary phase (dark grey) and eutectic phase (light grey). b) Corresponding segmented primary phase (white).

Microstructural parameter

The segmented images were analyzed using the open-source package ImageJ [189,191]. Connected domains were analyzed and labelled with a random color lookup table for rendering. Several microstructural quantities are extracted from the segmented 3D data, such as, eutectic volume fraction, eutectic surface fraction, eutectic thickness, MIL tensor, degree of anisotropy (DA), volume of eutectic (V_e), total VOI volume (V_total) and surface area of eutectic (A_e). The eutectic volume fraction, ϕ_e, is calculated with

$$\phi_\mathrm{e} = \frac{V_\mathrm{e}}{V_\mathrm{total}} , \tag{75}$$

and compared with CALPHAD calculations. The eutectic surface fraction, ψ_e, is obtained through

$$\psi_\mathrm{e} = \frac{A_\mathrm{e}}{V_\mathrm{total}} . \tag{76}$$

The eutectic thickness, t_e, is defined according to Hildebrand and Rüegsegger [47] as the largest

Die approbierte gedruckte Originalversion dieser Dissertation ist an der TU Wien Bibliothek verfügbar.
The approved original version of this doctoral thesis is available in print at TU Wien Bibliothek.
TU Bibliothek WIEN Your knowledge hub

diameter of a sphere completely inside the eutectic phase, which is written as

$$t_{\mathrm{e}}(x_{\mathrm{e}}) = 2 \cdot \max(\{r | x_{\mathrm{e}} \in \mathrm{sph}(x, r) \subseteq \Omega, x \in \Omega\}) \quad (77)$$

where $\Omega \subset \mathrm{R}^3$ is the set of all points within the eutectic structure and $x_{\mathrm{e}} \in \Omega$ is an arbitrary point in the eutectic structure. The expression sph(x,r) define the points inside a sphere with center x and radius r. A possible VOI size-dependence of several extracted parameters, such as, ϕ_{e}, A_{e} or DA is provided in the appendix. A morphology analysis based on the shape complexity, elongation and flatness was performed following the classifications found to be useful in describing the (healing of) damage during creep loading of steels [112]. The shape complexity parameter, Ω_3, is calculated as

$$\Omega_3 = \frac{A}{\pi^{\frac{1}{3}}(6V)^{\frac{2}{3}}}, \quad (78)$$

with A and V being the surface area and volume of the segmented domain, respectively. Furthermore, the elongation and flatness are evaluated based on the moment of inertia, I_j, of an equivalent ellipsoid. The semi-axes of the ellipsoid, a_j, are calculated from the eigenvalues of the inertia tensor, $\boldsymbol{I}$, as

$$a_j = \sqrt{\frac{5\,(tr(\boldsymbol{I}) - 2I_j)}{2\,V}}. \quad (79)$$

The elongation is calculated accordingly with

$$E = \frac{2\,a_1}{a_2 + a_3}, \quad (80)$$

and the flatness with

$$F = \frac{a_2}{a_3}, \quad (81)$$

Five shape categories are defined according to their combination of Ω_3, E and F, which is summarized in Tab. 6. A discussion on the correlation of shape and morphology parameters is given in [112].

Die approbierte gedruckte Originalversion dieser Dissertation ist an der TU Wien Bibliothek verfügbar.
The approved original version of this doctoral thesis is available in print at TU Wien Bibliothek.
TU WIEN Bibliothek Your knowledge hub

Tab. 6 Values for shape categorization based on complexity parameter Ω_3, elongation E and flatness F

	E	*F*	Ω_3
Sphere	-	-	$\Omega_3 \leq 1.15$
Equiaxed	< 5	< 5	$1.15 < \Omega_3 \leq 2.5$
Rod	≥ 5	< 5	$1.15 < \Omega_3 \leq 2.5$
Sheet	-	≥ 5	$1.15 < \Omega_3 \leq 2.5$
Complex	-	-	$\Omega_3 \geq 2.5$

An ellipsoid fit of the MIL tensor is computed [191] and the *DA* is calculated from the associated eigenvalues, λ_i, with

$$DA = 1 - \frac{\min(\lambda_i)}{\max(\lambda_i)} \tag{82}$$

RVE-FEM model

Voxel-based RVE-FE models were created from µ-XCT data to investigate the agreement with elastic mixing rules and a possible elastic anisotropy. The segmented binary images were converted into the mhd format and a voxel mesh was generated using the software package medtool (www.dr-pahr.at/medtool). A coarsening factor of 3 was applied on the 3D data, leading to an average voxel size of 6 µm, where a convergence analysis with a coarsening factor ranging from 3 to 5 was performed. Cuboid models with *x*, *y* and *z* dimensions of 356 µm x 356 µm x 1029 µm and kinematic periodic boundary conditions (PBC) were created in the commercial software package ABAQUS (www.3ds.com). The microstructure was approximated with 596.991 elements of type C3D8. Material parameters for elastic properties of primary and eutectic phase were taken from literature [187] and values are provided in Tab. 7. The Young´s moduli of microstructures with 20, 30, 47 and 58 wt.% Bi were evaluated numerically under uniaxial deformation in x-, y- and z- direction. For comparison with the *DA* parameter, the elastic anisotropy is evaluated from simulations as

$$DA_{\mathrm{el}} = 1 - \frac{\min(E_i)}{\max(E_i)}, \tag{83}$$

with $\min(E_i)$ and $\max(E_i)$ representing the minimal and maximal Young's modulus, respectively.

The linear and inverse rules of mixture were evaluated according to [192] for comparison with RVE-FE results.

Die approbierte gedruckte Originalversion dieser Dissertation ist an der TU Wien Bibliothek verfügbar.
The approved original version of this doctoral thesis is available in print at TU Wien Bibliothek.
TU Bibliothek WIEN Your knowledge hub

Tab. 7 Elastic material parameters of RVE-FE model [187].

Property	Value [Unit]
Young's modulus primary phase	50.0 [GPa]
Poisson number primary phase	0.33 [-]
Young's modulus eutectic phase	40.0 [GPa]
Poisson number eutectic phase	0.33[-]

3. Results

Tomographic rendering

Fig. 42 shows a rendering of the segmented eutectic phase from μ-XCT data of five alloy compositions, where the color indicates connected domains. The Sn-20 wt.% Bi sample in Fig. 42a reveals the highest fragmentation with isolated islands of eutectic phase. The Sn-30 wt.% Bi sample in Fig. 42b exhibits fewer disconnected regions, where a large connected eutectic domain is indicated in blue. The samples with 35, 47 and 58 wt.% Bi are illustrated in Fig. 42c, d and f, respectively. These latter compositions show a connected network of eutectic phase across the entire VOI.

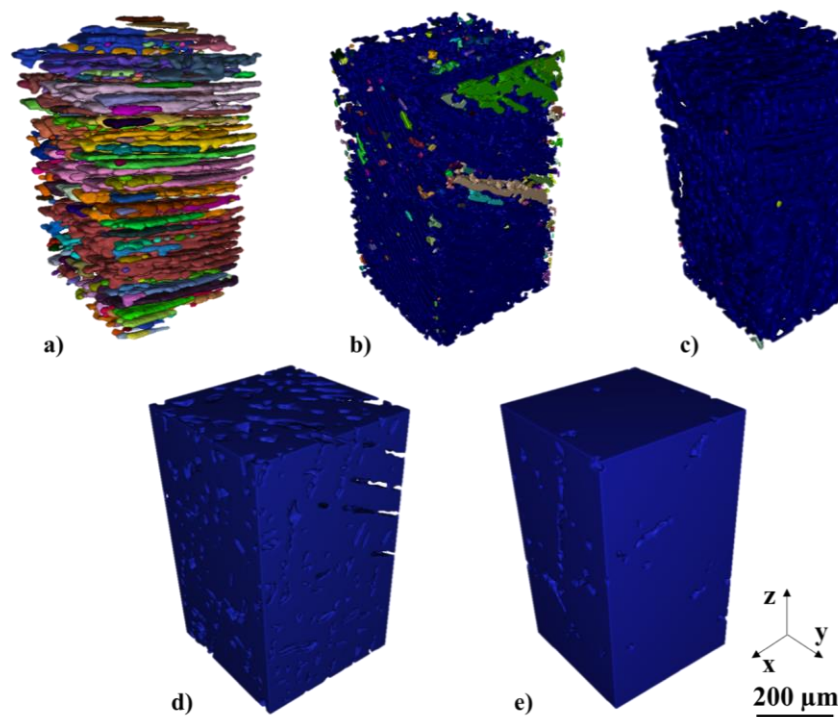

Fig. 42 Segmented eutectic phase obtained from μ-XCT. Color code: Each color represents a single connected phase. a) Sn- 20 wt.% Bi b) Sn- 30 wt.% Bi c) Sn- 35 wt.% Bi d) Sn- 47 wt.% Bi e) Sn- 58 wt.% Bi

Die approbierte gedruckte Originalversion dieser Dissertation ist an der TU Wien Bibliothek verfügbar.
The approved original version of this doctoral thesis is available in print at TU Wien Bibliothek.
TU WIEN Bibliothek Your knowledge hub

Complementary images of the primary phase are shown in Fig. 43. A network is indicated by red colored domains in Fig. 43a-c. A comparison among Fig. 42c and Fig. 43c of the Sn-35 wt.% Bi alloy shows an interpenetrating network of the primary and eutectic phases with a low fragmentation of domains. The Sn- 47 wt.% Bi and Sn-58 wt.% Bi reveal separated dendritic structures of primary phase in Fig. 43d and Fig. 43e, respectively. Despite the lower primary phase fraction in the Sn-58 wt.% Bi alloy, a connectivity of dendritic structures is visible. Furthermore, the primary and secondary dendrites are captured in Fig. 43e.

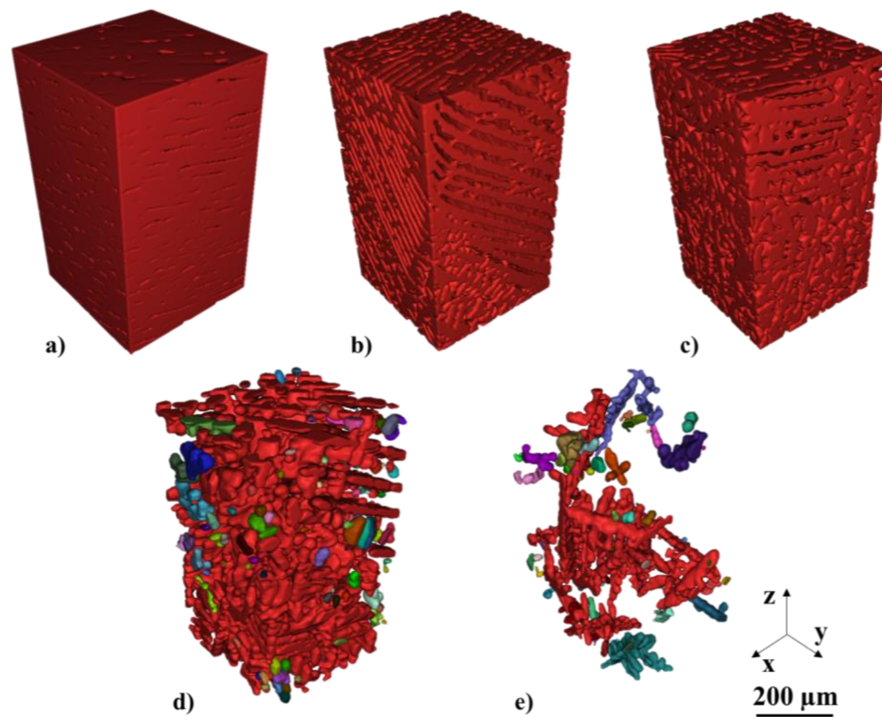

Fig. 43 Segmented primary phase obtained from µ -XCT. Color code: Each color represents a single connected phase. a) Sn- 20 wt.% Bi b) Sn- 30 wt.% Bi c) Sn- 35 wt.% Bi d) Sn- 47 wt.% Bi e) Sn- 58 wt.% Bi

Volume fractions

The eutectic volume fraction is extracted from the µ-XCT data and illustrated in Fig.44, where a comparison with CALPHAD calculations and the generated RVE-FE models is given. Fig.44a shows a correlation between the equilibrium eutectic fraction (black solid) with µ-XCT (green triangles) and RVE-FE (red squares) values. The µ-XCT data captures the increasing eutectic fraction, with slight deviations from the predicted CALPHAD phase fractions (black solid line). The deviations seem random, with compositions 20, 30 and 47 wt.% Bi underestimating and 35 and 58 wt.% overestimating the theoretical eutectic fraction. Due to the image coarsening of the RVE-FE models, these trends are further amplified. Fig.44b shows the error compared with CALPHAD calculations of µ-XCT and RVE-FE data. The deviation of the µ-XCT data remains

Die approbierte gedruckte Originalversion dieser Dissertation ist an der TU Wien Bibliothek verfügbar.
The approved original version of this doctoral thesis is available in print at TU Wien Bibliothek.
TU WIEN Bibliothek Your knowledge hub

below 10% for most alloys except the Sn- 47 wt.% Bi composition. The same holds for the RVE-FE data, whereas the Sn- 35 wt.% Bi alloy deviates considerable with 20 %. This originates from an unfavorable approximation due to the voxel-mesh. A refinement of the voxel-mesh would lead to a better representation of the eutectic fractions. However, a limit of about $5 \cdot 10^6$ elements prevents a further refinement and the Sn-35 wt.% Bi alloy was omitted from simulations. A comparison with Scheil calculations showed similar results with deviations from the theoretical values of about 10 %. Results of the Scheil analysis are given in the Fig.A2 and a variation of VOI and its effect on the volume fraction is given in Fig.B1.

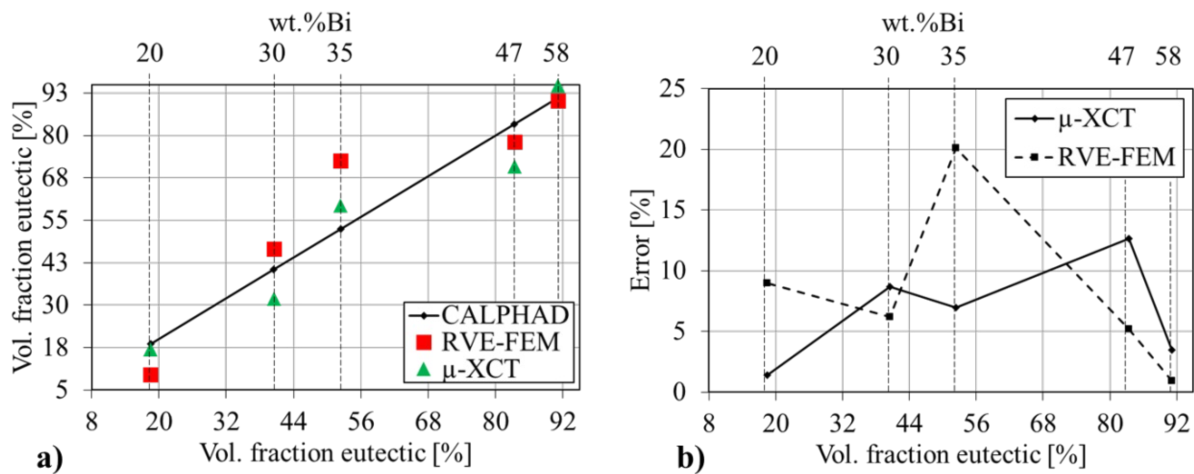

Fig. 44 Eutectic volume fraction obtained from CALPHAD calculations, image analysis of μ -XCT data and the RVE-FE model. a) eutectic volume fraction over composition b) relative error of μ-XCT data and RVE-FE model based on equilibrium CALPHAD calculations over composition.

Eutectic thickness

The eutectic thickness determined from μ-XCT data is shown in Fig.45. The eutectic thickness ranges from 3.6 μm for the Sn-20 wt.% Bi alloy to 73 μm for the Sn-58 wt.% Bi alloy. The data indicates a linearly increasing eutectic thickness among alloys with 20, 30, 35 and 47 wt.% Bi content. The Sn- 58 wt.% Bi alloy shows the largest mean eutectic thickness and highest scatter of the measured values. Furthermore, a steep increase of mean eutectic thickness is observed from 47 to 58 wt.% Bi. The large scatter might arise from the dendritic microstructure and the large eutectic network observed in Fig.42e.

Die approbierte gedruckte Originalversion dieser Dissertation ist an der TU Wien Bibliothek verfügbar.
The approved original version of this doctoral thesis is available in print at TU Wien Bibliothek.
TU WIEN Bibliothek Your knowledge hub

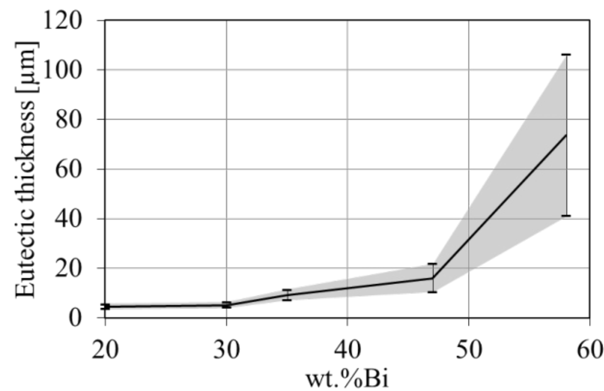

Fig. 45 Image analyzed eutectic phase thickness obtained from µ-XCT measurements as a function of Bi content. Error bars indicate the standard deviation of eutectic thickness.

Morphology parameters

The morphology parameters $\Omega_3,\ E,\ F$ of each Sn-Bi alloy are given in Fig. 46 and Fig. 47. The analysis shows that their microstructure is composed of equiaxed-, complex-, rod- and sheet-shaped domains. The shape complexity, Ω_3, over volume is presented in Fig. 46. The illustrated data points represent each segmented sub-domain and its corresponding shape class. The Sn-20 wt.% Bi alloy in Fig. 46 a is composed of equiaxed, complex, rod and sheet domains, where sheet and rod-like structures tend towards larger sub-volumes of 10^3 to 10^6 μm^3. The equiaxed and complex-shaped domains are spread across the total volume range. The other alloys of 30, 35, 47 and 58 wt.% Bi in Fig. 46 b-e, respectively, reveal similar complexity values. Each alloy contains a complex-shaped outlaying data point with a volume of around 10^7 μm^3, which is the connected network of primary and eutectic phase. The majority of the data points is equiaxed-shaped with a volume of 10 to 10^5 μm^3.

Die approbierte gedruckte Originalversion dieser Dissertation ist an der TU Wien Bibliothek verfügbar.
The approved original version of this doctoral thesis is available in print at TU Wien Bibliothek.
TU Bibliothek WIEN Your knowledge hub

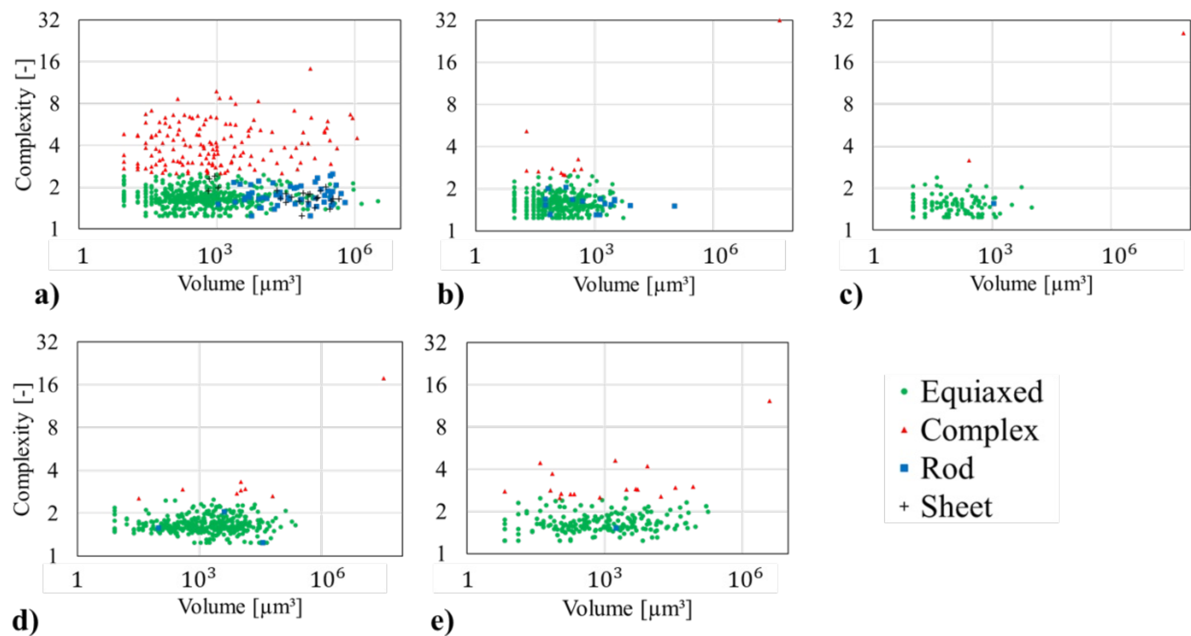

Fig. 46 Calculated complexity parameter based on the segmented µ-XCT data as a function of the domain volume for Sn-Bi alloys. Morphology classes are equiaxed (green), complex (red), rod (blue), sheet (grey). a) Sn-20 wt.% Bi b) Sn-30 wt.% Bi c) Sn-35 wt.% Bi d) Sn-47 wt.% Bi e) Sn-58 wt.% Bi

Flatness over elongation in Fig. 47 gives further morphological information on the microstructure. The Sn-20 wt.% Bi alloy is illustrated in Fig. 47a and shows the maximum range of elongation (1 to 25) and flatness (1 to 11) among the analyzed alloys. The rod-shaped structures have a maximum flatness F of 5 and an elongation E ranging from 5 to 25. Most data points are equiaxed and complex-shaped, where low values of E and F indicate uniformly-shaped structures. The 30, 35, 47 and 58 wt.% Bi alloys in Fig. 47b-e reveal high similarity in the E-F space, where, except for a few rod-shaped structures, most domains are equiaxed- and complex-shaped. Furthermore, the Sn-35 wt.% Bi alloy in Fig. 47c reveals the most isotropic geometry with $E_{\max} = 3$ and $F_{\max} = 7.2$ among the analyzed compositions. A large spread in E-F space is associated with a strong geometric orientation. Low and similar values among E and F characterize isotropic microstructures.

Die approbierte gedruckte Originalversion dieser Dissertation ist an der TU Wien Bibliothek verfügbar.
The approved original version of this doctoral thesis is available in print at TU Wien Bibliothek.
TU Bibliothek WIEN Your knowledge hub

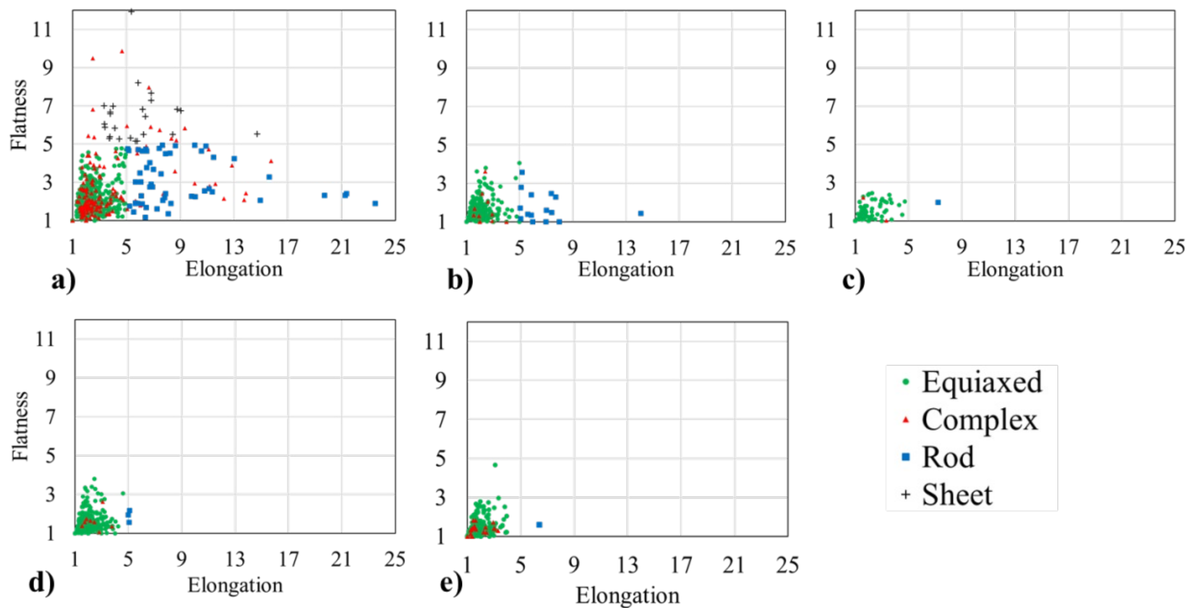

Fig. 47 Flatness over elongation for Sn-Bi alloys based on the segmented μ-XCT data. Morphology classes are equiaxed (green), complex (red), rod (blue), sheet (grey). a) Sn-20 wt.% Bi b) Sn-30 wt.% Bi c) Sn-35 wt.% Bi d) Sn-47 wt.% Bi e) Sn-58 wt.% Bi

Geometric anisotropy

The geometric orientation is analyzed using the MIL tensor and DA parameter, where DA=0 is spatial isotropy and DA= 1 fully anisotropic [191]. Eigenvalues and eigenvectors of the ellipsoid on the MIL tensor are given in Tab.D1 and the respective ellipsoids are provided in Fig.D1. Fig. 48 shows the DA over composition, where the Sn-20 wt.% Bi alloy reveals the highest degree of anisotropy. This is in agreement with the wide span of E and F in Fig. 47a, which indicated a flat and elongated microstructure. Furthermore, the Sn-35 wt.% Bi gives the lowest value of DA= 0.058, which is reflected by a low spread of E and F values in Fig. 47c. A VOI size variation with respect to *DA* is given in Fig.B4 and showed an insignificant variation with respect to VOI dimensions.

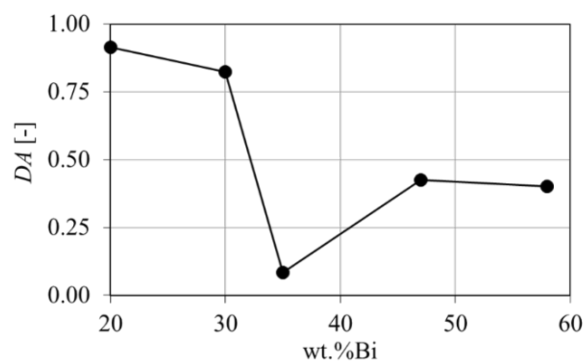

Fig. 48 Calculated degree of anisotropy from μ-XCT measurements over composition of Sn-Bi alloys

Die approbierte gedruckte Originalversion dieser Dissertation ist an der TU Wien Bibliothek verfügbar.
The approved original version of this doctoral thesis is available in print at TU Wien Bibliothek.
TU WIEN Bibliothek Your knowledge hub

Computed elastic response

In Fig. 49, the Young’s moduli calculated through RVE-FE models are shown (green, solid-dot). The analytical linear- and inverse mixing rules were evaluated (dashed) for comparison, where graphs of linear and inverse mixing rule appear congruent due to the low difference in Young`s moduli of primary and eutectic phase. Furthermore, values for Young`s moduli reported in literature are shown as a benchmark for computed results. The RVE-FE model shows good agreement with results from the analytical mixing rules. The RVE-FE calculations in Fig. 49 are also in good agreement with Young’s moduli reported by Lu et al. [187] through nano-indentation and values by El-Daly [193] through pulsed echo overlap (PEO). Values of Wu et al. [194], Mokhtari et al. [195] and Lai et al. [62] show considerable deviation from the RVE-FE values arising from the specific measurement methods used, where tensile tests in particular underestimate the elastic properties.

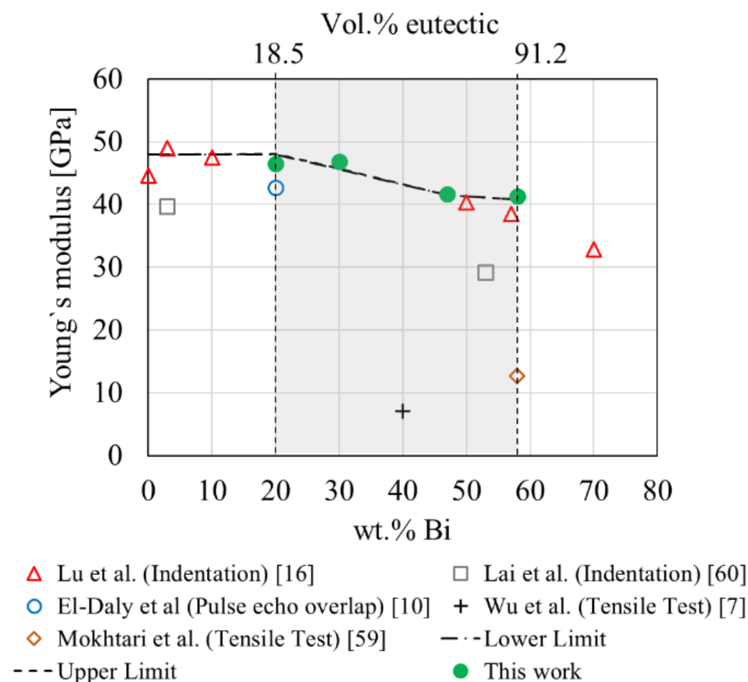

Fig. 49 RVE-FE results, linear/inverse mixing rule and literature values of Young's modulus.

4. Discussion

Eutectic surface fraction

The eutectic surface fraction according to Eq.76 for the μ-XCT data and RVE-FE models is given in Fig. 50. The μ-XCT data shows a maximum surface fraction for the Sn-35 wt.% Bi alloy, which corresponds to the interpenetrating network of eutectic- and primary phase observed in Fig. 42 and Fig. 43. Furthermore, it reveals that Sn-Bi alloys with around 50 %

Die approbierte gedruckte Originalversion dieser Dissertation ist an der TU Wien Bibliothek verfügbar.
The approved original version of this doctoral thesis is available in print at TU Wien Bibliothek.
TU Bibliothek WIEN Your knowledge hub

eutectic phase fraction create the maximum number of phase boundaries. The RVE-FE model in Fig. 50 properly reflects the tomography data. Yet, the surface fraction in the RVE-FE model is underestimated on average by roughly 50 %, which arises from the voxel approximation. Therefore, the model in its presented form has limitations with respect to properties that require a quantitative representation of phase boundaries. Nevertheless, the general trend is fulfilled for alloys with 20, 30, 47 and 58 wt.% Bi. The phase boundary surface area with respect to VOI size is given in Fig.B2.

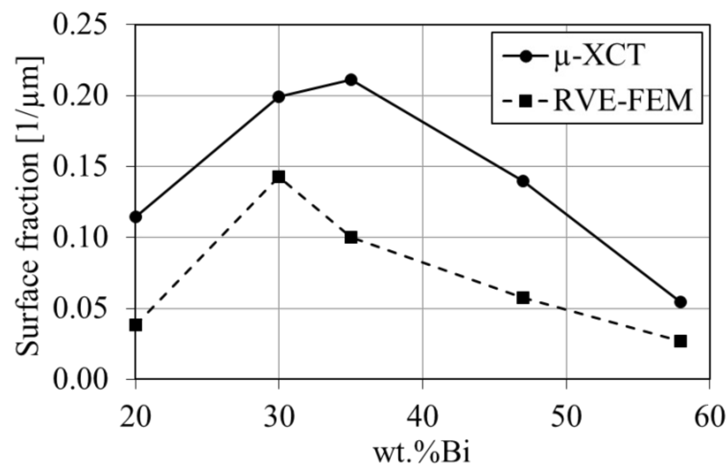

Fig. 50 Eutectic surface fraction over composition from µ-XCT (solid) measurements and RVE-FE (dashed) model

Eutectic thickness: SEM & µ-XCT

The eutectic thickness was evaluated from SEM cross-sections for Sn-20, 30, 35 and 47 wt.% Bi alloys for comparison with 3D measurement. The cross-sections are illustrated in Fig. 51, where Fig. 51a-d shows the microstructure of the 20, 30 and 47 wt.% Bi alloys, respectively. The white domains in Fig. 51a-d show the eutectic phase, embedded in gray primary phase. Secondary precipitates of Bi can be seen in the primary phase, which form due to a reduced solubility of Bi in β-Sn at room temperature. The corresponding local thickness map of the reference samples is illustrated in Fig. 52a-d. In case of the Sn-Bi system, the eutectic thickness provides a close estimate of the liquid film above the solidus temperature. The liquid film thickness defines the tensile strength of the alloy in the last stage of solidification [196] and is a determining factor for the formation of solidification cracks. The hot tearing criteria reviewed by Eskin et al. [196] show an inverse relation of liquid film thickness and strength. Therefore, the Sn- 20 wt.% Bi alloy is expected to provide the highest mechanical strength in the semi-solid configuration among the studied alloys.

TU Bibliothek Your knowledge hub WIEN
Die approbierte gedruckte Originalversion dieser Dissertation ist an der TU Wien Bibliothek verfügbar.
The approved original version of this doctoral thesis is available in print at TU Wien Bibliothek.

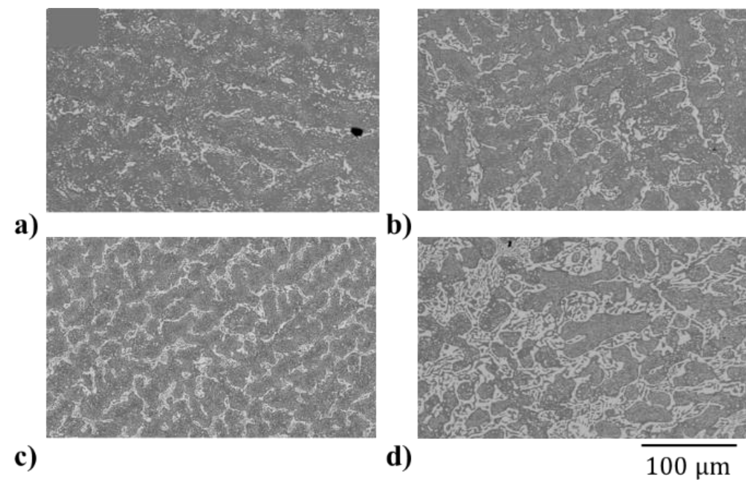

Fig. 51 SEM cross-sections of Sn-Bi alloys a) Sn-20 wt.% Bi b) Sn-30 wt.% Bi c) Sn-35 wt.% Bi d) Sn-47 wt.% Bi. Scale bar with 100 µm applies to all images.

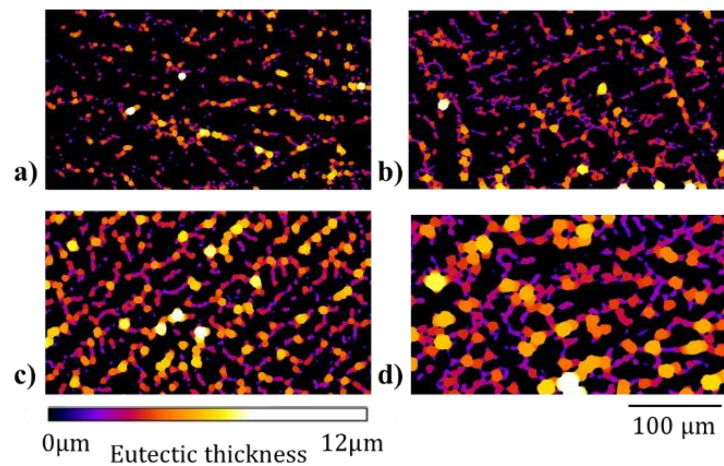

Fig. 52 Local eutectic thickness map of Sn-Bi alloys a) Sn-20 wt.% Bi b) Sn-30 wt.% Bi c) Sn-35 wt.% Bi d) Sn-47 wt.% Bi. The color spectrum defines the eutectic thickness, scale bar applies on all images.

A comparison of µ-XCT and SEM measurements is given in Fig. 53. A good correlation between both imaging techniques is observed over alloy compositions. It shows that SEM cross-sections provide a good estimate for the local phase thickness. Nevertheless, 2D measurements give a lower bound estimate for the actual local thickness. This is shown in Fig. 53 with SEM measurements being close to lower values of µ-XCT measurements. A possible size-dependence of the eutectic thickness on VOI was investigated with results given in Fig.B3.

Die approbierte gedruckte Originalversion dieser Dissertation ist an der TU Wien Bibliothek verfügbar.
The approved original version of this doctoral thesis is available in print at TU Wien Bibliothek.
TU WIEN Bibliothek Your knowledge hub

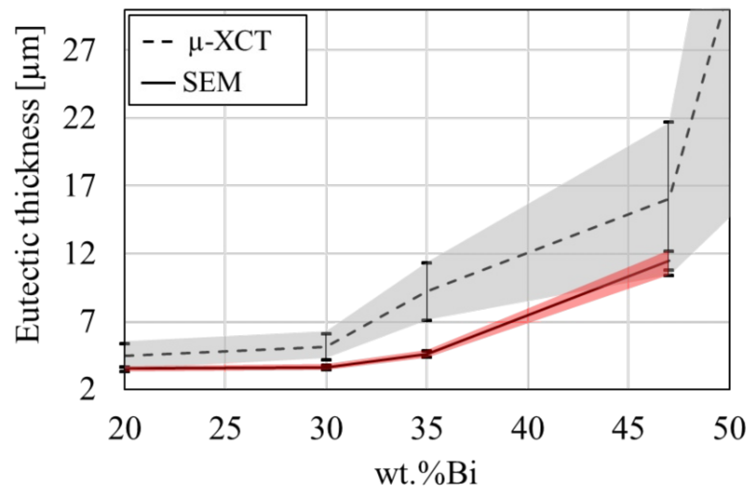

Fig. 53 Comparison of the image analyzed eutectic thickness obtained from the µ-XCT data and SEM data as a function of alloy composition. Error bars indicate the standard deviation of eutectic thickness.

Morphology classification

A volumetric classification is given in Fig. 54, which shows the volume fraction of each morphologic class for all alloy compositions. Detailed values can be found in Tab.C1. The Sn-20 wt.% Bi alloy is composed of complex, equiaxed, rod and sheet areas, where 40 % of the microstructure is composed of equiaxed domains. The Sn-30 wt.% Bi and Sn-35 wt.% Bi alloys reveal complex microstructures due to the large eutectic and primary networks. In Tab.C1, insignificant fractions of equiaxed and rod-shaped domains are given. The Sn-47 wt.% Bi and Sn-58 wt.% Bi alloys are composed of equiaxed and complex domains, where the equiaxed areas have a minor volume fraction of 7 % and 26 %. Overall, the relative volume fractions in Fig. 54 reveal similar morphologies among some of the investigated alloys. Three categories are suggested to group alloys with similar features. The Sn-20 wt.% Bi alloy represents a “mixed” microstructure with significant amounts of complex, equiaxed, rod and sheet domains. The Sn-30 wt.% Bi and Sn-35 wt.% Bi alloys show a “complex-dominated” structure with negligible contributions of equiaxed- and rod-shaped areas. Furthermore, the Sn-47 wt.% Bi and Sn-58 wt.% Bi alloys are summarized as “complex-equiaxed”, where the microstructure is dominated by complex areas with a significant presence of equiaxed domains. The data in Fig. 54 suggests that alloys with eutectic phase fraction between 30 and 60 % are complex dominated due to the formation of a fine network of eutectic phase. The dendritic primary phase for alloys with 47 and 58 wt.%Bi leads to a fraction of equiaxed domains of 7 % and 26 %.

Die approbierte gedruckte Originalversion dieser Dissertation ist an der TU Wien Bibliothek verfügbar.
The approved original version of this doctoral thesis is available in print at TU Wien Bibliothek.
TU WIEN Bibliothek Your knowledge hub

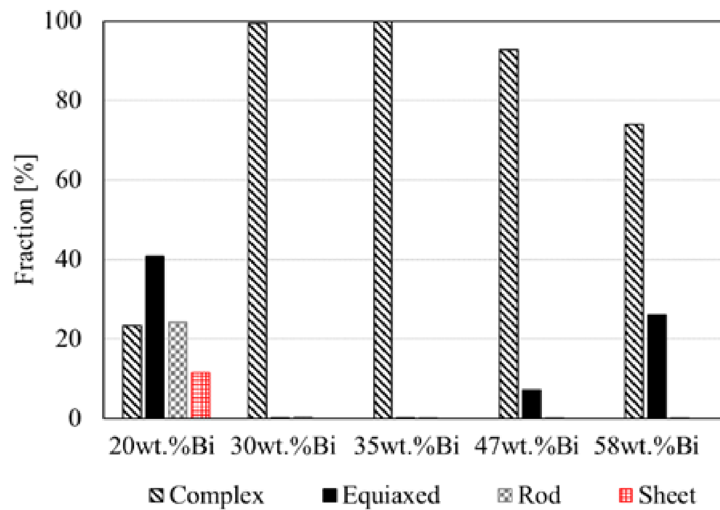

Fig. 54 Volume fractions of morphology classes in Sn-Bi alloys obtained from segmented µ-XCT data.

Morphology and elastic anisotropy

To investigate a possible correlation among geometric and elastic anisotropy, Young's moduli were computed with the RVE-FE models. Fig. 55 shows the elastic response over composition, where Fig. 55a shows the moduli in each spatial direction of the unit cell. Fig. 55b shows the elastic DA_{el} computed according to eq.5. The Sn-20 wt.% Bi alloy shows the most pronounced orientation dependency, with a 1.4 GPa higher modulus in z-direction. This agrees with the equivalent ellipsoid stretched in z-direction in Fig.D1a. The remaining alloys show a negligible orientation-dependence. The elastic DA_{el} parameter in Fig. 55b indicates an isotropic characteristic for all alloys. The highest anisotropy is found for the Sn-20 wt.% Bi alloy with $DA_{\mathrm{el}} = 0.03$. The similar elastic constants of primary and eutectic phase reduce the geometric anisotropy found in µ-XCT Data shown in Fig. 48. Furthermore, it is important to discuss the effect of crystal anisotropy on the elastic properties. In principle, single grains or grain boundaries are hardly detected through lab-scale µ-XCT. Nevertheless, a similar approach was reported by Wijaya et al. [197], where the local crystal orientation of the microstructure was neglected and good correlation of experimental and numerical results of elastic properties was achieved. However, in case of solder joints, the local crystal anisotropy becomes a determining factor for solder joint reliability [198]. The body-centered tetragonal crystal structure causes an elastic and thermal expansion misfit, where large-angle grain boundaries act as damage initiation sites.

Die approbierte gedruckte Originalversion dieser Dissertation ist an der TU Wien Bibliothek verfügbar.
The approved original version of this doctoral thesis is available in print at TU Wien Bibliothek.
TU Bibliothek WIEN Your knowledge hub

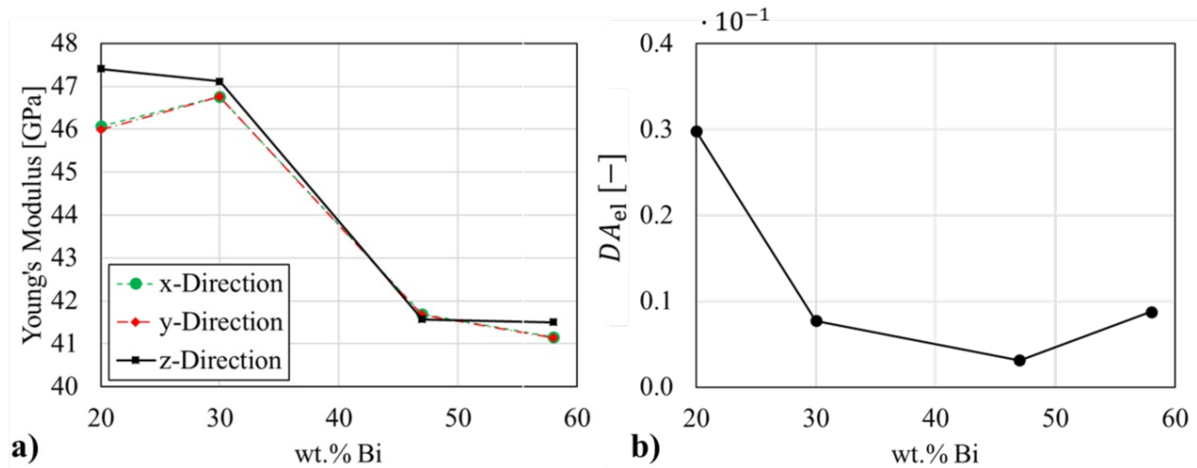

Fig. 55 Evaluation of calculated elastic anisotropy from RVE-FEM models a) Young's moduli from unidirectional tensile deformation b) degree of anisotropy from Young's modulus.

Semi-solid shear strength

The microstructural and morphology descriptors reported in the present work allow a discussion of several mechanical properties in the semi-solid state, with the eutectic phase still being liquid [178,199]. Under these conditions, the residual strength of the solder joint is an important measure to estimate tolerable external forces. The shear strength of Sn-Pb semi-solids of varying microstructure was studied by Martin et al. [200], which is used for a comparative discussion due to its close similarity to the Sn-Bi system. The authors reported a morphology-dependence of shear strength, where equiaxed microstructures showed lower values of about 1/10 compared to those for dendritic microstructures. The liquid fraction also influenced the shear strength in the semi-solid state, with values ranging from 3 MPa at liquid fraction of $\phi_L =$ 20 % to 1.2 MPa at $\phi_L = 37$ %. Assuming a condition close to the solidus temperature of $T_S =$ 138 °C. the liquid fraction of Sn-Bi alloys is equal to the volume fraction of eutectic, where measured values are given in Tab.8. Therefore, one can conclude that the expected shear strength during healing of the Sn-20 wt.% Bi alloy will be > 3 MPa, as a result of the presences of the solid skeleton of β-Sn illustrated in Fig. 43a. The remaining alloys with 30 wt.% to 58 wt.% Bi are likely to have a shear strength < 1 MPa in comparison with [200]. The shear strengthening effect of dendritic microstructures reported by Martin et al. [200] in case of the Sn-58 wt.% Bi is most likely overcompensated by the high liquid fraction of $\phi_L = 94.7$ %. Furthermore, the presence of a liquid film network shown in Fig. 42b-d is an additional limitation of semi-solid strength. The above analysis provides an estimate for choosing the handling conditions of solder joints during liquid-assisted healing.

Die approbierte gedruckte Originalversion dieser Dissertation ist an der TU Wien Bibliothek verfügbar.
The approved original version of this doctoral thesis is available in print at TU Wien Bibliothek.
TU WIEN Bibliothek Your knowledge hub

Tab.8 Liquid fraction at solidus temperature over solder composition

Composition	ϕ_L at T_S
Sn-20 wt.% Bi	17.1 %
Sn-30 wt.% Bi	31.8 %
Sn-35 wt.% Bi	59.4 %
Sn-47 wt.% Bi	70.8 %
Sn-58 wt.% Bi	94.7 %

Semi-solid uniaxial compression

Theoretical considerations of liquid-assisted healing reported in Refs. [178,199] suggest that external compressive deformation is a driving force for liquid-assisted healing. This effect is limited by the tendency of void formation under semi-solid compression, which has been investigated for Al-Cu alloys [201–203]. The eutectic character of this alloy system offers enough similarity with Sn-Bi solders for qualitative comparison. Kareh et al. [202] studied void formation in globular-equiaxed microstructures under variation of liquid fraction. The alloys deformed similarly to a cohesion-less granular material and showed a varying tendency of void formation under uniaxial compression, which was associated with shear-induced dilation of the microstructure. A critical liquid fraction of $\phi_S = 37.6\%$ was found above which void formation was fully inhibited. A minimal liquid channel thickness is required to compensate dilation and accommodate grain movement. In case of interacting solid grains, which is likely when the liquid film thickness drops below the minimal required value, void formation is observed. These results suggest that Sn-Bi alloys with > 30 wt.% Bi provide the required liquid film thickness to be insensitive to void formation during compression. The work of Cai et al. [203] supports this suggestions, as void shrinkage under compressive strains of $\epsilon < 1.2$ % in the semi-solid was observed in alloys with $\phi_S = 30$ %. Further uniaxial compression, however, leads to nucleation and growth of voids as soon as the liquid film thickness shrinks, inducing local tensile stresses and inhibiting liquid feeding. The microstructural data of Sn-Bi alloys, therefore, suggest a varying degree of maximum compression to be applied until void nucleation appears in the liquid. The critical value of ϕ_S reported by Kareh et al. [202] is fulfilled for Sn alloys with 35, 47 and 58 wt.% Bi. It is theorized that the Sn-35 wt.% Bi alloy with an average liquid film thickness of 9.2 µm will tolerate less uniaxial compression than the Sn- 47 wt.% and Sn- 58 wt.% Bi alloys with 16 µm and 73 µm liquid thickness, respectively, due to early closing of the liquid film. Further semi-solid compression experiments on these alloys could reveal the degree of tolerable deformation and provide a link between microstructural features and semi-solid void formation. In particular, the evolution of

Die approbierte gedruckte Originalversion dieser Dissertation ist an der TU Wien Bibliothek verfügbar.
The approved original version of this doctoral thesis is available in print at TU Wien Bibliothek.
TU Bibliothek WIEN Your knowledge hub

morphology parameters, such as, Ω_3, E, F with respect to semi-solid deformation, can identify the 'safe' and the 'damage-creating' conditions.

Semi-solid permeability

The theoretical considerations of liquid-assisted healing in Refs. [178,199] discussed the role of local material transport for void healing. It was mentioned that the local resistance against material transport will lead to a deviation of the theoretical healing efficiency. The Carman-Kozeny relation [204] is used to describe the permeability, K. This quantity provides an estimate for resistance against liquid flow as

$$K = \frac{(1-f_s)^3}{k_C S_v^2 f_s^2}, \tag{84}$$

with f_s being the solid fraction, k_c being a dimensional constant (3 for dendritic and 5 for equiaxed structures) and S_v the surface fraction. The dimensionless permeability indicates the required pressure gradient for fluid flow and is given in Fig. 56 from measured values of f_s. The pressure gradient and fluid flow was investigated by Sistaninia et al. [205], which showed a rising pressure gradient with increasing solid fraction. Considering Darcy's law, the permeability is linearly related to potential local fluid flow and, therefore, directly affects defect filling in the liquid-assisted healing concept. It is concluded that the dimensionless permeability in Fig. 56 provides a relative estimate for the healing efficiency among the Sn-Bi alloys and close above the solidus temperature. The high solid fraction and low surface ratio of the Sn-20 wt.% and Sn- 30 wt.% Bi alloys leads to very low permeability between 0.0014 and 0.01. Furthermore, the tomographic rendering in Fig. 42a indicates small fragmented islands of liquid domain, which most likely prevent feeding of neighboring areas. The Sn-35 wt.% Bi to Sn-58 wt.%Bi alloys have a permeability of factor 10 to 1000 higher than the high solid fraction alloys. It is, therefore, expected that the healing efficiency increases accordingly with solid fractions $\phi_s < 60$ %.

Die approbierte gedruckte Originalversion dieser Dissertation ist an der TU Wien Bibliothek verfügbar.
The approved original version of this doctoral thesis is available in print at TU Wien Bibliothek.
TU WIEN Bibliothek Your knowledge hub

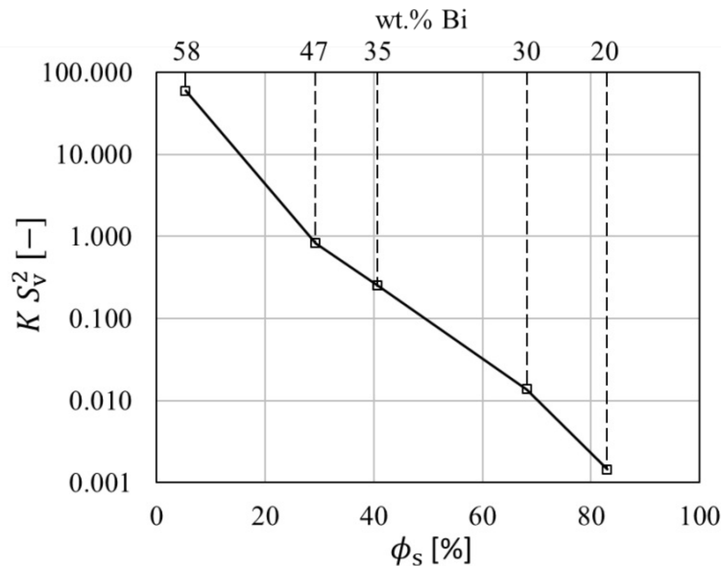

Fig. 56 Dimensionless permeability over solid fraction (just before the final formation of the eutectic fraction) and Sn-Bi alloy composition, calculated from µ-XCT measurements.

The discussion of shear strength, uniaxial compression and permeability in the semi-solid state provides necessary criteria for liquid phase healing. The presence of a liquid phase network is required to increase the microstructural permeability and to allow material transport for defect filling, which is fulfilled for the investigated solders except the Sn-20 wt.% Bi alloy. Furthermore, alloys with 35, 47 and 58 wt.% Bi provide a liquid fraction larger than the critical value of 38% reported by Kareh et al. [202] to prevent formation of porosities during compression. These alloys require a load free condition during healing, due to the low expected shear strength in the semi-solid state. Therefore, solders of 35, 47 and 58 wt.% Bi show the highest potential of liquid phase healing in absence of external loads.

5. Conclusion

This work presents a thorough microstructural analysis of µ-XCT data of five Sn alloys with varying Bi content. The following outcomes are reported:

1. Eutectic phase fractions measured with µ-XCT showed good correlation with expected values from CALPHAD calculations.
2. The Sn-20 wt.% Bi alloy show fragmented domains of eutectic embedded in primary phase. The Sn-35 wt.% Bi alloy reveals interpenetrating primary and eutectic phase, which is reflected by the highest phase boundary area fraction. The Sn-58 wt.% Bi, despite its high eutectic phase fraction, showed a connected dendritic network of primary phase.

Die approbierte gedruckte Originalversion dieser Dissertation ist an der TU Wien Bibliothek verfügbar.
The approved original version of this doctoral thesis is available in print at TU Wien Bibliothek.
TU WIEN Bibliothek Your knowledge hub

3. The morphology analysis shows microstructural similarities of the investigated alloys. The Sn-20 wt.% Bi alloy is composed of four geometric features and its microstructure is categorized as “mixed”. The alloys with 30 wt.% and 35 wt.% Bi are composed of mainly “complex-shaped” areas. The alloys of near-eutectic composition, Sn- 47 wt.% Bi and 58 wt.% Bi, constitute from “complex” and “equiaxed” domains.
4. The RVE-FE simulations showed an elastically isotropic response, despite significant spatial orientation of the microstructures. The similar elastic properties of primary and eutectic phase reduce the impact of geometric anisotropy. Results are in agreement with linear and inverse rule of mixture.

Finally, it can be concluded that the analysis of liquid phase fraction, liquid film thickness and permeability suggests that among the investigated Sn-Bi alloys, those with a Bi content between 35 and 58 wt.% have the highest potential for liquid phase healing. The low mechanical strength in this configuration requires a load free condition during healing.

Acknowledgment
Financial support by the Austrian Federal Government (in particular from Federal Ministry for Transport, Innovation and Technology) represented by the Austrian Research Promotion Agency (FFG), within the framework of the „24. Ausschreibung Produktion der Zukunft, nationale Projekte“ Programme (project number: 864808 project name: SOLARIS) is gratefully acknowledged. Sybrand van der Zwaag acknowledges support from the Dutch Innovative Research Program Self Healing Materials (IOP-SHM).

Appendix

A. Phase diagram & Scheil analysis

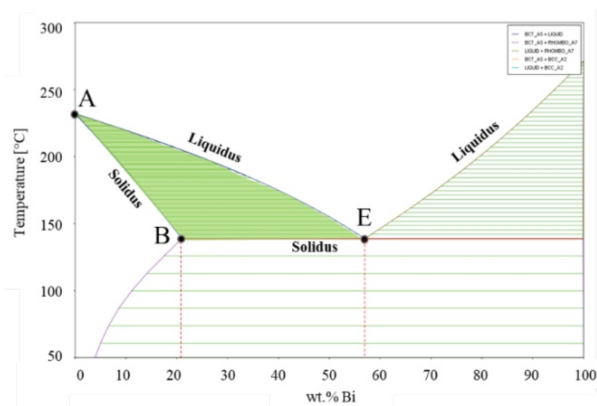

Fig.A1 Sn-Bi binary phase-diagram.

Die approbierte gedruckte Originalversion dieser Dissertation ist an der TU Wien Bibliothek verfügbar.
The approved original version of this doctoral thesis is available in print at TU Wien Bibliothek.
TU Wien Bibliothek Your knowledge hub

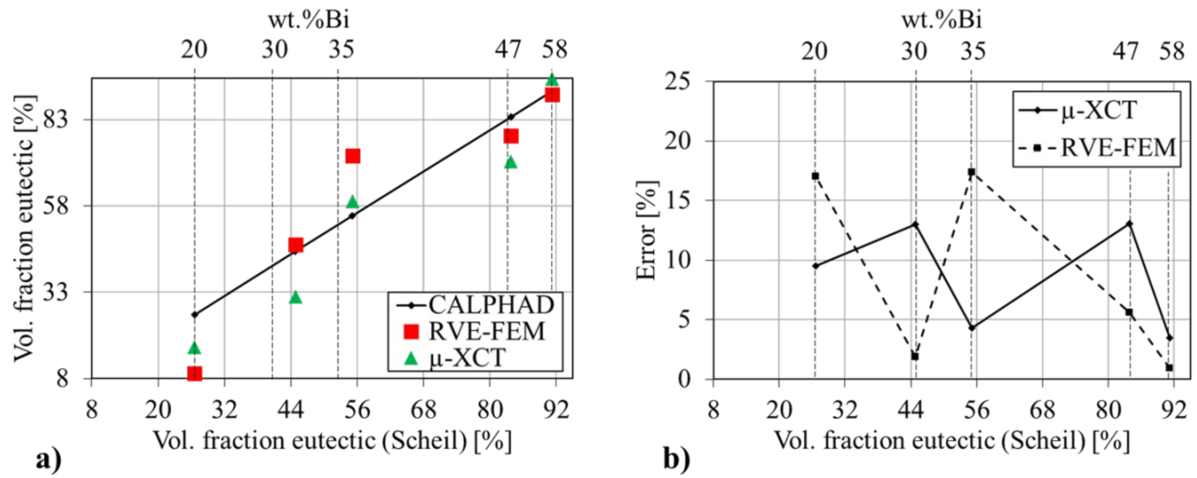

Fig.A2 Eutectic volume fraction from CALPHAD calculations, µ-XCT imaging and the RVE-FE model a) eutectic volume fraction over composition b) relative error of µ-XCT data and RVE-FE model based on Scheil CALPHAD calculations over composition.

B. Volume of interest variations

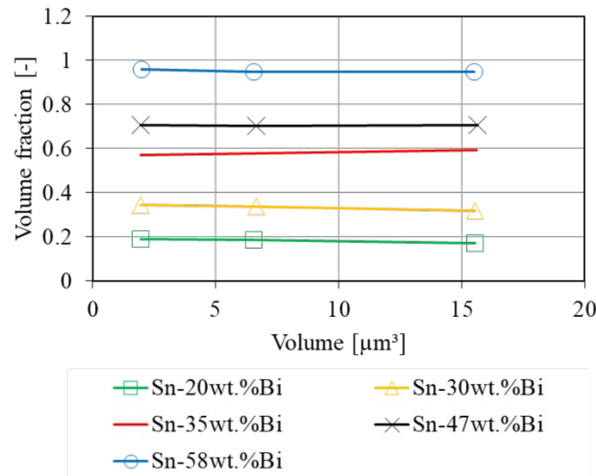

Fig.B1 Volume fraction over variation of VOI and alloy composition

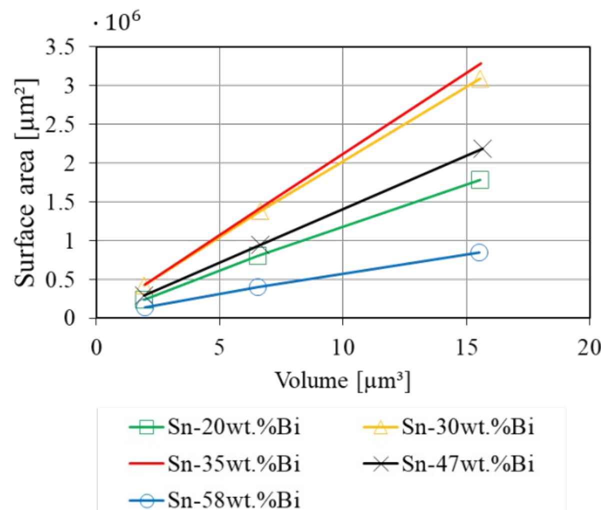

Fig.B2 Eutectic surface area over variation of VOI and alloy composition

Die approbierte gedruckte Originalversion dieser Dissertation ist an der TU Wien Bibliothek verfügbar.
The approved original version of this doctoral thesis is available in print at TU Wien Bibliothek.
TU Bibliothek Your knowledge hub WIEN

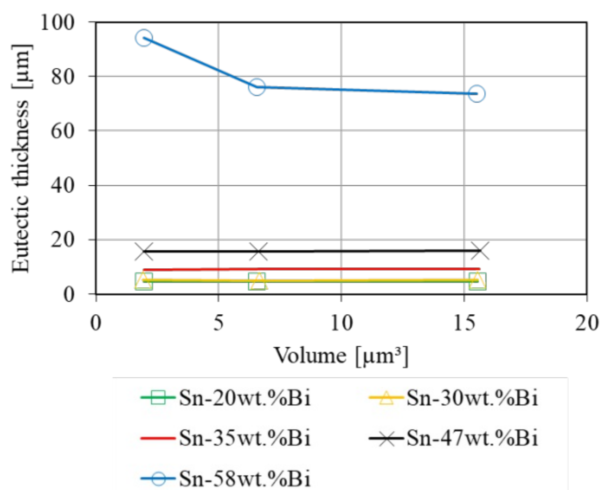

Fig.B3 Eutectic thickness over variation of VOI and alloy composition

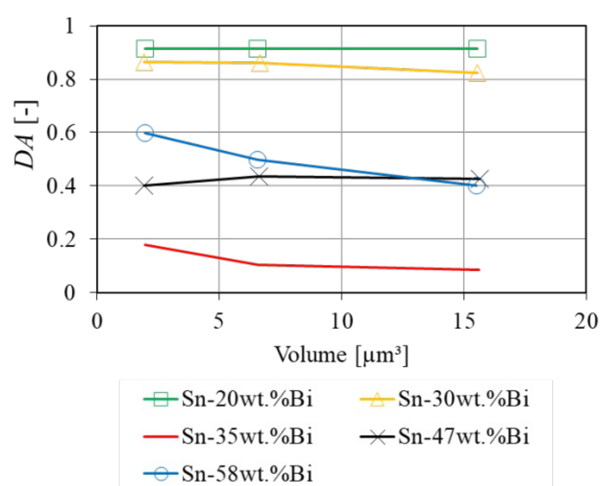

Fig.B4 Degree of anisotropy over variation of VOI and alloy composition

C. Volume fractions of morphologic classes

Tab.C1 Volume fraction of morphologic classes

wt.%Bi	Equiaxed	Rod	Sheet	Complex
58	26.034	0.033	0.0	74.0
47	7.076	0.108	0.0	92.8
35	0.065	0.002	0.0	99.9
30	0.244	0.271	0.0	99.5
20	40.859	24.171	11.5	23.4

Die approbierte gedruckte Originalversion dieser Dissertation ist an der TU Wien Bibliothek verfügbar.
The approved original version of this doctoral thesis is available in print at TU Wien Bibliothek.
TU WIEN Bibliothek Your knowledge hub

D. Ellipsoid fit

Tab.D1 Degree of anisotropy, eigenvectors m_{ij} and eigenvalues λ_i of ellipsoid fit.

wt. %Bi	DA	m_{11}	m_{12}	m_{13}	m_{21}	m_{22}	m_{23}	m_{31}	m_{32}	m_{33}	λ_1	λ_2	λ_3
20	0.914	0.159	-0.119	-0.980	0.415	-0.893	0.176	0.896	0.434	0.093	0.0008	0.0018	0.0088
30	0.825	-0.317	-0.776	0.545	-0.339	0.629	0.700	0.886	-0.037	0.463	0.0036	0.0067	0.0208
35	0.085	0.690	0.676	-0.259	0.660	-0.734	-0.160	-0.299	-0.061	-0.952	0.0089	0.0090	0.0097
47	0.425	0.061	0.059	0.996	0.808	-0.589	-0.014	0.586	0.806	-0.083	0.0025	0.0038	0.0044
58	0.401	0.824	0.565	0.050	0.564	-0.825	0.032	0.059	0.002	-0.998	0.0002	0.0004	0.0004

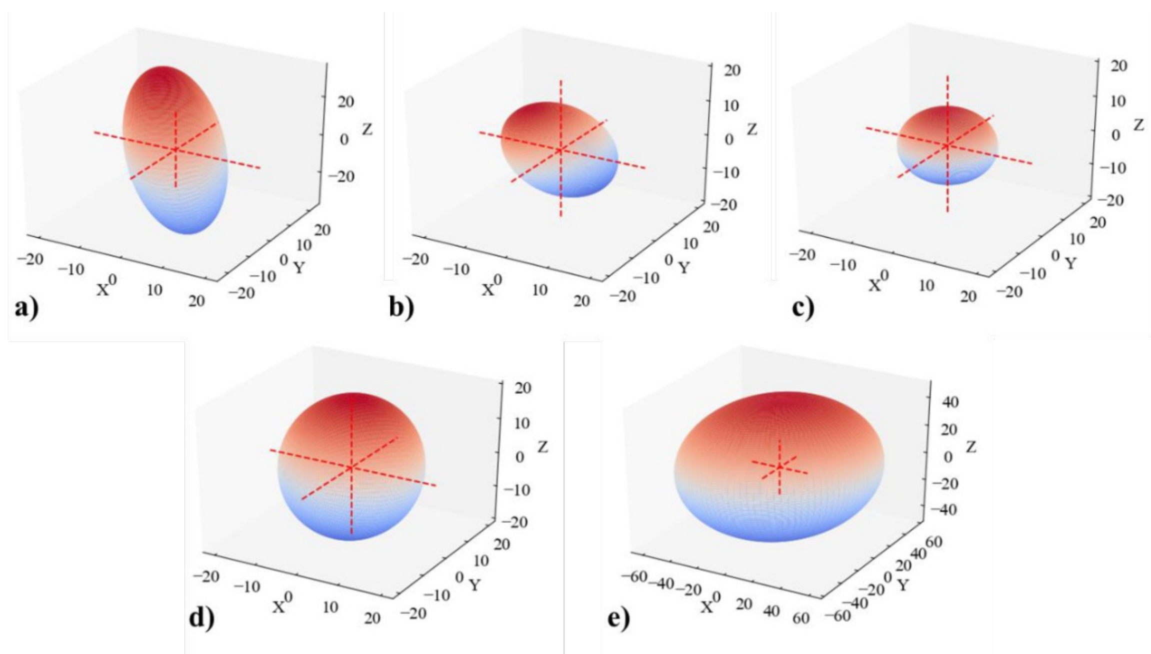

Fig.D1 Ellipsoids according to Tab.D1 of a) Sn-20 wt.% Bi b) Sn-30 wt.% Bi c) Sn-35 wt.% Bi d) Sn-47 wt.% Bi e) Sn-58 wt.% Bi

Die approbierte gedruckte Originalversion dieser Dissertation ist an der TU Wien Bibliothek verfügbar.
The approved original version of this doctoral thesis is available in print at TU Wien Bibliothek.
TU WIEN Bibliothek Your knowledge hub

2.6 Simulation and experimental characterization of microporosity during solidification in Sn-Bi alloys

Georg Siroky (georg.siroky@mcl.at) [1], Elke Kraker[1], Dietmar Kieslinger[2],, Ernst Kozeschnik[3], Werner Ecker[1]
[1] Materials Center Leoben Forschung GmbH (MCL), Roseggerstraße 12, 8700 Leoben, Austria
[2] ZKW Elektronik GmbH, Samuel Morse-Straße 18, 2700 Wiener Neustadt, Austria
[3] TU Wien, Institute of Materials Science and Technology, Getreidemarkt 9, 1060 Wien, Austria

Ready for submission to: Materials

Abstract

The formation of porosity during solidification is investigated in Sn-Bi alloys through experiments and simulations. Samples of varying composition with 20, 30, 47 and 58 wt.% Bi. are solidified in a copper mould and the pore fraction is measured through scanning electron microscopy. Finite element models are derived from X-ray micro computed tomography data and a material model is implemented to capture the effect of liquid pressure and volumetric swelling. The experimental assessment of solidification porosity shows a strong dependency on alloy composition. The round morphology of porosity found in the Sn-20 wt.% Bi alloy indicates its formation in the terminal stage of solidification. Micro-porosity formation is computed by means of Finite Element simulations and the results correlate with experimental findings. The analysis confirms volumetric shrinkage in the liquid state of confined eutectic domains as the mechanism for pore formation and determines the composition dependency of Sn-Bi alloys.

1. Introduction

Low melting solder materials have recently gained attention for the production of temperature-sensitive components [60]. The Sn-Bi systems is a promising candidate for future developments and has been investigated with respect to fracture [22,62], deformation [206], creep [207], interface strength [208], intermetallic compounds (IMC) [188], wetting [209,210], electromigration [211,212], aging [213,214] and surface tension [215]. Alloying elements, such as, In [216], Ni [195], Ag [216,217], Sb [218] and Zn [63,173] and their effect on mechanical and microstructural properties were investigated. Furthermore, the conditions during solidification and the resulting mechanical properties were studied [4,219–221].

Porosity in solder joints is a determining factor for mechanical reliability [222–225]. Zeng et al. [226] visualized the formation of microporosity during solidification of a Sn-based eutectic

Die approbierte gedruckte Originalversion dieser Dissertation ist an der TU Wien Bibliothek verfügbar.
The approved original version of this doctoral thesis is available in print at TU Wien Bibliothek.
TU WIEN Bibliothek Your knowledge hub

alloy with in-situ X-ray imaging. They observed pore formation at the last stage of solidification on the micro-scale, which is possibly caused by interdendritic shrinkage during eutectic solidification. Furthermore, it is discussed by Sona and Prabhu [227] that solidification cracks occur in solders due to tensile forces in the terminal stage of solidification. This is shown experimentally by Dong et al. [228] and Lu et al. [229] using a confining copper mould, which exerts tensile forces during cooling. They reported varying degrees of solidification cracks with respect to Ag content and trace amounts of Ni, P and Ce. Despite the reported studies, an investigation of microporosity in Sn-Bi alloys during confined solidification is missing. Furthermore, it was suggested by the authors that low melting solders can exhibit a healing effect, if operated in the semi-solid configuration and under appropriate external loads [178,230]. This additionally requires potential healing-solders to have a low tendency for micro-porosity formation during solidification.

The formation of porosity during solidification is a complex process, which arises from the microstructural morphology [231,232], alloy composition [233,234], geometric constraints [235] and deformation [236]. Several criteria were developed to calculate the hot cracking susceptibility of alloys [196,237,238]. According to Eskin et al. [196], these criteria can be classified as "stress-based", "strain-based" and "strain-rate based". Among the "stress-based" criterion, Lahaie and Bouchard [239] have formulated the fracture stress in the semi-solid configuration under consideration of deformation, liquid film thickness, liquid viscosity and solid volume fraction. This criterion is built on the assumption that the liquid film is the weakest element during solidification and transfers stresses limited by capillary forces. Sistaninia et al. [236] used a computational approach to obtain the local liquid pressure in the microstructure. There, a pore can nucleate and grow once the local pressure overcomes the surface energy to create a void. It is discussed in [196] that microporosity are most likely to form in the last stage of solidification with liquid fractions $< 10\%$, where the solid phase inhibits liquid feeding. Therefore, the liquid pressure before eutectic solidification is a feasible quantity to assess the formation of porosity.

The present work describes an experimental and numerical approach to quantify the compositional dependency of pore formation in Sn-Bi alloys. The formation of microporosity is assessed experimentally for Sn alloys with 20, 30, 47 and 58 wt.% Bi using a copper mould. Samples are analyzed through scanning electron microscopy (SEM), where area fractions and dimensions of porosity are measured. Representative unit cell Finite Element models are created on micro-scale (RVE-FE) from X-ray micro computed tomography (μ-XCT) data to

Die approbierte gedruckte Originalversion dieser Dissertation ist an der TU Wien Bibliothek verfügbar.
The approved original version of this doctoral thesis is available in print at TU Wien Bibliothek.
TU Bibliothek Your knowledge hub WIEN

compute the liquid pressure during solidification. A material model is implemented in the FE framework to include the volumetric expansion during the eutectic solidification and the hydrostatic behavior of the liquid film. Microporosity formation is quantified based on the liquid pressure and critical values for fracture stress and pore nucleation. A discussion of theoretical and experimental results is presented.

2. Experimental

Sample preparation

Sn-xBi alloys with x=20, 30, 47 and 58 wt.% Bi are prepared on a heating plate using a silicate glass under Argon atmosphere. Melts are homogenized for 60 min at 400 °C using a magnetic stirrer. Rods are cast by pipetting and pellets of 1 g are cut from the rods. Copper plates of 3 mm thickness are cut in 50 x 50 mm sheets and 2 mm deep groves are machined using a ø5 mm milling-cutter according to Fig. 57a. The copper moulds are ground and polished before ultra-sound cleaning in acetone. Then they are immersed in citrate acid to remove oxide layers and are air-dried prior to reflow soldering.

Solidification and microscopy

A mould with four grooves is reflowed per alloy under argon atmosphere. Pre-alloyed pellets with a total mass of 3 g are placed in the groove before reflow soldering. A thermo-couple measures the core temperature of the mould, where its position is indicated with a red dot in Fig. 57a. The temperature profile and cooling rate are given in Fig. 57b, where the cooling rate of about 1 K/s is maintained by air cooling and the peak temperature of 250 °C is held for 1 min. Moulds are cooled to room temperature and prepared for electron microscopy by mechanical grinding and polishing. The formation of solidification porosity is investigated using a FEI Philips XL30 SEM and the acquired images are analyzed using the open-source package ImageJ [159]. Porosity are segmented using a grey-value threshold and porosity area fractions as well as local thickness maps are evaluated.

Die approbierte gedruckte Originalversion dieser Dissertation ist an der TU Wien Bibliothek verfügbar.
The approved original version of this doctoral thesis is available in print at TU Wien Bibliothek.
TU WIEN Bibliothek Your knowledge hub

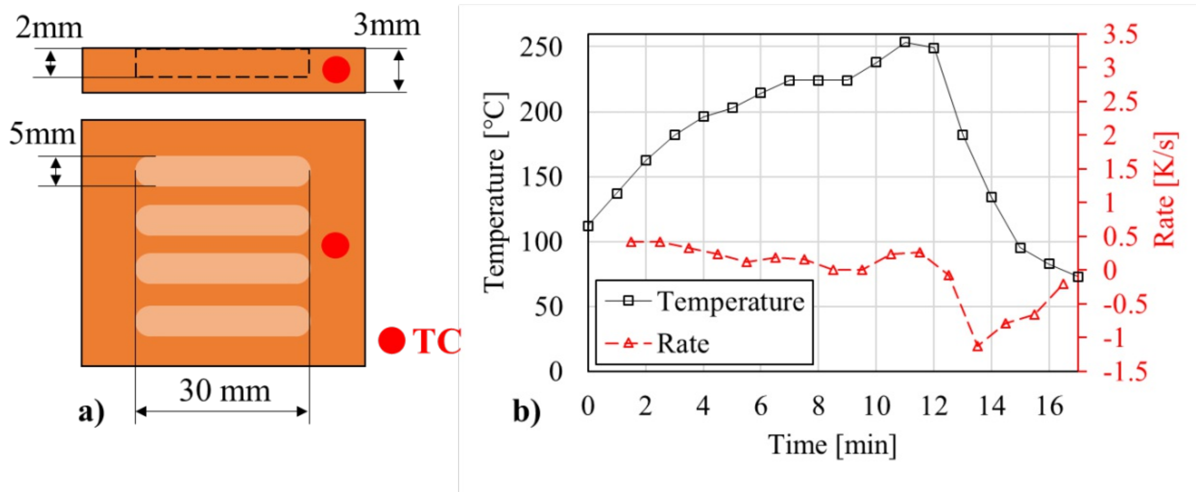

Fig. 57 Copper moulds for confined solidification and reflow process a) Geometry of copper mold with a red dot marking the thermo couple position b) Temperature and cooling rate during reflow process

Tensile test

Uniaxial tensile tests are performed to provide the required stress-strain data for RVE-FE models. The composition of primary- and eutectic phase are determined as Sn-2 wt.% Bi and Sn-53 wt.% Bi, respectively, from CALPHAD calculations using the COST531 database [158] and the software package MatCalc (www.matcalc.at). Cylindrical dog-bone shaped samples are cast in a silicon mold under air-cooling, where the mold temperature and cooling rates are similar to Fig. 57b. Tensile tests are performed on a uniaxial tensile test machine (Zwick Z050) at room temperature with a deformation velocity of 0.5 mm/min until fracture. Strains are measured on the sample surface at the narrowing, using a video-extensometer.

3. Modelling

Material model of eutectic phase

A material model is implemented in the FE framework that accounts for the liquid-solid transition in the eutectic phase. Above the solidus temperature of $T_{\mathrm{s}} = 138\ ^{\circ}\mathrm{C}$, the eutectic phase behaves like a hydrostatic, incompressible solid and undergoes volumetric swelling at $T = T_{\mathrm{s}}$. The model accounts for a temperature-dependent Poisson's ratio and introduces a viscous relaxation of stresses to obtain a hydrostatic stress state, free of shear stresses. Once the temperature reaches T_{s}, the Poisson's ratios reduces from the compressibility limit, ν_{limit}, to the solid state value, ν_0, during cooling

$$\nu(t_{\mathrm{t}}) = \nu_{\mathrm{limit}} - \frac{(\nu_{\mathrm{limit}} - \nu_0)}{t_{\mathrm{trans}}} \cdot t_{\mathrm{t}}, \tag{85}$$

with $\nu_{\mathrm{limit}} = 0.499$ and $\nu_0 = 0.3$. The transition interval is defined as $t_{\mathrm{trans}} = 0.4\ \mathrm{s}$ to allow rapid transition from liquid to solid values. Once the condition $T = T_{\mathrm{s}}$ is fulfilled, the transition

Die approbierte gedruckte Originalversion dieser Dissertation ist an der TU Wien Bibliothek verfügbar.
The approved original version of this doctoral thesis is available in print at TU Wien Bibliothek.
TU WIEN Bibliothek Your knowledge hub

time t_{t} runs in the limits $0 < t_{\mathrm{t}} < t_{\mathrm{trans}}$. The eutectic domain in liquid configuration can sustain hydrostatic loads, where the stress tensor is written as

$$\boldsymbol{\sigma} = \begin{bmatrix} -p_{\mathrm{hyd}} & 0 & 0 \\ 0 & -p_{\mathrm{hyd}} & 0 \\ 0 & 0 & -p_{\mathrm{hyd}} \end{bmatrix}. \tag{86}$$

with the hydrostatic pressure

$$p_{\mathrm{hyd}} = -tr(\boldsymbol{\sigma}). \tag{87}$$

Furthermore, the liquid is free of shear stresses in absence of viscous flow, which is indicated with the von Mises stress as

$$\sigma_{\mathrm{VM}} = \sqrt{\frac{1}{2}[(\sigma_{\mathrm{I}} - \sigma_{\mathrm{II}})^2 + (\sigma_{\mathrm{II}} - \sigma_{\mathrm{III}})^2 + (\sigma_{\mathrm{III}} - \sigma_{\mathrm{I}})^2]} = 0 \tag{88}$$

with σ_{I}, σ_{II} and σ_{III} as the three principal stresses. To satisfy the conditions in Eq. 86 and Eq. 88 a phenomenological relaxation of normal and shear stresses, similar to the Voigt model, is introduced. This allows normal stresses to converge towards the hydrostatic pressure according to

$$\sigma_{\mathrm{ii}} = \sigma_{\mathrm{ii}} - \left(p_{\mathrm{hyd}} + \sigma_{\mathrm{ii}}\right) \cdot (1 - e^{-\frac{\sigma_{\mathrm{VM}}}{\eta} \cdot t}), \tag{89}$$

with η the liquid viscosity of eutectic. Shear stresses follow a phenomenological relaxation with

$$\sigma_{\mathrm{ij}} = \sigma_{\mathrm{ij}} \cdot e^{-\frac{\sigma_{\mathrm{VM}}}{\eta} \cdot t}. \tag{90}$$

Hybrid elements (C3D8H) introduce the hydrostatic pressure as an additional degree of freedom in the model and allow to compute solutions close to the compressibility limit. The relaxation functions are implemented as an elastic predictor and viscous corrector scheme. Below T_{s}, the material behaves as an elasto-plastic solid with isotropic hardening and accounts for a temperature-dependent yield stress. Above T_{s}, the eutectic phase responds as a hydrostatic, shear stress-free medium. The numerical scheme is illustrated in Fig. 58, where, on the left branch, the standard elasto-plastic response is computed and, along the right branch, the incremental procedure to satisfy Eqs. 86 and 88 is shown. First, the Poisson's ratio increment is calculated according to Eq. 85. The elastic predictor provides the stresses for the next time step based on the strain increment and the isotropic Jacobian. The viscous corrector ensures hydrostatic and shear-free conditions of the liquid eutectic.

TU Bibliothek WIEN Your knowledge hub
Die approbierte gedruckte Originalversion dieser Dissertation ist an der TU Wien Bibliothek verfügbar.
The approved original version of this doctoral thesis is available in print at TU Wien Bibliothek.

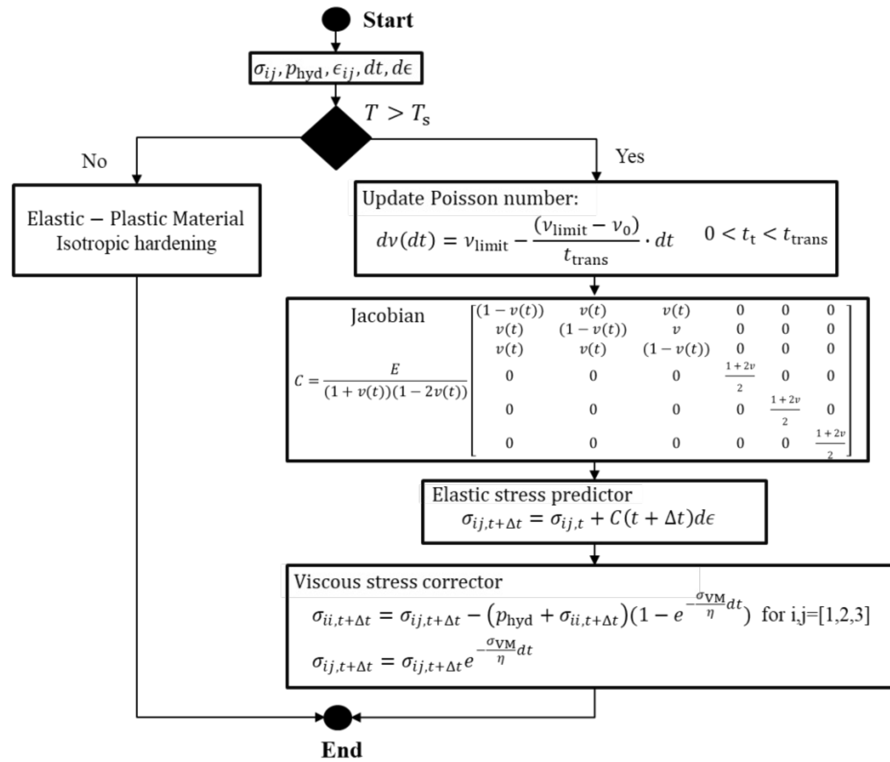

Fig. 58 Numerical scheme for stress update in solid and liquid configuration

The shrinkage during the eutectic solidification is implemented by means of a discontinuous thermal expansion model. In the solid configuration with $T < T_\mathrm{s}$, a linear thermal expansion law is used with

$$\epsilon_{\mathrm{th,s}} = \alpha_\mathrm{s} \cdot \Delta T, \tag{91}$$

with the solid thermal expansion coefficient, α_s. Above the solidus temperature, T_s, the thermal expansion in the liquid state is written as

$$\epsilon_{\mathrm{th,l}} = \alpha_\mathrm{l} \cdot \Delta T + \epsilon_{\mathrm{xc}}, \tag{92}$$

with the liquid thermal expansion coefficient, α_l, and excess strain term, ϵ_{xc}, which describes the discontinuous volumetric change at T_s. The excess strain term is applied instantly, once the condition $T \leq T_\mathrm{s}$ is fulfilled. The material model of the eutectic phase is implemented in Abaqus by means of a user-defined material (UMAT) and a user-defined expansion subroutine (UEXPAN).

RVE-FE model

RVE-FE models of Sn alloys with 20, 30, 47 and 58 wt.% Bi content are created from µ-XCT data. The 3D data acquisition and microstructural parameters are reported in accompanying work [240]. The models and their material assignment are illustrated in Fig. 59, where

Die approbierte gedruckte Originalversion dieser Dissertation ist an der TU Wien Bibliothek verfügbar.
The approved original version of this doctoral thesis is available in print at TU Wien Bibliothek.
TU Bibliothek Your knowledge hub WIEN

microstructures of alloys with 20, 30, 47 and 58 wt.% Bi are shown. The low eutectic content of the Sn-20 wt.% Bi alloy is shown in Fig. 59a with isolated domains of eutectic phase (green) and a large network of primary phase (grey). The Sn-30 wt.% Bi, Fig. 59b, shows an interpenetrating network of eutectic and primary phase. The Sn-47 wt.% Bi and Sn-58 wt.% Bi alloys in Fig. 59c and d have a low fraction of primary phase with dendritic structures. It is worth noting that higher voxel numbers would allow an improved discretization of the morphometric features. Yet, the upper boundary of 10^5 elements in this study limits the degree of accuracy.

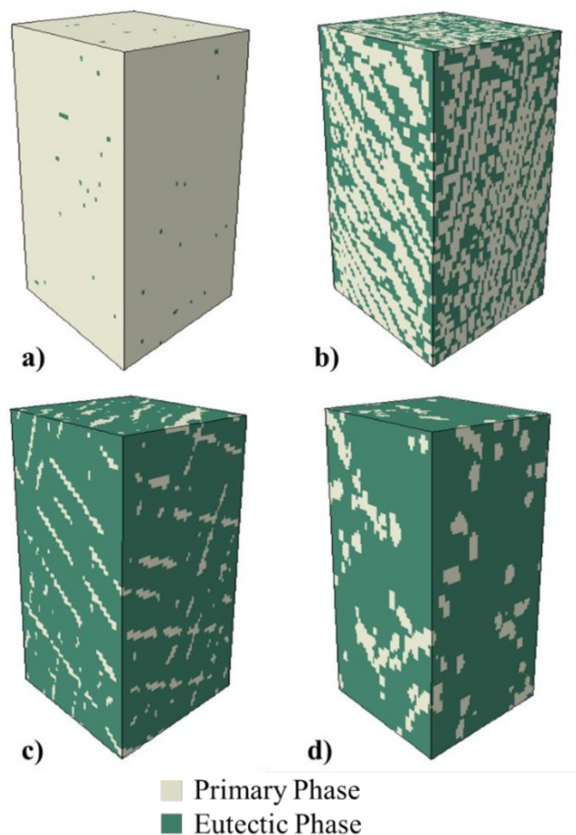

Fig. 59 Microstructures of Sn-Bi alloys for RVE-FE simulations a) Sn-20 wt.% Bi b) Sn-30 wt.% Bi c) Sn-47wt.% Bi d) Sn-58 wt.% Bi

The eutectic phase is assigned with the proposed material model and the primary phase is modelled as an elasto-plastic solid with isotropic hardening above and below T_S. Flow curves for the solid state are extracted from experimental stress-strain data to extract the yield stress and hardening parameters. Stress-strain curves in Fig. 60 are scaled by factors reported in Ref. [206] to include a temperature dependence. The initial yield stress is reduced by a factor of 3.5 at 138 °C compared with data at room temperature. In Fig. 60a, the stress-strain curves of the primary phase is given, which shows an initial yield stress of 32 MPa and a linear hardening regime until 42 MPa. The stress-strain behavior of the eutectic phase in Fig. 60b is modelled as

Die approbierte gedruckte Originalversion dieser Dissertation ist an der TU Wien Bibliothek verfügbar.
The approved original version of this doctoral thesis is available in print at TU Wien Bibliothek.
TU Bibliothek WIEN Your knowledge hub

an elastic - ideal plastic material with a yield stress at room temperature of 70 MPa, which is only active below T_s.

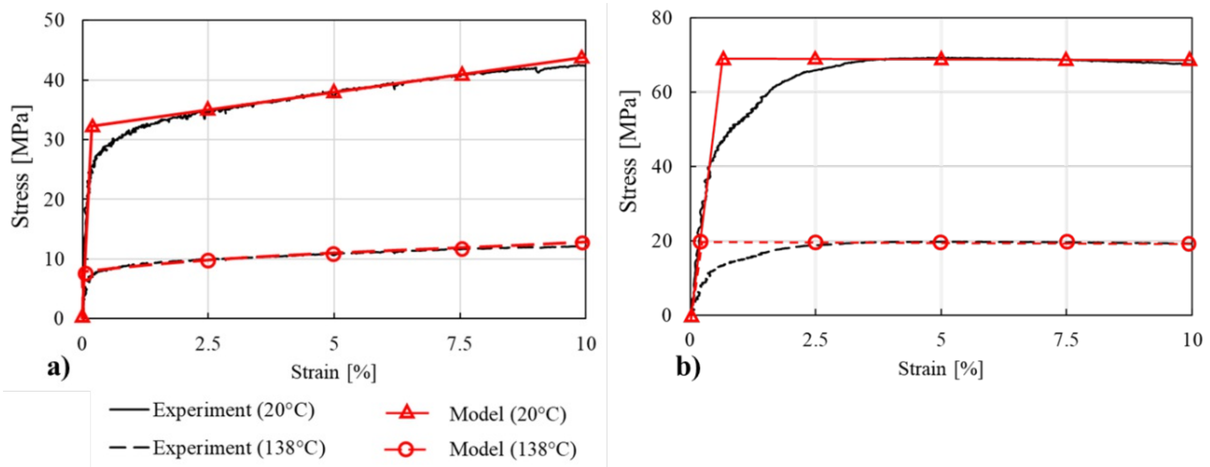

Fig. 60 Stress strain curves at room temperature and scaled curves at T=138°C a) Primary phase represented by Sn-2 wt.% Bi b) Eutectic phase represented by Sn-53 wt.% Bi

A volumetric expansion during the eutectic reaction was reported in literature for a Sn-58 wt.% Bi alloy [65]. The experimentally observed density over temperature is illustrated in Fig. 61, where the volume expansion during cooling is indicated by a discontinuous density at T=138 °C. The change below and above the melting point appears linear and the excess strain is determined from Fig. 61 as $\epsilon_{xc} = 0.2$ %, which will be used in the discontinuous expansion model. The assigned material parameters of primary and eutectic phase are provided in the appendix in Tab. A1.

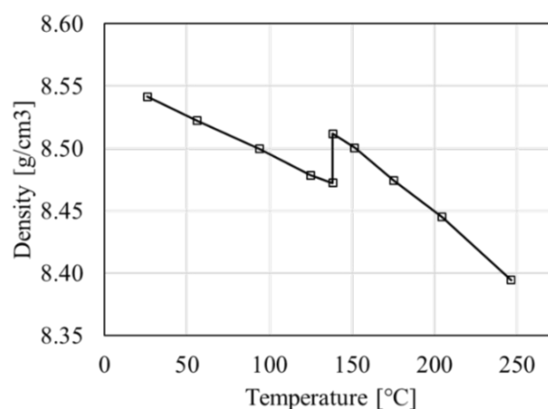

Fig. 61 Density over temperature of a Sn-57 wt.% Bi alloy, reproduced from Ref. [65]

Kinematic periodic boundary conditions are applied on the surface nodes, where the elongation in z-direction is suppressed to introduce a confinement similar to the experimental mould. The 8-node hybrid brick element is used to obtain convergence near the compressibility limit. The unit cells are cooled from $T_{start} = 148$ °C, where the eutectic is in the liquid configuration, to

Die approbierte gedruckte Originalversion dieser Dissertation ist an der TU Wien Bibliothek verfügbar.
The approved original version of this doctoral thesis is available in print at TU Wien Bibliothek.
TU Bibliothek WIEN Your knowledge hub

$T_{\mathrm{end}} = 20$ °C. The hydrostatic pressure in primary- and eutectic phase is evaluated. The elasto-plastic model neglects any rate dependencies, which might arise from material non-linearities, such as, visco-plastic material behavior or fluid flow.

The formation of microporosity is assessed by comparing the hydrostatic pressure in the eutectic phase with the expected strength of the liquid film. The fracture index (*FI*) indicates whether the hydrostatic pressure p_{hyd} exceeds the strength, σ_{crit}, and is written as

$$FI = \left\| \frac{p_{\mathrm{hyd}}}{\sigma_{\mathrm{crit}}} \right\|. \quad (93)$$

The *FI* is limited to cases of negative hydrostatic pressure, since porosity formation is not likely under compressive loads and small deformations. Porosity are expected to form for values $FI \geq 1$, where two criteria for σ_{crit} are evaluated based works of Sistaninia et al. [236] and Lahaie and Bouchard [239]. According to Sistaninia et al., porosity formation is possible if the liquid pressure falls below a critical value, given as

$$\sigma_{\mathrm{crit,1}} = p_{\mathrm{a}} - \frac{\gamma_{\mathrm{s}} \cos \Theta}{\lambda}, \quad (94)$$

where p_{a} is the atmospheric pressure, γ_{s} the surface energy, Θ the contact angle and λ the film thickness. Furthermore, Lahaie and Bouchard proposed the liquid film strength as

$$\sigma_{\mathrm{crit,2}} = \frac{4\,\eta}{3\,\lambda}\left(1 + \left(\frac{f_{\mathrm{s}}^{m}}{1-f_{\mathrm{s}}^{m}}\right)\epsilon\right)^{-1}, \quad (95)$$

with liquid viscosity η, liquid film thickness λ, volume fraction solid f_{s}, microstructural parameter m and macroscopic, uniaxial strain ϵ. The strength according to Eqs. 94 and 95 are calculated using values of λ and f_{s} from µ-XCT measurements. As described in Ref. [239], the parameter m=1/3 is chosen for equiaxed microstructures. Values for surface tension and contact angle are taken from literature, Ref. [215], and are provided in Tab. A1.

4. Results & Discussion

Experimental

In Fig. 62 to Fig. 65, representative SEM images of the microstructure after confined solidification are shown. The Sn-20 wt.% Bi alloy in Fig. 62 shows a high number of pores, which are aligned along the primary and eutectic interfaces indicated in Fig. 62a. There, the white dot-dash and the black dashed line show the main axis of the dendritic structures. The pores are preferably found along these main directions. A higher magnification in Fig. 62b shows a similar arrangement where pores are oriented in two direction, which are indicated by

Die approbierte gedruckte Originalversion dieser Dissertation ist an der TU Wien Bibliothek verfügbar.
The approved original version of this doctoral thesis is available in print at TU Wien Bibliothek.
TU WIEN Bibliothek Your knowledge hub

white dot-dashed and black dashed lines. The cross-section in Fig. 62c reveals details of microporosity, where rounded structures indicate their formation in the liquid state. The scallop shaped structures have similar dimensions as secondary dendrites.

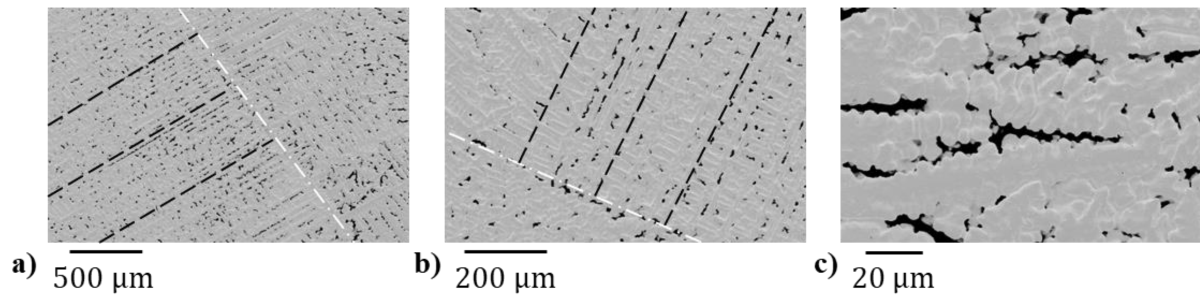

Fig. 62 SEM cross-sections of Sn-20 wt.% Bi samples after confined solidification a) overview of pores along primary dendrites (white dashed line) and secondary dendrites (black dashed line) b) close view of pores along dendritic structures c) pores at primary-eutectic interface

The SEM images of Sn-30 wt.% Bi alloy in Fig. 63 show a low fraction of microporosity. The overview in Fig. 63a shows dendritic structures with dark grey areas representing the dendritic primary phase. Furthermore, domains of varying dendrite orientation can be seen, which are separated by black dashed lines and indicate domains that have solidified at different times. The cross-section in Fig. 63b shows dark areas of primary phase, embedded in a network of white eutectic phase. A few pore containing areas are found in Fig. 63c, where scallop-like pores are indicated with black arrows. These reveal similar shapes to the ones observed in the Sn-20 wt.% Bi samples and possibly formed in the last stage of solidification, where the solid primary phase prevents volumetric shrinkage and liquid feeding. Yet, the overall fraction of porosity in the samples is low.

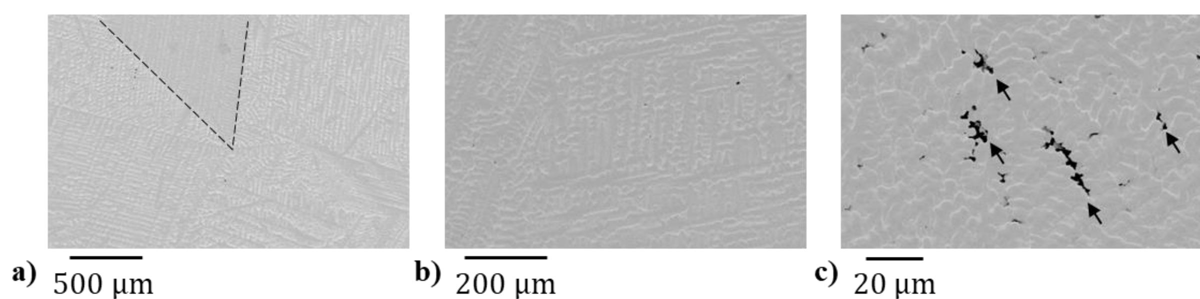

Fig. 63 SEM cross-sections of Sn-30 wt.% Bi samples after confined solidification a) overview of microstructure with domains of varying dendrite orientation b) eutectic microstructure with eutectic phase (white) primary phase (grey) c) pores at primary-eutectic interface

The Sn-47 wt.% Bi alloy illustrated in Fig. 64 shows no solidification cavities. A low number of spherical reflow pores indicated in Fig. 64a with black arrows are observed. The cross-section in Fig. 64b reveals a fine and homogenous microstructure. The eutectic domains can be

Die approbierte gedruckte Originalversion dieser Dissertation ist an der TU Wien Bibliothek verfügbar.
The approved original version of this doctoral thesis is available in print at TU Wien Bibliothek.
TU WIEN Bibliothek Your knowledge hub

seen in Fig. 64c in white and spherical pores induced by the reflow process are marked with black arrows.

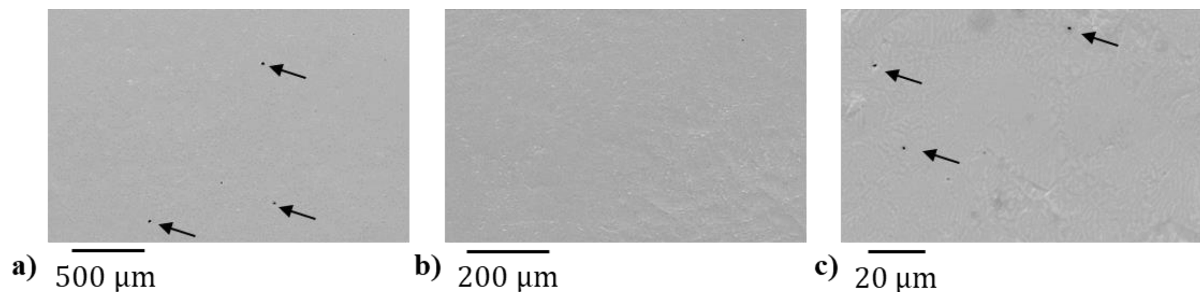

Fig. 64 SEM cross-sections of Sn-47 wt.% Bi samples after confined solidification a) overview of microstructure with reflow pores, indicated by arrows b) eutectic microstructure with eutectic phase (white) primary phase (grey) c) fine eutectic microstructure and spherical reflow pores, indicated by arrows

SEM images of the Sn-58 wt.% Bi alloy are illustrated in Fig. 65. The overview in Fig. 65a shows homogenous domains of low porosity that are interrupted by solidification boundaries, which are marked with black arrows. The cross-section in Fig. 65b reveals sharp-edged porosity at the boundaries. The edge-shape of these pores indicates that they have formed during cooling in the solid state, where the solidification boundary acts as the weakest link. The fine eutectic microstructure is shown in Fig. 65c, where white areas are Bi-rich domains. Despite the porosity found at boundary layers, the overall fraction of microporosity is low.

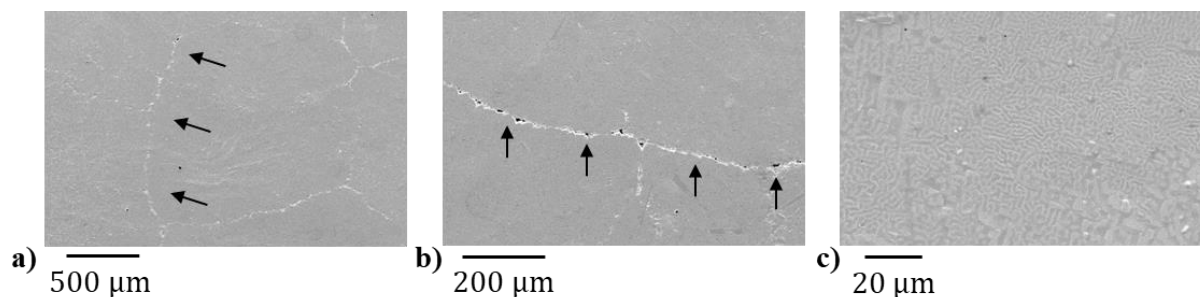

Fig. 65 SEM cross-sections of Sn-58 wt.% Bi samples after confined solidification a) overview of microstructure with solidifications boundaries, indicated by arrows b) sharp edged pores on solidification boundaries, indicated by arrows c) fine eutectic microstructure

Besides the representative cross-sections shown in Fig. 62 to Fig. 65, additional cross-sections are obtained for microporosity measurements. The area fraction and local thickness of microporosity over alloy composition is given in Fig. 66. The area fraction in Fig. 66a shows a high porosity content for the 20 wt.% Bi sample with 4.3% and a low porosity fraction of 0.16%, 0.02% and 0.04% for the 30, 47 and 58 wt.% Bi composition, respectively. The same trend can be seen in Fig. 66b with the local porosity thickness. The Sn-20 wt.% Bi shows the widest defects with 0.27 µm and a variation of about 0.08 µm. The remaining alloys have smaller porosity dimensions ranging from 0.002 µm to 0.01 µm.

Die approbierte gedruckte Originalversion dieser Dissertation ist an der TU Wien Bibliothek verfügbar.
The approved original version of this doctoral thesis is available in print at TU Wien Bibliothek.
TU WIEN Bibliothek Your knowledge hub

A comparison with measurements from µ-XCT data, reported in the accompanying work [240], shows that the porosity in the Sn-20 wt.% Bi alloy are about 10 times smaller than the eutectic domain thickness. This indicates that the liquid eutectic partially separates in the terminal stage of solidification and porosity form between primary structures. Their round shapes found in Fig. 62 and orientation along the dendritic structures also indicate porosity formation already in the liquid phase. These pores are likely to be created by a combined shielding effect of primary phase and a shrinkage of eutectic phase. The closing effect due to the volumetric expansion of eutectic at T_s as reported by [65] is apparently too small to fill porosity.

The few pores found in 30, 47 and 58 wt.% Bi samples have little influence on the pore area fraction in Fig. 66a and are most likely gas pores from the reflow process. The sharp edged pores found in Fig. 65 on solidification boundaries are possibly created during solid stage shrinkage and due to thermal misfit of neighboring domains. The solidification cracks along the longitudinal direction of the mould as reported by Dong et al. [228] and Lu et al. [229] for Sn-Ag-Cu alloys are not found in the Sn-Bi alloys. This suggests that pores are created due to local microstructural shrinkage rather than external tensile stresses induced by the confinement.

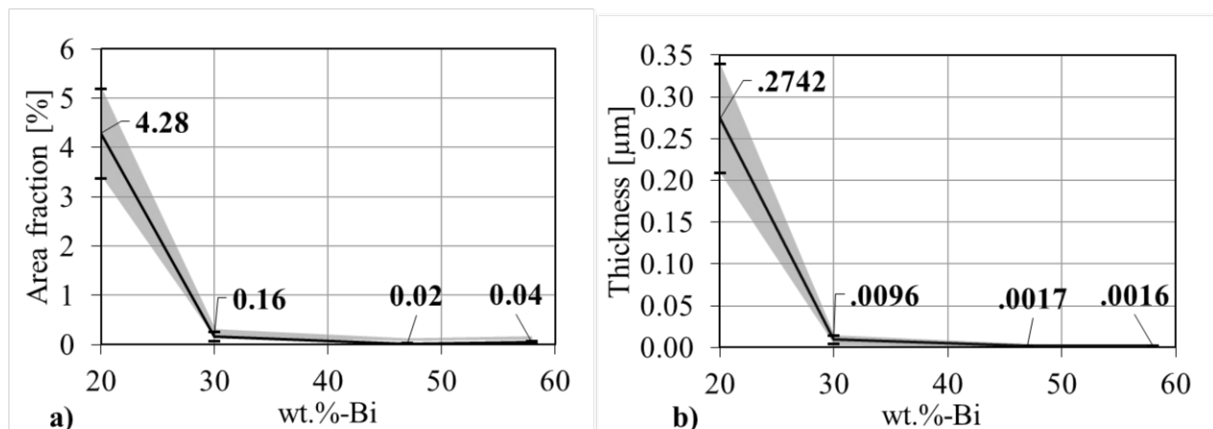

Fig. 66 Quantification of microporosity from SEM images a) Area fraction of porosity over alloy composition b) Local porosity thickness over alloy composition. Error bars indicate the standard deviation.

Simulation

The numerical assessment of microporosity by means of the fracture index (*FI*), requires knowledge of the estimated mechanical strength, $\sigma_{\mathrm{crit},i}$, and the hydrostatic pressure, p_{hyd}, in the liquid. In Fig. 67a and Fig. 67b, values of $\sigma_{\mathrm{crit},1}$ and $\sigma_{\mathrm{crit},2}$ are given, respectively, for alloys of 20, 30, 47 and 58 wt.% Bi. The strength according to Eq. 94 is given in Fig. 67a. The inverse dependence on λ in Eq. 94 predicts the lowest hydrostatic pressure in Sn-20 wt.% Bi of $p_{\mathrm{hyd}} = -0.9$ MPa and therefore the highest resistance against pore formation, compared with $p_{\mathrm{hyd}} =$

Die approbierte gedruckte Originalversion dieser Dissertation ist an der TU Wien Bibliothek verfügbar.
The approved original version of this doctoral thesis is available in print at TU Wien Bibliothek.
TU Wien Bibliothek Your knowledge hub

-0.01 MPa of the Sn-58 wt.% Bi alloy. Fig. 67b shows the liquid film strength according to Eq.95, where the influence of strain is shown as a parameter. Although strains of up to 1% are not expected during solidification, it defines a lower and upper bound for the estimated mechanical strength. The Sn-20 wt.% Bi alloy in Fig. 67b shows the largest variation with respect to strain. The liquid film strength reduces from -0.12 MPa at $\epsilon = 0.01$ % to -0.1 MPa at $\epsilon = 1.0$ %. Note, the tensile strength from Eq. 95 is modified with a negative sign in Fig. 67b for comparison with $\sigma_{\text{crit},1}$. Alloys with lower f_{s}, such as, Sn-47 wt.% Bi and Sn-58 wt.% Bi, show a negligible strain dependence. The inverse relation of Eq. 95 with respect to liquid film thickness leads to a reduction of mechanical strength for alloys with increasing Bi content, where the Sn-58 wt.% Bi alloy has only about 1/10 of the Sn-20 wt.% Bi alloys strength.

Despite similar trends of both criteria, lower hydrostatic pressure (higher pressure magnitude) for porosity formation are required according to Eq. 94 in Fig. 67a. The local liquid film thickness is assessed with μ-XCT data, where local thickness variations induce a deviation of strength from the mean value, indicated with error bars.

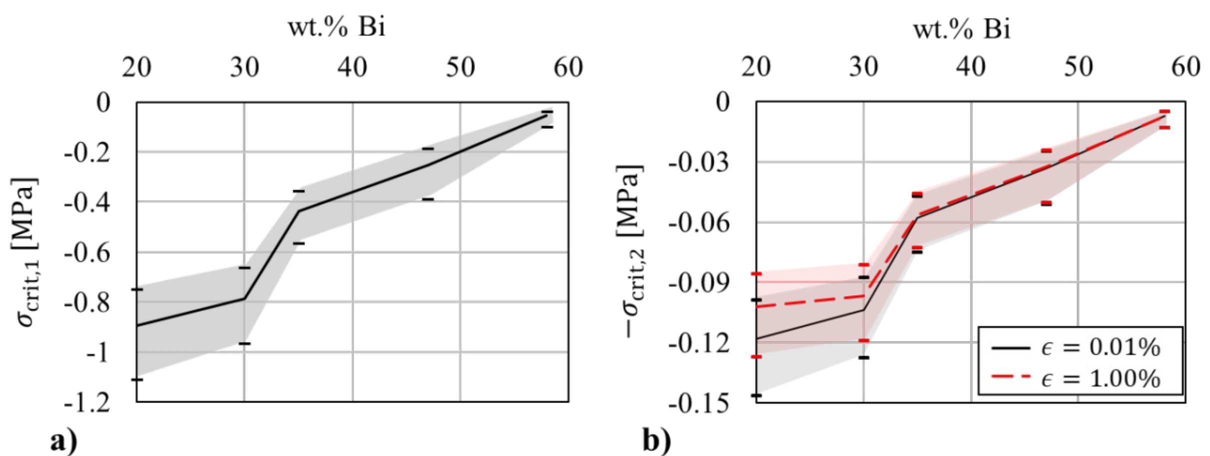

Fig. 67 Mechanical strength during solidification of Sn alloys with varying Bi content a) liquid film strength according to Sistaninia et al. [236] b) liquid film strength according to Lahaie and Bouchard [239]. Error bars indicate the standard deviation of liquid film strength due to local thickness variation.

RVE-FE simulation results are shown in Fig. 68 to Fig. 70, where Fig. 68 shows the evolution of p_{hyd} in the primary as well as eutectic phases and the total microstructure during cooling. The pressure evolution for Sn-20, 30, 47 and 58 wt.% Bi is shown in Fig. 68a to d, respectively. The eutectic phase in Fig. 69 is in the liquid configuration for temperatures $T > T_{\text{s}}$, where $T_{\text{s}} = 138$ °C is marked with a dashed line. The Sn-20 wt.% Bi alloy in Fig. 68a shows negative pressure in the liquid eutectic and solid primary phase at T_{s}. The volumetric expansion leads to positive pressure in the solid eutectic for $T < T_{\text{s}}$, which is reduced due to plastic deformation

Die approbierte gedruckte Originalversion dieser Dissertation ist an der TU Wien Bibliothek verfügbar.
The approved original version of this doctoral thesis is available in print at TU Wien Bibliothek.
TU WIEN Bibliothek Your knowledge hub

under continuous cooling. The total pressure in the Sn-20 wt.% Bi microstructure is determined by the negative pressure between -4 and -10 MPa of the solid phase. The pressure evolution among Sn-30, 47 and 58 wt.% Bi alloys is shown in Fig. 68b to d and reveals similar trends among alloys. There, a low pressure magnitude of around 0.1 to 0 MPa for $T > T_s$ is observed, which indicates a weak structural confinement of the solid primary phase. Compressive pressure is induced in the eutectic phase after solidification, which are reducing into the negative pressure during continuous cooling. The overall stresses in Fig. 68b to d are in the compressive domain after the eutectic reaction, which turn into tensile loads at about T= 115 °C.

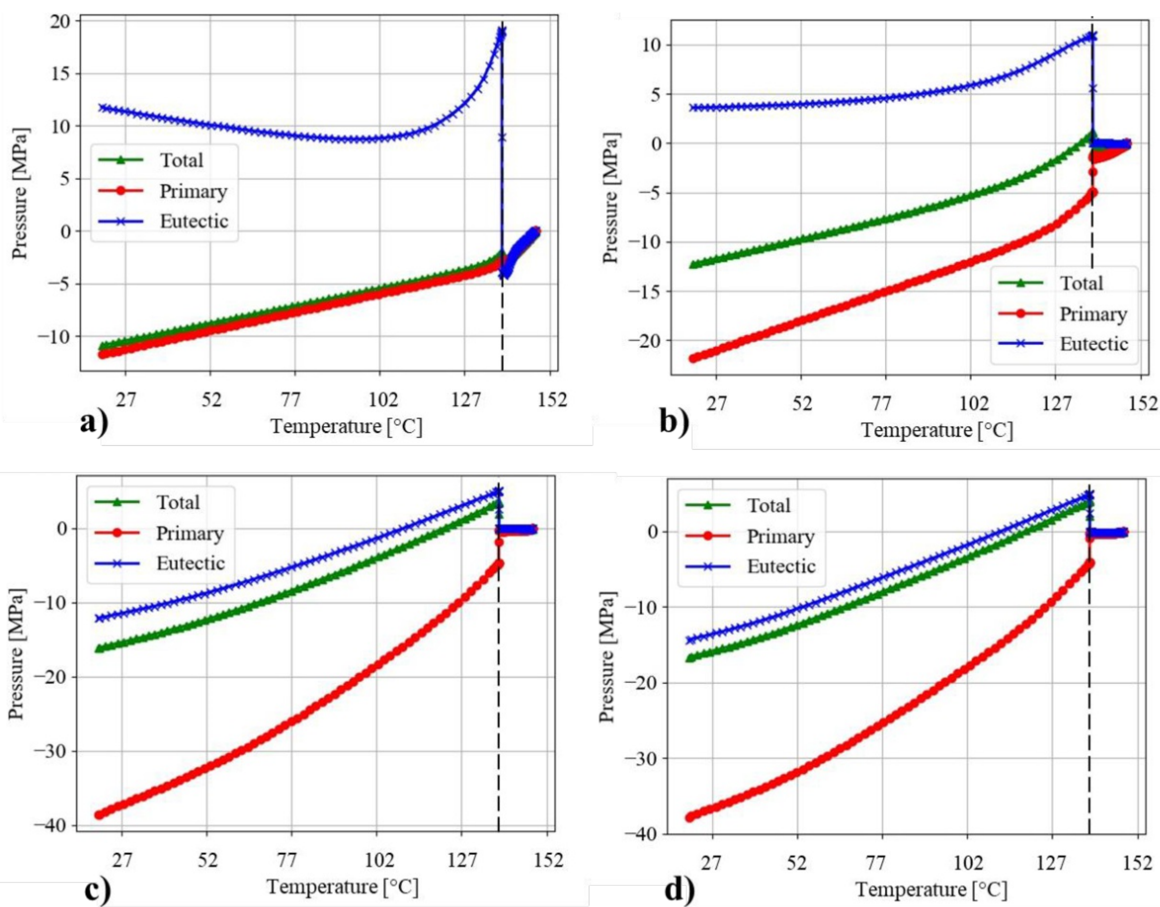

Fig. 68 Hydrostatic pressure during solidification and cooling a) Sn-20 wt.% Bi b) Sn-30 wt.% Bi c) Sn-47 wt.% Bi d) Sn-58 wt.% Bi

Fig. 69 shows the hydrostatic pressure near the eutectic solidification in detail, where point 1 refers to the increment before and point 2 to the increment after solidification. In Fig. 69a, the evolution of p_{hyd} is illustrated, where the liquid eutectic phase at point 1 shows hydrostatic pressure of -4.5 MPa and about -4 MPa in the solid primary phase. The strong mechanical interaction arises from the embedded areas of eutectic within the primary phase network. The misfit of thermal expansion coefficients, therefore, induces negative pressure among both

Die approbierte gedruckte Originalversion dieser Dissertation ist an der TU Wien Bibliothek verfügbar.
The approved original version of this doctoral thesis is available in print at TU Wien Bibliothek.
TU Wien Bibliothek Your knowledge hub

phases, which cannot reduce due the geometric confinement. After the volumetric expansion in Fig. 69a, the hydrostatic pressure in the solid eutectic rises to about 18 MPa at point 2, whereas the effect on the total microstructures is negligible due to the low volume fraction of eutectic. The 30, 47 and 58 wt.% Bi alloys reveal a similar evolution of p_{hyd} during solidification. These alloys show low pressure values close to 0 MPa for $T > T_{\mathrm{s}}$ in the liquid eutectic and solid primary phase. This indicates a weak interaction among both phases arising from the microstructural morphology. A similar microstructural morphology among the 30, 47 and 58 wt.% Bi was discussed in the accompanying work [240], which appears also in the mechanical response. The volumetric expansion causes similar compressive levels of p_{hyd} of 4.5MPa, which is illustrated in Fig. 69b to d at point 2. The total hydrostatic pressure is in the compressive domain with values of about $p_{\mathrm{hyd}} = 3.5$ MPa to $p_{\mathrm{hyd}} = 4.0$ MPa.

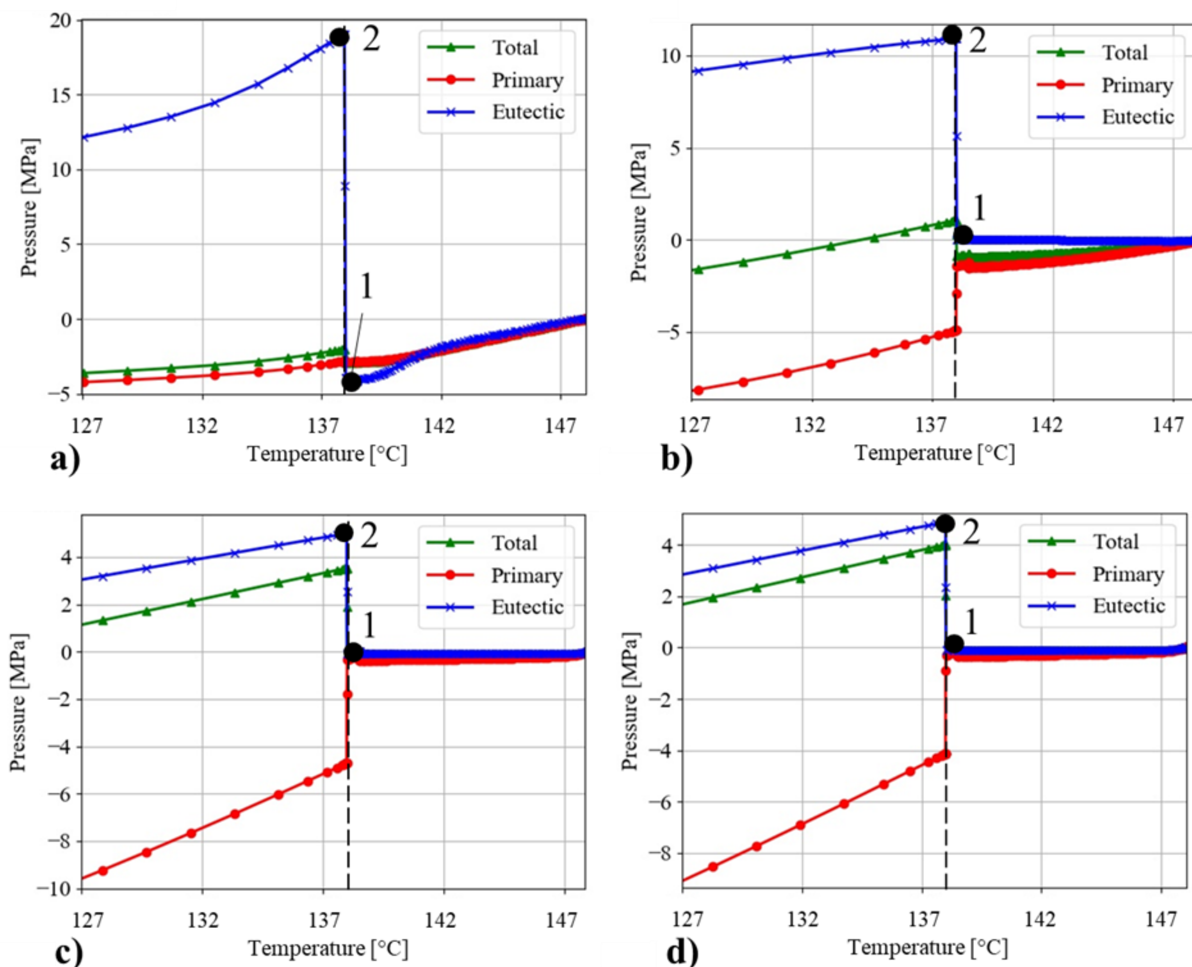

Fig. 69 Hydrostatic pressure before and after solidification of eutectic at T=138 °C a) Sn-20 wt.% Bi b) Sn-30 wt.% Bi c) Sn-47 wt.% Bi d) Sn-58 wt.% Bi

The pressure distribution in the liquid eutectic and solid primary phase is illustrated in Fig. 70, where the 20, 30, 47 and 58 wt.% Bi alloy are shown in Fig. 70a-d respectively. The eutectic

Die approbierte gedruckte Originalversion dieser Dissertation ist an der TU Wien Bibliothek verfügbar.
The approved original version of this doctoral thesis is available in print at TU Wien Bibliothek.
TU Bibliothek WIEN Your knowledge hub

pressure of Sn-20wt.%Bi alloy in Fig. 70a shows a peak at 5 MPa, which is close to the mean values of 4.5 MPa. A variation from -10 MPa to 2.5 MPa is observed due to stress concentrations in the local microstructure. Pressure of the solid primary phase in Fig. 70a shows a dominant peak at -2.5 MPa and ranges from -7.5 MPa to 0 MPa. The 30, 47 and 58 wt.% Bi alloy in Fig. 70b to d show similar pressure distributions, where the liquid eutectic pressures have a distinct peak around 0 MPa. The Sn-47 wt.% Bi alloy shows the largest variation with 0.1 MPa from its peak values. The comparison among the alloys in Fig. 70 suggests a similar mechanical response of the 30, 47 and 58 wt.% Bi alloys, which is in coherence with morphologic similarities reported in the accompanying work [240]. In the Sn-20 wt.% Bi alloy a variation of pressure distribution arises from the fragmented morphology with embedded domains of eutectic. The network of eutectic phase in the 30, 47 and 58 wt.% Bi alloys allows to accommodate the thermal shrinkage and leads to pressure variations in the liquid eutectic.

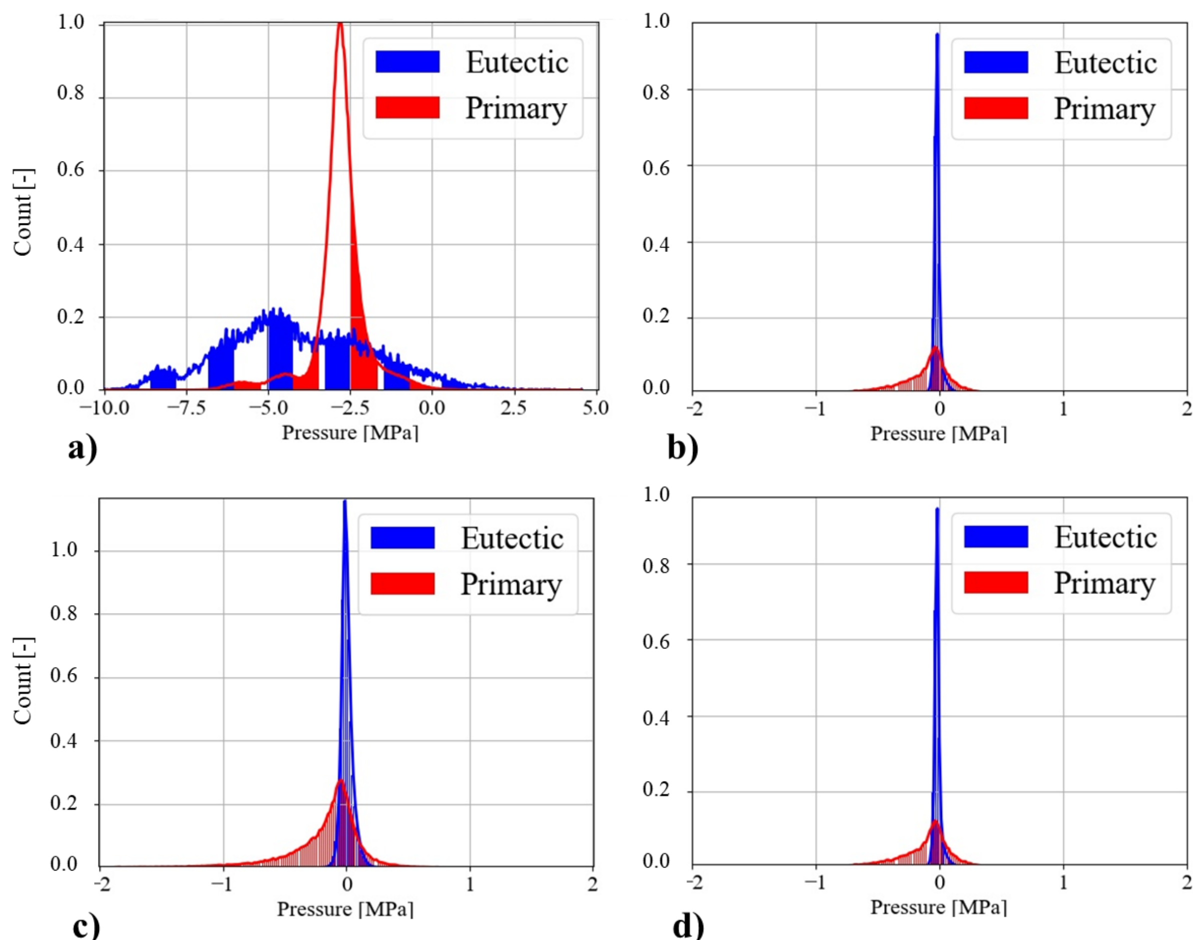

Fig. 70 Hydrostatic pressure distribution before solidification of eutectic at T=138 °C with eutectic phase in liquid configuration a) Sn-20 wt.% Bi b) Sn-30 wt.% Bi c) Sn-47 wt.% Bi d) Sn-58 wt.% Bi

Die approbierte gedruckte Originalversion dieser Dissertation ist an der TU Wien Bibliothek verfügbar.
The approved original version of this doctoral thesis is available in print at TU Wien Bibliothek.
TU Wien Bibliothek Your knowledge hub

As discussed in Ref. [196], where the liquid film before complete solidification is identified as the critical point for microporosity formation and hot cracking, negative pressure in the liquid eutectic phase shown in Fig. 69 and the round shape of porosity in Fig. 62 and Fig. 63 suggest porosity formation in the liquid state. Therefore, microporosity formation is evaluated based on eutectic liquid pressure. A fracture index $FI \geq 1$ indicates porosity formation due to negative liquid pressure, larger than the expected mechanical strength. Fig. 71a provides the *FI* with $\sigma_{\mathrm{crit},1}$ according to Sistaninia [236] and shows the same trend with regards to composition as Fig. 71b. The Sn-20 wt.% Bi alloy shows a $FI = 4.59$ that indicates high porosity formation, whereas alloys of 30, 47 and 58 wt.% Bi reveal no porosity due to $FI < 1$. The differences among the 30, 47 and 58 wt.% Bi alloys in Fig. 71a are negligible and, in all cases, considerably below 1. Fig. 71b shows the *FI* with $\sigma_{\mathrm{crit},2}$ proposed by Lahaie and Bouchard [239]. It shows high porosity formation with $FI = 40.7$ for the Sn-20 wt.% Bi alloy and values close to or below 1 for alloys with 30, 47 and 58 wt.% Bi. The mean *FI* of Sn-30 wt.% Bi and Sn-58 wt.% Bi are 0.91 and 0.72, respectively, where, under consideration of the local scatter, upper values of 1.08 and 1.03 are possible. The Sn-47 wt.% Bi reveals the lowest value of $FI = 0.17$, considerably lower than 1. Therefore, the local pressure in combination with $\sigma_{\mathrm{crit},2}$ shows high porosity formation for the Sn-20 wt.% Bi alloy and the lowest value for Sn-47 wt.% Bi. It is worth noting that Sistaninia et al. [236] proposed the critical pressure from a perspective of micro-mechanical modelling of semi-solid, which appears more applicable for the modelling approach in the presented work. The fracture stress of Lahaie and Bouchard [239] was proposed from a continuum perspective and applies to a macroscopic approach. Nevertheless, it is worth pointing out that both criteria provide the same trends in combination with RVE-FE simulations.

The experimental findings in Fig. 66 and the theoretical results in Fig. 71 correlate and provide a coherent picture of microporosity formation. The high fraction of porosity in Sn-20 wt.% Bi is induced by thermal misfit of embedded liquid in a network of primary phase and local negative pressure. Despite hydrostatic compression in the eutectic phase after solidification, negative pressure in the liquid causes porosity with dimensions smaller than the eutectic thickness. A low fraction of microporosity among 30, 47 and 58 wt.% Bi alloys is observed, which correlates with alloys of $FI < 1$ from RVE-FE simulations. A liquid pressure close to zero is possible before solidification due to accommodation of thermal shrinkage in these alloys. A network of liquid eutectic reduces the accumulation of misfit stresses and prevents the nucleation of porosity. The experimental assessment supports the theoretical findings to the

Die approbierte gedruckte Originalversion dieser Dissertation ist an der TU Wien Bibliothek verfügbar.
The approved original version of this doctoral thesis is available in print at TU Wien Bibliothek.
TU Bibliothek WIEN Your knowledge hub

extent that no considerable amount of porosity is found in 30, 47 and 58 wt.% Bi alloys. The results also reveal a correlation of morphology parameters and mechanical behavior. Similarities among 30, 47, and 58 wt.% Bi alloys are analyzed based on their morphology and it is concluded that these alloys contain a high fraction of "complex" shaped structures, which lead to a high surface to volume ratio. Results, reported in the accompanying work [240], indicate that similar morphology parameters cause similar mechanical behavior in the semi-solid state.

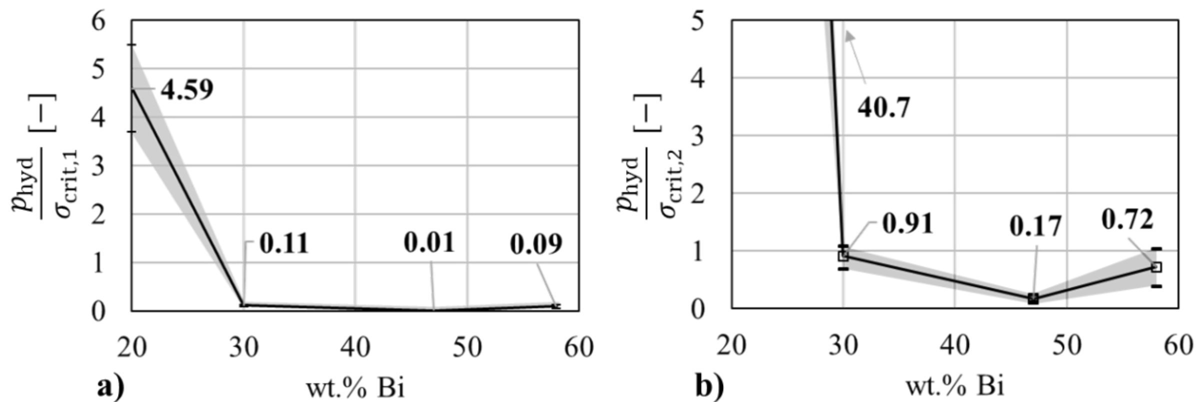

Fig. 71 Fracture index over alloy composition a) *FI* with $\sigma_{crit,1}$ according to Sistaninia et al. [236] b) *FI* with $\sigma_{crit,2}$ according to Lahaie and Bouchard [239]. Error bars indicate the standard deviation of *FI* due to local liquid film thickness variation.

5. Conclusion

The present work present an investigation of microporosity formation in Sn-Bi alloys with varying composition. Experimental and theoretical methods are used to quantify the extent and mechanisms behind porosity formation during solidification in alloys with 20, 30, 47 and 58 wt.% Bi. A copper mould for confined solidification reported in literature is used to assess the area fraction and dimensions of porosity through electron microscopy. Finite Element models are created from µ-XCT data to include material and microstructural effects in the solidification simulation. Pore formation is assessed using the fracture index, *FI*, which indicates whether the liquid pressure exceeds the expected mechanical strength of the liquid film. The experimental and theoretical results show a good correlation and several conclusion are made:

1. A compositional dependency of microporosity formation is observed in Sn-Bi alloys. The Sn-20 wt.% Bi reveals the highest fraction of porosity in experiments. SEM images indicate that these are formed during the terminal stage of solidification, which is supported by the round pore morphology.

Die approbierte gedruckte Originalversion dieser Dissertation ist an der TU Wien Bibliothek verfügbar.
The approved original version of this doctoral thesis is available in print at TU Wien Bibliothek.
TU WIEN Bibliothek Your knowledge hub

2. The proposed RVE-FE model framework allows to compute the liquid film pressure before solidification and takes microstructural effects and volumetric shrinkage into account. The Sn-20 wt.% Bi alloy reveals the lowest hydrostatic pressure in the liquid phase, which arises from the confined domains of eutectic in the solid primary phase.
3. Microporosity formation is assessed from simulations through the *FI*, which relates the hydrostatic pressure to the expected liquid film strength. Two strength criteria are included for comparison and reveal similar compositional dependency. Microporosity formation correlates among theoretical and experimental results.
4. It is observed that alloys of 30, 47 and 58 wt.% Bi have a similar mechanical response during solidification due to eutectic phase network. This allows to accommodate the thermal shrinkage and leads to reduced hydrostatic pressure. The low *FI* in these microstructures correlate with low porosity-fractions from experiments.

Appendix

A. Elastic and thermal material parameters

Tab. A1 Elastic and thermal material parameters of primary and eutectic phase

Description	Symbol	Value [Unit]
Young's modulus primary	E_P	50 [GPa]
Poisson number primary	ν_P	0.3 [-]
Thermal expansion coefficient primary	α_P	$22 \cdot 10^{-6} \left[\frac{1}{\mathrm{K}}\right]$
Young's modulus eutectic	E_E	40 [GPa]
Poisson number eutectic	ν_E	liquid: 0.499; solid: 0.3 [-[
Thermal expansion coefficient primary	α_E	$15 \cdot 10^{-6} \left[\frac{1}{\mathrm{K}}\right]$
Liquid surface tension	γ_S	$0.438 \left[\frac{\mathrm{N}}{\mathrm{m}}\right]$
Contact angle	Θ	23 [°]

Die approbierte gedruckte Originalversion dieser Dissertation ist an der TU Wien Bibliothek verfügbar.
The approved original version of this doctoral thesis is available in print at TU Wien Bibliothek.
TU WIEN Bibliothek Your knowledge hub

Literature

[1] K.-N. Chen, K.-N. Tu, Materials challenges in three-dimensional integrated circuits, MRS Bull. 40 (2015) 219–222. doi:10.1557/mrs.2015.8.

[2] Y. Tan, X. Li, X. Chen, Fatigue and dwell-fatigue behavior of nano-silver sintered lap-shear joint at elevated temperature, Microelectron. Reliab. 54 (2014) 648–653. doi:10.1016/j.microrel.2013.12.007.

[3] M. Yunus, K. Srihari, J.M. Pitarresi, A. Primavera, Effect of voids on the reliability of BGA/CSP solder joints, Microelectron. Reliab. 43 (2003) 2077–2086. doi:10.1016/S0026-2714(03)00124-0.

[4] T.O.R. Covre, E. Da, B.L. Silva, E. Spinelli, A. Garcia, Effects of Solidification Thermal Parameters on Microstructure and Mechanical Properties of Sn-Bi Solder Alloys, J. Electron. Mater. 46 (2017) 1754–1769. doi:10.1007/s11664-016-5225-7.

[5] K. Zeng, K.N. Tu, Six cases of reliability study of Pb-free solder joints in electronic packaging technology, Mater. Sci. Eng. R Reports. 38 (2002) 55–105. doi:10.1016/S0927-796X(02)00007-4.

[6] S. Choi, K.N. Subramanian, J.P. Lucas, T.R. Bieler, Thermomechanical fatigue behavior of Sn-Ag solder joints, J. Electron. Mater. 29 (2000) 1249–1257. doi:10.1007/s11664-000-0020-9.

[7] Y. Zuo, L. Ma, S. Liu, Y. Shu, F. Guo, Evolution of Microstructure Across Eutectic Sn-Bi Solder Joints Under Simultaneous Thermal Cycling and Current Stressing, J. Electron. Mater. 44 (2015) 597–603. doi:10.1007/s11664-013-2972-6.

[8] M. Mostofizadeh, J. Pippola, L. Frisk, Shear strength of eutectic Sn-Bi lead-free solders after corrosion testing and thermal aging, J. Electron. Mater. 43 (2014) 1335–1346. doi:10.1007/s11664-014-3085-6.

[9] S. Van der Zwaag, Self Healing Materials: An Alternative Approach to 20 Centuries of Materials Science, 2007. http://journals.sagepub.com/doi/10.1177/002203458506400512 01.

[10] U.G.K. Wegst, H. Bai, E. Saiz, A.P. Tomsia, R.O. Ritchie, Bioinspired structural materials, Nat. Mater. 14 (2015) 23–36. doi:10.1038/nmat4089.

[11] U. Lafont, H. Van Zeijl, S. Van Der Zwaag, Increasing the reliability of solid state lighting systems via self-healing approaches: A review, Microelectron. Reliab. 52 (2012) 71–89. doi:10.1016/j.microrel.2011.08.013.

[12] E. Wehrle, D.C. Tourolle né Betts, G.A. Kuhn, A.C. Scheuren, S. Hofmann, R. Müller, Evaluation of longitudinal time-lapsed in vivo micro-CT for monitoring fracture healing in mouse femur defect models, Sci. Rep. 9 (2019) 1–12. doi:10.1038/s41598-019-53822-x.

[13] C. Mattheck, WHY THEY GROW, HOW THEY GROW: THE MECHANICS OF TREES, Int. J. Urban For. 14 (1990) 1–17.

[14] M.Q. Zhang, M.Z. Rong, Self-Healing Polymers and Polymer Composites, in: Self-Healing Mater. Polym. Polym. Compos., 2011: pp. 29–71. doi:10.1002/9781118082720.

[15] E. Schlangen, C. Joseph, Self-Healing Processes in Concrete, in: Self-Healing Mater. Fundam. Des. Strateg. Appl., 2009: pp. 141–182. doi:10.1002/9783527625376.ch5.

Die approbierte gedruckte Originalversion dieser Dissertation ist an der TU Wien Bibliothek verfügbar.
The approved original version of this doctoral thesis is available in print at TU Wien Bibliothek.
TU WIEN Bibliothek Your knowledge hub

[16] W. Nakao, K. Takahashi, K. Ando, Self-Healing of Surface Cracks in Structural Ceramics, in: Adv. Nanomater., 2010: pp. 555–593. doi:10.1002/9783527628940.ch17.

[17] N. Shinya, Self-Healing of Metallic Materials: Self-Healing of Creep Cavity and Fatigue Cavity/Crack, in: Self-Healing Mater. Fundam. Des. Strateg. Appl., 2009: pp. 219–250. doi:10.1002/9783527625376.ch7.

[18] P. Sun, C. Andersson, X.C. Wei, L.Q. Cao, Z.N. Cheng, J.H. Liu, Low cycle fatigue testing and simulation of Sn-8Zn-3Bi and Sn-37Pb solder joints, Solder. Surf. Mt. Technol. 17 (2005) 38–45. doi:10.1108/09540910510630421.

[19] J. Keller, D. Baither, U. Wilke, G. Schmitz, Mechanical properties of Pb-free SnAg solder joints, Acta Mater. 59 (2011) 2731–2741. doi:10.1016/j.actamat.2011.01.012.

[20] H. Ma, J.C. Suhling, A review of mechanical properties of lead-free solders for electronic packaging, J. Mater. Sci. 44 (2009) 1141–1158. doi:10.1007/s10853-008-3125-9.

[21] A.A. El-Daly, A.E. Hammad, G.S. Al-Ganainy, M. Ragab, Influence of Zn addition on the microstructure, melt properties and creep behavior of low Ag-content Sn-Ag-Cu lead-free solders, Mater. Sci. Eng. A. 608 (2014) 130–138. doi:10.1016/j.msea.2014.04.070.

[22] D. Ye, C. Du, M. Wu, Z. Lai, Microstructure and mechanical properties of Sn–xBi solder alloy, J. Mater. Sci. Mater. Electron. 26 (2015) 3629–3637. doi:10.1007/s10854-015-2880-z.

[23] S.K. Ghosh, Self-Healing Materials: Fundamentals, Design Strategies, and Applications, in: Self-Healing Mater. Fundam. Des. Strateg. Appl., 2009: pp. 1–291. doi:10.1002/9783527625376.

[24] R.A. Schmidt, H. Wright, Introduction to Break-even Analysis, in: Financ. Asp. Mark., Macmillan Education UK, London, 1996: pp. 177–183. doi:10.1007/978-1-349-25020-2_22.

[25] A. Imanian, M. Modarres, A thermodynamic entropy-based damage assessment with applications to prognostics and health management, Struct. Heal. Monit. (2017) 1–15. doi:10.1177/1475921716689561.

[26] S. Danzi, V. Schnabel, J. Gabl, A. Sologubenko, H. Galinski, R. Spolenak, Rapid On-Chip Healing of Metal Thin Films, Adv. Mater. Technol. 1800468 (2019) 1–6. doi:10.1002/admt.201800468.

[27] T.T. Nguyen, D. Lee, J.B. Kwak, S. Park, Effect of glue on reliability of flip chip BGA packages under thermal cycling, Microelectron. Reliab. 50 (2010) 1000–1006. doi:10.1016/j.microrel.2010.04.003.

[28] P. Lall, P. Choudhary, S. Gupte, J. Hofmeister, Statistical Pattern Recognition and Built-in Reliability Test for Feature Extraction and Health Monitoring of Electronics Under Shock Loads, IEEE Trans. Components Packag. Technol. 32 (2009) 600–616. doi:10.1109/TCAPT.2009.2026426.

[29] G.Z. Voyiadjis, A. Shojaei, Continuum Damage-Healing Mechanics, in: Handb. Damage Mech., 2014: pp. 1515–1539.

[30] G.Z. Voyiadjis, A. Shojaei, G. Li, A thermodynamic consistent damage and healing model for self healing materials, Int. J. Plast. 27 (2011) 1025–1044. doi:10.1016/j.ijplas.2010.11.002.

Die approbierte gedruckte Originalversion dieser Dissertation ist an der TU Wien Bibliothek verfügbar.
The approved original version of this doctoral thesis is available in print at TU Wien Bibliothek.
TU WIEN Bibliothek Your knowledge hub

[31] C.C. Tasan, J.P.M. Hoefnagels, M.G.D. Geers, Identification of the continuum damage parameter: An experimental challenge in modeling damage evolution, Acta Mater. 60 (2012) 3581–3589. doi:10.1016/j.actamat.2012.03.017.

[32] J. Lemaitre, J.-L. Chaboche, Mechanics of Solid Materials, Cambridge University Press, 1994. http://amazon.com/o/ASIN/0521477581/.

[33] M. V Manuel, G.B. Olson, Biomimetic Self-Healing Metals, Proc. 1st Intl. Conf. Self-Healing Mater. (2007) 1–10. http://srg.northwestern.edu/Publications Library/Journals/2007_BiomimeticSelf-HealingMetals_Manuel_2008.pdf.

[34] A.S. Review, C. Oucif, L.M. Mauludin, Continuum Damage-Healing and Super Healing Mechanics in Brittle Materials, Appl. Sci. 8 (2018) 1–34. doi:10.3390/app8122350.

[35] E.J. Barbero, K.J. Ford, J.A. Mayugo, Modeling Self-Healing of Fiber-Reinforced Polymer-Matrix Composites with Distributed Damage, in: Self-Healing Mater. Fundam. Des. Strateg. Appl., 2009: pp. 267–283. doi:10.1002/9783527625376.ch9.

[36] S. Zhang, N. van Dijk, S. van der Zwaag, A Review of Self-healing Metals: Fundamentals, Design Principles and Performance, Acta Metall. Sin. (English Lett. 33 (2020) 1167–1179. doi:10.1007/s40195-020-01102-3.

[37] S. Zhang, N. van Dijk, S. van der Zwaag, A Review of Self-healing Metals: Fundamentals, Design Principles and Performance, Acta Metall. Sin. (English Lett. (2020). doi:10.1007/s40195-020-01102-3.

[38] G.Z. Voyiadjis, A. Shojaei, G. Li, P.I. Kattan, A theory of anisotropic healing and damage mechanics of materials, Proc. R. Soc. A Math. Phys. Eng. Sci. 468 (2012) 163–183. doi:10.1098/rspa.2011.0326.

[39] B. Grabowski, C.C. Tasan, Self-Healing Metals, in: Self-Healing Mater. Adv. Polym. Sci., 2016: pp. 387–407. doi:https://doi.org/10.1007/12_2015_337.

[40] H. Fang, C.D. Versteylen, S. Zhang, Y. Yang, P. Cloetens, D. Ngan-Tillard, E. Brück, S. van der Zwaag, N.H. van Dijk, Autonomous filling of creep cavities in Fe-Au alloys studied by synchrotron X-ray nano-tomography, Acta Mater. 121 (2016) 352–364. doi:10.1016/j.actamat.2016.09.023.

[41] H. Fang, N. Szymanski, C.D. Versteylen, P. Cloetens, C. Kwakernaak, W.G. Sloof, F.D. Tichelaar, S. Balachandran, M. Herbig, E. Brück, S. van der Zwaag, N.H. van Dijk, Self healing of creep damage in iron-based alloys by supersaturated tungsten, Acta Mater. 166 (2019) 531–542. doi:10.1016/j.actamat.2019.01.014.

[42] C.R. Fisher, H.B. Henderson, M.S. Kesler, P. Zhu, G.E. Bean, M.C. Wright, J.A. Newman, L.C. Brinson, O. Figueroa, M. V Manuel, Repairing large cracks and reversing fatigue damage in structural metals, Appl. Mater. Today. 13 (2018) 64–68. doi:10.1016/j.apmt.2018.07.003.

[43] P. Zhu, Z. Cui, M.S. Kesler, J.A. Newman, M. V. Manuel, M.C. Wright, L.C. Brinson, Characterization and modeling of three-dimensional self-healing shape memory alloy-reinforced metal-matrix composites, Mech. Mater. 103 (2016) 1–10. doi:10.1016/j.mechmat.2016.09.005.

[44] J. Martinez Lucci, R.S. Amano, P. Rohatgi, B. Schultz, Experiment and Computational Analysis of Self-Healing in an Aluminum Alloy, (2008) 1759–1768. doi:10.1115/IMECE2008-68304.

Die approbierte gedruckte Originalversion dieser Dissertation ist an der TU Wien Bibliothek verfügbar.
The approved original version of this doctoral thesis is available in print at TU Wien Bibliothek.
TU WIEN Bibliothek Your knowledge hub

[45] H. Song, Z.J. Wang, Microcrack healing and local recrystallization in pre-deformed sheet by high density electropulsing, Mater. Sci. Eng. A. 490 (2008) 1–6. doi:10.1016/j.msea.2007.12.037.

[46] H. Song, Z.J. Wang, X.D. He, J. Duan, Self-healing of damage inside metals triggered by electropulsing stimuli, Sci. Rep. 7 (2017) 1–11. doi:10.1038/s41598-017-06635-9.

[47] Z. Hsain, J.H. Pikul, Low-Energy Room-Temperature Healing of Cellular Metals, Adv. Funct. Mater. 29 (2019) 1–7. doi:10.1002/adfm.201905631.

[48] C. Basaran, S. Nie, J. Gomez, E. Gunel, S. Li, M. Lin, H. Tang, C. Yan, W. Yao, H. Ye, Thermodynamics Theory for Damage Evolution in Solids, in: Handb. Damage Mech., 2014: pp. 721–762. doi:https://doi.org/10.1007/978-1-4614-5589-9_31.

[49] D. Mitlin, C.H. Raeder, R.W. Messler, Solid solution creep behavior of Sn-xBi alloys, Metall. Mater. Trans. A Phys. Metall. Mater. Sci. 30 (1999) 115–122. doi:10.1007/s11661-999-0199-1.

[50] J.F. Li, S.H. Mannan, M.P. Clode, D.C. Whalley, D.A. Hutt, Interfacial reactions between molten Sn-Bi-X solders and Cu substrates for liquid solder interconnects, Acta Mater. 54 (2006) 2907–2922. doi:10.1016/j.actamat.2006.02.030.

[51] L. Xu, J.H.L. Pang, F. Che, Impact of thermal cycling on Sn-Ag-Cu solder joints and board-level drop reliability, J. Electron. Mater. 37 (2008) 880–886. doi:10.1007/s11664-008-0400-0.

[52] Y. Goh, A.S.M.A. Haseeb, H.L. Liew, M.F.M. Sabri, Deformation and fracture behaviour of electroplated Sn–Bi/Cu solder joints, J. Mater. Sci. 50 (2015) 4258–4269. doi:10.1007/s10853-015-8978-0.

[53] C. Chen, L. Zhang, J. Zhao, L. Cao, J.K. Shang, Gap size effects on the shear strength of Sn/Cu and Sn/FeNi solder joints, J. Electron. Mater. 41 (2012) 2487–2494. doi:10.1007/s11664-012-2156-9.

[54] M.A. Matin, E.W.C. Coenen, W.P. Vellinga, M.G.D. Geers, Correlation between thermal fatigue and thermal anisotropy in a Pb-free solder alloy, Scr. Mater. 53 (2005) 927–932. doi:10.1016/j.scriptamat.2005.06.034.

[55] M. Erinc, P.J.G. Schreurs, M.G.D. Geers, Intergranular thermal fatigue damage evolution in SnAgCu lead-free solder, Mech. Mater. 40 (2008) 780–791. doi:10.1016/j.mechmat.2008.04.005.

[56] C. Chen, H.M. Tong, K.N. Tu, Electromigration and Thermomigration in Pb-Free Flip-Chip Solder Joints, (2010). doi:10.1146/annurev.matsci.38.060407.130253.

[57] Y.W. Chang, Y. Cheng, F. Xu, L. Helfen, T. Tian, M. Di Michiel, C. Chen, K.N. Tu, T. Baumbach, Study of electromigration-induced formation of discrete voids in flip-chip solder joints by in-situ 3D laminography observation and finite-element modeling, Acta Mater. 117 (2016) 100–110. doi:10.1016/j.actamat.2016.06.059.

[58] L.T. Chen, C.M. Chen, Electromigration study in the eutectic SnBi solder joint on the Ni/Au metallization, J. Mater. Res. 21 (2006) 962–969. doi:10.1557/jmr.2006.0113.

[59] W.R. Osório, L.R. Garcia, L.C. Peixoto, A. Garcia, Electrochemical behavior of a lead-free SnAg solder alloy affected by the microstructure array, Mater. Des. 32 (2011) 4763–4772. doi:10.1016/j.matdes.2011.06.032.

TU WIEN Bibliothek Your knowledge hub
Die approbierte gedruckte Originalversion dieser Dissertation ist an der TU Wien Bibliothek verfügbar.
The approved original version of this doctoral thesis is available in print at TU Wien Bibliothek.

[60] F. Wang, H. Chen, Y. Huang, L. Liu, Z. Zhang, Recent progress on the development of Sn–Bi based low-temperature Pb-free solders, J. Mater. Sci. Mater. Electron. 30 (2019) 3222–3243. doi:10.1007/s10854-019-00701-w.

[61] Q.K. Zhang, F.Q. Hu, Z.L. Song, Z.F. Zhang, Viscoplastic creep and microstructure evolution of Sn-based lead-free solders at low strain, Mater. Sci. Eng. A. 701 (2017) 187–195. doi:10.1016/j.msea.2017.06.083.

[62] Z. Lai, D. Ye, Microstructure and fracture behavior of non eutectic Sn–Bi solder alloys, J. Mater. Sci. Mater. Electron. 27 (2016) 3182–3192. doi:10.1007/s10854-015-4143-4.

[63] W.R. Osório, L.C. Peixoto, L.R. Garcia, N. Mangelinck-Noël, A. Garcia, Microstructure and mechanical properties of Sn-Bi, Sn-Ag and Sn-Zn lead-free solder alloys, J. Alloys Compd. 572 (2013) 97–106. doi:10.1016/j.jallcom.2013.03.234.

[64] Z. Moser, W. Gasior, J. Pstrus, Surface tension measurements of the Bi-Sn and Sn-Bi-Ag liquid alloys, J. Electron. Mater. 30 (2001) 1104–1111. doi:10.1007/s11664-001-0136-6.

[65] L. Wang, A. Xian, Density Measurement of Sn-40Pb , Sn-57Bi , and Sn-9Zn by Indirect Archimedean Method, J. Electron. Mater. 34 (2005) 1414–1419. doi:https://doi.org/10.1007/s11664-005-0199-x.

[66] N. Chawla, Y.-L. Shen, X. Deng, E.S. Ege, An evaluation of the lap-shear test for Sn-rich solder/Cu couples: Experiments and simulation, J. Electron. Mater. 33 (2004) 1589–1595. doi:10.1007/s11664-004-0102-1.

[67] P. Zimprich, A. Betzwar-Kotas, G. Khatibi, B. Weiss, H. Ipser, Size effects in small scaled lead-free solder joints, J. Mater. Sci. Mater. Electron. 19 (2008) 383–388. doi:10.1007/s10854-007-9349-7.

[68] A. Lövberg, P. Tegehall, The Stress State of BGA Solder Joints Influenced by the Grain Orientations of Neighboring Joints, in: 2018 IEEE 68th Electron. Components Technol. Conf., IEEE, 2018: pp. 882–889. doi:10.1109/ECTC.2018.00136.

[69] Y.L. Shen, N. Chawla, E.S. Ege, X. Deng, Deformation analysis of lap-shear testing of solder joints, Acta Mater. 53 (2005) 2633–2642. doi:10.1016/j.actamat.2005.02.024.

[70] K. Aluru, F.L. Wen, Y.L. Shen, Direct simulation of fatigue failure in solder joints during cyclic shear, Mater. Des. 32 (2011) 1940–1947. doi:10.1016/j.matdes.2010.11.072.

[71] E. Maire, P.J. Withers, Quantitative X-ray tomography, Int. Mater. Rev. 59 (2014) 1–43. doi:10.1179/1743280413Y.0000000023.

[72] E. Maire, C. Bordreuil, L. Babout, J.C. Boyer, Damage initiation and growth in metals. Comparison between modelling and tomography experiments, J. Mech. Phys. Solids. 53 (2005) 2411–2434. doi:10.1016/j.jmps.2005.06.005.

[73] M.L. Bouxsein, S.K. Boyd, B.A. Christiansen, R.E. Guldberg, K.J. Jepsen, R. Müller, Guidelines for assessment of bone microstructure in rodents using micro-computed tomography, J. Bone Miner. Res. 25 (2010) 1468–1486. doi:10.1002/jbmr.141.

[74] P. Hermanek, J.S. Rathore, V. Aloisi, S. Carmignato, Principles of X-ray Computed Tomography BT - Industrial X-Ray Computed Tomography, in: S. Carmignato, W. Dewulf, R. Leach (Eds.), Springer International Publishing, Cham, 2018: pp. 25–67. doi:10.1007/978-3-319-59573-3_2.

TU WIEN Bibliothek Your knowledge hub
Die approbierte gedruckte Originalversion dieser Dissertation ist an der TU Wien Bibliothek verfügbar.
The approved original version of this doctoral thesis is available in print at TU Wien Bibliothek.

[75] J.H. Hubbell, S.M. Seltzer, NIST Standard Reference Database 126, X-Ray Mass Attenuation Coefficients. (2004). doi:https://dx.doi.org/10.18434/T4D01F.

[76] L.F.M. da Silva, R.J.C. Carbas, G.W. Critchlow, M.A.V. Figueiredo, K. Brown, Effect of material, geometry, surface treatment and environment on the shear strength of single lap joints, Int. J. Adhes. Adhes. 29 (2009) 621–632. doi:10.1016/j.ijadhadh.2009.02.012.

[77] M.Y. Tsai, D.W. Oplinger, J. Morton, Improved theoretical solutions for adhesive lap joints, Int. J. Solids Struct. 35 (1998) 1163–1185. doi:10.1016/S0020-7683(97)00097-8.

[78] M.S. Kafkalidis, M.D. Thouless, The effects of geometry and material properties on the fracture of single lap-shear joints, Int. J. Solids Struct. 39 (2002) 4367–4383. doi:10.1016/S0020-7683(02)00344-X.

[79] L.F.M. da Silva, T.N.S.S. Rodrigues, M.A. V Figueiredo, M.F.S.F. de Moura, J.A.G. Chousal, Effect of adhesive type and thickness on the lap shear strength, J. Adhes. 82 (2006) 1091–1115. doi:10.1080/00218460600948511.

[80] Q.K. Zhang, Z.F. Zhang, In situ observations on shear and creep-fatigue fracture behaviors of SnBi/Cu solder joints, Mater. Sci. Eng. A. 528 (2011) 2686–2693. doi:10.1016/j.msea.2010.12.041.

[81] L.M. Yang, Q.K. Zhang, Z.F. Zhang, Effects of solder dimension on the interfacial shear strength and fracture behaviors of Cu/Sn-3Cu/Cu joints, Scr. Mater. 67 (2012) 637–640. doi:10.1016/j.scriptamat.2012.07.024.

[82] S.J. Subramanian, V.K.R. Penmetcha, Strain Evolution during Lap Shear Testing of SnCu Solder, Appl. Mech. Mater. 70 (2011) 303–308. doi:10.4028/www.scientific.net/AMM.70.303.

[83] X. Xiao, P.H. Foss, J.A. Schroeder, Stiffness prediction of the double lap shear joint. Part 2: Finite element modeling, Int. J. Adhes. Adhes. 24 (2004) 239–246. doi:10.1016/j.ijadhadh.2003.10.004.

[84] J.Y. Cognard, R. Créachcadec, J. Maurice, Numerical analysis of the stress distribution in single-lap shear tests under elastic assumption - Application to the optimisation of the mechanical behaviour, Int. J. Adhes. Adhes. 31 (2011) 715–724. doi:10.1016/j.ijadhadh.2011.07.001.

[85] S.A. Meguid, Y. Sun, On the tensile and shear strength of nano-reinforced composite interfaces, Mater. Des. 25 (2004) 289–296. doi:10.1016/j.matdes.2003.10.018.

[86] J. Magnien, G. Khatibi, M. Lederer, H. Ipser, Materials Science & Engineering A Investigation of interfacial behavior in miniaturized solder interconnects, Mater. Sci. Eng. A. 673 (2016) 541–550. doi:10.1016/j.msea.2016.07.060.

[87] Q.K. Zhang, Z.F. Zhang, In situ observations on shear and creep-fatigue fracture behaviors of SnBi/Cu solder joints, Mater. Sci. Eng. A. 528 (2011) 2686–2693. doi:10.1016/j.msea.2010.12.041.

[88] Q.K. Zhang, Z.F. Zhang, Thermal fatigue behaviors of Sn-4Ag/Cu solder joints at low strain amplitude, Mater. Sci. Eng. A. 580 (2013) 374–384. doi:10.1016/j.msea.2013.05.061.

[89] K. Aluru, F.-L. Wen, Y.-L. Shen, Modeling of Solder Fatigue Failure due to Ductile Damage, J. Mech. 26 (2010) N23–N27. doi:10.1017/S1727719100004627.

TU WIEN Bibliothek Your knowledge hub
Die approbierte gedruckte Originalversion dieser Dissertation ist an der TU Wien Bibliothek verfügbar.
The approved original version of this doctoral thesis is available in print at TU Wien Bibliothek.

[90] Y. Han, H. Jing, L. Xu, J. Wei, Optimal Design of SnAgCu-CNT Solder Lap-shear Specimen under Thermal Cycles with FEM, IEEE 2007 8th Int. Conf. Electron. Packag. Technol. 00 (2007) 3–8.

[91] X. Deng, R.S. Sidhu, P. Johnson, N. Chawla, Influence of reflow and thermal aging on the shear strength and fracture behavior of Sn-3.5Ag solder/Cu joints, Metall. Mater. Trans. A Phys. Metall. Mater. Sci. 36 A (2005) 55–64. doi:10.1007/s11661-005-0138-8.

[92] O.M. Abdelhadi, L. Ladani, J. Razmi, Mechanics of Materials Fracture toughness of bonds using interfacial stresses in four-point bending test, Mech. Mater. 43 (2011) 885–900. doi:10.1016/j.mechmat.2011.09.006.

[93] Q.K. Zhang, Z.F. Zhang, In situ observations on creep fatigue fracture behavior of Sn-4Ag/Cu solder joints, Acta Mater. 59 (2011) 6017–6028. doi:10.1016/j.actamat.2011.06.010.

[94] S. Pin, H. Frémont, A. Guédon-gracia, Combined creep characterisation from single lap shear tests and 3D implementation for fatigue simulations, Microelectron. Reliab. 76–77 (2017) 368–372. doi:10.1016/j.microrel.2017.07.053.

[95] H. Ma, Constitutive models of creep for lead-free solders, J. Mater. Sci. 44 (2009) 3841–3851. doi:10.1007/s10853-009-3521-9.

[96] Q.B. Tao, L. Benabou, L. Vivet, V.N. Le, F.B. Ouezdou, Effect of Ni and Sb additions and testing conditions on the mechanical properties and microstructures of lead-free solder joints, Mater. Sci. Eng. A. 669 (2016) 403–416. doi:10.1016/j.msea.2016.05.102.

[97] Y. Tian, C. Hang, C. Wang, S. Yang, P. Lin, Effects of bump size on deformation and fracture behavior of Sn3.0Ag0.5Cu/Cu solder joints during shear testing, Mater. Sci. Eng. A. 529 (2011) 468–478. doi:10.1016/j.msea.2011.09.063.

[98] T.T. Nguyen, D. Yu, S.B. Park, Characterizing the mechanical properties of actual SAC105, SAC305, and SAC405 solder joints by digital image correlation, J. Electron. Mater. 40 (2011) 1409–1415. doi:10.1007/s11664-011-1534-z.

[99] S.F. Choudhury, L. Ladani, Local shear stress-strain response of Sn-3.5Ag/Cu solder joint with high fraction of intermetallic compounds: Experimental analysis, J. Alloys Compd. 680 (2016) 665–676. doi:10.1016/j.jallcom.2016.04.184.

[100] D.W. Henderson, J.J. Woods, T.A. Gosselin, J. Bartelo, D.E. King, The microstructure of Sn in near-eutectic Sn – Ag – Cu alloy solder joints and its role in thermomechanical fatigue, J. Mater. Res. 19 (2004) 1608–1612. doi:10.1557/JMR.2004.0222.

[101] A. Dasgupta, P. Sharma, K. Upadhyayula, Micro-mechanics of fatigue damage in Pb-Sn solder due to vibration and thermal cycling, Int. J. Damage Mech. 10 (2001) 101–132. doi:10.1106/NM1B-1UQH-DJCT-4YH1.

[102] C. Basaran, S. Nie, An irreversible thermodynamics theory for damage mechanics of solids, Int. J. Damage Mech. 13 (2004) 205–223. doi:10.1177/1056789504041058.

[103] C. Basaran, M. Lin, Damage mechanics of electromigration induced failure, Mech. Mater. 40 (2008) 66–79. doi:10.1016/j.mechmat.2007.06.006.

[104] J. Gomez, M. Lin, C. Basaran, Damage Mechanics Modeling of Concurrent Thermal and Vibration Loading on Electronics Packaging, Multidiscip. Model. Mater. Struct. 2 (2006) 309–326. doi:10.1163/157361106777641387.

Die approbierte gedruckte Originalversion dieser Dissertation ist an der TU Wien Bibliothek verfügbar.
The approved original version of this doctoral thesis is available in print at TU Wien Bibliothek.
TU Bibliothek WIEN Your knowledge hub

[105] S. Cheng, C. Huang, M. Pecht, A review of lead-free solders for electronics applications, Microelectron. Reliab. 75 (2017) 77–95. doi:10.1016/j.microrel.2017.06.016.

[106] J. Gomez, C. Basaran, A thermodynamics based damage mechanics constitutive model for low cycle fatigue analysis of microelectronics solder joints incorporating size effects, Int. J. S. 42 (2005) 3744–3772. doi:10.1016/j.ijsolstr.2004.11.022.

[107] D.Y. Wu, S. Meure, D. Solomon, Self-healing polymeric materials : A review of recent developments, Prog. Polym. Sci. 33 (2008) 479–522. doi:10.1016/j.progpolymsci.2008.02.001.

[108] Y. Pan, F. Tian, Z. Zhong, A continuum damage-healing model of healing agents based self-healing materials, Int. J. Damage Mech. 27 (2018) 754–778. doi:10.1177/1056789517702211.

[109] K. Van Tittelboom, N. De Belie, Self-Healing in Cementitious Materials—A Review, Materials (Basel). 6 (2013) 2182–2217. doi:10.3390/ma6062182.

[110] M.D. Hager, S. Van Der Zwaag, U.S. Schubert, Self-healing materials, Springer International Publishing Switzerland 2016, 2010. doi:10.1002/adma.201003036.

[111] N. van Dijk, S. van der Zwaag, Self-Healing Phenomena in Metals, Adv. Mater. Interfaces. 1800226 (2018) 1–13. doi:10.1002/admi.201800226.

[112] H. Fang, C.D. Versteylen, S. Zhang, Y. Yang, P. Cloetens, D. Ngan-tillard, Autonomous filling of creep cavities in Fe-Au alloys studied by synchrotron X-ray nano-tomography, Acta Mater. 121 (2016) 352–364. doi:10.1016/j.actamat.2016.09.023.

[113] B.S. Zhang, C. Kwakernaak, W. Sloof, E. Brück, S. Van Der Zwaag, N. Van Dijk, Self Healing of Creep Damage by Gold Precipitation in Iron Alloys, Adv. Eng. Mater. (2015). doi:10.1002/adem.201400511.

[114] R. Xin, Q. Ma, W. Li, Microstructure and mechanical properties of internal crack healing in a low carbon steel, Mater. Sci. Eng. A. 662 (2016) 65–71. doi:10.1016/j.msea.2016.03.045.

[115] H. Yu, X. Liu, X. Li, A. Godbole, Crack Healing in a Low-Carbon Steel Under Hot Plastic Deformation, Metall. Mater. Trans. A. 45 (2014) 1001–1009. doi:10.1007/s11661-013-2049-4.

[116] R. Xin, J. Luo, Q. Ma, Effect of Parameters on Internal Crack Healing in 30Cr2Ni4MoV Steel for 600-Ton Ultra-Super Ingots, Metals (Basel). (2017) 1–12. doi:10.3390/met7040149.

[117] W. Yao, C. Basaran, Electromigration damage mechanics of lead-free solder joints under pulsed DC: A computational model, Comput. Mater. Sci. 71 (2013) 76–88. doi:10.1016/j.commatsci.2013.01.016.

[118] J. Tao, B.K. Liew, J.F. Chen, N.W. Cheung, C. Hu, Electromigration under time-varying current stress, Microelectron. Reliab. 38 (1998) 295–308. doi:10.1016/S0026-2714(97)00057-7.

[119] W. Xu, C. Yang, H. Yu, X. Jin, B. Guo, D. Shan, Microcrack healing in non-ferrous metal tubes through eddy current pulse treatment, Sci. Rep. 8 (2018) 1–11. doi:10.1038/s41598-018-24354-7.

Die approbierte gedruckte Originalversion dieser Dissertation ist an der TU Wien Bibliothek verfügbar.
The approved original version of this doctoral thesis is available in print at TU Wien Bibliothek.
TU WIEN Bibliothek Your knowledge hub

[120] A.D. Moghadam, B.F. Schultz, J.B. Ferguson, E. Omrani, P.K. Rohatgi, N. Gupta, Functional metal matrix composites: Self-lubricating, self-healing, and nanocomposites-an outlook, Jom. 66 (2014) 872–881. doi:10.1007/s11837-014-0948-5.

[121] P. Zhu, Z. Cui, M.S. Kesler, J.A. Newman, M. V Manuel, M.C. Wright, L.C. Brinson, N. Langley, Characterization and modeling of three-dimensional self-healing shape memory alloy-reinforced metal-matrix composites, Mech. Mater. 103 (2016) 1–10. doi:10.1016/j.mechmat.2016.09.005.

[122] G. Siroky, E. Kraker, J. Magnien, D. Kieslinger, E. Kozeschnik, W. Ecker, Numerical study on local effects of composition and geometry in self-healing solders, in: 2019 20th Intl. Conf. Th. Mech. Mlt.Pys. Sim. Exp. Mic.El. Mic.Sys., 2019.

[123] R. Davies, A. Jefferson, Micromechanical modelling of self-healing cementitious materials, Int. J. Solids Struct. 113–114 (2017) 180–191. doi:10.1016/j.ijsolstr.2017.02.008.

[124] R.K.A. Al-rub, M.K. Darabi, D.N. Little, E.A. Masad, A micro-damage healing model that improves prediction of fatigue life in asphalt mixes, Int. J. Eng. Sci. 48 (2010) 966–990. doi:10.1016/j.ijengsci.2010.09.016.

[125] C.D. Versteylen, N.K. Szymański, M.H.F. Sluiter, N.H. Van Dijk, Finite element modelling of creep cavity filling by solute diffusion, Philos. Mag. 6435 (2018) 1–14. doi:10.1080/14786435.2017.1418097.

[126] W. Xu, X. Sun, B.J. Koeppel, H.M. Zbib, A continuum thermo-inelastic model for damage and healing in self-healing glass materials, Int. J. Plast. 62 (2014) 1–16. doi:10.1016/j.ijplas.2014.06.011.

[127] E.J. Barbero, F. Greco, P. Lonetti, Continuum Damage-Healing Mechanics with application to self-healing composites, Int. J. Damage Mech. 14 (2005) 51–81. doi:10.1177/1056789505045928.

[128] J. Mergheim, P. Steinmann, Phenomenological modelling of self-healing polymers based on integrated healing agents, Comput. Mech. 52 (2013) 681–692. doi:10.1007/s00466-013-0840-0.

[129] G.Z. Voyiadjis, A. Shojaei, G. Li, A generalized coupled viscoplastic – viscodamage – viscohealing theory for glassy polymers, Int. J. Plast. 28 (2012) 21–45. doi:10.1016/j.ijplas.2011.05.012.

[130] G.Z. Voyiadjis, P.I. Kattan, Mechanics of damage, healing, damageability, and integrity of materials: A conceptual framework, Int. J. Damage Mech. 26 (2017) 49–102. doi:10.1177/1056789516635730.

[131] M.K. Darabi, R.K. Abu Al-Rub, D.N. Little, A continuum damage mechanics framework for modeling micro-damage healing, Int. J. Solids Struct. 49 (2012) 492–513. doi:10.1016/j.ijsolstr.2011.10.017.

[132] C.D. Versteylen, M.H.F. Sluiter, N.H. Van Dijk, Modelling the formation and self-healing of creep damage in iron-based alloys, J. Mater. Sci. 53 (2018) 14758–14773. doi:10.1007/s10853-018-2666-9.

[133] X.D. Liu, D.G. Shang, G.Q. Sun, Fatigue damage-healing model based on plasticity change for copper film by laser repair, Int. J. Damage Mech. 28 (2019) 1053–1074. doi:10.1177/1056789518812923.

Die approbierte gedruckte Originalversion dieser Dissertation ist an der TU Wien Bibliothek verfügbar.
The approved original version of this doctoral thesis is available in print at TU Wien Bibliothek.
TU WIEN Bibliothek Your knowledge hub

[134] G.Z. Voyiadjis, C. Oucif, P. Kattan, T. Rabczuk, Damage and healing mechanics in plane stress, plane strain, and isotropic elasticity, Int. J. Damage Mech. 0 (2020) 105678952090534. doi:10.1177/1056789520905347.

[135] C. Oucif, G.Z. Voyiadjis, P.I. Kattan, T. Rabczuk, Investigation of the super healing theory in continuum damage and healing mechanics, Int. J. Damage Mech. 28 (2019) 896–917. doi:10.1177/1056789518799822.

[136] G.Z. Voyiadjis, P.I. Kattan, Decomposition of healing tensor: In continuum damage and healing mechanics, Int. J. Damage Mech. 27 (2018) 1020–1057. doi:10.1177/1056789517720969.

[137] A.L. Gurson, Continuum Theory of Ductile Rupture by Void Nucleation and Growth : Part 1 — Yield Criteria and Flow Rules for Porous Ductile Media, J. Eng. Mater. Technol. 99 (1977) 2–15. doi:https://doi.org/10.1115/1.3443401.

[138] V. Tvergaard, A. Needleman, Analysis of the cup-cone fracture in a round tensile bar, Acta Metall. 32 (1984) 157–169.

[139] M.F. Horstemeyer, A.M. Gokhale, A void-crack nucleation model for ductile metals, Int. J. Solids Struct. 36 (1999) 5029–5055.

[140] Y. Hammi, M.F. Horstemeyer, A physically motivated anisotropic tensorial representation of damage with separate functions for void nucleation , growth , and coalescence, Int. J. Plast. 23 (2007) 1641–1678. doi:10.1016/j.ijplas.2007.03.010.

[141] J.R. Rice, D.M. Tracey, On the ductile enlargement of voids in triaxial stress fields, J. Mech. Phys. Solids. 17 (1969) 201–217. doi:https://doi.org/10.1016/0022-5096(69)90033-7.

[142] F.A. McClintock, A Criterion for Ductile Fracture by the Growth of Holes, J. Appl. Mech. (1968) 363–371.

[143] T. Pardoen, L. Lecarme, C. Teko, Void growth and coalescence in ductile solids with stage III and stage IV strain hardening, Int. J. Plast. 27 (2011) 1203–1223. doi:10.1016/j.ijplas.2011.01.004.

[144] A. Chandra, V. Tvergaard, Void Nucleation and Growth during Plane Strain Extrusion, Int. J. Damage Mech. 2 (1993) 330–348. doi:10.1177/105678959300200402.

[145] A. Matzenmiller, J. Lubliner, R.E. Taylor, An Anisotropic Damage Model for Ductile Metals, Int. J. Damage Mech. 12 (2003) 1–33. doi:10.1177/105678903033631.

[146] M. Djouabi, A. Ati, P.Y. Manach, Identification strategy influence of elastoplastic behavior law parameters on Gurson–Tvergaard–Needleman damage parameters: Application to DP980 steel, Int. J. Damage Mech. 28 (2019) 427–454. doi:10.1177/1056789518772130.

[147] A.C.F. Cocks, M.F. Ashby, On creep fracture by void growth, Prog. Mater. Sci. 27 (1982) 189–244. doi:https://doi.org/10.1016/0079-6425(82)90001-9.

[148] M.E. Kassner, T.A. Hayes, Creep cavitation in metals, Int. J. Plast. 19 (2003) 1715–1748.

[149] A.C.F. Cocks, M.F. Ashby, Creep fracture by coupled power-law creep and diffusion under multiaxial stress, Met. Sci. 16 (1982) 465–474. doi:https://doi.org/10.1179/msc.1982.16.10.465.

Die approbierte gedruckte Originalversion dieser Dissertation ist an der TU Wien Bibliothek verfügbar.
The approved original version of this doctoral thesis is available in print at TU Wien Bibliothek.
TU WIEN Bibliothek Your knowledge hub

[150] A. Needleman, J.R. Rice, Plastic creep flow effects in the diffusive cavitation of grain boundaries, Third Edit, Pergamon Press Ltd, 1980. doi:10.1016/B978-0-08-030541-7.50009-6.

[151] D. Hull, D.E. Rimmer, The growth of grain-boundary voids under stress, Philos. Mag. (2010) 37–41. doi:http://dx.doi.org/10.1080/14786435908243264.

[152] B.Z. Margolin, G.P. Karzov, V.A. Shvetsova, V.I. Kostylev, Modeling for transcrystalline and intercrystalline fracture by void nucleation and growth, Fatigue Fract. Eng. Mater. Struct. 21 (1998) 123–137.

[153] M.F. Horstemeyer, D.J. Bammann, Historical review of internal state variable theory for inelasticity, Int. J. Plast. 26 (2010) 1310–1334. doi:10.1016/j.ijplas.2010.06.005.

[154] M.F. Horstemeyer, J. Lathrop, A.M. Gokhale, M. Dighe, Modeling stress state dependent damage evolution in a cast Al-Si-Mg aluminum alloy, Theor. Appl. Fract. Mech. 33 (2000) 31–47.

[155] J. Lemaitre, Coupled Elasto-Plasticity and Damage Constitutive Equations, Comput. Methods Appl. Mech. Eng. (1985).

[156] J.L. Chaboche, Continuum Damage Mechanics: Part II - Damage Growht, Crack Initiation and Crack Growth, J. Appl. Mech. 55 (2014) 56–72.

[157] Y. Lee, C. Basaran, A Creep Model for Solder Alloys, J. Electron. Packag. 133 (2011) 044501. doi:10.1115/1.4005288.

[158] A. Kroupa, A.T. Dinsdale, A. Watson, J. Vrestal, J. Vízdal, A. Zemanova, The development of the COST 531 lead-free solders thermodynamic database, J. Miner. Met. Mater. Soc. 59 (2007) 20–25. doi:10.1007/s11837-007-0084-6.

[159] J. Schindelin, I. Arganda-Carreras, E. Frise, E. Al., Fiji: an open-source platform for biological-image analysis, Nat. Methods. 9 (2012) 676–682. doi:10.1038/nmeth.2019.

[160] Z.P. Wang, Q.J. Yang, Creep Behavior and Deformation Mechanism Map of Sn-Pb, J. Eng. Mater. Technol. 125 (2016) 81–88. doi:10.1115/1.1525254.

[161] Y. Yao, X. He, L.M. Keer, M.E. Fine, A continuum damage mechanics-based unified creep and plasticity model for solder materials, Acta Mater. 83 (2015) 160–168. doi:10.1016/j.actamat.2014.09.051.

[162] D.L. McDowell, M.P. Miller, Unified creep-plasticity theory for solder alloys, in: Symp. Fatigue Electron. Mater. Atlanta, GA, USA;, 1994: pp. 42–59.

[163] J.L. Chaboche, G. Gailletaud, On the calculation of structures in cyclic plasticity or viscoplasticity, Comput. Struct. 23 (1986) 23–31. doi:10.1016/0045-7949(86)90103-3.

[164] J.L. Chaboche, Constitutive equations for cyclic plasticity and cyclic viscoplasticity, Int. J. Plast. 5 (1989) 247–302. doi:DOI: 10.1016/0749-6419(89)90015-6.

[165] G.Z. Voyiadjis, A. Shojaei, G. Li, P. Kattan, Continuum damage-healing mechanics with introduction to new healing variables, Int. J. Damage Mech. 21 (2012) 391–414. doi:10.1177/1056789510397069.

[166] P. Sharma, A. Dasgupta, Micro-Mechanics of Creep-Fatigue Damage in PB-SN Solder Due to Thermal Cycling—Part I: Formulation, J. Electron. Packag. 124 (2002) 292–297. doi:10.1115/1.1493202.

TU WIEN Bibliothek Your knowledge hub
Die approbierte gedruckte Originalversion dieser Dissertation ist an der TU Wien Bibliothek verfügbar.
The approved original version of this doctoral thesis is available in print at TU Wien Bibliothek.

[167] P. Sharma, A. Dasgupta, G. Cuddalorepatta, The connection between microstructural damage modeling and continuum damage modeling for eutectic Sn-Pb solder alloys, Int. J. Damage Mech. 14 (2005) 343–363. doi:10.1177/1056789505054302.

[168] H. Alehossein, Z. Qin, Numerical analysis of Rayleigh – Plesset equation for cavitating water jets, Int. J. Numer. Methods Eng. (2007) 780–807. doi:10.1002/nme.

[169] C.E. Brennen, Fundamentals of Multiphase Flows, Cambridge University Press 2005, 2005.

[170] J.P. Chem, R. Data, Reference Data for the Density , Viscosity , and Surface Tension of Liquid Al – Zn , Ag – Sn , Bi – Sn , Cu – Sn , and Sn – Zn Eutectic Alloys, 013102 (2018) 1–18. doi:10.1063/1.5010151.

[171] A. Dobosz, T. Gancarz, Reference Data for the Density, Viscosity, and Surface Tensionof Liquid Al–Zn, Ag–Sn, Bi–Sn, Cu–Sn, and Sn–ZnEutectic Alloys, J. Phys. Chem. Ref. Data. 47 (2018). doi:10.1063/1.5010151.

[172] K.S. Kim, S.H. Huh, K. Suganuma, Effects of intermetallic compounds on properties of Sn–Ag–Cu lead-free soldered joints, J. Alloys Compd. 352 (2003) 226–236. doi:10.1016/S0925-8388(02)01166-0.

[173] Y.S. Kim, K.S. Kim, C.W. Hwang, K. Suganuma, Effect of composition and cooling rate on microstructure and tensile properties of Sn-Zn-Bi alloys, J. Alloys Compd. 352 (2003) 237–245. doi:10.1016/S0925-8388(02)01168-4.

[174] S. Cheng, C. Huang, M. Pecht, Microelectronics Reliability Review paper A review of lead-free solders for electronics applications, Microelectron. Reliab. 75 (2017) 77–95. doi:10.1016/j.microrel.2017.06.016.

[175] P. Liu, P.E.I. Yao, J.I.M. Liu, Effect of SiC Nanoparticle Additions on Microstructure and Microhardness of Sn-Ag-Cu Solder Alloy, J. Electron. Mater. 37 (2008) 874–879. doi:10.1007/s11664-007-0366-3.

[176] G. Siroky, E. Kraker, J. Rosc, D. Kieslinger, R. Brunner, S. van der Zwaag, E. Kozeschnik, W. Ecker, Analysis of Sn-Bi Solders: X-ray Micro Computed Tomography Imaging and Microstructure Characterization in Relation to Properties and Liquid Phase Healing Potential, Mater. . 14 (2021). doi:10.3390/ma14010153.

[177] Y. Lai, X. Hu, Y. Li, X. Jiang, Influence of Bi Addition on Pure Sn Solder Joints: Interfacial Reaction, Growth Behavior and Thermal Behavior, J. Wuhan Univ. Technol. Sci. Ed. 34 (2019) 668–675. doi:10.1007/s11595-019-2102-2.

[178] G. Siroky, E. Kraker, D. Kieslinger, E. Kozeschnik, W. Ecker, Micromechanics-based damage model for liquid-assisted healing, Int. J. Damage Mech. 0 (2020) 1–22. doi:10.1177/1056789520948561.

[179] Y. Liu, R. Tandon, R.M. German, Modeling of Supersolidus Liquid Phase Sintering: II. Densification, Metall. Mater. Trans. A. 26 (1995) 2423–2430.

[180] S. Wen, L.M. Keer, H. Mavoori, Constitutive and Damage Model for a Lead-Free Solder, 30 (2001) 1190–1196.

[181] R.L.J.M. Ubachs, P.J.G. Schreurs, M.G.D. Geers, Elasto-viscoplastic nonlocal damage modelling of thermal fatigue in anisotropic lead-free solder, Mech. Mater. 39 (2007) 685–701. doi:10.1016/j.mechmat.2006.11.001.

TU WIEN Bibliothek Your knowledge hub
Die approbierte gedruckte Originalversion dieser Dissertation ist an der TU Wien Bibliothek verfügbar.
The approved original version of this doctoral thesis is available in print at TU Wien Bibliothek.

[182] C.-Y.Y. Basaran C., A Thermodynamic Framework for Damage Mechanics of Solder Joints, J. Electron. Packag. 120 (1998) 379–384. doi:https://doi.org/10.1115/1.2792650.

[183] M. Kuna, S. Wippler, A cyclic viscoplastic and creep damage model for lead free solder alloys, Eng. Fract. Mech. 77 (2010) 3635–3647. doi::10.1016/j.engfracmech.2010.03.015.

[184] J. Lemaitre, Mechanics of Solid Materials, 2000.

[185] P. V Petkov, B.P. Radoev, Colloids and Surfaces A : Physicochemical and Engineering Aspects Statics and dynamics of capillary bridges, Colloids Surfaces A Physicochem. Eng. Asp. 460 (2014) 18–27. doi:10.1016/j.colsurfa.2014.03.038.

[186] M.K. Darabi, R.K. Abu Al-Rub, D.N. Little, A continuum damage mechanics framework for modeling micro-damage healing, Int. J. Solids Struct. 49 (2012) 492–513. doi:10.1016/j.ijsolstr.2011.10.017.

[187] L. Shen, P. Septiwerdani, Z. Chen, Elastic modulus, hardness and creep performance of SnBi alloys using nanoindentation, Mater. Sci. Eng. A. 558 (2012) 253–258. doi:10.1016/j.msea.2012.07.120.

[188] F. Wang, Y. Huang, Z. Zhang, C. Yan, Interfacial reaction and mechanical properties of Sn-Bi solder joints, Materials (Basel). 10 (2017) 1–16. doi:10.3390/ma10080920.

[189] J. Schindelin, I. Arganda-Carreras, E. Frise, V. Kaynig, M. Longair, T. Pietzsch, S. Preibisch, C. Rueden, S. Saalfeld, B. Schmid, J.Y. Tinevez, D.J. White, V. Hartenstein, K. Eliceiri, P. Tomancak, A. Cardona, Fiji: An open-source platform for biological-image analysis, Nat. Methods. 9 (2012) 676–682. doi:10.1038/nmeth.2019.

[190] G. Siroky, E. Kraker, D. Kieslinger, L. Romaner, E. Kozeschnik, W. Ecker, Modelling of Void Collapse with Molecular Dynamics in Pure Sn, Proc. . 56 (2020). doi:10.3390/proceedings2020056029.

[191] M. Doube, M.M. Klosowski, I. Arganda-Carreras, F.P. Cordelières, R.P. Dougherty, J.S. Jackson, B. Schmid, J.R. Hutchinson, S.J. Shefelbine, BoneJ: Free and extensible bone image analysis in ImageJ, Bone. 47 (2010) 1076–1079. doi:10.1016/j.bone.2010.08.023.

[192] N. Chawla, R.S. Sidhu, V. V. Ganesh, Three-dimensional visualization and microstructure-based modeling of deformation in particle-reinforced composites, Acta Mater. 54 (2006) 1541–1548. doi:10.1016/j.actamat.2005.11.027.

[193] A.A. El-Daly, A.A. Ibrahiem, A.E. Hammad, Impact of permanent magnet stirring on dendrite growth and elastic properties of Sn–Bi alloys revealed by pulse echo overlap method, J. Alloys Compd. 767 (2018) 464–473. doi:10.1016/j.jallcom.2018.07.122.

[194] X. Wu, J. Wu, X. Wang, J. Yang, M. Xia, B. Liu, Effect of In addition on microstructure and mechanical properties of Sn–40Bi alloys, J. Mater. Sci. 55 (2020) 3092–3106. doi:10.1007/s10853-019-04148-6.

[195] O. Mokhtari, H. Nishikawa, Correlation between microstructure and mechanical properties of Sn – Bi – X solders, Mater. Sci. Eng. A. 651 (2016) 831–839. doi:10.1016/j.msea.2015.11.038.

[196] D.G. Eskin, Suyitno, L. Katgerman, Mechanical properties in the semi-solid state and hot tearing of aluminium alloys, Prog. Mater. Sci. 49 (2004) 629–711. doi:10.1016/S0079-6425(03)00037-9.

Die approbierte gedruckte Originalversion dieser Dissertation ist an der TU Wien Bibliothek verfügbar.
The approved original version of this doctoral thesis is available in print at TU Wien Bibliothek.
TU Bibliothek Your knowledge hub WIEN

[197] A. Wijaya, B. Eichinger, F.F. Chamasemani, B. Sartory, R. Hammer, V. Maier-Kiener, D. Kiener, M. Mischitz, R. Brunner, Multi-method characterization approach to facilitate a strategy to design mechanical and electrical properties of sintered copper, Mater. Des. 197 (2020) 109188. doi:10.1016/j.matdes.2020.109188.

[198] T.R. Bieler, B. Zhou, L. Blair, A. Zamiri, P. Darbandi, F. Pourboghrat, T.K. Lee, K.C. Liu, The role of elastic and plastic anisotropy of Sn in recrystallization and damage evolution during thermal cycling in SAC305 solder joints, J. Electron. Mater. 41 (2012) 283–301. doi:10.1007/s11664-011-1811-x.

[199] G. Siroky, D. Melinc, J. Magnien, E. Kozeschnik, D. Kieslinger, E. Kraker, W. Ecker, Healing solders: A numerical investigation of damage-healing experimentse, in: 2020 21st Int. Conf. Therm. Mech. Multi-Physics Simul. Exp. Microelectron. Microsystems, 2020: pp. 1–7.

[200] C.L. Martin, S.B. Brown, D. Favier, M. Suéry, Shear deformation of high solid fraction (>0.60) semi-solid SnPb under various structures, Mater. Sci. Eng. A. 202 (1995) 112–122. doi:10.1016/0921-5093(95)09797-X.

[201] D. Fuloria, P.D. Lee, An X-ray microtomographic and finite element modeling approach for the prediction of semi-solid deformation behaviour in Al-Cu alloys, Acta Mater. 57 (2009) 5554–5562. doi:10.1016/j.actamat.2009.07.051.

[202] K.M. Kareh, P.D. Lee, R.C. Atwood, T. Connolley, C.M. Gourlay, Revealing the micromechanisms behind semi-solid metal deformation with time-resolved X-ray tomography, Nat. Commun. 5 (2014) 1–7. doi:10.1038/ncomms5464.

[203] B. Cai, S. Karagadde, L. Yuan, T.J. Marrow, T. Connolley, P.D. Lee, In situ synchrotron tomographic quantification of granular and intragranular deformation during semi-solid compression of an equiaxed dendritic Al-Cu alloy, Acta Mater. 76 (2014) 371–380. doi:10.1016/j.actamat.2014.05.035.

[204] P.C. Carman, Fluid flow through granular beds, Chem. Eng. Res. Des. 75 (1997). doi:https://doi.org/10.1016/S0263-8762(97)80003-2.

[205] M. Sistaninia, A.B. Phillion, J.M. Drezet, M. Rappaz, Three-dimensional granular model of semi-solid metallic alloys undergoing solidification: Fluid flow and localization of feeding, Acta Mater. 60 (2012) 3902–3911. doi:10.1016/j.actamat.2012.03.036.

[206] X. Chen, J. Zhou, F. Xue, Y. Yao, Mechanical deformation behavior and mechanism of Sn-58Bi solder alloys under different temperatures and strain rates, Mater. Sci. Eng. A. 662 (2016) 251–257. doi:10.1016/j.msea.2016.03.072.

[207] L. Shen, P. Lu, S. Wang, Z. Chen, Creep behaviour of eutectic SnBi alloy and its constituent phases using nanoindentation technique, J. Alloys Compd. 574 (2013) 98–103. doi:10.1016/j.jallcom.2013.04.057.

[208] F. Wang, H. Chen, Y. Huang, C. Yan, Interfacial behavior and joint strength of Sn – Bi solder with solid solution compositions, J. Mater. Sci. Mater. Electron. 29 (2018) 11409–11420. doi:10.1007/s10854-018-9233-7.

[209] F. Wang, Y. Ding, L. Liu, Y. Huang, M. Wu, Wettability, Interfacial Behavior and Joint Properties of Sn-15Bi Solder, J. Electron. Mater. 48 (2019) 6835–6848. doi:10.1007/s11664-019-07473-3.

[210] Q. Lii, Y. Leii, J. Lin, S. Yangi, Design and properties of Sn-Bi-In low-temperature solders, in: 16th Int. Conf. Electron. Packag. Technol., 2015: pp. 497–500.

Die approbierte gedruckte Originalversion dieser Dissertation ist an der TU Wien Bibliothek verfügbar.
The approved original version of this doctoral thesis is available in print at TU Wien Bibliothek.
TU Bibliothek Your knowledge hub WIEN

[211] C.M. Chen, L.T. Chen, Y.S. Lin, Electromigration-induced Bi segregation in eutectic SnBi solder joint, J. Electron. Mater. 36 (2007) 168–172. doi:10.1007/s11664-006-0025-0.

[212] J. Sun, G. Xu, F. Guo, Z. Xia, Y. Lei, Y. Shi, X. Li, X. Wang, Effects of electromigration on resistance changes in eutectic SnBi solder joints, J. Mater. Sci. 46 (2011) 3544–3549. doi:10.1007/s10853-011-5265-6.

[213] O. V. Gusakova, V.G. Shepelevich, L.P. Scherbachenko, Aging of rapidly solidified eutectic alloys Sn–Bi, Sn–Pb, and Bi–Cd, Inorg. Mater. Appl. Res. 7 (2016) 698–703. doi:10.1134/S2075113316050087.

[214] Z. Lai, D. Ye, Effect of cooling method and aging treatment on the microstructure and mechanical properties of Sn – 10Bi solder alloy, J. Mater. Sci. Mater. Electron. 27 (2016) 1398–1407. doi:10.1007/s10854-015-3903-5.

[215] Y. Plevachuk, V. Sklyarchuk, G. Gerbeth, S. Eckert, R. Novakovic, Surface tension and density of liquid Bi-Pb , Bi-Sn and Bi-Pb-Sn eutectic alloys, Surf. Sci. 605 (2011) 1034–1042. doi:10.1016/j.susc.2011.02.026.

[216] R.M. Shalaby, Effect of silver and indium addition on mechanical properties and indentation creep behavior of rapidly solidified Bi-Sn based lead-free solder alloys, Mater. Sci. Eng. A. 560 (2013) 86–95. doi:10.1016/j.msea.2012.09.038.

[217] H. Sun, Q. Li, Y.C. Chan, A study of Ag additive methods by comparing mechanical properties between Sn57.6Bi0.4Ag and 0.4 wt% nano-Ag-doped Sn58Bi BGA solder joints, J. Mater. Sci. Mater. Electron. 25 (2014) 4380–4390. doi:10.1007/s10854-014-2177-7.

[218] C. Zhang, S. Liu, G. Qian, J. Zhou, F. Xue, Effect of Sb content on properties of SníBi solders, Trans. Nonferrous Met. Soc. China. 24 (2014) 184–191. doi:10.1016/S1003-6326(14)63046-6.

[219] B.L. Silva, G. Reinhart, H. Nguyen-Thi, N. Mangelinck-Noël, A. Garcia, J.E. Spinelli, Microstructural development and mechanical properties of a near-eutectic directionally solidified Sn-Bi solder alloy, Mater. Charact. 107 (2015) 43–53. doi:10.1016/j.matchar.2015.06.026.

[220] B.L. Silva, A. Garcia, J.E. Spinelli, Complex eutectic growth and Bi precipitation in ternary Sn-Bi-Cu and Sn-Bi-Ag alloys, J. Alloys Compd. 691 (2017) 600–605. doi:10.1016/j.jallcom.2016.09.003.

[221] B.L. Silva, M.G.C. Xavier, A. Garcia, J.E. Spinelli, Cu and Ag additions affecting the solidification microstructure and tensile properties of Sn-Bi lead-free solder alloys, Mater. Sci. Eng. A. 705 (2017) 325–334. doi:10.1016/j.msea.2017.08.059.

[222] M.I. Okereke, Y. Ling, A computational investigation of the effect of three-dimensional void morphology on the thermal resistance of solder thermal interface materials, Appl. Therm. Eng. 142 (2018) 346–360. doi:10.1016/j.applthermaleng.2018.07.002.

[223] L. Jiang, N. Chawla, M. Pacheco, V. Noveski, Three-dimensional (3D) microstructural characterization and quantification of reflow porosity in Sn-rich alloy/copper joints by X-ray tomography, Mater. Charact. 62 (2011) 970–975. doi:10.1016/j.matchar.2011.07.011.

TU WIEN Bibliothek Your knowledge hub
Die approbierte gedruckte Originalversion dieser Dissertation ist an der TU Wien Bibliothek verfügbar.
The approved original version of this doctoral thesis is available in print at TU Wien Bibliothek.

[224] M. Rauer, A. Volkert, T. Schreck, S. Härter, M. Kaloudis, Computed-tomography-based analysis of voids in SnBi57Ag1 solder joints and their influence on the reliability, J. Fail. Anal. Prev. 14 (2014) 272–281. doi:10.1007/s11668-014-9801-y.

[225] E. Padilla, V. Jakkali, L. Jiang, N. Chawla, Quantifying the effect of porosity on the evolution of deformation and damage in Sn-based solder joints by X-ray microtomography and microstructure-based finite element modeling, Acta Mater. 60 (2012) 4017–4026. doi:10.1016/j.actamat.2012.03.048.

[226] G. Zeng, S.D. McDonald, C.M. Gourlay, K. Uesugi, Y. Terada, H. Yasuda, K. Nogita, Solidification of Sn-0.7Cu-0.15Zn solder: In situ observation, Metall. Mater. Trans. A Phys. Metall. Mater. Sci. 45 (2014) 918–926. doi:10.1007/s11661-013-2008-0.

[227] M. Sona, K.N. Prabhu, Review on microstructure evolution in Sn – Ag – Cu solders and its effect on mechanical integrity of solder joints, J. Mater. Sci. Mater. Electron. 24 (2013) 3149–3169. doi:10.1007/s10854-013-1240-0.

[228] W. Dong, Y. Shi, Y. Lei, Z. Xia, F. Guo, Study of solidification cracks in Sn-Ag-Cu lead-free solder joints, J. Electron. Mater. 38 (2009) 1906–1912. doi:10.1007/s11664-009-0839-7.

[229] W. Lu, Y. Shi, Y. Lei, Effect of Ag content on solidification cracking susceptibility of Sn-Ag-Cu solder joints, J. Electron. Mater. 39 (2010) 1298–1302. doi:10.1007/s11664-010-1175-7.

[230] G. Siroky, D. Melinc, J. Magnien, E. Kozeschnik, D. Kieslinger, E. Kraker, W. Ecker, Healing solders: A numerical investigation of damage-healing experiments, in: 2020 21th Intl. Conf. Th. Mech. Mlt.Pys. Sim. Exp. Mic.El. Mic.Sys., n.d.

[231] M. Sistaninia, A.B. Phillion, J.M. Drezet, M. Rappaz, A 3-D coupled hydromechanical granular model for simulating the constitutive behavior of metallic alloys during solidification, Acta Mater. 60 (2012) 6793–6803. doi:10.1016/j.actamat.2012.08.057.

[232] L. Wang, N. Wang, N. Provatas, Liquid channel segregation and morphology and their relation with hot cracking susceptibility during columnar growth in binary alloys, Acta Mater. 126 (2017) 302–312. doi:10.1016/j.actamat.2016.11.058.

[233] J. Liu, S. Kou, Crack susceptibility of binary aluminum alloys during solidification, Acta Mater. 110 (2016) 84–94. doi:10.1016/j.actamat.2016.03.030.

[234] S. Li, D. Apelian, Hot Tearing of Aluminum Alloys, Int. J. Met. 5 (2011) 23–40. doi:10.1007/bf03355505.

[235] C. Pequet, M. Rappaz, M. Gremaud, Modeling of microporosity, macroporosity, and pipe-shrinkage formation during the solidification of alloys using a mushy-zone refinement method: Applications to aluminum alloys, Metall. Mater. Trans. A Phys. Metall. Mater. Sci. 33 (2002) 2095–2106. doi:10.1007/s11661-002-0041-5.

[236] M. Sistaninia, S. Terzi, A.B. Phillion, J.M. Drezet, M. Rappaz, 3-D granular modeling and in situ X-ray tomographic imaging: A comparative study of hot tearing formation and semi-solid deformation in Al-Cu alloys, Acta Mater. 61 (2013) 3831–3841. doi:10.1016/j.actamat.2013.03.021.

[237] S. Kou, A criterion for cracking during solidification, Acta Mater. 88 (2015) 366–374. doi:10.1016/j.actamat.2015.01.034.

Die approbierte gedruckte Originalversion dieser Dissertation ist an der TU Wien Bibliothek verfügbar.
The approved original version of this doctoral thesis is available in print at TU Wien Bibliothek.
TU WIEN Bibliothek Your knowledge hub

[238] M. Rappaz, J.M. Drezet, M. Gremaud, A new hot-tearing criterion, Metall. Mater. Trans. A Phys. Metall. Mater. Sci. 30 (1999) 449–455. doi:10.1007/s11661-999-0334-z.

[239] D.J. Lahaie, M. Bouchard, Physical modeling of the deformation mechanisms of semisolid bodies and a mechanical criterion for hot tearing, Metall. Mater. Trans. B Process Metall. Mater. Process. Sci. 32 (2001) 697–705. doi:10.1007/s11663-001-0124-5.

[240] G. Siroky, E. Kraker, J. Rosc, D. Kieslinger, R. Brunner, S. van der Zwaag, E. Kozeschnik, W. Ecker, Analysis of Sn-Bi solders: X-ray micro computed tomography imaging and microstructure characterization in relation to properties and liquid phase healing potential, Unpubl. Res. (Submitted Mater. MDPI). (2020).

Die approbierte gedruckte Originalversion dieser Dissertation ist an der TU Wien Bibliothek verfügbar.
The approved original version of this doctoral thesis is available in print at TU Wien Bibliothek.
TU WIEN Bibliothek Your knowledge hub